Silver Filament Formation/Dissolution Dynamics Through a Polymer/Ionic liquid Composite by Direct-write

by

Zhongmou Chao

Master of Science, Columbia University, 2015

Submitted to the Graduate Faculty of

the Swanson School of Engineering in partial fulfillment

of the requirements for the degree of

Doctor of Philosophy

University of Pittsburgh

2020

UNIVERSITY OF PITTSBURGH

SWANSON SCHOOL OF ENGINEERING

This dissertation was presented

by

Zhongmou Chao

It was defended on

October 28, 2020

and approved by

Susan Fullerton-Shirey, Ph.D, Associate Professor, Department of Chemical and Petroleum Engineering

James McKone, Ph.D, Assistant Professor, Department of Chemical and Petroleum Engineering

Eric Beckman, Ph.D, Professor, Department of Chemical and Petroleum Engineering

Jennifer Laaser, Ph.D, Assistant Professor, Department of Chemistry

Dissertation Director: Susan Fullerton-Shirey, Ph.D, Associate Professor, Department of Chemical and Petroleum Engineering

Silver Filament Formation/Dissolution Dynamics Through a Polymer/Ionic liquid Composite by Direct-write

Zhongmou Chao, PhD

University of Pittsburgh, 2020

A direct-write, electrochemical approach to the formation and dissolution of silver nanofilaments is demonstrated through a novel polymer electrolyte consisting of a UV-crosslinkable polymer, polyethylene glycol diacrylate (PEGDA) and an ionic liquid (IL), 1-butyl-3-methylimadozolium hexafluorophosphate ([BMIM]PF_6). Nanofilaments are formed and dissolved at pre-programmed locations with a conductive atomic force microscope (c-AFM) using a custom script. Although the formation time generally decreases with increasing bias from 0.7 to 3.0 V, an unexpected non-monotonic maximum is observed ∼2.0 V. At voltages approaching this region of inverted kinetics, IL electric double layers (EDLs) become detectable; thus, the increased nanofilament formation time can be attributed to electric field screening, which hinders silver electromigration and deposition. Scanning electron microscopy confirms that nanofilaments formed in this inverted region have significantly more lateral and diffuse features. Time dependent formation currents reveal two types of nanofilament growth dynamics: abrupt, where the resistance decreases sharply over as little as a few ms, and gradual where it decreases more slowly over hundreds of ms. Whether the resistance change is abrupt or gradual depends on the extent to which the EDL screens the electric field. Silver nanofilaments with gradual growth dynamics have potential application in neuromorphic computing. In this study, a linear ($R^2 > 0.9$) dependence of conductance on the number of bias pulses is demonstrated—a signature feature that is required for neuromorphic application. Hundreds of distinguishable conductance states ranging from 235 to 260 microsimens can be accessed using a low read bias. These results show that novel PEGDA/IL composite electrolyte enables the gradual formation and dissolution of silver nanofilament with tunable conductance states, making it a promising candidate to advance neuromorphic applications.

Table of Contents

List of Figures

Preface

I would like to first thank my advisor, Prof. Susan Fullerton, for being the most supporting character throughout this journey. Your meticulousness towards science has shaped the way I conduct research and no doubt it will continue benefit me beyond my academia career. I also want to thank my colleagues and collaborators both at Pitt (Dr. Jierui Liang, Dr. Ke Xu, Shubham Awate, Huiran Wang, Eli Bostian, Aaron Woeppel, Brian Radka, Abigale Gray, Dr. Kutay Sezginel, Prof. Chris Wilmer) and Notre Dame (Dr. Garrison Crouch, Dr. Donghoon Han, Prof. David Go, Prof. Paul Bohn), working with you are always enjoyable and the four (and counting) co-authored publications will always remind me of our fruitful discussions. My dissertation committee, Prof. Jennifer Laaser, Prof. Eric Beckman and Prof. James McKone, your insights on my project have broadened my horizons and I want to thank you for making my dissertation a smooth process in this challenging time (2020 is really something).

I am also very grateful to my friends and family, things were not always plain sailing in the past five years but you always gave me unconditional support when needed. I wish I have made you proud.

At last, I want to thank myself, Dr. Chao, for always remembering that I am not the brightest mind in the room, but smart enough to believe hard work pays off.

1.0 Chapter 1: Introduction

1.1 Metal Nanofilament

A metal nanofilament often forms as a branch-shape cluster of metal atoms with the stem width ranging from dozens to hundreds of nanometers, and length sometimes reaching microns. [1] Because of their delicate form, metal nanofilaments can only grow and exist inside a solid scaffold which provides the needed structural stability. The formation of metal nanofilaments usually takes place within a metal-insulator-metal (MIM) structure, where redox reactions initiate near two metal electrodes. The filament grows by electrochemistry inside the ion-conducting material, such as a metal oxide or a solid polymer electrolyte (SPE). Because the solid scaffold that supports filament growth is electrically insulating, once formed, the nanofilament creates a conductive pathway connecting the two electrodes across the solid insulator. An example is shown in **Figure 1** for a silver filament traversing a polyethylene oxide film.

The rupture (dissolution) of the nanofilament induces a discontinuity along filament structure usually due to either Joule heating where large current densities give rise to a higher temperature and promotes migration of the metal, or an external stimulus such a electrochemical oxidation via an applied bias, which breaks the electrical connection between electrodes. As described below, metal nanofilaments are useful for several applications not only because they are electrically conductive, but also because the electrical switching between insulating (i.e., ruptured filament) and conductive (i.e., connected filament) structures can be achieved by a controllable external electrical field.

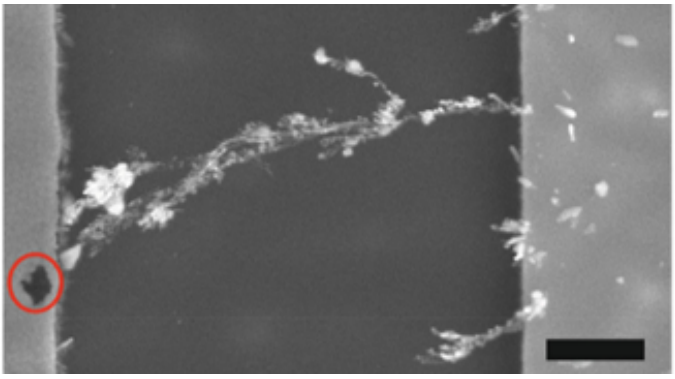

Figure 1: Scanning electron microscope image of silver filament connecting two metal electrodes through a polyethyelene oxide (PEO) film (200 nm thick and 5 µm wide) in a planar MIM structure after formation under a constant +2 V formation bias. The scale bar is 1 µm. Reproduced with permission from John Wiley and Sons. [1]

1.2 Applications of Nanofilaments and Key Challenges

1.2.1 Resistive Memory

Resistive memory, also known as resistive random access memory (ReRAM), is a type of random access memory (RAM) that works by modulating the resistance of a solid-state, dielectric material. [4–7] Different from direct-access data storage media such as magnetic tapes or hard disks, data stored in RAM can be accessed regardless of its physical location on the recording medium. However, RAM is typically a volatile memory, meaning its stored data will be lost if the power source is removed. On the contrary, ReRAM is a non-volatile memory, meaning that it can retrieve stored data after the power is removed. ReRAM is gaining interest because its simple structure allows for 3D crossbar architecture, as illustrated in **Figure 2**. Also, it can operate at lower voltage (sub 2 V) than conventional flash memory ($>$ 5 V) [8–11] and other emerging memories such as phase-change memory (PRAM) [12–14] and magnetoresistive random-access memory (MRAM). [14, 15]

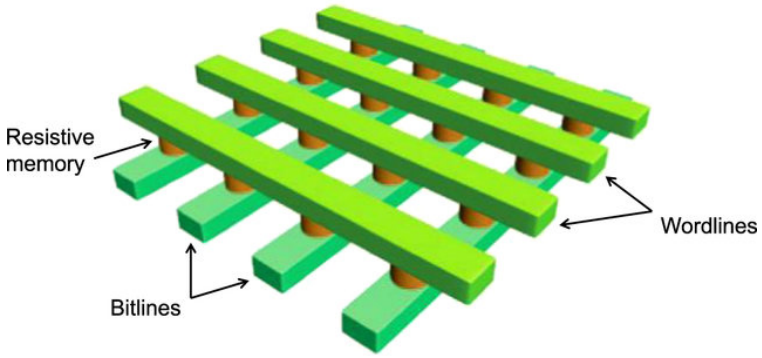

Figure 2: Crossbar architecture for resistive memories. The array is obtained by perpendicular conductive wordlines (rows) and bitlines (columns), where a memory element exists at the intersection between each row and column. The memory element can be accessed for read and write by biasing the corresponding wordline and bitline. Reproduced with permission from IOP Publishing under the terms of the Creative Commons Attribution 3.0 licence. [2]

There are several types of ReRAMs based on the type of material used to achieve the resistance change. Conductive bridge random-access memory (CBRAM), for example, is a type of ReRAM that relies on the nanofilaments introduced above. [5, 16–18] In memory applications, the low and high resistance states are used to represent logic "1" and "0" respectively, so the connected or disconnected nanofilaments in CBRAM are thus used to represent data and achieve memory function. CBRAM is also a type of non-volatile memory, meaning after filament formation it can maintain its low resistance state until external bias is applied to dissolve the filament. The distinctive advantage of metal nanofilament-based CBRAM over other ReRAMs (such as oxygen vacancy filamentary ReRAM) is the low voltage (sub 1 V) [18–20] CBRAM requires to set the conductive pathway. This is the result of the two different mechanisms involved. The metal atoms in nanofilament CBRAM dissolve back into the dielectric under an applied electrical field, whereas the movement of oxygen vacancies requires larger electric fields (i.e., higher voltage and therefore more energy) with a mechanism akin to dielectric breakdown. [21, 22]

1.2.2 Optical Metamaterials

In addition to memory and memory-based computing applications, metal nanofilaments are also promising for applications that require reconfigurable optical properties. For example, when an ordered array of nanoparticles (NPs) is embedded in a solid matrix (i.e., a metamaterial), the optical properties of this matrix can be tuned by adjusting the size and spacing of the NPs, which changes the interaction with electromagnetic radiation over a specific range of wavelengths. [23, 24] For a system that is not reconfigurable, once the NP array is embedded in a solid matrix, no further adjustments can be made to the optical properties. However, it has been shown that nanofilaments that are densely packed in a dielectric can give rise to strong anisotropy in optical properties. [25] Thus, another application where metal nanofilaments can be used is to introduce optical reconfigurability by selectively forming and dissolving nanofilaments between metal NPs embedded in the metamaterial. This concept is shown in **Figure 3**a. Such metamaterials consisting of an array of NPs connected by metal filaments could potentially be developed into a new type of reconfigurable coating that could be used for both civilian and military applications (e.g., glass coatings that decrease light transmission depending on the solar intensity at that moment, or military gear that offers on-demand, reconfigurable camouflage). This new generation of metamaterials with dynamically reconfigurable optical properties would represent a major advance in intelligent coatings, nicely complementing achievements in the internet of things (IOT), where local sensors could trigger the intelligent material to change properties in response to a stimulus.

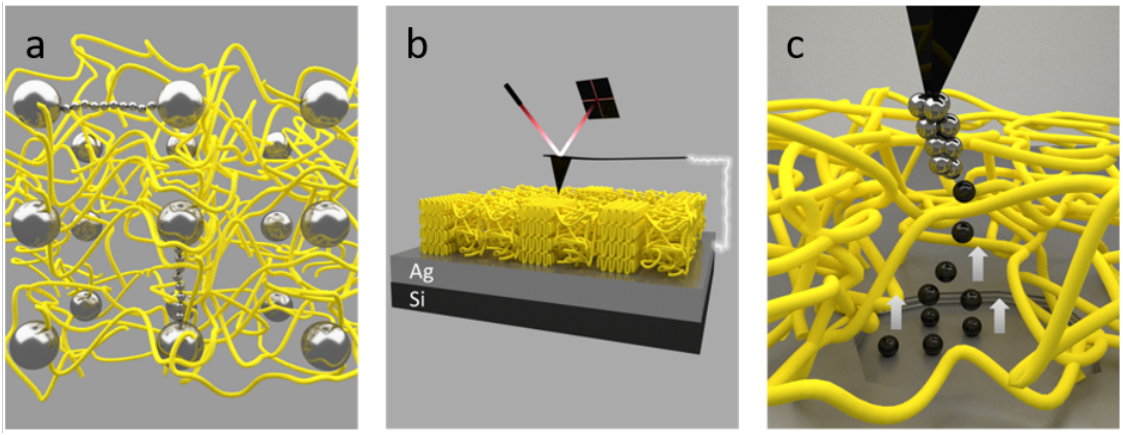

Figure 3: **(a)** Metamaterial with a lattice of metal nanoparticles (large gray spheres) embedded. Some NPs are electrically connected by metal nanofilaments (small gray spheres). **(b)** Conductive-AFM based system controlling the electrochemical formation and dissolution of conductive metal filaments. **(c)** Magnified view of filament formation between the conductive AFM tip and a sacrificial metal layer.

1.2.3 Neuromorphic Computing

Memristor-based devices, such as CBRAM, have drawn heavy attention for their potential use in neuromorphic computing. Neuromorphic computing is a brain-inspired computing paradigm. Human brain is highly efficient in task such as pattern recognition due to its ability of massive parallel information processing [26], which is made possible by utilizing more than 10^{15} synapses while consumes only 20 Watts of power. [27] Unlike the silicon based modern computer which is limited to use digital "0" and "1" for computation, biological neural networks exhibit analog changes in synaptic weights during the decision-making and learning processes. One way to think about the difference between the logic states used in silicon based computer versus neuromorphic computing is illustrated in **Figure 4**. Traditional computing uses only two (digital) logic states to fulfill computing tasks, meaning each command or data used needs to be assigned with a long string consisting of "0"s and "1"s; while neuromorphic computing computes by assigning multiple (analog) logic states, thus

improves computing efficiency. It is worth mentioning, however, in Figure 4 the color of candies coming out from both machines is random, while in neuromorphic computing the logic states change is usually continuous, which is another key difference to traditional computer.

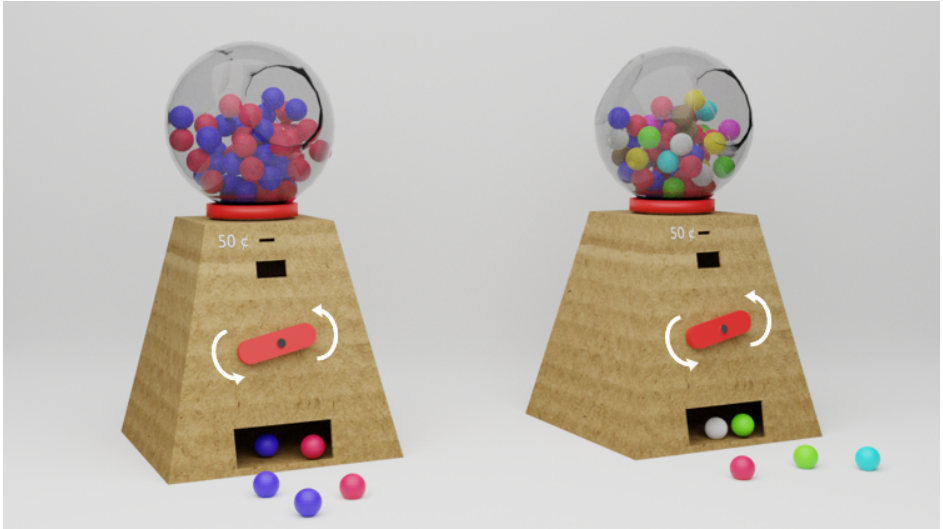

Figure 4: An analogy to describe digital versus analog computing using candy dispensers: traditional computing (left) uses only two logic states (candies with only two different colors) while neuromorphic computing (right) computes by assigning multiple logic states (candies with many different colors).

In addition to analog logic states, neuromorphic computing also mimics the biological brain by operating in a parallel rather than sequential fashion. In tasks such as pattern recognition and classification, the sequential operating mode of neuromorphic computing is a more energy-efficient architecture compared with traditional computers that operates in series. [28, 29] The simple structure of two-terminal CBRAM based device also makes it easier to fulfill the neuromorphic network array configuration requirements.

Non-volatile CBRAM has the potential to work as a artificial synapse in neuromorphic computing by emulating synaptic weights with variable resistance states in response to input signal (bias pulse). [28] More recently, systems that combine non-volatile and volatile CBRAMs have demonstrated more complex synaptic functionalities such as spike-timing-

dependent plasticity (STDP) and spike-rate-dependent plasticity (SRDR) together with some key artificial neuron functionalities. [30,31] In brief, these applications take advantages of the two-terminal structure of CBRAM devices, integrating them with other electrical elements (such as resistors or capacitors) to create a circuit that is capable of outputting distinctive signals depending on the frequency or sequence of input pulses, stepping closer to biological neural network functionalities.

1.2.4 Key Challenges

Stochastic switching process. Although CBRAM is considered by many as the next generation memory technology, some key roadblocks such as large device-to-device variability and poor reliability remain till date. [14, 28, 32–34] These issues are largely resulting from the stochastic switching between *on/off* states involving uncontrolled metal atom nucleation in electrochemistry [35, 36] and random metal ion migration. [14] Because of the stochastic switching process, the physical configuration of the nanofilament can be changed after each formation or dissolution cycle, [14] causing unstable resistance at the same logic state (either *on* or *off*) among different operation cycles. This uncontrolled switching prevents practical implementations for almost all applications.

Mechanical inflexibility. In addition to the limitations imposed by stochastic switching mechanism, currently the most studied CBRAMs are inorganic based materials. [2, 37] However, inorganics lack mechanical flexibility to be solution-processable for flexible electronics and impose design complexity in 3D crossbar architectures for neuromorphic applicaiton. Polymer-based resistive memories have been considered as a promising alternative or supplement to conventional inorganic semiconductor-based memory technology due to their advantages of good scalability, flexibility, and ease of processing. [32] For the optically reconfigurable metamaterial, however, there is an additional challenge that must be overcome when using a polymer-based dielectric: the NPs must be precisely positioned into an array within the polymer. For commonly used ion-conducting polymers (*i.e.*, polymer electrolytes) such as high molecular weight PEO-based electrolytes, [19,38] the room-temperature rigidity of the solid film makes it impossible to align NPs into an ordered array.

Lacking multiple resistance states. One specific requirement of CBRAM for neuromorphic applications that differs from memory applications is the need for multiple resistance states. While binary resistance states (*on/off* states) will be adequate for conventional memory, a material that is capable of providing multiple resistance states (synaptic weights) is required to enable analog logic operation for neuromorphic computing. Although the connection between neurons in artificial neural network (ANN) can be implemented by devices with only binary states, such as the transistor, this approach is an energy-intensive and nonscalable. [39] Therefore, a single device with tunable multi-resistance states is preferred over a binary device for more efficient neural network operation. [28, 29, 40] For CBRAM, multiple resistance states can be achieved by tuning metal nanofilament growth dynamics in the electrolyte. In the majority of reports, however, switching CBRAM between *on* and *off* states is abrupt and difficult to make gradual due to the lack of control over the electrochemisty in the switching layer (electrolyte) which tends to be stochastic, as described above. The lack of controlled metal filament dynamics usually also leads to nonlinear conductance change during filament growth and dissolution, which will degrade neural network classification accuracy in neuromorphic computing. [40–43]

1.3 Introduction to PEGDA/IL System and C-AFM setup

To address all three challenges CBRAM faces for the applications listed above, we have come up with a non-aqueous electrolyte combining a photo-crosslinkable polymer (polyethylene glycol diacrylate, PEGDA) with an ionic liquid (1-butyl-3-methylimadazolium hexafluorophosphate, [BMIM]PF_6). PEGDA is an ion-conducting polymer [44, 45] which is also commonly used in biological applications. [46] PEGDA provides design flexibility, because the material can start at low-viscosity and be converted to a high-viscosity solid simply by exposing the film to light. This design could support the precise positioning of NPs in a liquid-like dielectric, and the NPs could subsequently be locked into place by simple exposure to ultraviolet light. Previous studies showed that as little as 4 wt.% PEGDA blended with an ionic liquid (IL) was sufficient to yield a solid. [47, 48] ILs—liquid salts at room temperature

that are commonly added to solid polymer electrolytes for various electrochemical applications [47–51]—are being considered to address the challenges in polymer-based ReRAM. In a recent report, ILs were added to polymer-based CBRAM to reduce the formation (set) bias and increase endurance. [52] Here, [BMIM]PF_6 is chosen as the IL, because it has good chemical and thermal stability, negligible vapor pressure, high ionic conductivity (1.8×10^{-3} S cm^{-1} at 300 K), [53] and a large electrochemical window ($\approx$4.7 V). [54] Thus, PEGDA provides tunable mechanical properties, while [BMIM]PF_6 enhances ionic conductivity which is required for ion migration during forming and dissolving filaments.

In this study, we use conductive-AFM (C-AFM) where the AFM tip serves as an inert mobile top electrode, while a sacrificial bottom electrode supplies the silver for electrodeposition (Figure 3b). The AFM tip and the Ag substrate represent the metals of the MIM structure with dielectric between. Filament growth inside the PEGDA/IL/salt electrolyte is controlled by the polarity and magnitude of the bias applied between the two electrodes (Figure 3c). C-AFM enables the direct-writing of nanofilaments by precisely defining the nucleation sites, yielding more uniform nucleation and growth. [35, 36] Using an automated script (**attached in Appendix A**), nanofilament formation events at hundreds of *xy* locations on the film are recorded. This spatially dense sampling allows us to fully capture the stochasticity of nanofilament growth and enables statistical analyses of the data, which are particularly crucial for a polymer electrolyte containing microscopic heterogeneities.

1.4 Key Findings

In Chapter 3, I discuss our findings on the reduced stochasticity in resistive switching and improved mechanical flexibility for the PEGDA/IL system. Specifically, I describe our choice of host dielectric material consisting of UV crosslinkable PEGDA and room temperature ionic liquid [BMIM]PF_6 that balances the structural and ion-conducting requirements. I investigate formation and dissolution of silver filament arrays at preselected locations through PEGDA/IL thin film as a function of IL composition. The IL enhances uniform nanofilament formation kinetics under constant applied bias and enables modulus tuning over a range of a

few hundred MPa to several GPa, [47, 48, 55] making it more versatile than IL-free polymer electrolytes. Also, adding a sufficient amount of IL (>10 wt.%) enables 5× faster nanofilament formation compared to the IL-free electrolyte, but adding too much (50 wt.%) slows the nanofilament kinetics by a factor of 7. These observations suggest complex dynamics, which further motivate investigation of the underlying mechanisms. **This work is published in *Small*, attached in Appendix B**.

In Chapter 4, I present the impact of formation bias on filament formation. The data reveal an unexpected relationship between formation times and applied bias. Specifically, the formation times do not decrease monotonically with increasing driving force—as expected for oxide-based dielectrics [56–58]—but instead exhibit a pronounced maximum near 2.0 V. We interpret this behavior as the result of a competition between IL EDL formation and electrochemical filament growth. This finding is exciting because it suggests that the competition can be used to control nanofilament morphology over multiple, well-defined resistance states. In other words, we uncovered a new control mechanism that should lend itself to the production and engineering of neuromorphic architectures where multiple distinguishable resistance states must be achieved to emulate the connections between neurons in an artificial neural network. [28, 29] **This work is published in *Advanced Functional Materials*, attached in Appendix C**.

To demonstrate this control mechanism on filament formation dynamics can be applied for practical neuromorphic applications. In Chapter 5 I describe my most recent efforts to scale up the CBRAM device from a c-AFM MIM with one M being the AFM tip to more practical MIM devices on a chip where both M's are lithographically patterned electrodes. I continue to explore filaments with multiple conductance states formed in the PEGDA/IL system, but this time focusing on benchmarking their performance against requirements for neuromorphic applications. I fabricated devices using photolithography that will enable additional electrical characterization such as conductance state retention, switching time, and endurance. Thus far, I have demonstrated that the conductance of a single filament can be tuned reversibly (increase and decrease) in the PEGDA/IL system to achieve hundreds of distinguishable states with cycles of bias pulses. Moreover, the data show a highly linear correspondence ($R^2 > 0.9$) between these two, making it favorable for artificial neural network

(ANN) application as linear and symmetric weight update (conductance change) is critical for training accuracy and fast training convergence speed in neural network. **Manuscript in preparation**.

1.5 Co-authored Publications

My first-authored publications focused on silver nanofilament formation dynamics in the PEGDA/IL system; additionally, I contributed to a manuscript on fabricating nanopore-templated Ag nanoparticle arrays in dielectrics (**published in *Frontiers in Chemistry*, attached in Appendix D**). Specifically, the PEGDA system that I developed for c-AFM filament formation was used in the *Frontiers* publication. Additionally, I contributed differential scanning calorimetry (DSC) measurements and analysis of a single-ion conductor, EDL-gated transistor to a manuscript **published in *ACS Applied Materials & Interfaces* (attached in Appendix E)**.

2.0 Chapter 2: Experimental Details

2.1 Spin-coating of PEGDA/IL Thin Film Sample

While the composition of PEGDA/IL electrolyte used at different chapters in this dissertation varies, the sample preparation of PEGDA/IL thin film for AFM measurement can be generalized as follows: $AgPF_6$, $[BMIM]PF_6$, and PEGDA were dissolved in acetonitrile (ACN) to make the ACN solutions of each individual component, respectively; then the solutions were mixed by different volumetric ratios to make the final electrolyte solutions with various PEGDA/$[BMIM]PF_6$/$AgPF_6$ compositions. In all final electrolyte solutions, the PEGDA concentration was kept at 1 wt.% with 0.02 wt.% of HMPP (photoinitiator) added. The electrolyte solutions were spin-coated on the Ag-coated silicon substrate at 4000 rpm for 30 seconds to obtain a homogeneous PEGDA/IL thin film, followed by 2 mins of annealing at 80 °C to drive-off ACN residue. Following PEGDA/IL deposition, samples were then photo-crosslinked with a UV lamp, (λ = 365 nm, P = 1.3 mW/cm^2 at 3 inches) at a working distance of 0.5 inch for 1 h. All steps mentioning above were completed inside an argon-filled glovebox.

2.2 Silver Nanofilmanet Formation and Dissolution by Conductive-AFM

Nanofilament formation and dissolution usually took place in an insulator sandwiched between two metal electrodes (metal-insulator-metal structure, MIM) as shown in **Figure 5**. If a sufficiently high positive bias was applied between the two metal electrodes, the redox active metal anode would be oxidized and injected metal ions into the dielectric. In response to electrical field, the metal ion would migrate towards the inert cathode where it received free electrons and was reduced to a metal atom. When the positive bias was held for enough time, a filament consisting of reduced metal atoms would continue to grow until it connected both electrodes, i.e., the electrical circuit would be shorted once a filament was formed. In

contrast to filament formation, the exact mechanism for filament dissolution is still under debate. One theory suggested that filament dissolution was driven by "thermal-assisted" electrochemical-oxidation [59] when a negative bias was applied: because the nanoscale conductive filament formed was far from being a perfect conductor (i.e., it would still have a large electrical resistance), the potential drop along the filament could drive metal atom oxidation (dissolution) likely at the location with the weakest electrical connection.

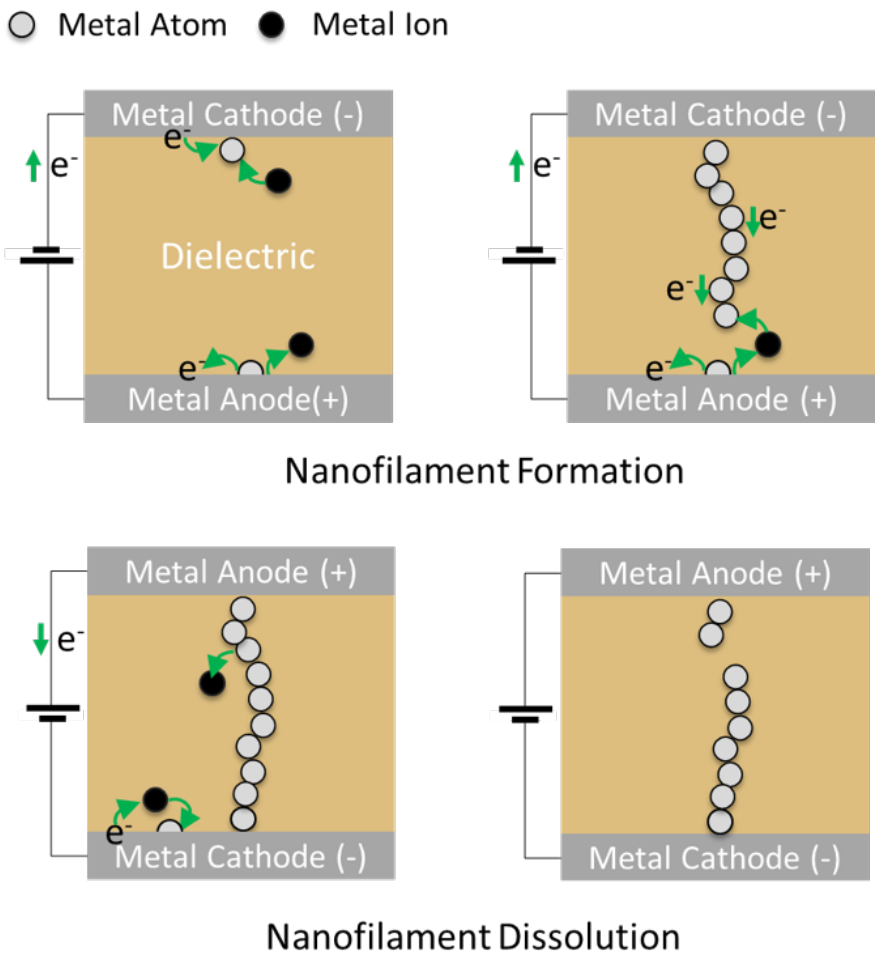

Figure 5: Schematic of nanofilament formation (top) and dissolution (bottom) processes in a MIM structure by applying bias with opposite polarity

In this dissertation we used a conductive-AFM (c-AFM) based setup to form and dissolve silver nanofilaments between a silver sacrificial electrode and a c-AFM probe as shown in Figure 3b,c. Thin films of PEGDA/IL were prepared through spin-coating on an Ag-coated silicon wafer using the method described above. A Bruker Dimension Icon AFM coupled with conductive AFM probe (SCM-PIT-V2) was operated in contact mode inside the glovebox. Electrical contact was made between the AFM stage and the Ag layer of the substrate using copper tape. Bias was applied to the silver bottom layer through the AFM stage while AFM tip was grounded throughout the process: when a positive bias is applied, silver electrode will be oxidized and initiates filament formation; after filament formation a negative bias can be applied to oxidize and dissolve the filament. The current flowing through the AFM tip has been monitored once bias was applied and served as the indicator of formation/dissolution events: the current remained low until nanofilament formation has completed to short the circuit; when bias polarity was reversed to dissolve the filament, the current would first remain high (but now at a negative value) until the electrical connection was broken due to filament dissolution. The formation current thresholds were chosen to be about 100× higher than the noise level under different current sensitivity while the dissolution current threshold was chosen to be close to 0. For example, thresholds for formation and dissolution were chosen as +4 nA and -0.5 nA, respectively, at current sensitivity of 1 nA/V. As a contrast, the compliance current of the instrument was ca. ±5 nA at current sensitivity of 1 nA/V.

2.2.1 Representative Silver Nanofilament Formation and Dissolution

c-AFM was operated under contact mode during nanofilament formation and dissolution, a working setting which allows constant contact between the AFM tip and the sample surface and ideal for electrochemical deposition. Representative time-dependent current data after bias was applied during a formation and dissolution cycle are plotted in **Figure 6**, together with time-dependent bias data. Here, the sample had a composition of 90/10 PEGDA/IL wt.% with 0.2 mM $AgPF_6$. Current sensitivity was set at 100 nA/V with a system compliance of approximately 600 nA. As shown in the figure, the formation bias was set to 2.5 V at t =

4 s. At t = 60 s, the current starts to increase from 0 to 200 nA within a short time range (i.e., seconds), indicating nanofilament formation. A stable current was achieved at 200 nA with a constant bias of 2.5 V from t = 62 to 75 s. To dissolve the nanofilament, the bias was set to -2.5 V at t = 75 s. The current first decreased to -500 nA and then returned to 0 nA within dozens of ms, indicating dissolution of the filament.

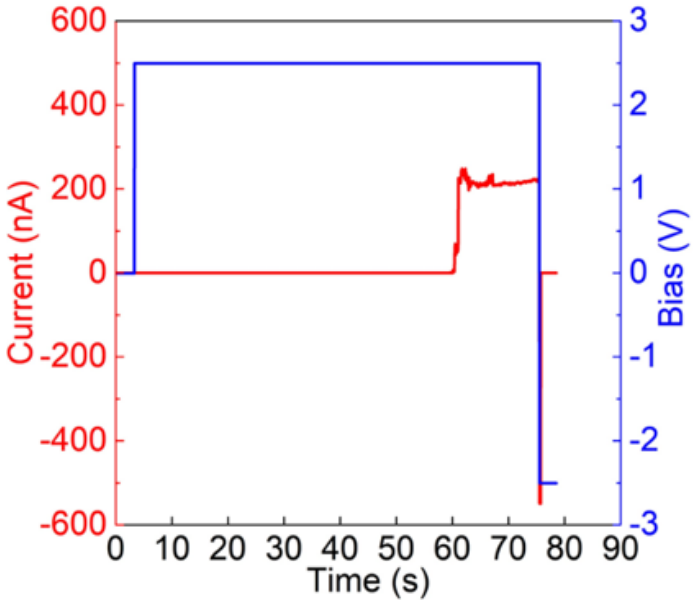

Figure 6: Time dependent current and applied bias plot for a representative nanofilament formation and dissolution event. Current is plotted in red and bias is plotted in blue.

We noticed the timescale of dissolution is three orders of magnitude faster than formation, indicating the fundamental difference in mechanisms between formation and dissolution kinetics. This difference is sensible, because initial formation requires the movement of many silver ions to form a percolating conduction path, dissolution only requires the oxidation of a few silver atoms into the nearby electrolyte to disconnect the filament.

2.2.2 Direct-write of Nanofilament Array Using Customized Script

For large-scale direct write of filaments over a preselected region, we developed a script (see Appendix A) to automate the formation and dissolution of nanofilaments at multiple precise locations over a preselected area. The algorithm of this script used the following protocol: a user-defined positive bias was applied until a nanofilament was created, as indicated reaching the formation threshold current. After formation, the bias was held for only 2 ms to avoid nanofilament overgrowth. Then, the bias polarity was reversed to a user-defined negative bias to initiate dissolution. When the filament was dissolved, the current decreased to zero. The c-AFM tip was then moved to the next selected location and the protocol was repeated. The time for both formation and dissolution of filament at each location, and current versus time data during formation and dissolution were recorded for further analysis.

To demonstrate the large scale direct-write of nanofilament array, 36 nanofilaments were formed at 36 locations in an array covering a 5 × 5 µm region with a 1 µm pitch in 70/30 PEGDA/IL wt.%. Topography maps were captured before and after the experiment, as shown in **Figure 7**a and b, respectively. An array of 6 × 6 protrusions is clearly distinguishable in Figure 7b and the approximate height of the protrusions is 10 nm (note that the height scale is adjusted to highlight the height of the protrusions). A line scan is also provided in Figure 7c to show the periodic protrusions.

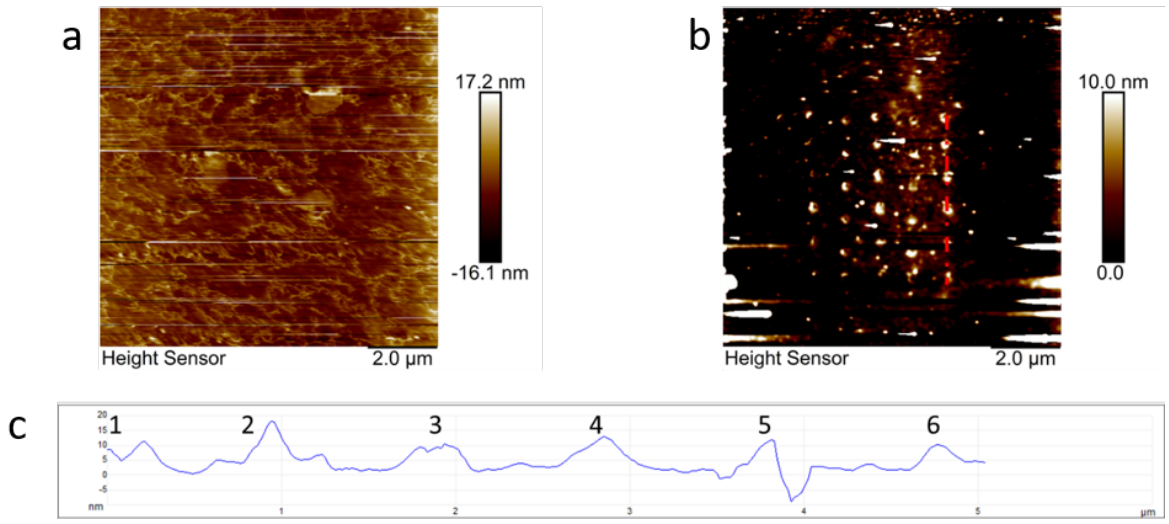

Figure 7: Topography map for the 70/30 PEGDA/IL wt.% sample (no $AgPF_6$) **(a)** before electrodeposition; **(b)** after electrodeposition; and **(c)** fluctuations in height along the red dashed line in (b) indicating the approximate height of 6 protrusions.

3.0 Chapter 3: Impact of Composition on Nanofilament Formation Dissolution Kinetics

Published in: Chao, Z.; Radka, B.P.; Xu, K.; Crouch, G. M.; Han, D. Go, D. B., Bohn, P. W., Fullerton-Shirey, S.K. "Direct-Write Formation and Dissolution of Silver Nanofilaments in Ionic Liquid-Polymer Electrolyte Composites" *Small* 14(19) 1802023 (2018).

In this chapter, we focused on studying systems with different IL (10 wt.% to 50 wt.%) and $AgPF_6$ salt (0 to 2 mM) compositions. Mechanical strength, preliminary study of kinetics, and thermal property for above mentioned systems are covered in this chapter.

3.1 PEGDA/IL Film Thickness Measurements

Electrolyte samples were prepared as described above, cross-sectioned by focused ion beam (FIB) milling, and then imaged by scanning electron microscopy (SEM). Cross sections of the 90/10, 70/30 and 50/50 wt.% PEGDA/IL at 0.2 mM $AgPF_6$ are shown in **Figure 8**. To protect the film during ion milling, Pt was deposited on the 90/10 sample and Pt and Pd-Au were deposited on the 70/30 and 50/50 films. The thicknesses are 41 $\pm$2, 44 $\pm$ 2, and 52 $\pm$5 nm, for 90/10, 70/30 and 50/50 PEGDA/IL with 0.2 mM $AgPF_6$, respectively. We notice fluctuations in the apparent thickness of the film with increasing IL concentration, which is likely due to the interaction between the charged IL and the ion and electron beams.

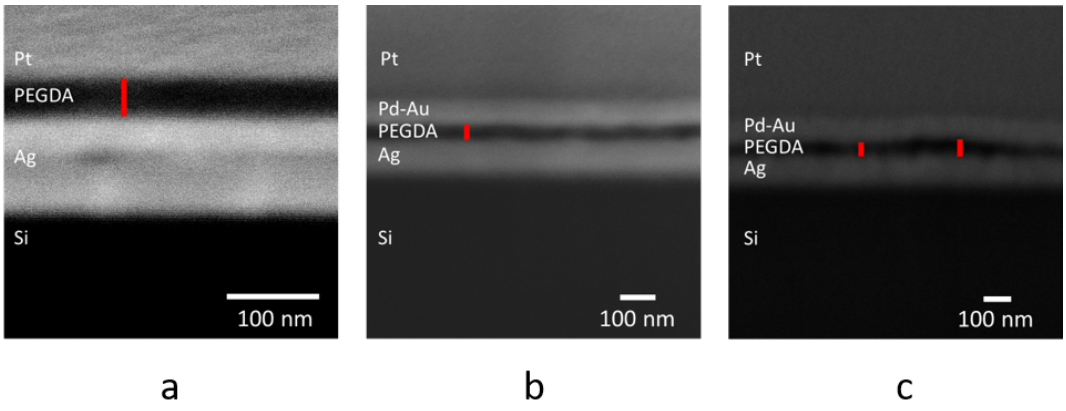

Figure 8: SEM of FIB cross-sectioned films containing 0.2 mM $AgPF_6$. **(a)** 90/10 **(b)** 70/30 and **(c)** 50/50 wt.% PEGDA/IL. Note the different scale bar sizes are all for 100 nm.

3.2 Modulus Measurement

Thin films of PEGDA with IL and AgPF6 were fabricated by spin-coating, and cross-sectional scanning electron microscopy (SEM) images show that the thickness of the films is ∼50 nm (Figure 8), independent of the IL concentration. First, we measure how the IL impacts the mechanical properties of the electrolyte film. Modulus maps of the cross-linked electrolytes over a 5 × 5 µm region and modulus-composition data with varying IL compositions are shown together in **Figure 9**. Clearly, modulus decreases with increasing IL content. For example, increasing the IL composition by a factor of 3 (10 to 30 wt.%), decreases the average Young's modulus by one order of magnitude. This trend is predictable, because the IL is a low viscosity liquid compared to the UV-crosslinked polymer. In contrast, adding Ag salt increases the modulus, which is most obvious for the electrolytes with the highest PEGDA concentration. For example, the modulus nearly doubles by adding 2 mM $AgPF_6$ to a sample with 90 wt.% PEGDA. The silver cations electrostatically interact with the ether oxygens in the polymer backbone; [60] the resulting non-covalent interactions decrease the polymer mobility [61] and therefore increase the modulus. The data show that the modulus of the polymer coating can be tuned more than 10-fold by relatively small adjustments

in the PEGDA/IL ratio (ether oxygen to BMIM ratio from 22:1 to 65:1, corresponding to 70/30 and 90/10 PEGDA/IL wt.%). In contrast, increasing the silver salt concentration by one order of magnitude (0.2 to 2.0 mM) increases modulus by at most a factor of two. A complete set of modulus maps for all the electrolytes investigated in the study are provided in the Figure S3 (Supporting Information, Appendix B).

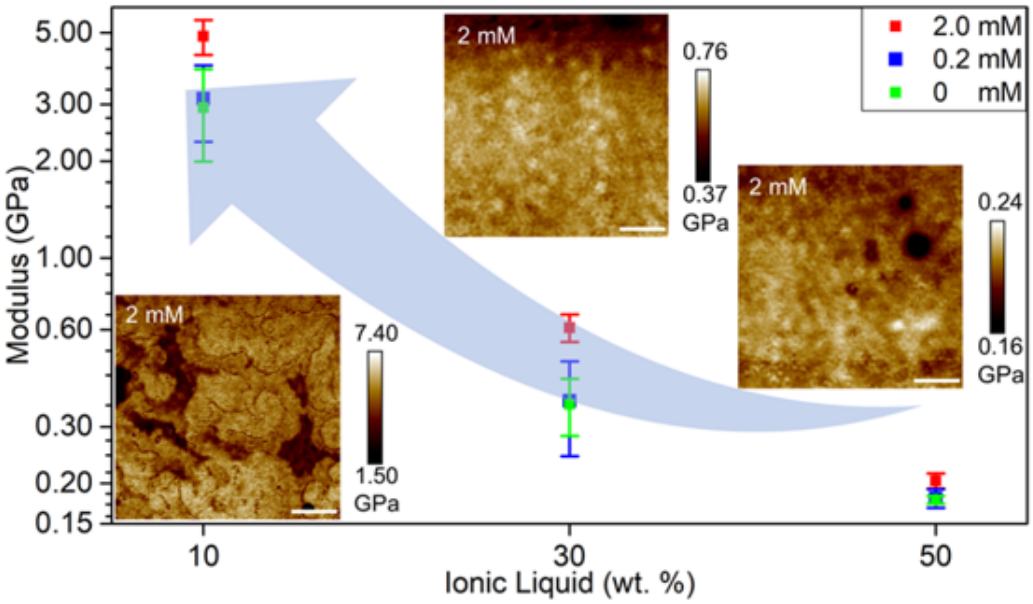

Figure 9: Average Young's modulus measured by PF-QNM over a 5 × 5 µm region for samples with different PEGDA/IL/$AgPF_6$ compositions. Inset left to right. Modulus maps of the surface of cross-linked electrolytes containing 2 mM $AgPF_6$ at 90/10, 70/30 and 50/50 PEGDA/IL wt.% composition, respectively. Scale bars indicate 1 µm.

3.3 Filament Formation and Dissolution Kinetics

Nanoscale Ag filaments were formed and dissolved by controlling the magnitude and polarity of bias applied between a conductive AFM tip and the Ag sacrificial electrode

(Figure 3b). To avoid asperities in the data caused by macroscopic inhomogeneities in the spin-coated samples, formation and dissolution events were measured at multiple regions separated by > 100 µm. Within each region, filaments were formed and dissolved at 100 locations in a 6×6 µm array, with a pitch of 600 nm. The algorithm used to collect the initial filament formation and dissolution times at hundreds of different locations used the following protocol: a +2 V positive bias was applied until a filament was created, as indicated by a significant increase in the current, until compliance was reached. After formation, the bias was held for only 2 ms to avoid filament overgrowth. Then, the bias polarity was reversed to 2 V to start dissolution. When the filament was broken, the current decreased abruptly to zero.

At least 700 formation and dissolution events were captured for each sample, and histograms of filament formation and dissolution times are given in **Figure 10**. A Gaussian (normal) distribution was used to fit all data sets with skewness adjusted to capture the asymmetries. The formation time distributions are normal, Figures 10a and c, while the dissolution events show a log normal distribution, Figures 10b and d. These are the same types of distributions reported for filaments formed in PEO-based electrolytes, [19] and the different distributions suggest that the underlying formation and dissolution mechanisms are fundamentally different. This difference is reasonable, because it takes longer to form a filament for the first time, i.e., the formation step, than it does to break the filament. Whereas formation requires the movement of many silver ions to form a percolating conduction path, dissolution only requires the oxidation of a few silver atoms into the nearby electrolyte to disconnect the filament.

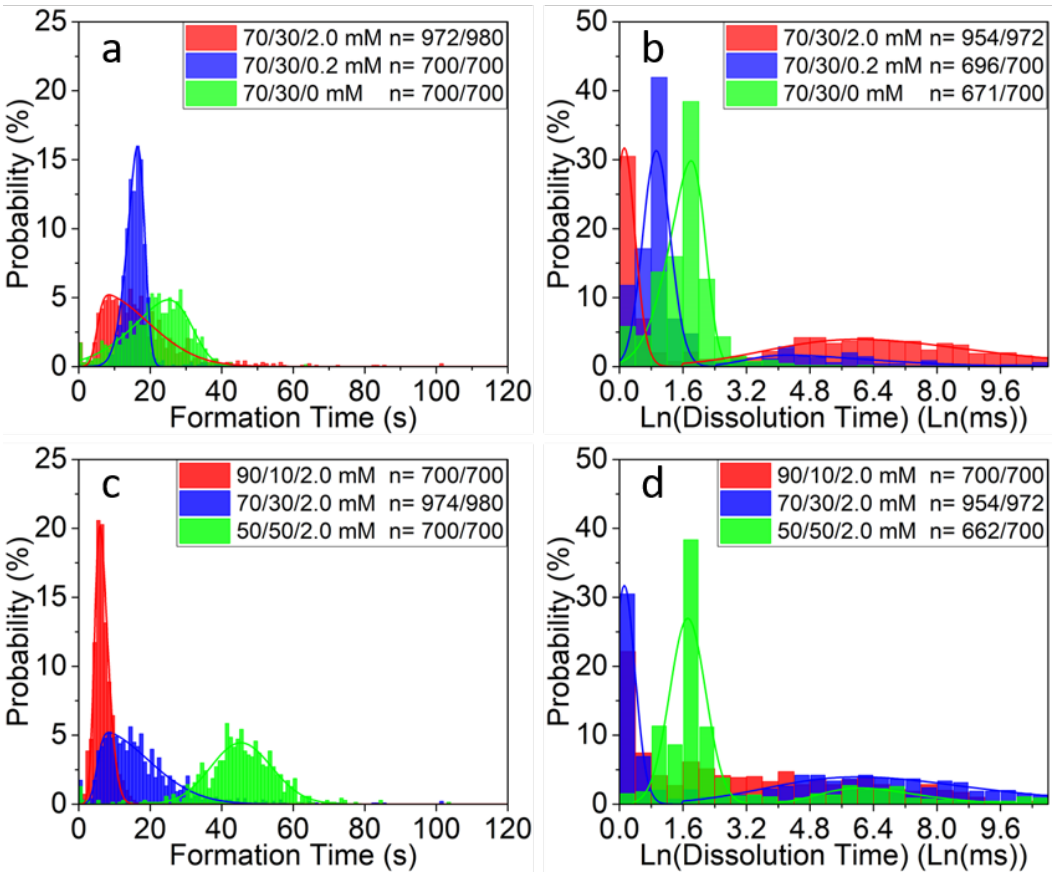

Figure 10: Nanofilament formation **(a)** and dissolution **(b)** time distributions in electrolytes at 70/30 wt.% PEGDA/IL with 0, 0.2 and 2 mM $AgPF_6$. Filament formation **(c)** and dissolution **(d)** time distributions for electrolytes with 2 mM $AgPF_6$ at 90/10, 70/30 and 50/50 wt.% PEGDA/IL.

Both the Ag salt and the IL strongly affect filament formation kinetics, as shown in Figures 10a and c, respectively. The addition of up to 2 mM Ag salt in the 70/30 wt.% PEGDA/IL electrolyte decreases the formation time by as much as 42 % (Figure 10a) as expected from straightforward electrodeposition kinetics. The shift in formation times indicate that the kinetics of filament formation can be controlled by adjusting the Ag^+ concentration without varying electrical field strength.

Decreasing the IL concentration from 50 to 10 wt.% with 2 mM $AgPF_6$ increases the filament formation rate by approximately 6.5 times as shown in Figure 10c. Faster filament

formation with decreasing IL content is unexpected, because the IL is conventionally thought to function as a plasticizer, [62, 63] enhancing polymer chain segmental motion [64, 65] and improving ionic conductivity. [66, 67] In addition, the magnitude of the formation time distribution is related to specific features in the time-dependent current data. Specifically, there are two different types of processes, denoted type-1 and type-2, as shown in **Figure 11**a,b, respectively. Type-1 formation involves an abrupt increase in current from zero to the compliance current over a narrow (few ms) time window, whereas type-2 formation involves current fluctuations over longer timescales (>1 s) prior to reaching the compliance current. Whether a data set exhibits type-1 or type-2 behavior is distinguished by setting the total number of data points that exceed a user-defined current level. In this study, we choose this cutoff current as 3.8 nA, and classify the data as type-1 formation if the total number of data points for which $I \geq 3.8$ nA is less than 4. Conversely, if more than four points in the data set include $I \geq 3.8$ nA, then the formation is considered type-2. We know type-2 formation is not dielectric breakdown because when the bias is reversed, the current returns to zero. In the case of dielectric breakdown, an irreversible conductive pathway would be created through the dielectric.

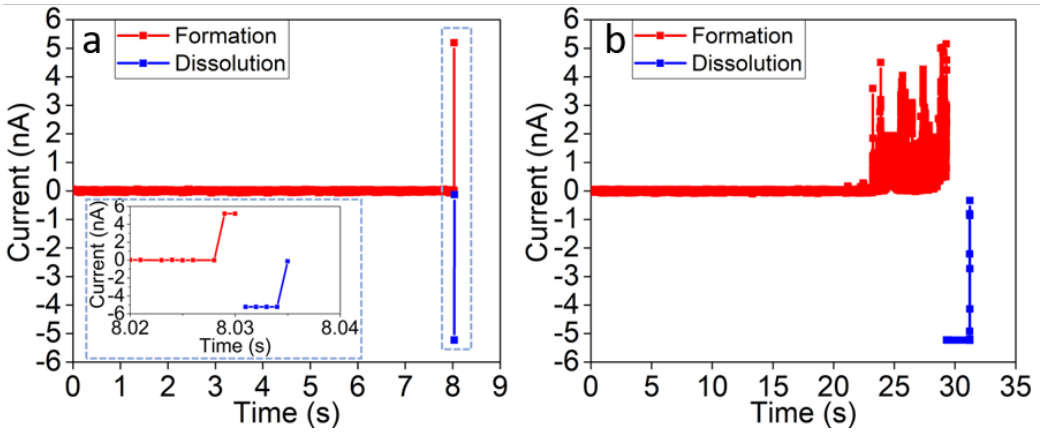

Figure 11: Current (I) vs time (t) data during filament formation at +2 V and dissolution at -2 V for **(a)** type-1 and **(b)** type-2 filament formation processes. Inset of (a) in the blue rectangular box is a magnified plot with expanded time axis.

The percentage of type-1 formation events are provided in Table S1 (Supporting Information, Appendix B) for all the samples in this study. Systems with faster formation kinetics and the highest modulus have a higher percentage of type-1 formation events. For example, the 90/10/2 mM system with average formation time of 7 s has a 75 % type-1, while the slower 50/50/2 mM system, with average formation time of 45 s, exhibits only 5 % type-1 events. While further studies are needed to confirm the origin of these two distinct types of formation dynamics, they may relate to the physical structure of the filament. For example, type-1 filaments that are more commonly formed in the high modulus electrolyte (90/10/2 mM) may have well-defined structure, whereas type-2 filaments that dominate in lower modulus electrolyte (50/50/2 mM) may be more dendritic, causing current fluctuations as they form and disconnect.

Additional support for a correlation between filament morphology and modulus arises in the 50/50 PEGDA/IL samples. Specifically, for the 0 and 0.2 mM salt concentrations, overgrowth of silver at the surface of the film was observed. Figure S5 (Supporting Information, Appendix B) shows direct evidence of silver overgrowth via AFM topology and current maps. Furthermore, as shown in Figure S6 (Supporting Information, Appendix B), formation and dissolution events for the 50/50/0 mM and 0.2 mM systems indicating that $> 50\%$ of the filaments that form do not dissolve during the timescale of the measurement, which would be expected for overgrown filaments connected at multiple locations. In contrast, no similar surface overgrowth was observed in systems with higher modulus, such as 70/30/0 mM system, as shown in Figure S7 (Supporting Information, Appendix B). Thus, varying the Ag concentration and PEGDA/IL ratio not only changes the kinetics, but also the morphology of the filaments from well-defined to overgrown.

Similar to filament formation, the Ag salt and IL compositions also affect dissolution kinetics, as shown in Figure 10b,d, respectively. The dissolution distributions are more complex than the formation distributions, showing a bimodal structure with filaments that dissolve quickly (tens of milliseconds, type-A) coexisting with long-lived filaments (tens of seconds, type-B). In addition, systems exhibiting a higher percentage of type-1 formation events also tend to dissolve faster. This provides further support for the interpretation that type-1 filaments have a more well-defined structure than those formed in type-2 events, be-

cause more well-defined filaments would require less time to dissolve than dendritic filaments that may need to disconnect at multiple locations.

Figure 10b also shows that the bimodal distribution is more prevalent at higher Ag salt concentrations. Similar experiments addressing Ag atomic-scale junction formation and dissolution also show a marked dependence of dissolution time on Ag activity in the surrounding medium. [68,69] This is sensible because adjusting the Ag salt concentration shifts the equilibrium potential of the system relative to the applied potential. Hence, the dissolution data suggest that a concentration overpotential-limited dissolution process is operating on a small, but non-negligible fraction of the nanofilaments.

3.4 Thermal Measurements

The observation that electrolytes with the highest PEGDA concentration (90 wt.%) and the largest modulus display the fastest filament formation/dissolution kinetics was surprising. It thus motivated using differential scanning calorimetry (DSC) to characterize the polymer films across the entire range of compositions. Heat traces showing the melting temperature (T_m) in the range of 20 to 55 °C are given in **Figure 12**a. IL and silver salt suppress PEGDA crystallization as observed by a decrease in area under the melting peak (IL-free DSC traces are provided in Figure S8, Supporting Information, Appendix B). A secondary peak at lower temperature ($\sim$ 20 °C) emerges with increasing IL addition, and this feature is particularly apparent in the 0.2 mM samples. The observation of multiple peaks at a specific salt concentration is similar to the behavior of PEO-based electrolytes at their eutectic composition. [61, 70]

The glass transition temperatures (T_g), shown in Figure 12b, provide insight on how the IL and silver salt affect polymer mobility, which governs ion mobility in amorphous domains. The addition of IL from 0 to 30 wt.% at low silver salt concentration (0 and 0.2 mM) increases T_g by more than 7 K, showing that it does not plasticize the system. Generally, the data show that when the ion concentration is increased (either by adding IL or silver salt), T_g increases, reaching a maximum value around -50 °C for the concentration ranges measured.

However, it is noteworthy to highlight the 0.2 mM salt concentration in the 90/10 system. Although we expect the Ag salt to increase T_g, because electrostatic interactions between cations and ether oxygens decrease segmental mobility of the polymer, the 0.2 mM salt *decreases* T_g in the 90/10 PEGDA/IL concentration. This anomalous behavior is consistent with the possibility that 0.2 mM is a potential eutectic concentration as mentioned above. A similar T_g minimum at the eutectic has been reported for a PEO:$LiClO_4$ electrolyte. [61]

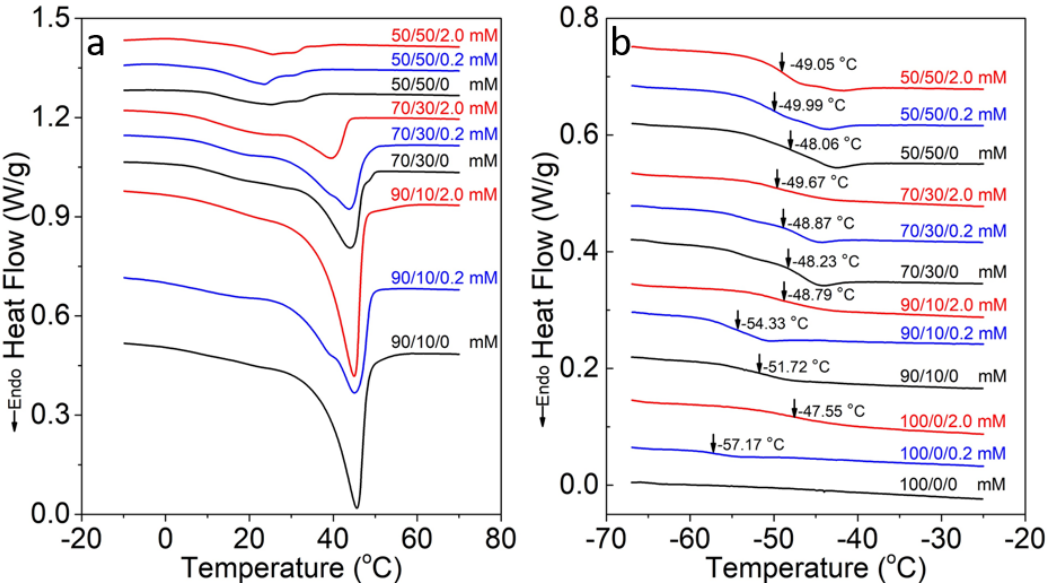

Figure 12: Heat flow *vs.* temperature for PEGDA/IL/$AgPF_6$ showing: (a) melting (T_m) features and **(b)** glass transition (T_g) features. Data are from the second heating scan.

3.5 Relating Nanofilament Kinetics to Polymer Structure

Based on the DSC data and the prevailing view that less crystal structure in polymer electrolytes correlates with faster ion mobility, we would expect the 50/50 PEGDA/IL sample to have the fastest filament formation/dissolution kinetics. In fact, we observe the opposite—the 50/50 PEGDA/IL electrolyte shows the slowest kinetics. The result suggests

that the local structure of the polymer—which can be evaluated by AFM—could be important for understanding the kinetics. Regions of highly crystalline versus highly amorphous electrolyte can be differentiated by optical microscopy in the 90/10/2 mM electrolyte (Figure S9, Supporting Information, Appendix B). We therefore focused on measuring the mechanical properties the filament kinetics in these two regions. Modulus measurements in **Figure 13** show that the primarily crystalline region has an average modulus of 4.8 GPa, nearly an order of magnitude higher than the primarily amorphous region (0.6 GPa). The nanofilament formation kinetics measured in these regions indeed show distinct distributions: the primarily amorphous domain has a right-skewed Gaussian distribution with long formation times (21 % of the filaments formed within 5 s), while the primarily crystalline region has a power-law distribution with a larger percentage of fast formation events (52 % of filaments formed within 5 s). Indeed, when we compare the kinetics to the 100/0 PEGDA/IL system, which is the most highly crystalline system by a wide margin, we observe similar formation distributions as the primarily crystalline 90/10/2 mM sample (Figure S10, Supporting Information, Appendix B). Thus, we conclude that a power-law distribution in the formation kinetics is associated with large amounts of crystallinity. Moreover, regions of high crystallinity also have the highest percentage of type-1 formation events (Table S1, Supporting Information, Appendix B). Therefore, the picture that emerges is that ion transport within primarily amorphous domains is mediated by polymer chain mobility and can be described by drift-diffusion that leads to poorly ordered filaments. In contrast, faster ion transport occurs in crystalline regions likely by a hoping mechanism that gives rise to a power law distribution and well-ordered filaments.

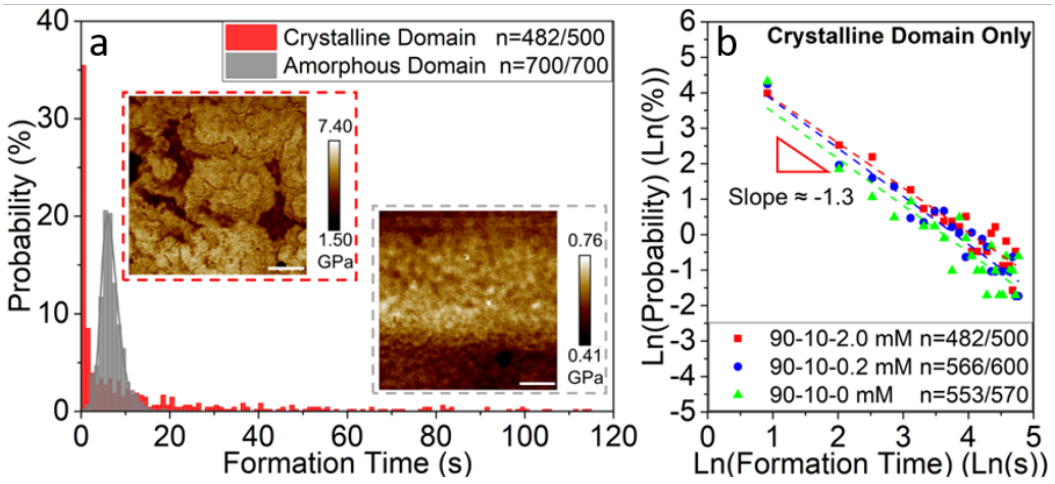

Figure 13: **(a)** Formation time distributions in primarily crystalline (red) and amorphous (gray) regions of the 90/10 PEGDA/IL wt.% with 2mM $AgPF_6$ sample using a 1 s bin width. Insets show modulus maps captured in each domain; **(b)** Log-log plot of formation time distributions *vs.* count percentages in primarily crystalline regions for 90/10 PEGDA/IL at 0, 0.2 and 2 mM of $AgPF_6$. 120 s is the cutoff time for formation, bin width is 5 s.

The data show that some amount of IL is essential to achieve fast and reliable formation events. For example, in the IL-free system, only 72% of the locations tested form filaments within the 120 s window of the measurement (Figure S9, Supporting Information, Appendix B). The electrolytes loaded with 10 wt.% IL further show that ion mobility is decoupled from PEGDA chain mobility, and indicate two different formation mechanisms in the two phases (amorphous and crystalline). While it is well understood that ion mobility in the amorphous phase is driven by chain mobility, there is also support for the notion that specific crystalline structures in PEO-based electrolytes can provide faster pathways for ion transport than their amorphous equivalents. [71–73] Based on the results obtained here, we suggest a similar explanation for the observation that primarily crystalline domains exhibit faster formation kinetics. Specifically, a balance is achieved at ∼10 wt.% IL, where conduction through crystalline regions is favored over primarily amorphous regions. In contrast to the crystalline regions, the amorphous regions have strong electrostatic interactions that suppress polymer/ ion transport and therefore filament kinetics.

3.6 Conclusion

We developed a UV-crosslinkable electrolyte consisting of PEGDA/IL/Ag salt where direct-write electrodeposition of silver nanofilaments is produced by conductive AFM with possible applications as flexible films with designer optical properties. By tuning the IL and salt concentration, the mechanical strength was varied from hundreds of MPa to a few GPa in modulus. Silver nanofilament formation and dissolution events were correlated to local structure, showing that while the addition of Ag salt in up to a concentration of 2 mM improves filament kinetics, the addition of IL beyond 10 wt% slows the kinetics. Moreover, surprisingly, the electrolyte with the largest polymer crystal fraction and the best mechanical strength shows the fastest filament kinetics. The results indicate that ion mobility in this system is likely governed more by the local polymer structure than by PEGDA chain mobility, thus creating an opportunity to tune the filament kinetics by tuning the structure of the polymer. If the kinetics can be controlled reproducibly by local morphology, one could envision a system where both the timescale and the spatial location for reconfiguring optical properties could be tuned, offering a novel approach to smart coating materials with, for example, reconfigurable optical properties.

4.0 Chapter 4: Impact of Bias on Nanofilament Formation Dynamics

Published in: Chao, Z., Sezginel, K. B., Xu, K., Crouch, G. M., Gray, A. E., Wilmer, C. E., Bohn, P. W., Go. David. B., Fullerton-Shirey, S. K. (2020). "Silver Nanofilament Formation Dynamics in a Polymer-Ionic Liquid Thin Film by Direct Write" *Advanced Functional Materials* 30(6) 1907950 (2020).

We have previously reported on the formation and dissolution of silver nanofilaments in a new type of polymer electrolyte consisting of PEGDA and an ionic liquid, [BMIM]PF_6. The IL enhances uniform nanofilament formation kinetics under constant applied bias and enables modulus tuning over a range of a few hundred MPa to several GPa, [47,48,55] making it more versatile than IL-free polymer electrolytes. Also, adding a sufficient amount of IL (> 10 wt.%) enables $5\times$ faster nanofilament formation compared to the IL-free electrolyte, but adding too much (50 wt.%) slows the nanofilament kinetics by a factor of 7. These observations suggest complex dynamics, which further motivate investigation of the underlying mechanisms.

In this work, we focus on one IL concentration and study the impact of applied bias on nanofilament formation dynamics using the same c-AFM setup depicted in Figure 3. c-AFM enables the direct writing of nanofilaments by precisely defining the nucleation sites, yielding more uniform nucleation and growth. [35, 36] Using an automated script, nanofilament formation events at hundreds of xy locations on the film are recorded as a function of applied bias. This spatially dense sampling allows us to fully capture the stochasticity of nanofilament growth and enables statistical analyses of the data, which are particularly crucial for a polymer electrolyte containing microscopic heterogeneities.

The data reveal an unexpected relationship between formation times and applied bias. Specifically, the formation times do not decrease monotonically with increasing driving force—as expected for oxide-based dielectrics [56–58]—but instead exhibit a pronounced maximum near 2.0 V. We interpret this behavior as the result of a competition between IL EDL formation and electrochemical filament growth. This competition can be used to con-

trol nanofilament morphology over multiple, well-defined resistance states—a control mechanism that should lend itself to the production and engineering of neuromorphic architectures where multiple distinguishable resistance states must be achieved to emulate the connections between neurons in an artificial neural network. [28, 29]

4.1 Impact of Applied Bias on Nanofilament Formation Kinetics

Formation times of all ∼500 nanofilaments formed at each bias over a range of 0.7 to 3.0 V are shown in **Figure 14** for three IL concentrations. At all IL concentrations, the formation times decrease with increasing bias over the low bias range of 0.7 to 1.8 V. Specifically, for 70/30 PEGDA/IL wt.% in Figure 14a, the average formation time decreases from 8.8 s at 0.7 V to 0.5 s at 1.8 V. The trend of decreasing formation time with increasing voltage is expected and can be explained by straightforward electrochemical kinetics. That is, the driving force for both electrochemical redox reactions and silver ion migration increases with increasing formation bias. However, unexpectedly, the average formation time increases abruptly when the bias is increased to just below 2.0 V. In addition to longer formation times, a more scattered distribution of formation times is also observed. For the 30 wt.% IL sample, this distribution is highlighted in the insets in Figure 14a showing formation histograms at 0.7, 2.0 and 3.0 V. At voltages larger than 2.1 V, the formation times continue to decrease as expected, and the distribution returns to a standard Gaussian that is also observed for voltages less than 1.8 V.(For a complete set of nanofilament formation and dissolution histograms, see Figure S1 in Supporting Information, Appendix C.) We refer to nanofilament formation kinetics near 2.0 V as "inverted" kinetics, where the average formation time first increases with increasing formation bias and then decreases again, causing unexpected non-monotonic behavior and giving rise to a peak in the average formation time versus voltage plot. Inverted formation kinetics appear for all three IL concentrations at ca. 2.0 V, with the formation time generally increasing with increasing IL concentration.

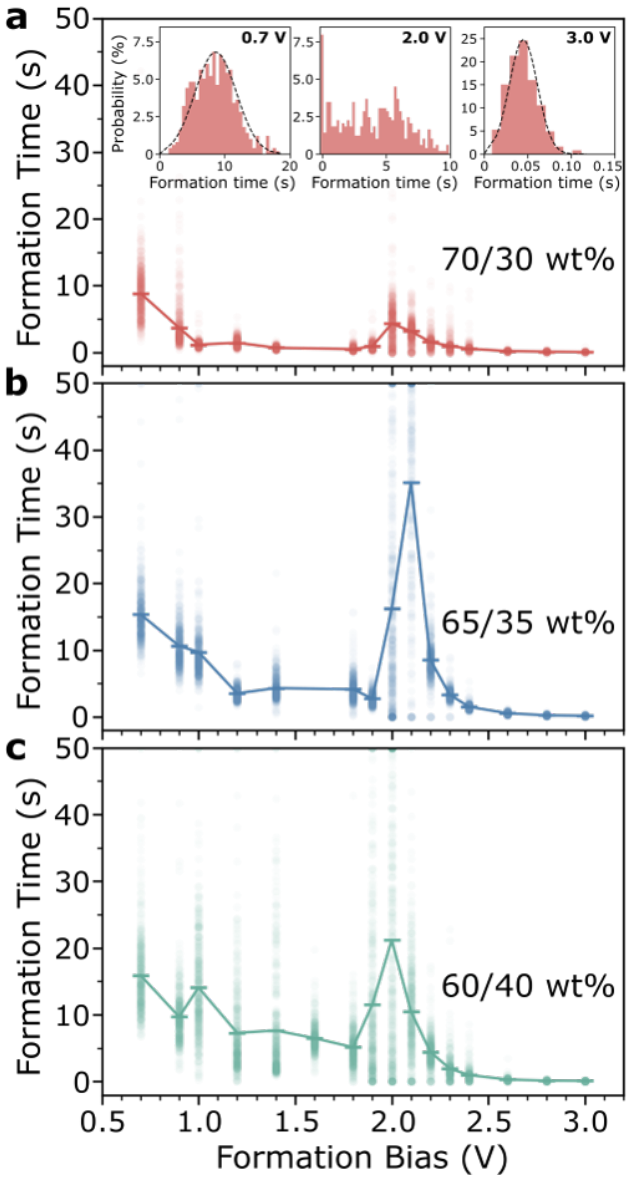

Figure 14: Nanofilament formation times as a function of applied bias for **(a)** 70/30, **(b)** 65/35 and **(c)** 60/40 PEGDA/IL wt.% samples. 500 formation events were collected for all samples at each bias with the exception of data at 2.1 V for 65/35 %, where 339 events were collected. The average formation time at each bias is indicated by a horizontal marker and connected by the solid line. Insets in (a) are the histograms of formation time distributions at 0.7, 2.0 and 3.0 V, respectively for the 70/30 PEGDA/IL wt.% sample.

4.2 The Role of Electrical Double Layer (EDL) on Formation Kinetics

The observation that inverted kinetics at 2.0 V becomes more pronounced with increasing IL concentration motivates further investigation with an eye toward the possible role of the IL. One clue regarding the contribution of the IL comes from their use as high-capacitance gate dielectrics in electrolyte-gated transistors. [74, 75] Here, electric double layers (EDLs) are formed by drift and diffusion of cations and anions to the surface of electrodes with opposite polarity. Specifically, when a positive bias is applied to the anode, cations drift to the cathode surface forming an EDL at the interface between the electrolyte and the cathode and induce an image charge in the electrode that is detected as a charging current. Simultaneously, an anionic EDL forms at the anode surface. In our case, we expect the cations in the IL (i.e., $[BMIM]^+$) to accumulate near the c-AFM tip (cathode) when a positive formation bias is applied. Thus, one piece of evidence for IL EDL formation would be a non-zero current at the first measurement time after a positive voltage is applied followed by a temporal decay—assuming that EDL formation is faster than nanofilament formation. Figure S2 (Supporting Information, Appendix C) confirms this behavior, showing the current decay over 10 ms, which is orders of magnitude faster than nanofilament formation. This behavior is identical in form to the charging current associated with EDL formation in a parallel plate capacitor. [76]

Up to half of the applied potential can drop across the EDL [77, 78] (depending on the ion concentration and the geometry of the electrodes) leaving relatively little drop in the bulk of the electrolyte to drive ion migration. Thus, residual charge accumulated within any remaining EDL is likely to impact sequential nanofilament formation as the tip is moved from location to location. To address this issue, we modified the algorithm of the automation script to discharge residual EDL by grounding the tip for 100 s both before applying the formation bias at a new location, and after applying dissolution bias. The modified script was tested on the 65/35 PEGDA/IL wt.% sample at 50 locations for each of six formation biases over two regions separated by $>$ 100 µm (i.e., 25 points/region) in a 4.8 $\times$4.8 µm array, with a pitch of 1.2 µm. Formation times with and without the tip set to ground are shown in **Figure 15**. The data clearly show that grounding the tip decreases the formation

time independent of bias. Notice that this approach does not eliminate the contribution from EDL formation during the measurement, but it eliminates any residual EDL that may persist from one location to the next.

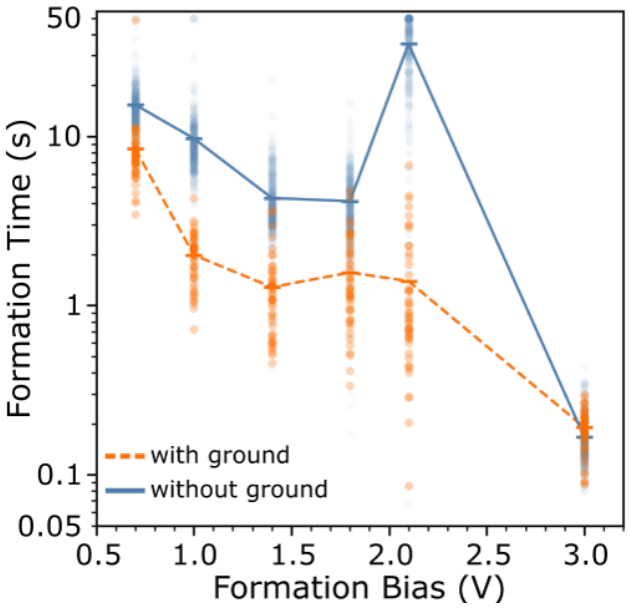

Figure 15: Filament formation times versus bias at 500 locations without grounding (blue, same data as Figure 14b) and 50 locations with grounding (orange) for 65/35 PEGDA/IL wt.%; the average formation times are connected using a solid line (without ground) and dotted line (with ground).

Grounding the electrode has an especially strong impact on the formation times at voltages corresponding to the region of "inverted" formation kinetics. For example, the average formation time at 2.1 V is 20 times faster with the grounding step, whereas it is only up to 3 times faster at other biases. In contrast, at the highest applied bias of 3.0 V, filament formation is less affected by EDL formation as filaments are likely formed before the EDL screening can take effect. Therefore the grounding has relatively little effect on the formation times, as confirmed by the overlapping data at 3.0 V.

While grounding the AFM tip decreases the formation time, the distribution of times at 2.1 V remain widely scattered with a relative standard deviation of 94%, compared to $\sim$ 25%

at 0.7 and 3.0 V. The results show that while discharging the previously formed EDL via grounding decreases the magnitude of the peak, it does not decrease the variability. Based on these results, we conjecture that there is an additional factor contributing to the inverted kinetics region, and we hypothesize that it is due to competition between EDL screening and silver ion electrodeposition. That is, the timescales of EDL formation and nanofilament formation are comparable at applied biases near 2.1 V, resulting in both longer nanofilament formation times and a wider distribution of formation times.

4.3 Quantifying IL EDL Formation Times As a Function of Bias

While the data in Figure 15 suggest that there may be important physics occurring at timescales shorter than those involved with nanofilament formation, it is difficult to decouple the electrical response of EDL formation from faradic electron transfer due to electrodeposition (Ag^+ to Ag(s)) in the nanofilament growth data. Thus, we prepared control samples in which silver nanofilaments cannot form by using a Au counter electrode instead of a sacrificial Ag electrode. One control sample, consisting of 65/35 PEGDA/IL wt.%, was designed to isolate the effects of IL EDL formation, and a second control sample, consisting of pure PEGDA, eliminates IL EDL formation altogether. Current-time data were collected for 50 s at three locations (separated by more than 100 m) at biases in the range of 0.7 to 3.0 V with grounding between measurements. These data for the pure PEGDA thin film are shown in Figure S3 (Supporting Information, Appendix C) and as expected, there is no detectable current above the noise threshold at any of the applied biases, because an EDL cannot form. In contrast, in **Figure 16** we observe clear current signatures of EDL formation in the 65/35 PEGDA/IL wt.% sample at biases greater than 1.8 V, where three measurements are made at each voltage. Specifically, when the bias is $\geq$ 2.1 V, up to 0.1 nA of current is captured on timescales ranging from milliseconds to seconds.

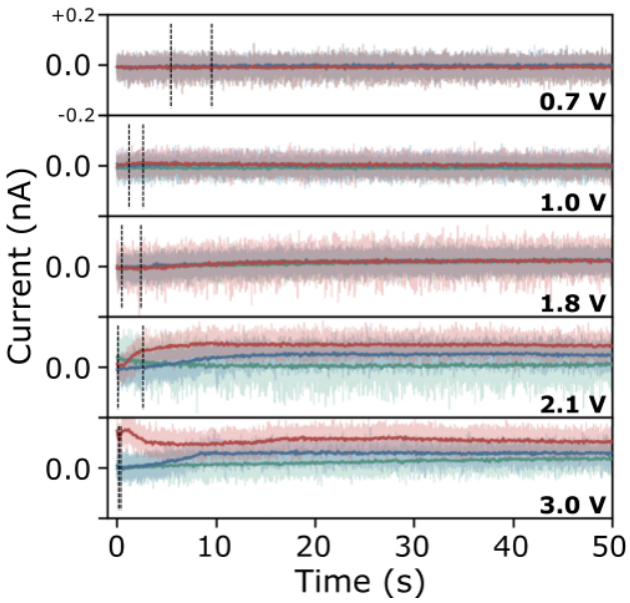

Figure 16: Time-dependent current response at various biases for the 65/35 PEGDA/IL wt.% sample on Au. At each bias, three consecutive measurements are plotted in three different colors. All of the current data are included on the plot, and the average of every 10 consecutive data points is extracted and plotted as a solid line to show the trend in the current through the noise. Note that the Y axis is linear. Dotted, vertical lines at each bias indicate ± one standard deviation of the average formation times from Figure 15 for the data that included grounding between measurements.

Because of the low signal-to-noise ratio in these extremely low-current measurements, it is not possible to quantify a time constant for the EDL response; however, we can use these data to identify the voltage at which the EDL contribution becomes detectable. This voltage could reflect the driving force required to overcome the barrier to diffusion for the IL ions through the heavily cross-linked polymer chains. That is, while small silver cations may be able to easily traverse the crosslinked PEGDA, the much larger IL ions may only gain appreciable mobility once the voltage is sufficiently large (i.e., $\geq$ 2.0 V). In addition, the variability between the three measurements at each voltage for biases *geq* 2.0 V likely reflects the stochastic nature of IL EDL formation in the PEGDA/IL system. This is not surprising given the known complexity of IL EDL dynamics in parallel plate geometries. [79]

Nevertheless, the EDL formation data in Figure 16 combined with the nanofilament formation data in Figure 15 provide insight as to why EDL formation is likely to have a stronger impact on nanofilament formation kinetics in the inverted region than at lower voltages. Note that the vertical dotted lines in Figure 16 indicate ± one standard deviation from the average formation times enabling the direct comparison of nanofilament formation timescales to EDL formation. At low biases, no appreciable EDL formation occurs and, therefore, there is no competition between silver nanofilament and EDL formation. However, at a bias of 2.1 V, where the inverted region is observed in Figure 15, the nanofilament formation time is comparable to the timescale over which the EDL current becomes appreciable. This result suggests that the silver nanofilament formation is competing with EDL formation, and the screening of the field by the EDL likely gives rise to longer formation times. Because EDL formation is disruptive to nanofilament formation, this competition could also account for the larger distribution of formation times at 2.1 V. In contrast to the inverted region, at a bias of 3.0 V the nanofilaments have already formed before the EDL has a chance to respond, giving rise to fast formation times with a tight time distribution.

4.4 Impact of Formation Bias on Nanofilament Growth Dynamics

We have established how the nanofilament formation times at various locations and IL concentrations depend on bias, and how IL EDL formation can disrupt nanofilament formation. Here, we turn our attention to the nanofilament formation dynamics. Previous reports show how the final structure of a conductive metal nanofilament is strongly associated with its growth dynamics, [1, 58, 80] which are further governed by kinetic and transport properties such as the redox reaction rate and metal ion mobility in the specific dielectric system. [80] As the principal driving force for silver migration and electrodeposition in our PEGDA/IL system, the magnitude of the applied bias is expected to affect nanofilament growth dynamics, especially when a field-sensitive IL is present. Thus, we analyze the time-dependent current data and compare these results to direct imaging of the nanofilament structure as a function of bias.

Two types of time-dependent current data are detected during formation: abrupt growth and gradual growth, and both are shown schematically in **Figure 17**a. Here, we define the *nucleation time* (t_n) as the time for the current to reach a low, but detectable value of 0.5 nA, defined as the *nucleation current* (i_n). This current is $\sim$ 100 times higher than system noise, defined as i_o. The *growth time* (t_g) is defined as the time required for the current to increase from textiti$_n$ to the formation threshold (4 nA at a current sensitivity of 1 nA/V). The distributions of filament growth time (t_g) at different biases are plotted in Figure 17b, where we define $t_g = 0.10$ s as the boundary that distinguishes abrupt ($t_g < 0.1$ s) versus gradual ($t_g > 0.1$ s) growth.

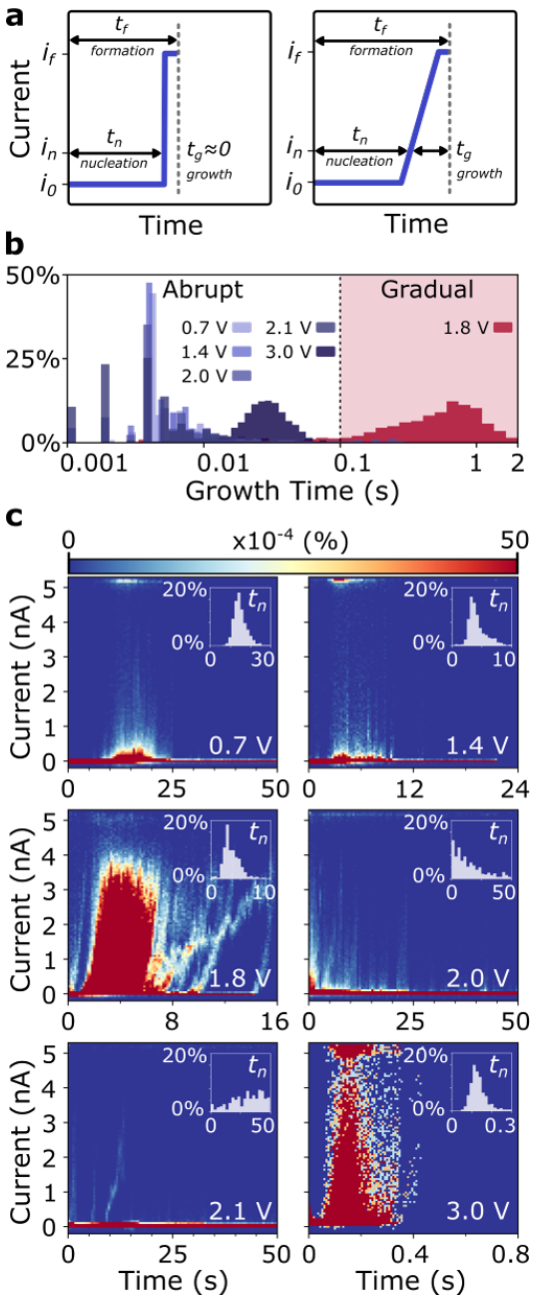

Figure 17: Time-dependent current data during nanofilament formation at various applied biases. **(a)** Schematic of abrupt (top) versus gradual (bottom) growth. **(b)** Growth time (t_g) distributions for filaments formed at different biases **(c)** All current versus time measurements are plotted at each bias. Data density is represented by color, calculated by dividing the number of data points in each bin over the total number of data points for each bias. The scale of color bar is set from 0 to 50 $\times 10^{-4}$ % and each plot contains 100 $\times$ 100 bins (*i.e.*, the time and current scales are equally divided into 100 parts).

We extracted the t_g values in Figure 17b from the time-dependent current data leading up to nanofilament formation, which are shown in Figure 17c at six biases for the 65/35 PEGDA/IL wt.% sample. Note that all current signals from hundreds of formation events at different xy locations are included in Figure 17c, where the color contours are used to represent the relative fraction of measurements with a specific current and formation time (i.e. the current data density). For nanofilaments formed at 0.7 and 1.4 V, the growth type is abrupt with an average t_g of 0.01 s; similarly abrupt transitions are observed at 3.0 V with average t_g of 0.03 s. The major difference at these voltages is the distribution of nucleation times (highlighted in the insets of Figure 17c): the wide tn distributions at 0.7 and 1.4 V lead to low data density between textiti$_n$ and textiti$_f$, whereas the narrower t_n distribution at 3.0 V increases the density of data as indicated by red.

In contrast, nanofilaments formed at 1.8 V show a more gradual growth (average t_g = 0.62 s), as shown in the t_g histogram in Figure 17b and as indicated in Figure 17c by the red data with a noticeable positive slope. When the applied bias enters the inverted region at 2.0 and 2.1 V, abrupt growth is again observed (average t_g = 0.03 and 0.02 s, respectively), but here it is accompanied by extremely scattered textitt$_n$. It is notable that the textitt$_n$ distributions at biases outside the inverted region exhibit a normal distribution, while those in the inverted region do not.

Because the current at 1.8 V changes gradually with time after the current reaches in, it suggests the possibility of achieving multiple resistance states—a requirement for neuromorphic computing [28, 29, 40]—during a single nanofilament formation under constant formation bias. To test whether or not the PEGDA/IL system can accommodate such a requirement, we set the system compliance to 100 nA and selected eight nanofilament "programming currents" ranging from 15 to 50 nA with a step of 5 nA. The formation bias was set to 1.8 V, and after each program current was reached and maintained for 20 ms, a read bias of 0.8 V was applied for 2 s while monitoring the conductance of the nanofilament. The data are plotted in **Figure 18**. The conductance initially decreases on the timescale of ms, consistent with the discharge of a portion of the EDL formed at 1.8 V, followed by a more stable current. While we cannot rule out a read disturbance at 0.8 V, the time constant for forming a nanofilament at 0.8 V is more than 50 times longer than the 2 s read time,

and when the nanofilament does eventually form, the formation is abrupt and not gradual (Figure S4, Supporting Information, Appendix C). In addition, a linear correspondence (R^2 = 0.95) between nanofilament resistance states and program pulses is observed—as indicated by the dashed line in Figure 18—which is desirable for artificial neural networks. [29, 40] In most cases, repeated programming pulses are used to controllably adjust resistance, [29, 40] but Figure 18 strongly suggests that multiple resistance states may be achieved via the competition between the EDL formation and Ag redox reaction—thereby introducing a new mechanism to tune resistance.

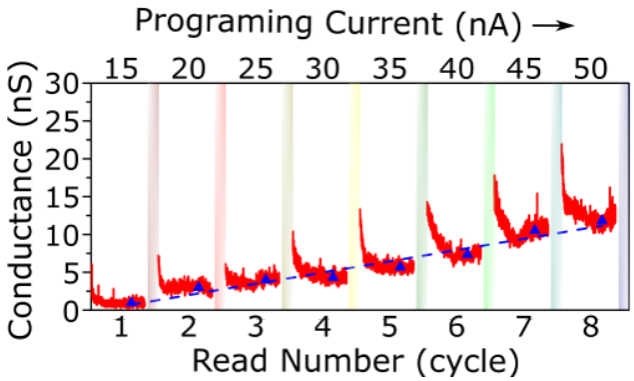

Figure 18: Conductance measured for 2 s at a 0.8 V read bias after nanofilament reached 8 programming currents (15, 20, 25, 30, 35, 40, 45 and 50 nA) at 1.8 V for 20 ms (65/35 PEGDA/IL wt.%). Shaded bars indicate the locations where a 1.8 V formation bias was applied.

The nanofilament growth dynamics captured in Figure 17 are likely to result in different nanofilament morphologies; therefore, SEM was used to image the nanofilaments directly, producing both top-down and cross-section views (**Figure 19**). Four, 5 × 5 arrays of nanofilaments were created using 0.7, 1.4, 2.1 and 3.0 V nanofilament formation biases, respectively (4.8 × 4.8 µm square with a pitch of 1.2 µm). Surprisingly, the cross-sectional images in Figure 19 combined with c-AFM conductivity mapping (Figure S5, Supporting Information, Appendix C) show that the majority of the nanofilament structure is confined below the surface of the polymer film. The plan view image makes it clear that nanofilaments formed

at 2.1 V have the largest features among all arrays, followed by 0.7 V and 1.4 V, while only subtle features in the nanofilament array can be resolved at 3.0 V. The cross-section imaging shows nanofilaments formed at 0.7, 1.4 and 2.1 V all have obvious lateral buildup, especially those formed at 2.1 V. In contrast, no nanofilament structure formed at 3.0 V can be resolved through cross-section imaging.

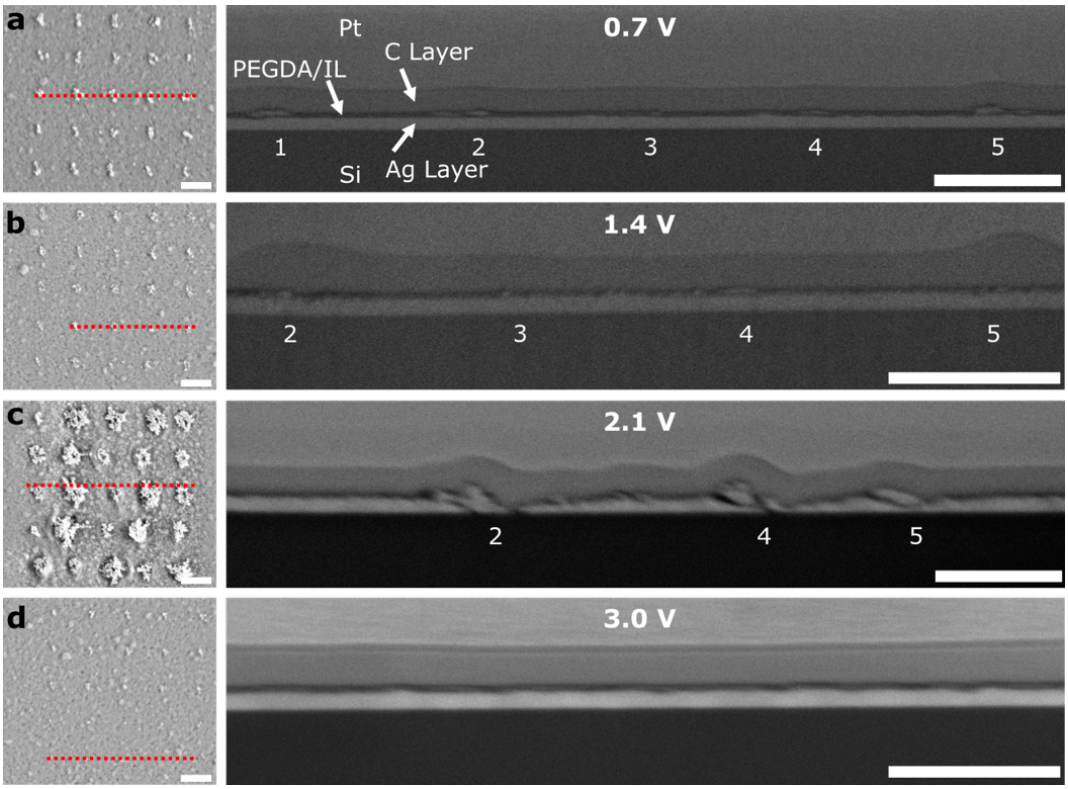

Figure 19: Plan view (left) and cross-section (right) SEM images of arrays of silver nanofilaments formed at **(a)** 0.7, **(b)** 1.4, **(c)** 2.1 and **(d)** 3.0 V. The locations of the cross-sections are indicated by red dashed line on the surface image. All scale bars are 1 µm.

Combining the time-dependent current data in Figure 17 with the SEM images of Figure 19 leads us to hypothesize a model of bias-dependent nanofilament growth shown schematically in **Figure 20**. At biases $\leq$ 1.4 V where abrupt nanofilament connections are made and for which nanofilaments are visible by SEM, the relatively weak vertical electric field

results in more lateral build-up (i.e., thicker nanofilaments) before the final connection is made. The switching behavior shown in Figure S6 (Supporting Information, Appendix C) provides additional support for this interpretation in that it becomes increasingly difficult to dissolve nanofilaments with increasing switching cycles—consistent with thickening of the nanofilament during switching. While similar abrupt current transitions are also observed at 3.0 V, the vertical field is stronger, leading to faster and more directed (i.e., less lateral) growth. The hundreds of nanofilaments formed at this higher field remain switchable for at least 20 cycles (Figure S6, Supporting Information, Appendix C)

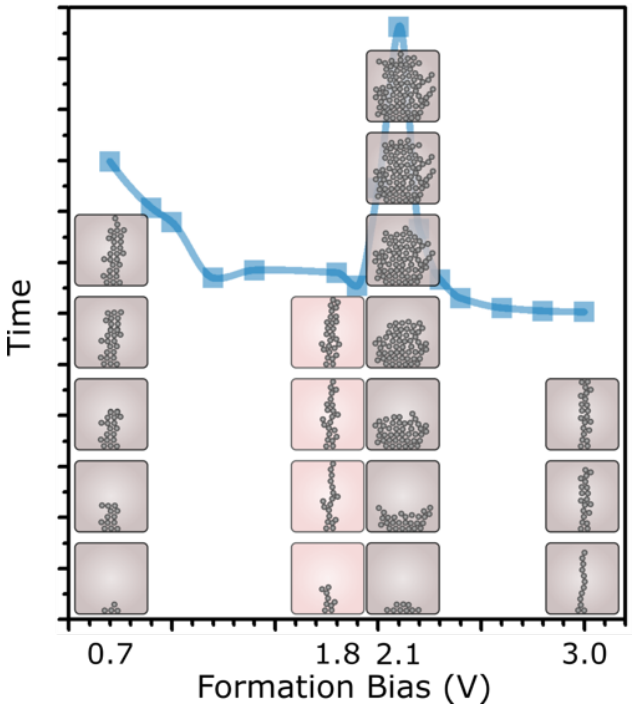

Figure 20: Schematic illustration of nanofilament formation dynamics at different applied biases. Gradual growth type (shaded red) is only observed at 1.8 V for the 65/35 PEGDA/IL wt.% system. Silver atoms are represented by grey spheres. The width of the nanofilaments relative to the depicted atom sizes are purely for illustrative purposes and do not reflect the actual ratios.

In the inverted region, we measure a wider distribution of nucleation times, extreme lateral growth, and both gradual and abrupt formation events consistent with a competition between redox reactions and EDL formation that weakens the vertical electric field. Clearly, 1.8 V represents the threshold at which EDL formation impacts the growth kinetics in our PEGDA/IL system—changing them from abrupt to gradual by interfering with the electric field. Here, the nanofilament morphology also changes from thin (high resistance) to thick (low resistance) over longer timescales, and this gradual and controllable thickening could lead to enhanced switching characteristics. In fact, of the three measured voltages, the nanofilaments formed at 1.8 V retain the best switching characteristics among those tested (Figure S6, Supporting Information, Appendix C). In addition, when the nanofilament does reform at 1.8 V during the switching measurements, the switching is also gradual (Figure S6, Supporting Information, Appendix C), another characteristic which is required for neuromorphic applications.

4.5 Conclusion

C-AFM-based direct-writing of nanofilaments in a PEGDA/IL electrolyte reveals an unexpected relationship between formation times and applied bias. Specifically, the nanofilament formation time does not decrease monotonically with increasing driving force, but instead exhibits a pronounced maximum near 2.0 V, described as the "inverted region". We interpret this behavior as resulting from a competition between IL EDL screening and electrochemical nanofilament growth. Time-dependent analysis of formation current over hundreds of formation events reveals two types of growth dynamics – abrupt and gradual. Gradual dynamics are observed at $\sim$ 1.8 V representing the threshold where EDL formation begins to interfere with nanofilament growth, changing it from abrupt to gradual. Here, multiple resistance states can be accessed within a single nanofilament, due to the gradual growth. The voltage-dependent dynamics are also correlated with filament structure: nanofilaments formed in the inverted region have more lateral and diffuse structures than those formed outside the voltage window. The results suggest that by tuning the competition between the

IL EDL and electrochemistry, the growth dynamics and nanofilament morphology can be tuned. This control mechanism could potentially be exploited in applications such as artificial neural networks, where multiple, distinguishable resistance states are required. Further optimization of this electrolyte is expected to extend the accessible range of resistance states to smaller write/read biases, making the PEGDA/IL electrolyte a highly customizable system and potential candidate for organic electronics requiring low-power neuromorphic computing operation.

5.0 Chapter 5: Study of Nanofilament with Gradual Growth for Neuromorphic Application

Among many attributes, one unique aspect of the human brain that amazes engineers is how it can utilize more than 10^{15} synapses to compute and make complex decisions while maintaining its energy consumption to around 20 Watts, [27] (i.e., 20 femtojoules (fJ, $1\times$ 10^{-15} J) energy consumption per synapse per operation.) As a comparison, a transistor-based TrueNorth deep neural network (DNN) system developed by IBM integrates 256 million synapses that can operate at 20 picojoules (pJ, $1\times$ 10^{-12} J) per synapse per operation. [81] To simulate energy efficient synaptic operation in biological neurons, the most common approach is to use analog switching via input pulses to modulate the current signal. Analog current signals (conductance states) can be used to represent continuous logic states in neuromorphic computing, making it efficient in tasks for artificial intelligence and deep learning applications. Instead of integrating multiple devices with binary conductance states (such as transistors) to achieve multiple analog states, it is much more desirable to have a *single device* capable of accessing many stable conductance states in response to inputs for neuromorphic applications.

Over the past a few years, impressive progress has been made on synaptic devices using organic materials for neuromorphic application. For example, organic electrochemical redox-based switching devices have been reported to have efficient switching energy consumption $\sim$10 pJ per operation. [26,82] Owing to their ability to operate in global or shared electrolytes, organic neuromorphic systems further demonstrate effectiveness in mimicking brain-like functionality as it enables functional connectivity among multiple devices. [83–85] These three-terminal devices also show promising retention time. However, scaling up such devices to achieve practical neuromorphic computing function ($>$ 1000 devices in parallel structure) remains more challenging than their simpler two-terminal memristor based counterparts.

Although in Figure 18 we have shown multiple conductance states of a single nanofilament formed in the PEGDA/IL system, its capabilities in the context of artificial neuromorphic

applications is far from being realized. These shortcomings include a gradual decrease in conductance states during dissolution, a broader range of tunable conductance with multiple and distinguishable and stable states. In addition, the previous results are collected using a mobile electrode (c-AFM tip) that lacks scability for practical applications. Therefore, the device geometry tested in this chapter is different than those described in previous chapters. Specifically, the electrode dimensions are decreased to increase device packing density which is practical for neuromorphic application. Here, we present lithographically patterned devices for which the electrical characterization is completed not on a conductive AFM (with rather crude current and voltage range and resolution), but instead on a probe station coupled to a semiconductor parameter analyzer with a current range of 0.1 fA to 1 A and a voltage range 0.5 μV to 200 V. Pulse modulation of conductance states have been conducted on the probe station setup and reported. In this chapter, some of the critical parameters required for neuromorphic application are benchmarked for our PEGDA/IL system against desired metrics of organic neuromorphic devices, including number of conductance states, linear and symmetric correspondence between conductance and pulse cycles, and switching noise level.

5.1 Sample Preparation for Probe Station Measurements

The device fabrication process is shown in **Figure 21**. An electrically insulating SiO_2(90 nm)/Si wafer was used as the substrate. The location and dimension of the bottom Ag electrodes were directly patterned using photolithography (Heidelberg MLA100), followed by the deposition of 25 nm of Ag using an e-beam evaporator (Plassys MEB550). The dimensions of the Ag electrodes were set to 25 µm × 25 µm. Au contact pads were also patterned using MLA, followed by e-beam deposition (140 nm thick). The electrical connection between each Ag electrode and its designated Au contact pad was made by a 15 µm wide Ag extension arm (25 nm thick). Notice that we use Ag as the arms even though it is more electrochemically active than Au to avoid polymer electrolyte film inhomogeneity caused by spin-coating. In first attempts, we observed that PEGDA, which is hydrophilic, tends to aggregate on Ag at Ag/Au interfaces possibly due to better wettability of Ag compared to

Au. [86,87] For the contact pads, Au is selected because it is mechanically strong for landing the sharp probe station probe. Au pad (140 nm) is deposited as the location where electrical contact will be made using both the c-AFM and the probe station: during the initial filament formation using AFM, Au contact pads serve as the electrical contact between the device and the copper tape; under the probe station setup, the Au contact pads are the landing locations for the probe station probes. (Note, this is the equivalent location to where we make contact with copper tape in the AFM set up). A thin film of PEGDA/IL ($\sim$40 nm) was then spin-coated following the procedure described in Chapter 2. Next, the Ag nanofilament was directly-written using c-AFM as described in previous chapters. Only one filament was written on each Ag pad, creating a filament embedded in polymer electrolyte ready for the electrical characterizations using the probe station. Finally, 140 nm of Au was deposited as a universal top electrode.

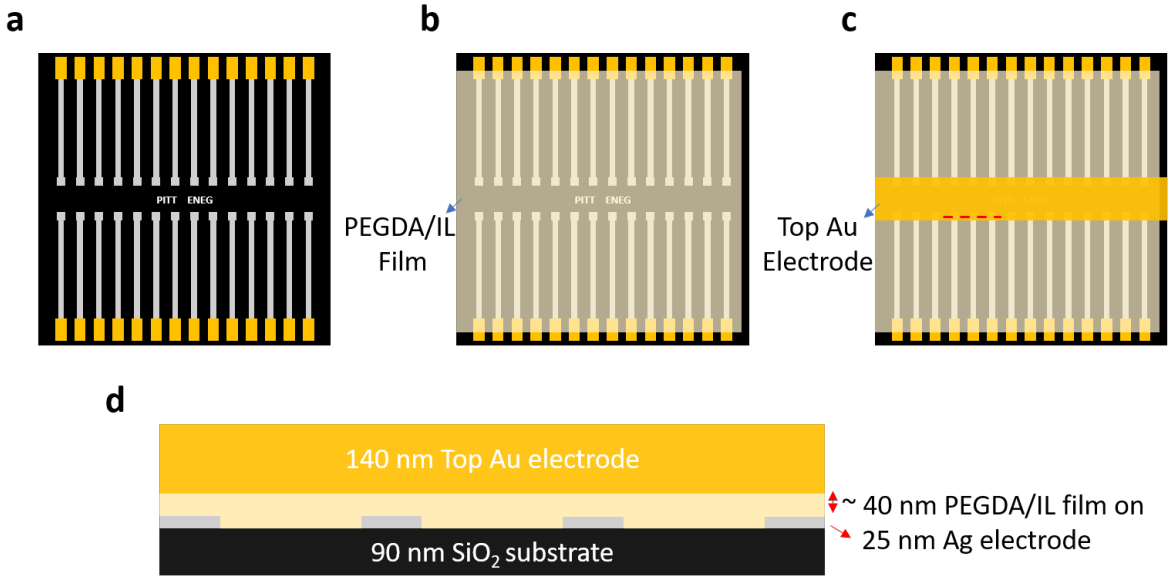

Figure 21: Process flow of sample preparation for probe station **(a)** schematic of fabricated devices after lithographic patterning and e-beam evaporation of bottom Ag electrode (25 × 25 µm) and Au contact pad (100 × 300 µm). Electrical connection is made by Ag extension arms. **(b)** PEGDA/IL film is deposited by spin-coating and followed by filament direct-write by c-AFM. **(c)** A universal Au top electrode is evaporated onto PEGDA/IL. A shadow mask was optically aligned using a microscope to minimize the electrolyte area between the Ag arm and the top Au electrode before e-beam deposition. A cross-sectional view of device is shown in **(d)** with the cross sectional area corresponding to the dashed cutline in (c).

5.2 Temperature-Dependent EDL Charging Effect

As explained above, the c-AFM is used to direct-write the filaments and then the PEGDA/IL electrolyte is capped by a top Au electrode. In the absence of the filament, the structure would be considered a MIM; however, once the filament is written and the bottom Ag pad and top Au electrode are connected, we create an electrically shorted device that can be toggled back to an MIM device by dissolving a section of the filament. Here

it is important to point out differences in size between the c-AFM direct-write only devices describe in previous chapters and the ones described here. Specifically, the difference arises in the size of the working electrode (i.e., the AFM tip in the AFM set-up and the bottom Ag pad in the modified device configuration), (shown in **Figure 22**). The Ag pad is significantly larger than the AFM tip, meaning that the contact area between the electrolyte and the working electrode is larger. Specifically, the contact area of the AFM tip is typically $<$ 1 µm², while the contact area between Ag pad + arm and the electrolyte typically exceeds 3000 µm² (taking 25 µm square Ag pad and 150 µm $\times$ 25 µm Ag arm exposed to electrolyte as an example). This means it is especially critical to nucleate the Ag filament growth using C-AFM at desired location (within the Ag pad) to avoid unwanted electrochemisty on the arm region.

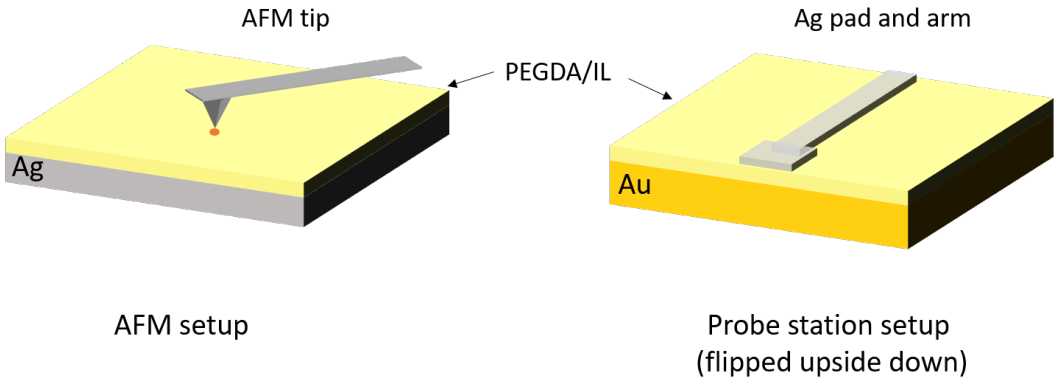

Figure 22: A schematic comparison between the AFM setup (left) where the AFM tip is the working electrode and probe station (right) where the Ag pad is the working electrode. The schematic of probe station setup is flipped upside down to better compare the two (i.e., the AFM tip on the left is analogous to the Ag pad and arm on the right).

As discussed in Chapter 4, the gradual growth filament type is the outcome of a competition between electrochemical deposition and EDL screening. To better understand the impact of the EDL screening on Ag filament formation using the probe station setup, we first made control measurements on Ag pads at which no filament was direct written (i.e.,

an MIM structure). The EDL current response at three applied biases (1, 2 and 3 V) are plotted at different temperatures (260 K to 290 K) as shown in **Figure 23**. Under all biases we tested we find at room temperature (290 K) the EDL charging current is much higher when comparing with the control experiment under the AFM setup. For example, at 2 V, the charging current exceeds 1 nA during the first moments of the measurement, while the charging current is significantly smaller at a similar bias (2.1 V, $<$ 0.2 nA) under the AFM setup as shown in Figure 16. A strong EDL response at the filament formation bias is expected to interfere with filament formation dynamics and make it challenging to distinguish filamentry current from EDL current under the probe station setup. It is actually no surprise that current response attributed to the EDL is stronger in these devices compared to the c-AFM setup, because the bottom Ag pad and arm dimensions are much larger (more than 1000×) than the radius of AFM tip (as discussed above and illustrated in Figure 22). This difference in geometry has such a strong impact because the density of ions that can accumulate at the electrode will increase monotonically with electrode area, which amplifies the EDL response to electrical field.

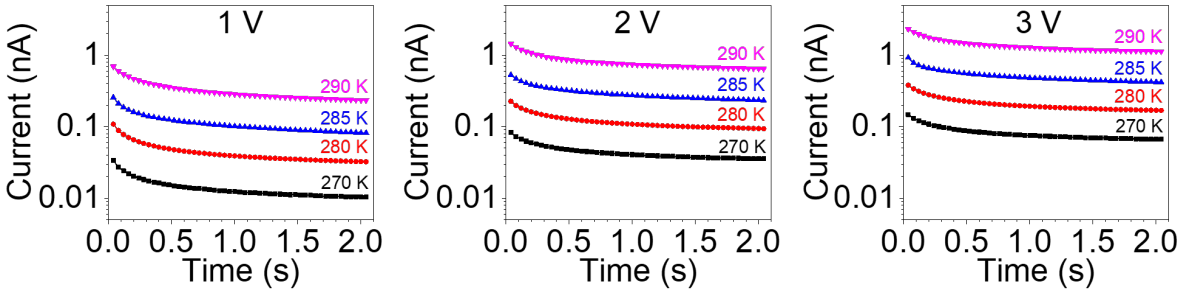

Figure 23: EDL charging current *versus* time ranging from 260 K to 290 K under 1 V (left); 2 V (middle) and 3 V (right) on a filament-free control device. Positive bias was applied on bottom Ag pad while top Au electrode was set at 0 V.

In addition to the magnitude of applied bias, temperature also has a strong impact on the EDL responsive as shown in Figure 23. The magnitude of EDL charging current is reduced by almost one order of magnitude when lowering the temperature by less than 5%

from 290 to 280 K. This is sensible as lowering temperature will suppress the mobility of the polymer chains and therefore the ions, thereby slowing down EDL dynamics. [61] The temperature-dependent EDL response suggests temperature can be used as another knob to tune the degree to which the EDL competes with filament formation. To better distinguish the filamentary current signal from the EDL current, all measurements on this specific device were conducted slightly below room temperature (285 K). This is the highest temperature for which the magnitude of the induced EDL charging current (< 0.2 nA after 0.5 s) remains about 10 $\times$lower than the filamentary current range observed in c-AFM setup ($\sim$ 2 to 5 nA) at 2 V.

5.3 Pulse Modulation of Filament Conductance

In our previous work, we applied a fixed bias to create and dissolve the filaments; however, for the purposes of energy efficiency, it is better to use a train of pulsed biases to modulate the conductance of metal filaments for neuromorphic application. To demonstrate the pulse modulation of filament conductance, we first ensure that the pre-written filaments are connecting both electrodes after the deposition of the top electrode. However, we noticed a large portion of filaments formed by AFM were not responsive to bias input from probe station measurement. Example data are shown in **Figure 24** for a device that included one, pre-written filament (note that the direct write was terminated at 1.6 nS during AFM writing to limit surface overgrowth). The current simply follows the voltage and no obvious electrochemical signatures are observed when ramping the bias from $\pm$1 to $\pm$4 V (note that the bias was held for 22 s at each selected potential provide ample time for electrochemisry to occur). We can, however, distinguish a weak filamentary conductance at around 0.1 nS (i.e., where the current flattens out at 0.15 nA under 1 V in Figure 24) after subtracting the EDL contribution (i.e, 0.05 nA under 1 V EDL charging current in Figure 23). A small conductance of 0.1 nS suggests a much weaker than expected connection was detected between the top and bottom electrodes via the pre-written filament; however, the filament is surprisingly electrochemically unresponsive to bias input under the probe station setup. We

hypothesize that this electrochemical inactivity could result from large contact resistance between the Au electrode and the polymer surface, which could account for the non-tunable filament conductance. One piece of evidence that supports this conclusion is the observation from SEM in Chapter 4 that the majority of the filament volume formed via direct-write in the c-AFM is embedded underneath the polymer film, as shown in Figure 19. The limited amount of surface overgrowth could readily result in large contact resistance when capped by top Au electrode.

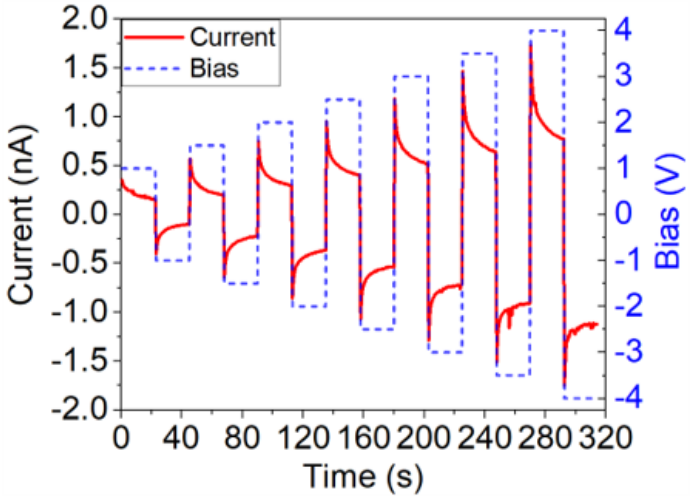

Figure 24: Current (red line) and bias (blue dot) *versus* time when the bias applied on bottom Ag electrode was increased step-wise from ±1 V to ±4 V. At each bias time was held for 22 s. Measurement was conducted at 285 K.

In contrast to the weakly connected filaments that are not responsive to bias input, we also observed pre-written filaments that *are* electrochemically responsive. Interestingly, both polarities of bias applied to the Ag bottom electrode could set the filament when the top Au electrode was held at 0 V. As shown in **Figure 25**a, after initial EDL charging, a constant bias of -2 V drives the filament formation and sets the conductance to 0.85 nS (i.e., -1.7 nA at -2 V) after 45 s. Such a "negative-set" is not surprising as it has been widely reported in literature, [56] [88] [89] and its cause can be attributed to active metal

precipitation near the cathode during previous"positive-set" process as illustrated in **Figure 26**. [3] During initial filament formation under a positive bias (Figure 26a-b), Ag atoms from the active Ag top electrode (TE) are first oxidized to Ag^+ then are reduced near the Pt bottom electrode (BE), penetrating into the BE; dissolution under negative bias (Figure 26c) breaks the connection, but does not dissolve the remaining Ag at the BE. When the negative bias is held long enough, the previously broken filament can be reconnected ("negative-set"), because the remaining Ag at the BE can be oxidized and now function as an anode, as shown in Figure 26d. For our system under the probe station measurement, negative-set means that Ag deposits near the top surface (i.e., where the AFM tip was located during filament formation) acts as the cationic source (i.e., anode) when negative bias is applied to the opposite, bottom Ag electrode.

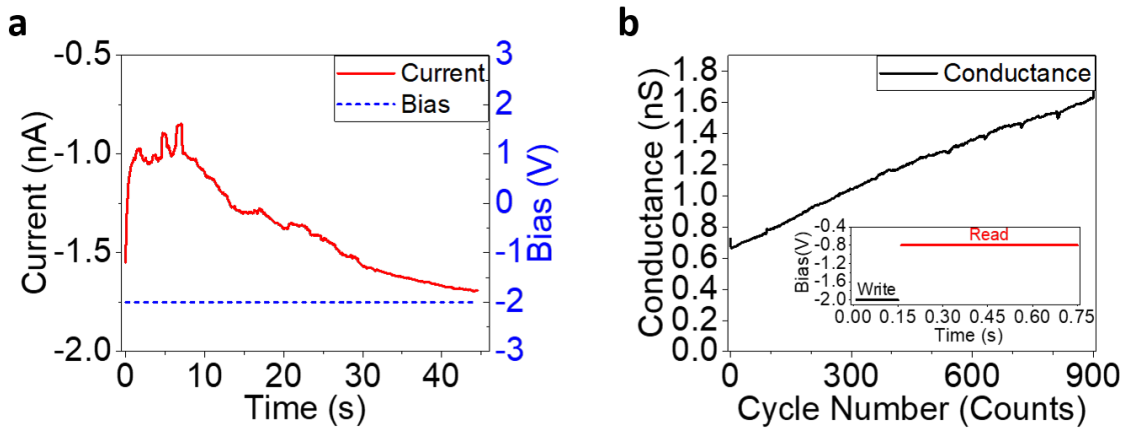

Figure 25: Demonstration of filament growth under constant negative bias and pulses of negative bias. **(a)** Current (red) *versus* time when a constant negative bias (blue) was applied showing filament "negative-se". **(b)** Read filament conductance change vs. pulse cycles; details of the pulse within each cycle are included in the inset. Measurements were conducted at 285 K.

As discussed in the introduction, a linear correspondence between conductance and number of bias pulses is required for artificial synaptic devices as they can improve neural network

training accuracy. "Negative-set" enabled the demonstration of linear increase of filament conductance by pulse cycles as shown in Figure 25b. The write/ read pulses information within each cycle are included in the inset of Figure 25b: 0.15 s at -2 V write bias followed by a 0.6 s at -0.8 V read bias. Within each pulse, to eliminate the impact of EDL discharging current when switching from higher write bias (-2 V) to read bias (-0.8 V), only the read current from 0.45 to 0.75 s was averaged and used to calculate the filament conductance. As shown in Figure 25b, the filament conductance *versus* pulse number is clearly linear (R^2= 0.99), and the filament conductance is tuned from 0.8 to 1.6 nS (ΔG = 100 %) over 900 writing cycles. This is a promising result because it suggests that hundreds of conductance states within a single Ag filament can be achieved using pulse modulation in the PEGDA/IL system, and that this modulation is regulated by the IL EDL. However, we have yet demonstrated a linear decrease in filament conductance using pulses modulation.

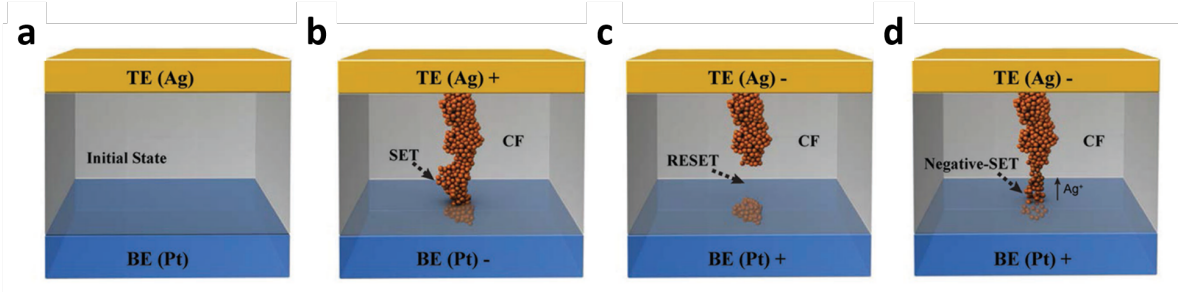

Figure 26: Schematic showing the "negative-set" mechanism. **(a)** MIM structure before filament formation; **(b)** during "positive se", the conductive filament forms and overgrown into the Pt electrode; **(c)** metal filament disconnected under negative bias, but part of the ruptured metal filament still remains in the Pt electrode; **(d)** the ruptured metal filament at the RESET process can be repaired due to the electromigration and redox reaction of metal precipitation in Pt electrode, leading to "negative set". Reproduced with permission from John Wiley and Sons. [3]

To reduce the contact resistance between pre-written Ag filaments and the Au electrode deposited on top of them, we took a new approach to device fabrication. Figure 19 suggests

that filaments will build-up laterally when the applied bias is less than 3.0 V. Therefore, we decreased the filament formation bias from 3.0 V to a set of bias ranging from 1.2 to 2.6 V. In addition, we also allow the initial Ag filament to overgrow on the electrolyte surface by holding the bias for $>$ 30 ms after the connection was made (in contrast, growth in the previous device was terminated prior to 30 ms). Similar to the previous device structure, 140 nm of Au was deposited as a top electrode. Interestingly, though we have overgrown the filament for a longer time than the previous device, the connection between the bottom and top electrodes was not detected using the probe station. We think it is less likely that the filament is disconnected at the top Au electrode because of the massive overgrowth that we achieve via a lower bias and a longer formation time using the c-AFM. Therefore, it is more reasonable to assume that the filament ruptures at some point during the "processing time", which corresponds to the time after the filament was written but before the probe station measurement (i.e., during Au deposition, storage, transfer, etc.). We cannot know the location of the disconnection, but we do know that disconnections are not unexpected. One reason is that Ag filament dissolution is a rapid and abrupt process, as we shown in chapter 3, and another reason is that dissolution can occur spontaneously to minimize the high surface energy of the filament, even when no external bias is applied. [30, 31, 82, 90] It is thus not surprising when Ag atoms along the filament diffuse back into electrolyte and break the connection over an extended period of time after electrical field is removed.

To reconnect the broken filament for probe station measurements, we first applied a constant negative bias to "negative set" the filament; once the electrical connection has been made, we switched to bias pulses to further modulate the filament conductance. As shown in **Figure 27**, when using pulses of 100 ms of -1.2 V bias the filament conductance can be linearly increased from 235 to 260 µS over 250 cycles; after 250 cycles, the conductance can be decreased to 237 µS using 250 cycles of 200 ms of 0.2 V bias pulse. Figure 27 clearly demonstrated highly symmetric and linear conductance modulation (R^2= 0.9 from cycle 0 to 250 and R^2= 0.97 from cycle 251 to 500) using pulses of bias enabled by EDL regulated gradual filament formation and dissolution, making PEGDA/IL based CBRAM highly promising for artificial synapse applications.

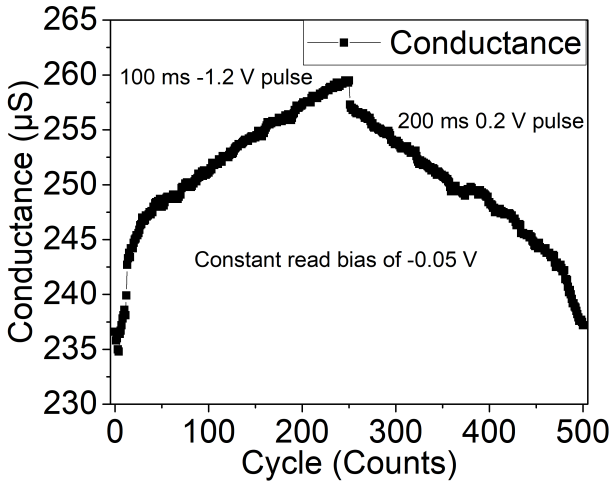

Figure 27: Read filament conductance *versus* pulse cycle. 100 ms of -1.2 V bias was applied to write the first 250 cycles and 200 ms of 0.2 V bias was applied to erase from cycle 251 to 500. Read pulse (30 ms of -0.05 V) followed each write/ erase bias pulse is used to read the conductance. Measurement was conducted at 295 K.

One major difference between Figures 27 and 25b is the magnitude of conductance: the starting conductance of filament in Figure 27 is more than 5 orders of magnitude larger than the filament in Figure 25(b). We hypothesize that this is due to the long overgrowth under c-AFM creating a less resistive filament and improved electrical contact with top Au electrode in the new device. In Figure 27 we demonstrated a linear decrease in conductance using bias pulses, but for the filament reported in Figure 25(b), no such demonstration could be achieved. In fact, the change in filament conductance is typically quite unpredictable and abrupt during dissolution with no indication that a gradual—let alone linear—dissolution is possible.

We suspect that the competition created by the EDL may have a weaker effect during filament dissolution than formation. One reason is that dissolution has a different mechanism and dynamics than formation, as discussed in Chapter 3: in brief, filament dissolution is faster ($\sim$ ms) and more abrupt than formation ($\sim$ seconds) as only a few atoms need to be oxidized to break an electrical connection. An overgrown filament will require a longer

time to dissolve, thus extending the time window for the EDL to equilibrate, while a weakly connected (i.e., non-overgrown) filament will dissolve more rapidly preventing the EDL from creating a competition.

A major breakthrough in this portion of the dissertation work is the demonstration of linear filament conductance increase *and* decrease using trains of bias pulses, but only for filaments with high conductance ($>$ 200 µS). To date, the data shown that when the filament conductance is lower (sub µs), the change in filament conductance is typically quite abrupt during dissolution. We rationalize this as a difference between the timescales over which the EDL has the opportunity to form—and therefore compete—with the electrochemistry. However, while we feel confident about our understanding of IL EDL regulation of filament formation, we are still uncertain how much of this can be applied to dissolution—especially because they occur on significantly different timescales. Measurements to tease out the differences between formation and dissolution are ongoing.

5.4 Conclusion

In this chapter we take a leap from a laboratory scale AFM-based setup to more practical lithography based setup, with the possible exception of the direct-write step which perhaps could become massively parallelized at scale. We have used this new geometry to measure filament formation dynamics, and to a lesser extent, dissolution dynamics in a PEGDA/IL system for neuromorphic applications. Multiple hundreds of filament conductance states (exceeding ∼100, which is the desired states number for organic neuromorphic devices) [28] are demonstrated using bias pulse modulation and the correspondence between conductance over pulse number is linear ($R^2 >$ 0.9 for both increase and decrease) and symmetric, as required. [28, 40] We have shown 10 % reversible modulation (from 235 to 260 µS) with low noise level ($<$ 0.5% conductance range, 1.3 µS, which is recommend for organic neuromorphic device) [28] in filament conductance over 250 cycles (average 0.1 µS per switching). These results are promising because they suggest EDL regulation of gradual filament formation and dissolution can be replicated within distinct device geometries, and this scalability suggests

a possible opportunity to exploit this phenomenon within a PEGDA/IL-based memristor to create an artificial synapse. In addition to applied bias, as reported in Chapter 4, temperature can also be used as another variable to tune the competition between EDL formation dynamics and filament formation dynamics. However, there are also key challenges such as abrupt filament dissolution for filament with low conductance (sub µS) while filament with high conductance ($>$ 200 µS) suffers from a limited tunable conductance range. In future work we will focus on understanding the dynamics of EDL discharging when switching the polarity of the applied bias and its impact on filament dissolution. We will continue working on tuning the EDL contribution to make it optimal for decreasing the analog conductance while dissolving Ag filament.

6.0 Chapter 6: Conclusions

This chapter includes a review of the complex roles that [BMIM]PF_6 plays on Ag nanofilament formation and dissolution in PEGDA, and provides an outlook for PEGDA/IL-based CBRAM.

6.1 Understanding the Roles of IL in Metal Nanofilament Formation and Dissolution Dynamics

The first documented report of ILs occured in the mid-19th centry. Formed from Friedel–Crafts reactions for toluene production, the red-colored phase, then called as "red oil", was later identified as heptachlorodialuminate salt thanks to invention of NMR spectroscopy. [91] When reviewing the history of ionic liquids, I was impressed by how far researchers have extended their understanding an usage over the past a few decades: from solvents for petroleum recovery, [92] additives for battery electrolytes [93, 94] to the "X factor" in resistive memory. [52, 95, 96] With respect to memory, there are two examples showing that when ILs are introduced to either organic or inorganic based resistive memories, both the operation performance and reliability improved. [52, 95] The authors claimed that the IL improved the switching performance of CBRAM mostly by promoting ionic mobility in the insulating/electrolyte layer, which is a similar reasoning given in many IL-containing electrochemical devices. [93, 94] While enhanced ionic conductivity may certainly play a role in CBRAM as well, the work in this dissertation paints a much more complex picture of the mechanisms involved.

In the IL-filled polymer electrolyte studied here, we revealed the transition of roles the IL plays from a facilitator to a competitor depending on the strength of external electrical field: when bias is < 1.8 V or > 2.2 V, electrochemistry happens faster than the EDL screening the field. In this case, the IL seems to operate like a plasticizer to facilitate filament formation. However, when the bias is in the range of 1.8 and 2.2 V, a competition is generated between

the EDL and electrochemistry; in this range, the IL can slow down electrodeposition of the filament. In addition to this newly uncovered role of the IL, it also plays some more predictable roles in our system. Specifically, similar to charge-neutral (non-ionic) plasticizers used in polymer electrolytes, [97,98] we found that the IL also decreases PEGDA crystallinity and the addition of a small weight percentage of IL (up to 10 wt.%) improves the Ag filament formation rate, presumably by the improved ionic mobility and facile path for ion movement.

Although we have no direct measurement of Ag^+ and $[BMIM]^+$ conductivity in the PEGDA medium, we can speculate that the Ag^+ will likely move faster under the same field strength because it is 23 % lighter in weight and 60 % to 88 % smaller in ionic radius [99]). However, its travel distance towards the AFM tip (cathode) is typically larger than $[BMIM]^+$. This is because IL ions are positioned (homogeneously) in the electrolyte *before* the electric field is applied, whereas Ag ions are generated only at the opposite electrode (anode, *i.e.*, in this case, the bottom Ag electrode). In addition, because Ag^+ does not exist the electrolyte prior to electrochemical oxidation reactions, Ag^+'s movement towards the cathode depends, in part, on the rate at which it is generated by electrochemical oxidation. In contrast, $[BMIM]^+$ can immediately start migrating towards the anode. In other words, even though they may be slower, the ions in the IL get a "head start" on the migration of the Ag^+ because of their preexistence in electrolyte. One piece of evidence to support this picture is found in Chapter 3: at 2.0 V formation bias, a 70/30 wt.% PEGDA/IL system that contains no $AgPF_6$ gave gradual filament growth, whereas the electrolyte with 2 mM of $AgPF_6$ resulted in filaments with abrupt growth. This observation confirms that the IL EDL is unable to strongly regulate Ag nanofilament formation when Ag ions are abundant and readily available in the electrolyte for electrodeposition.

6.2 PEGDA/IL Based CBRAM for Neuromorphic and Resistive Memory Applications: An Outlook

While CBRAM for non-volatile memory has made it all the way from benchtop to commercialization in the last a few decades, the use of CBRAM for neuromorphic application

lags. Most of the demonstrations remain at laboratory scale due to some key challenges limiting their commercial production. The main roadblock is an inability to tune metal filament dynamics gradually (both the increase and the decrease of resistance), resulting in abrupt set/reset and unpredictable changes in conductance in response to bias. Comparing to a metal oxide or polymer electrolyte-based CBRAM, the IL-filled PEGDA system first described here shows promise for the gradual modulation of Ag filament formation and dissolution dynamics. We show that this modulation is accomplished via EDL screening of the electrochemical redox reactions. More specifically, in response to an applied electrical field, the IL ions will migrate towards the electrodes, forming an EDL, which decreases the driving force for electrochemial oxidation (of Ag atom) or deposition (of Ag^+), shifting the Ag filament formation and dissolution dynamics from abrupt to gradual. In addition, we demonstrated this EDL regulation can be replicated under different device configurations (i.e., mobile AFM tip to plate *versus* lithographically patternend MIM structure), and can be further tuned with applied bias and temperature. These results suggest that a PEGDA/IL based two-terminal memristor is a promising alternative for the prevailing three-terminal devices for neuromorphic and multi-bit memory applications.

From an energy efficiency perspective, an exciting aspect of our work to date is that there is still plenty of room for scaling and improvements that are sure to decrease the energy requirements. Calculated from data presented in Figure 25, our current device configuration requires a large energy pulse input (480 pJ) to increase filamentary conductance. The larger energy requirement could be due, in part, to the overpotential required to overcome the EDL screening effect that competes with the electrodeposition. We can further scale the dimensions of the bottom Ag electrode (arm + pad) to reduce EDL screening and therefore regulate the competition at lower applied bias. Assuming that we can reduce the Ag pad size of a device to < 1 µm^2 using E-beam lithography (EBL), which is comparable to the AFM tip contact area with polymer electrolyte, we expect filament formation to occur at only 0.5 V (Figure S1, Supporting Information, Appendix C) at the same electrolyte thickness. This is 4 times less bias than required in Figure 25), resulting in a 16 times decreased energy requirement.

We can also consider the energy requirements in the context of the way in which the filament is grown. When both linear formation and dissolution has been achieved using bias pulses, the filament was deliberately *overgrown* using c-AFM to reduce contact resistance. One consequence of overgrowth is that when the filament is reconnected via subsequent measurements on the probe station, the filamentary conductance is already high ($>$ 100 µS). This larger conductance significantly increases the write pulse energy input (i.e., the write current is high ($>$ 100 µA) compared to non-overgrown filament). Future work will focus on exploring the lower limit of the conductance range where both filament formation and dissolution can be linearly modulated using pulses, thus decreasing the required write current and improving pulse energy efficiency.

We propose two approaches to tackle lowering the conductance range: (1) avoid filament overgrow when starting the pulse modulation; (2) reduce the pulse width. One possible way to avoid overgrowth is to reduce the bottom Ag dimension using EBL, as mentioned above, and then use the probe station to direct-write the filament (i.e., nucleate and grow) and then modulate filament conductance at an early stage. The idea is to create a non-overgrown filament as in Chapter 4 and extend the tunable filament conductance range using bias pulses. The range is currently limited to only 10% reversible modulation from 235 to 260 µS. The approach will also significantly reduce pulse energy input because the writing current will be lower for a lower conductance filament.

The second approach is to tackle the pulse width. The long pulse width ($>$ 100 ms) used in this study represents an instrumental limitation; therefore, the minimum pulse width has yet to be determined. Currently the average conductance change per pulse is 100 nS when using a pulse width of 114 ms. If we assume the minimum detectable increase in conductance between two distinctive state is 1 nS, then the a pulse width can potentially be reduced to $<$ 1 ms, which will scale the energy required by more than 100 times. If we can further reduce the energy consumption used to modulate filament conductance to $\sim$ 10 pJ per switching), [26] we believe this PEGDA/IL based two terminal memristor will become a promising candidate in the development of neuromorphic computing devices.

6.3 How Does This Dissertation Help?

In this dissertation we, for the first time, revealed that an IL can control Ag nanofilament formation dynamics in a polymer electrolyte through the intervention of an IL EDL. Further, we showed that the extent to which the EDL intervenes can be tuned easily by IL composition, adding Ag salt to the electrolyte, electrical field strength, and temperature to give abrupt or gradual Ag nanofilament growth dynamics. There is no reason to believe that such a competition is unique to our system, and therefore could be exploited for other materials systems or for different applications. This work extends our understanding of the role of IL on CBRAM performance from a perspective that has not been explored before. After learning about the fundamentals, we explored the possibility of using PEGDA/IL-based CBRAM as an artificial synapse and demonstrated highly linear filament conductance increase and decrease using bias pulses. This dissertation exemplifies how fundamental materials research can reveal a new mechanism —in this case, EDL-regulated filament dynamics—and, this new mechanism can be matured in an engineering setting toward use in an exciting new device—an artificial synapse—to push forward advances in neuromorphic computing.

Appendix A

Nanoscript for Automated Filament Formation on conductive-AFM Setup

In this appendix the script used in Chapters 4 and 5 for automated filament formation and dissolution is provided. The script is based on C++ environment and needs to be compiled as **dll** file for Bruker Dimension Icon AFM to execute. The early version of script was written by Dr. Garrison Crouch at University of Notre Dame and later updated by Brian Radka and myself here at University of Pittsburgh.

/* The script is used for automated filament formation and dissolution at predefined locations.

Garrison Crouch, University of Notre Dame

Bohn Research Group

Brian Radka, Zhongmou Chao, University of Pittsburgh

Howdy Campers! and welcome to the filament-formation ball! We'll start off with an

oldie but goodie- the Casper Slide!

Algorithm:

1. Ask for inputs:

tip voltage -> float

rest (moving) voltage ->float

scan size -> float

number of points -> int

current threshold -> float

max time -> int (?)

1.5 Compute:

interpoint spacing

2. Move tip to upper left corner

Loop over rows

Loop over columns

3. Go to formation voltage, take data

Current limit or time limit, whichever comes first

4. Go to dissolution voltage, take data

Current limit or time limit, whichever comes first

5. Go to rest voltage

6. Move to next point

end loop

7. Ask if user wants to continue on next line

```
if no, center piezo
end loop
8. Move tip to center again

*/

#include "NanoScript_Litho.h"
#include "NanoScript_GUI.h"
#include "NanoScript_Scan.h"

#include <fstream> //saving data
#include <math.h> //power function
#include <string> //filenames
#include <Windows.h> //timing
#include <chrono>

using namespace std;

extern "C" __declspec(dllexport) int macroMain()
{
	//Set default values
	float Vhigh = 1.8;				// volts
	float Vlow = -0.5;				// volts
	float Vrest = 0;			// volts
	float scansize = 6;				// microns
	int numpoints = 5;				// number of points in each colum/number of rows
	float formIthresh = 4;		// the current threshold for the first filament (nA)
	float stepI = 0.1;		// the step of current threshold between two ajacent filaments
	int FormCounts = 2;		// number of counts needs to be collected before dissolution
```

```
float dissIthresh = -0.5;  // nA
float formTmax = 50;                // seconds
float dissTmax = 50;                // seconds
int dissCounts = 2;       // number of dissolution counts needs to be collected before exit
double rate = 2;                    // move the tip in X-Y at 20 um/s
char FileNmChar[] = "Filename";
float gain = 1;                     // nA per volt



                                                        //For processing & timing
double current = 0;
float zero = 0;
int ret = 0;
bool success = true;
std::chrono::high_resolution_clock::time_point start;
std::chrono::high_resolution_clock::time_point  now;
std::chrono::microseconds  expttime;


//Ask user for inputs
DialogBoxHandle dlg = ModalDialog("Scan Parameters"); // One ModalDialog call is required for every RunDialog call
AddFloatControl(dlg, "Formation voltage (sample bias)", Vhigh, -9.999f, 9.999f);
AddFloatControl(dlg, "Dissolution voltage (sample bias)", Vlow, -9.999f, 9.999f);
AddFloatControl(dlg, "Rest (moving) voltage (sample bias)", Vrest, -9.999f, 9.999f);
AddFloatControl(dlg, "Scan area (side, microns)", scansize, 0.001f, 100.00f);
AddIntControl(dlg, "Number of points per row/column", numpoints, 1, 1024);
AddFloatControl(dlg, "Formation current trigger threshold (nA)", formIthresh, -999.9f, 999.9f);
AddFloatControl(dlg, "Step of Formation current threshold (nA)", stepI, -999.9f, 999.9f);
```

```
	AddIntControl(dlg, "Number of current counts needs to be collected before dissolution", FormCounts, 1, 9999);

	AddFloatControl(dlg, "Dissolution current trigger threshold (nA)", dissIthresh, -999.9f, 999.9f);

	AddFloatControl(dlg, "Sensitivity in nA/V", gain, -999.9f, 999.9f);

	AddFloatControl(dlg, "Formation Timeout (s)", formTmax, 0.001f, 9999.99f);

	AddFloatControl(dlg, "Dissolution Timeout (s)", dissTmax, 0.01f, 9999.99f);

	AddIntControl(dlg, "Number of dissolution counts needs to be collected before exit", dissCounts, 1, 9999);

	AddStringEntry(dlg, "Filename (no extension)", FileNmChar, 50);


	//Display dialog box

	ret = RunDialog(dlg); //When this function returns, the DialogBoxHandle memory is deleted, so it cannot be reused.



                                                //Setup between-point dialog


	if (ret == 0)

	{

		return 0; // 0 makes macro unload

	}



	//Open output files

	string FileNmString(FileNmChar);


	string location("E:\\capture\\RADKA\\New Data\\2019\\");
	//change to where you usually store your data


                                                        //string currentsuffix("_timeseries.txt");
```

```
string formationsuffix("_formtimes.txt");

string formFileNmString = location + FileNmString + formationsuffix;

fstream formOutputFile;
formOutputFile.open(formFileNmString, fstream::out);

SayWarning(formFileNmString.c_str());

formFileNmString.clear(); // it doesn't, but will leave in anyway
location.clear();
formationsuffix.clear();
formFileNmString.clear();

if (formOutputFile.is_open()) {
	SayWarning("This is somethin' new, the Casper Slide part 2");
}
else {
	return 0;
}


formOutputFile << "Point,Formation Time, Dissolution Time" << endl;


//Calculate parameters
float pointdist = scansize / numpoints; //Distance to move between each point
float base = 10; float exponent = -9; //nA to A. Not really elegant but it works
formIthresh = formIthresh * pow(base, exponent); //Current threshold in A
```

```
stepI = stepI * pow(base, exponent); //Step of FormationCurrent threshold in A
dissIthresh = dissIthresh * pow(base, exponent);
gain = gain * pow(base, exponent);
double halfside = scansize / 2;

int point = 0;
float formTime;
float dissTime;
float poscurrent;
float negcurrent;
int count = 0;
int dcount = 0;

//Convert to miliseconds
formTmax = formTmax * 1000;
dissTmax = dissTmax * 1000;

string diagstring = "Gonna do the basic steps of " + to_string(pointdist);
SayWarning(diagstring.c_str());

LITHO_BEGIN

        LithoScan(false);                       // turn off scanning
SayWarning("Everybody clap your hands");
LithoFeedback(true);            // Keep z-piezo feedback on
LithoCenterXY();                        // move tip to center of field
try {
        // move to upper left corner of scan area
        LithoTranslate(-halfside, halfside, rate);
```

```
		// Raster loops


		for (int row = 0; row < numpoints; row++)
		{
			for (int column = 0; column < numpoints; column++)
			{
//engage command and check
engage


//opens new file for current
data
				point = row * numpoints + column;
				string location("E:\\capture\\RADKA\\New Data\\2019\\");
				string currentsuffix("_timeseries.txt");
				string currFileNmString = location + FileNmString + "_" + to_string(point)
+ currentsuffix;
				fstream currentOutputFile;
				currentOutputFile.open(currFileNmString, fstream::out);
				//Insert file header for time series file


				currentOutputFile << endl << endl << "Time,Point " << point << "
Formation" << endl;


				//Set formation voltage
				success = LithoSet(lsBias, Vhigh);
				if (!success)
				{
					SayWarning("Reverse, reverse!");
				}
```

```
//Start timing
start = std::chrono::high_resolution_clock::now();
count = 0;

//Scan while loop
do
{
	//Get data
	current = LithoGet(lsNS5FPInput1); //Double-check channel assignment
	current = current * gain;
	if (current >= formIthresh)
	{
		count = count + 1;
	}
	else
		count = 0;
	//Update time
	now = std::chrono::high_resolution_clock::now();
	expttime = std::chrono::duration_cast<std::chrono::microseconds> (now - start); //microseconds

	//SayWarning(ctime(&now)); //for debug purposes

//Save data
```

```
                currentOutputFile << expttime.count() / 1000 << "," << current
<< endl;
            } while ((count< FormCounts) && (expttime.count() / 1000 <
formTmax));

            formTime = expttime.count() / 1000;
            //adjust the formation current threshold by adding the step current
            formIthresh = formIthresh + stepI;

            currentOutputFile << endl << endl << "Time,Point " << point << "
Dissolution" << endl;

            //Set dissolution voltage
            success = LithoSet(lsBias, Vlow);
            if (!success)
            {
                SayWarning("Reverse, reverse!");
            }

            //Restart timing
            start = std::chrono::high_resolution_clock::now();

            dcount = 0;

            do
            {
                //Get data
                current = LithoGet(lsNS5FPInput1); //Double-check channel
assignment
                current = current * gain;
```

```
                    if (current >= dissIthresh)
                    {
                        dcount = dcount + 1;
                    }
                    else
                        dcount = 0;

                    //Update time
                    now = std::chrono::high_resolution_clock::now();
                    expttime =
std::chrono::duration_cast<std::chrono::microseconds> (now - start); //microseconds

                                                                                    //Save
data
                    currentOutputFile << expttime.count() / 1000 << "," << current
<< endl;
                } while ((dcount < dissCounts) && (expttime.count() / 1000 < dissTmax));

                dissTime = expttime.count() / 1000;

                //Record formation and dissolution times
                formOutputFile << point << "," << formTime << "," << dissTime << endl;


                //Set rest voltage
                success = LithoSet(IsBias, Vrest);
                if (!success)
                {
                    SayWarning("Reverse, reverse!");
```

```
                    }
                    //withdraw
                    //Move to next point. Show point number to indicate progress
                    if ((column < numpoints - 1) && (row % 2 == 0))
                    {
                            diagstring = "sliiiide to the right, " + to_string(point) + " hops
this time";
                            LithoTranslate(pointdist, zero, rate);
                    }
                    else if (column < numpoints - 1)
                    {
                            diagstring = "sliiiide to the left, " + to_string(point) + " hops this
time";
                            LithoTranslate(-pointdist, zero, rate);
                    }
                    else {
                            diagstring = "Let's go to work";
                    }

                    SayWarning(diagstring.c_str());

                    currentOutputFile << endl << endl;
                    currentOutputFile.close();
            }
            //Take it back now y'all
            if ((row < numpoints - 1) && (row % 2 == 1))
            {

                    //Confirm proceed
```

```
                        if (!AskOkCancel("Continue to next line?", "End of line"))
                        {
                                LithoCenterXY();
                                //currentOutputFile.close();
                                SayWarning("Criss-cross, criss-cross");

                                return 0; //Make macro unload here
                        }
                        SayWarning("Take it back now y'all");
                        LithoTranslate(zero, -pointdist, rate); // move down a row
                }
                else if (row < numpoints - 1)
                {
                        SayWarning("Take it back now y'all");
                        LithoTranslate(zero, -pointdist, rate);
                }
        }

        LithoCenterXY();
        //currentOutputFile.close();
        formOutputFile.close();

}
catch (...)
{
        SayWarning("Get funky with it");
}

LITHO_END
```

```
        diagstring.clear();

    SayWarning("I'm out y'all peace!");

    return 0;       // 0 makes the macro unload. Return 1 to keep the macro loaded.
}
```

Appendix B

Publication #1 of 4

In this appendix the paper published in *Small* [55] and its supporting information are attached.

NANO · MICRO small

www.small-journal.com

Direct-Write Formation and Dissolution of Silver Nanofilaments in Ionic Liquid-Polymer Electrolyte Composites

*Zhongmou Chao, Brian P. Radka, Ke Xu, Garrison M. Crouch, Donghoon Han, David B. Go, Paul W. Bohn, and Susan K. Fullerton-Shirey**

Materials with reconfigurable optical properties are candidates for applications such as optical cloaking and wearable sensors. One approach to fabricate these materials is to use external fields to form and dissolve nanoscale conductive channels in well-defined locations within a polymer. In this study, conductive atomic force microscopy is used to electrochemically form and dissolve nanoscale conductive filaments at spatially distinct points in a polyethylene glycol diacrylate (PEGDA)-based electrolyte blended with varying amounts of ionic liquid (IL) and silver salt. The fastest filament formation and dissolution times are detected in a PEGDA/IL composite that has the largest modulus (several GPa) and the highest polymer crystal fraction. This is unexpected because filament formation and dissolution events are controlled by ion transport, which is typically faster within amorphous regions where polymer mobility is high. Filament kinetics in primarily amorphous and crystalline regions are measured, and two different mechanisms are observed. The formation time distributions show a power-law dependence in the crystalline regions, attributable to hopping-based ion transport, while amorphous regions show a normal distribution. The results indicate that the timescale of filament formation/dissolution is determined by local structure, and suggest that structure could be used to tune the optical properties of the film.

1. Introduction

Solid-polymer electrolytes (SPE) contain a salt dissolved in a polymer host. They are candidate materials to replace flammable liquid-phase electrolytes in devices such as rechargeable lithium-ion batteries.[1,2] In addition, SPEs have recently been used for memory devices based on resistive switching,[3] in which conductive filaments formed and dissolved in response to an external electric field are used to achieve on and off states typically separated by several orders of magnitude in resistance. The formation of metal filaments through polymer electrolytes has been demonstrated previously for polyethylene oxide (PEO)-based electrolytes,[4] including our group's recent report on silver filament formation kinetics through PEO.[5]

In addition to batteries and memory, SPEs can potentially form the basis for a new class of metamaterials with reconfigurable optical properties. A metamaterial can be formed by embedding metal nanoparticles (NPs) in a well-defined array within a dielectric, in which the optical properties are tuned by adjusting the spacing of the NPs to interact with electromagnetic radiation over a designed wavelength range.[6,7] In addition to NPs, densely packed nanofilaments in a dielectric can give rise to strong anisotropy in optical properties.[8] One approach to introduce optical configurability is to selectively form and dissolve conductive filaments within an ordered NP metamaterial (**Figure 1**a). Such metamaterials with dynamically reconfigurable optical properties would represent a major advance in intelligent coatings, nicely complementing achievements in the internet of things (IOT), where local sensors could trigger the intelligent material to change properties in response to a stimulus. However, designing the scaffold for a dynamically tunable metamaterial is quite challenging, because it must allow precise NP positioning, while simultaneously supporting facile motion of conducting ions, which are needed to form and dissolve the nanofilaments. Commonly studied polymer electrolytes, such as high molecular weight PEO-based electrolytes,[5] are ionically conductive, but the mechanical properties of the solid film make it difficult to position NPs precisely within the polymer.

Z. Chao, B. P. Radka, Dr. K. Xu, Prof. S. K. Fullerton-Shirey
Department of Chemical and Petroleum Engineering
University of Pittsburgh
Pittsburgh, PA 15213, USA
E-mail: fullerton@pitt.edu

G. M. Crouch, Dr. D. Han, Prof. D. B. Go, Prof. P. W. Bohn
Department of Chemical and Biomolecular Engineering
University of Notre Dame
Notre Dame, IN 46556, USA

Prof. D. B. Go
Department of Aerospace and Mechanical Engineering
University of Notre Dame
Notre Dame, IN 46556, USA

Prof. P. W. Bohn
Department of Chemistry and Biochemistry
University of Notre Dame
Notre Dame, IN 46556, USA

Prof. S. K. Fullerton-Shirey
Department of Electrical and Computer Engineering
University of Pittsburgh
Pittsburgh, PA 15213, USA

The ORCID identification number(s) for the author(s) of this article can be found under https://doi.org/10.1002/smll.201802023.

DOI: 10.1002/smll.201802023

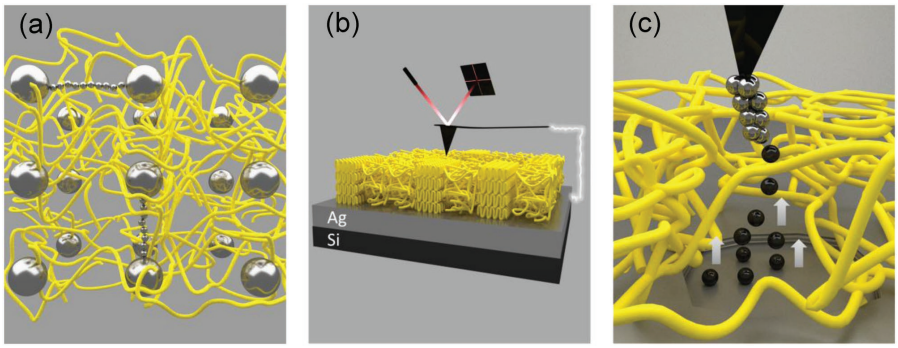

Figure 1. Schematic of PEGDA/IL/Ag salt composite. a) Metamaterial with a lattice of Ag NPs (large gray spheres) embedded in a PEGDA/IL composite (yellow). Some NPs are electrically connected by Ag nanofilaments (small gray spheres). b) Polymer electrolyte film where conductive AFM controls the electrochemical formation and dissolution of conductive Ag filaments. The polymer chains are represented in a semicrystalline conformation, that is, with regions of order and disorder. c) Magnified view of filament formation between the conductive AFM tip and a sacrificial Ag layer within an amorphous region of the polymer electrolyte. Silver ions, Ag^+, (black spheres) are reduced to Ag^0 atoms (gray spheres) at the apex of the growing filament.

To address this challenge, we have investigated a non-aqueous electrolyte system combining a photo-crosslinkable polymer (polyethylene glycol diacrylate, PEGDA) with an ionic liquid (1-butyl-3-methylimadazolium hexafluorophosphate, [BMIM]PF_6, Figure S1, Supporting Information). PEGDA is an ion-conducting polymer[9] which is also commonly used in biological applications.[10] PEGDA provides design flexibility, because the material can start at low-viscosity and be converted to a high-viscosity solid simply by exposing the film to light. This design could support the precise positioning of NPs in a liquid-like dielectric, and the NPs could subsequently be locked into place by simple exposure to ultraviolet light. Previous studies showed that as little as 4 wt% PEGDA blended with an ionic liquid (IL) was sufficient to yield a solid.[11,12] In addition, ILs are commonly used to increase ionic conductivity in SPEs at room temperature.[11–13] Here, [BMIM]PF_6 is chosen as the IL, because it has good chemical and thermal stability, negligible vapor pressure, high ionic conductivity (1.8×10^{-3} S cm^{-1} at 300 K),[14] and a large electrochemical window (≈4.7 V).[15] Thus, PEGDA provides tunable mechanical properties, while [BMIM]PF_6 enhances ionic conductivity which is required for forming and dissolving filaments.

While electrolytes containing both IL and polymer have been reported previously,[11–13,16,17] a comprehensive understanding of how the IL affects the ionic conductivity and mechanical strength of the electrolyte is still developing. Such understanding is especially crucial here, because one might presume that the kinetics of nanofilament formation and dissolution are a function of ionic conductivity, which is also related to the mechanical properties of the host material. But, as we show, fast nanofilament formation occurs in regions of high polymer crystallinity and high modulus, rather than amorphous regions with high ionic conductivity, indicating that our intuitive understanding of polymer/IL systems is incomplete. Although the eventual application of this work is to form and dissolve filaments between metal NPs, functioning as bipolar electrodes within the host material, the present study focuses entirely on filament formation in the PEGDA-IL electrolyte.

2. Results and Discussion

As shown in Figure 1b,c, a conductive atomic force microscopy (C-AFM) tip and a Ag substrate constitute a model system in which the AFM tip and the Ag substrate represent the two electrodes. We use the AFM to characterize the mechanical properties of PEGDA/IL/silver hexafluorophosphate ($AgPF_6$) electrolyte films, create Ag nanofilaments through the films via electrodeposition, and correlate the filament formation/dissolution kinetics with the mechanical properties of the polymer composite. PeakForce Quantitative Nanomechanical Mapping (PF-QNM) is used to map the Young's modulus, while a conductive AFM is used to form and dissolve the Ag filaments electrochemically.[5,18] The location of the AFM tip is controlled over the x–y plane to enable the direct-write fabrication of filaments in a predefined grid pattern. As shown in Figure 1c, the conductive AFM tip operates as a mobile top electrode, while an Ag thin film below the electrolyte functions as a sacrificial counterelectrode. Filament growth inside the PEGDA/IL/salt electrolyte is controlled by the polarity and magnitude of the bias applied between the two electrodes.

2.1. Modulus Measurements

Thin films of PEGDA with IL and $AgPF_6$ were fabricated by spin-coating, and cross-sectional scanning electron microscopy (SEM) images show that the thickness of the films is ≈50 nm (Figure S2, Supporting Information), independent of the IL concentration. First, we measure how the IL impacts the mechanical properties of the electrolyte film. Modulus maps of the cross-linked electrolytes over a 5×5 μm region and modulus-composition data with varying IL compositions are shown together in **Figure 2**. Clearly, modulus decreases with increasing IL content. For example, increasing the IL composition from 10 to 30 wt% decreases the average Young's modulus by one order of magnitude. This trend is predictable, because the IL is a low-viscosity liquid compared to the UV-crosslinked polymer. In contrast, adding Ag salt increases the modulus, which is most obvious for the electrolytes with the highest

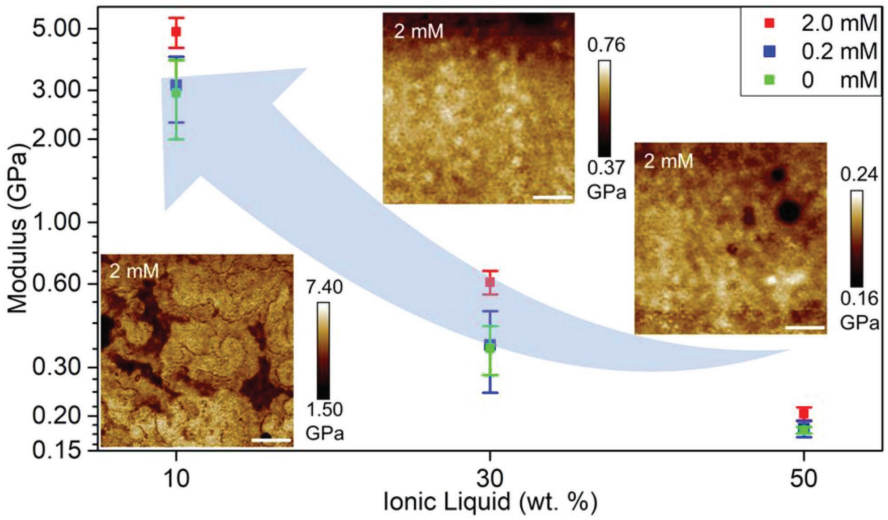

Figure 2. Average Young's modulus measured by PF-QNM over a 5 × 5 µm region for samples with different PEGDA/IL/$AgPF_6$ compositions. Inset left to right: Modulus maps of the surface of cross-linked electrolytes containing 2×10^{-3} M $AgPF_6$ at 90/10, 70/30, and 50/50 PEGDA/IL wt% composition, respectively. Scale bars indicate 1 µm.

PEGDA concentration. For example, the modulus nearly doubles by adding 2×10^{-3} M $AgPF_6$ to a sample with 90 wt% PEGDA. The silver cations electrostatically interact with the ether oxygens in the polymer backbone;[19] the resulting noncovalent interactions decrease the polymer mobility[20] and therefore increase the modulus. The data show that the modulus of the polymer coating can be tuned more than tenfold by relatively small adjustments in the PEGDA/IL ratio (ether oxygen to BMIM ratio from 22:1 to 65:1, corresponding to 70/30 and 90/10 PEGDA/IL wt%). In contrast, increasing the silver salt concentration by one order of magnitude (0.2 to 2.0×10^{-3} M) increases modulus by at most a factor of two. A complete set of modulus maps for all the electrolytes investigated in the study are provided in Figure S3 (Supporting Information).

2.2. Filament Formation and Dissolution Kinetics

Nanoscale Ag filaments were formed and dissolved by controlling the magnitude and polarity of bias applied between a conductive AFM tip and the Ag sacrificial electrode (Figure 1b). To avoid asperities in the data caused by macroscopic inhomogeneities in the spin-coated samples, formation and dissolution events were measured at multiple regions separated by >100 µm. Within each region, filaments were formed and dissolved at 100 locations in a 6 × 6 µm array, with a pitch of 600 nm. An example of time-dependent current and voltage data showing a representative formation and dissolution event is provided in Figure S4 (Supporting Information). The algorithm used to collect the initial filament formation and dissolution times at hundreds of different locations used the following protocol: a +2 V positive bias was applied until a filament was created, as indicated by a significant increase in the current, until compliance was reached. After formation, the bias was held for only 2 ms to avoid filament overgrowth. Then, the bias polarity was reversed to −2 V to start dissolution. When the filament was broken, the current decreased abruptly to zero.

At least 700 formation and dissolution events were captured for each sample, and histograms of filament formation and dissolution times are given in **Figure 3**. A Gaussian (normal) distribution was used to fit all data sets with skewness adjusted to capture the asymmetries. The formation time distributions are normal, Figure 3a,c, while the dissolution events show a log normal distribution, Figure 3b,d. These are the same types of distributions reported for filaments formed in PEO-based electrolytes,[5] and the different distributions suggest that the underlying formation and dissolution mechanisms are fundamentally different. This difference is reasonable, because it takes longer to form a filament for the first time, that is, the formation step, than it does to break the filament. Whereas formation requires the movement of many silver ions to form a percolating conduction path, dissolution only requires the oxidation of a few silver atoms into the nearby electrolyte to disconnect the filament.

Both the Ag salt and the IL strongly affect filament formation kinetics, as shown in Figure 3a,c, respectively. The addition of up to 2×10^{-3} M Ag salt in the 70/30 wt% PEGDA/IL electrolyte decreases the formation time by as much as 42% (Figure 3a) as expected from straightforward electrodeposition kinetics. The shift in formation times indicates that the kinetics of filament formation can be controlled by adjusting the Ag^+ concentration without varying electrical field strength.

Decreasing the IL concentration from 50 to 10 wt% with 2×10^{-3} M $AgPF_6$ increases the filament formation rate by ≈6.5 times as shown in Figure 3c. Faster filament formation with decreasing IL content is unexpected, because the IL is conventionally thought to function as a plasticizer[21,22]—enhancing polymer chain segmental motion[23,24] and improving ionic conductivity.[25,26] In addition, the magnitude of the formation time distribution is related to specific features in the time-dependent current data. Specifically, there are two different types of

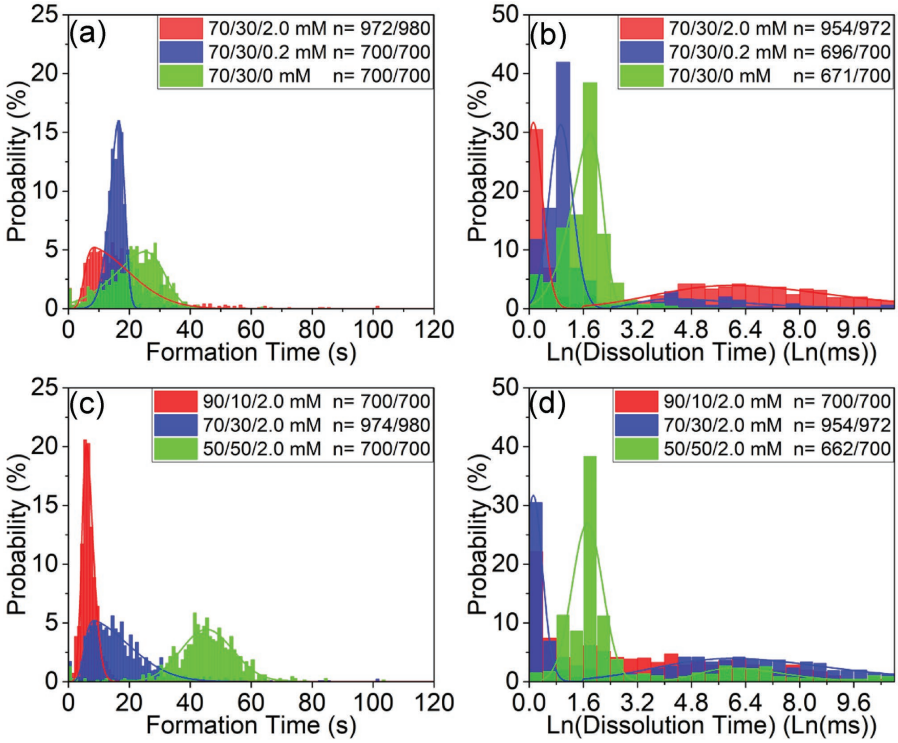

Figure 3. a,b) Filament formation and dissolution time distributions in electrolytes at 70/30 wt% PEGDA/IL with 0, 0.2, and 2×10^{-3} M $AgPF_6$. c,d) Filament formation and dissolution time distributions for electrolytes with 2×10^{-3} M $AgPF_6$ at 90/10, 70/30, and 50/50 wt% PEGDA/IL. The bin width is 1 s for all formation times and 0.4 Ln(ms) for all dissolution times. The data are fit by Gaussian distributions with adjustments in skewness to capture the asymmetric shape.

processes, denoted type-1 and type-2, as shown in **Figure 4**a,b, respectively. Type-1 formation involves an abrupt increase in current from zero to the compliance current over a narrow (few ms) time window, whereas type-2 formation involves current fluctuations over longer timescales (>1 s) prior to reaching the compliance current. Whether a data set exhibits type-1 or type-2 behavior is distinguished by setting the total number of data points that exceed a user-defined current level. In this study, we choose this cutoff current as 3.8 nA, and classify the data as type-1 formation if the total number of data points for which $I \geq 3.8$ nA is less than 4. Conversely, if more than four points in the data set include $I \geq 3.8$ nA, then the formation is considered type-2. We know type-2 formation is not dielectric breakdown because when the bias is reversed, the current returns to zero. In the case of dielectric breakdown, an irreversible conductive pathway would be created through the dielectric.

The percentage of type-1 formation events are provided in Table S1 (Supporting Information) for all the samples in this

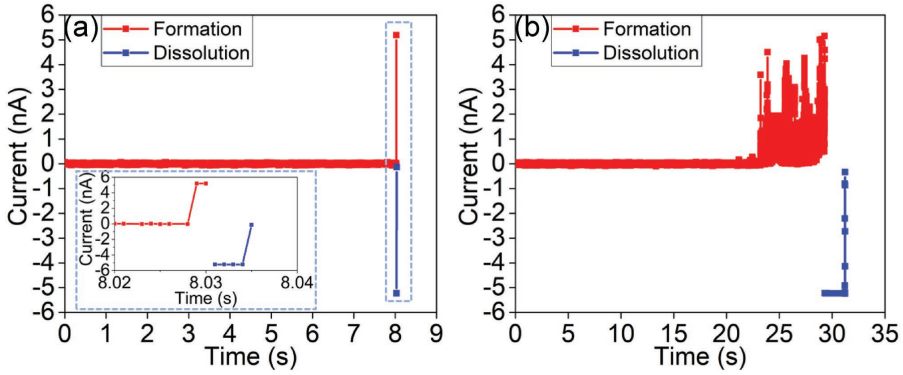

Figure 4. a,b) Current versus time data during filament formation at +2 V and dissolution at −2 V for type-1 and type-2 filament formation processes. Inset of (a) in the blue rectangular box is a magnified plot with expanded time axis.

study. Systems with faster formation kinetics and the highest modulus have a higher percentage of type-1 formation events. For example, the $90/10/2 \times 10^{-3}$ M system with average formation time of 7 s has a 75% type-1, while the slower $50/50/2 \times 10^{-3}$ M system, with average formation time of 45 s, exhibits only 5% type-1 events. While further studies are needed to confirm the origin of these two distinct types of formation dynamics, they may relate to the physical structure of the filament. For example, type-1 filaments that are more commonly formed in the high modulus electrolyte ($90/10/2 \times 10^{-3}$ M) may have well-defined structure, whereas type-2 filaments that dominate in lower modulus electrolyte ($50/50/2 \times 10^{-3}$ M) may be more dendritic, causing current fluctuations as they form and disconnect.

Additional support for a correlation between filament morphology and modulus arises in the 50/50 PEGDA/IL samples. Specifically, for the 0 and 0.2×10^{-3} M salt concentrations, overgrowth of silver at the surface of the film was observed. Figure S5 (Supporting Information) shows direct evidence of silver overgrowth via AFM topology and current maps. Furthermore, as shown in Figure S6 (Supporting Information), formation and dissolution events for the $50/50/0 \times 10^{-3}$ M and 0.2×10^{-3} M systems indicating that >50% of the filaments that form do not dissolve during the timescale of the measurement, which would be expected for overgrown filaments connected at multiple locations. In contrast, no similar surface overgrowth was observed in systems with higher modulus, such as $70/30/0 \times 10^{-3}$ M system, as shown in Figure S7 (Supporting Information). Thus, varying the Ag concentration and PEGDA/IL ratio not only changes the kinetics, but also the morphology of the filaments from well-defined to overgrown.

Similar to filament formation, the Ag salt and IL compositions also affect dissolution kinetics, as shown in Figure 3b,d, respectively. The dissolution distributions are more complex than the formation distributions, showing a bimodal structure with filaments that dissolve quickly (tens of milliseconds, type-A) coexisting with long-lived filaments (tens of seconds, type-B). In addition, systems exhibiting a higher percentage of type-1 formation events also tend to dissolve faster. This provides further support for the interpretation that type-1 filaments have a more well-defined structure than those formed in type-2 events, because more well-defined filaments would require less time to dissolve than dendritic filaments that may need to disconnect at multiple locations.

Figure 3b also shows that the bimodal distribution is more prevalent at higher Ag salt concentrations. Similar experiments addressing Ag atomic-scale junction formation and dissolution also show a marked dependence of dissolution time on Ag activity in the surrounding medium.[27,28] This is sensible because adjusting the Ag salt concentration shifts the equilibrium potential of the system relative to the applied potential. Hence, the dissolution data suggest that a concentration overpotential-limited dissolution process is operating on a small, but non-negligible fraction of the nanofilaments.

2.3. Thermal Measurements

The observation that electrolytes with the highest PEGDA concentration (90 wt%) and the *largest* modulus display the *fastest* filament formation/dissolution kinetics was surprising. It thus motivated using differential scanning calorimetry (DSC) to characterize the polymer films across the entire range of compositions. Heat traces showing the melting temperature (T_m) in the range of 20–55 °C are given in **Figure 5**a. IL and silver salt suppress PEGDA crystallization as observed by a decrease in area under the melting peak (IL-free DSC traces are provided in Figure S8, Supporting Information, for reference). A secondary peak at lower temperature (≈20 °C) emerges with increasing IL addition, and this feature is particularly apparent in the 0.2×10^{-3} M samples. The observation of multiple peaks at a specific salt concentration is similar to the behavior of PEO-based electrolytes at their eutectic composition.[20,29]

The glass transition temperatures (T_g), shown in Figure 5b, provide insight on how the IL and silver salt affect polymer

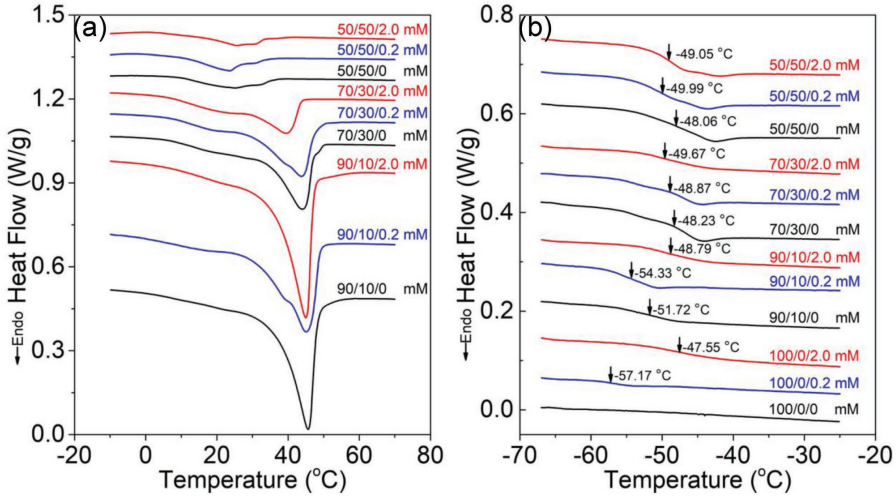

Figure 5. Heat flow versus temperature for PEGDA/IL/$AgPF_6$ showing: a) melting (T_m) features and b) glass transition (T_g) features. Data are from the second heating scan.

mobility, which governs ion mobility in amorphous domains. The addition of IL from 0 to 30 wt% at low silver salt concentration (0 and 0.2×10^{-3} M) increases T_g by more than 7 K, showing that it does not plasticize the system. Generally, the data show that when the ion concentration is increased (either by adding IL or silver salt), T_g increases, reaching a maximum value around −50 °C for the concentration ranges measured. However, it is noteworthy to highlight the 0.2×10^{-3} M salt concentration in the 90/10 system. Although we expect the Ag salt to increase T_g, because electrostatic interactions between cations and ether oxygens decrease segmental mobility of the polymer, the 0.2×10^{-3} M salt *decreases* T_g in the 90/10 PEGDA/IL concentration. This anomalous behavior is consistent with the possibility that 0.2×10^{-3} M is a potential eutectic concentration as mentioned above. A similar T_g minimum at the eutectic has been reported for a PEO:$LiClO_4$ electrolyte.[20]

2.4. Relating Filament Kinetics to Polymer Structure

Based on the DSC data and the prevailing view that less crystal structure in polymer electrolytes correlates with faster ion mobility, we would expect the 50/50 PEGDA/IL sample to have the fastest filament formation/dissolution kinetics. In fact, we observe the opposite—the 50/50 PEGDA/IL electrolyte shows the slowest kinetics. The result suggests that the local structure of the polymer—which can be evaluated by AFM—could be important for understanding the kinetics. Regions of highly crystalline versus highly amorphous electrolyte can be differentiated by optical microscopy in the $90/10/2 \times 10^{-3}$ M electrolyte (Figure S9, Supporting Information). We therefore focused on measuring the mechanical properties the filament kinetics in these two regions. Modulus measurements in **Figure 6** show that the primarily crystalline region has an average modulus of 4.8 GPa, nearly an order of magnitude higher than the primarily amorphous region (0.6 GPa). The filament formation kinetics measured in these regions indeed show distinct distributions: the primarily amorphous domain has a right-skewed Gaussian distribution with long formation times (21% of the filaments formed within 5 s), while the primarily crystalline region has a power-law distribution with a larger percentage of fast formation events (52% of filaments formed within 5 s). Indeed, when we compare the kinetics to the 100/0 PEGDA/IL system, which is the most highly crystalline system by a wide margin, we observe similar formation distributions (Figure S10, Supporting Information) as the primarily crystalline $90/10/2 \times 10^{-3}$ M sample. Thus, we conclude that a power-law distribution in the formation kinetics is associated with large amounts of crystallinity. Moreover, regions of high crystallinity also have the highest percentage of type-1 formation events (Table S1, Supporting Information). Therefore, the picture that emerges is that ion transport within primarily amorphous domains is mediated by polymer chain mobility and can be described by drift diffusion that leads to poorly ordered filaments. In contrast, faster ion transport occurs in crystalline regions likely by a hoping mechanism that gives rise to a power-law distribution and well-ordered filaments.

The data show that some amount of IL is essential to achieve fast and reliable formation events. For example, in the IL-free system, only 72% of the locations tested form filaments within the 120 s window of the measurement (Figure S9, Supporting Information). The electrolytes loaded with 10 wt% IL further show that ion mobility is decoupled from PEGDA chain mobility, and indicate two different formation mechanisms in the two phases (amorphous and crystalline). While it is well understood that ion mobility in the amorphous phase is driven by chain mobility, there is also support for the notion that specific crystalline structures in PEO-based electrolytes can provide faster pathways for ion transport than their amorphous equivalents.[30–32] Based on the results obtained here, we suggest a similar explanation for the observation that primarily crystalline domains exhibit faster formation kinetics. Specifically, a balance is achieved at ≈10 wt% IL, where conduction through crystalline regions is favored over primarily amorphous regions. In contrast to the crystalline regions, the amorphous regions have strong electrostatic interactions that suppress polymer/ion transport and therefore filament kinetics.

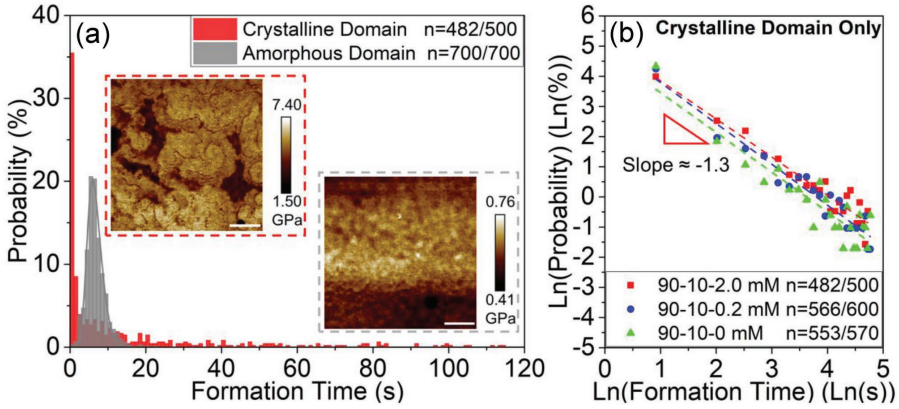

Figure 6. a) Formation time distributions in primarily crystalline (red) and amorphous (gray) regions of the 90/10 PEGDA/IL wt% with 2×10^{-3} M $AgPF_6$ sample using a 1 s bin width. Insets show modulus maps captured in each domain; b) Log–log plot of formation time distributions versus count percentages in primarily crystalline regions for 90/10 PEGDA/IL at 0, 0.2, and 2×10^{-3} M of $AgPF_6$. 120 s is the cutoff time for formation, bin width is 5 s.

3. Conclusions

We developed a UV-crosslinkable electrolyte consisting of PEGDA/IL and silver salt where direct-write electrodeposition of silver nanofilaments is produced by conductive AFM with possible applications as flexible films with designer optical properties. By tuning the IL and salt concentration, the mechanical strength was varied from hundreds of MPa to a few GPa in modulus. Silver nanofilament formation and dissolution events were correlated to local structure, showing that while the addition of Ag salt in up to a concentration of 2×10^{-3} M improves filament kinetics, the addition of IL beyond 10 wt% slows the kinetics. Moreover, surprisingly, the electrolyte with the largest polymer crystal fraction and the best mechanical strength shows the fastest filament kinetics. The results indicate that ion mobility in this system is likely governed more by the local polymer structure than by PEGDA chain mobility, thus creating an opportunity to tune the filament kinetics by tuning the structure of the polymer. If the kinetics can be controlled reproducibly by local morphology, one could envision a system where both the timescale and the spatial location for reconfiguring optical properties could be tuned, offering a novel approach to smart coating materials with, for example, reconfigurable optical properties.

4. Experimental Section

Reagents: PEGDA (M_n = 2000), [BMIM]PF_6 (≥98.5%), 2-hydroxy-2-methylpropiophenone (HMPP, 97%), $AgPF_6$ (99.99%), and anhydrous acetonitrile (ACN, 99.8%) were purchased from Sigma-Aldrich. All reagents were used as received without further purification.

Sample Preparation for AFM Characterization: Silicon wafers (University Wafer, P/Boron, 500 ± 15 µm) were cleaned by sonication in acetone followed by a 2-propanol rinse and nitrogen (N_2) blow dry. 5/100 nm of Ti/Ag was deposited by electron-beam evaporation (Plassys, MEB 550s) at 5×10^{-7} mbar base pressure. The following steps were completed inside an argon-filled glove box (Mbraun, MB-200B) where O_2 and H_2O < 1 ppm. $AgPF_6$, BMIMPF_6, and PEGDA were dissolved in ACN and combined to prepare a total of nine samples with PEGDA/BMIMPF_6 compositions of 90/10, 70/30, and 50/50 wt% at 0, 0.2, and 2×10^{-3} M $AgPF_6$. In all nine samples, the PEGDA concentration was 1 wt% together with 0.02 wt% of HMPP (photoinitiator). The polymer electrolytes were spin-coated on the Ag-coated silicon substrate at 4000 rpm for 30 s, and annealed at 80 °C for 2 min to drive off ACN. Samples were photo-crosslinked with a UV lamp (UVP Compact UV Lamp, λ = 365 nm, P = 1.3 mW cm^{-2} at 3 in.) at a working distance of 1.25 cm for 1 h.

C-AFM Characterization: A Bruker Dimension Icon AFM coupled with conductive AFM probe (SCM-PIT-V2) was operated in contact mode. A custom script was used to modulate the location and potential applied to the tip, and was reported by a group previously;[5] additional details of the tip automation are provided in the Supporting Information. Electrical contact was made between the AFM stage and the Ag layer of the substrate using copper tape (76555A711, McMaster-Carr). A formation voltage of +2 V, dissolution voltage of −2 V, and a rest voltage of 0 V relative to ground were used. Formation and dissolution current thresholds were chosen as +4 and −0.5 nA, respectively. The compliance current of the instrument is ≈5 nA at a current sensitivity of 1 nA V^{-1}, which is selected by the user.

PF-QNM Measurement: A Bruker Dimension Icon AFM was operated at PF-QNM mode. Different types of AFM probes were used for the measurement of nine samples based on their working ranges for sample modulus with details provided in the Section S3 (Supporting Information). All probes were calibrated for their deflection sensitivity, spring constant, and tip radius before each measurement. The force applied to the electrolyte was then correlated with the surface indentation to give a quantitative measurement of its mechanical properties.

DSC Sample Preparation and Measurement: Each DSC sample was prepared inside the glove box. PEGDA, BMIMPF_6, and $AgPF_6$ were dissolved in ACN and drop-cast onto Teflon, where the solvent evaporated. ≈10 mg of the resulting films were hermetically sealed in an aluminum DSC pan. In addition to the nine samples described above, three additional control samples containing silver salt without ionic liquid were measured (100/0 PEGDA/IL wt% with 0, 0.2, and 2×10^{-3} M $AgPF_6$). Measurements were made on a Pyris DSC 6000 calibrated with an indium standard. To measure T_g, T_c, and T_m, samples were heated to 80 °C to erase thermal history, cooled to −70 °C at 3 °C min^{-1} and heated to 80 °C at 5 °C min^{-1}.

Supporting Information

Supporting Information is available from the Wiley Online Library or from the author.

Acknowledgements

This work was supported by the Defense Advanced Research Projects Agency FA8650-15-C-7546 and a NASA Space Technology Research Fellowship NNX16AM45H. The authors also wish to thank Jierui Liang at the University of Pittsburgh for helpful discussion and suggestions.

Conflict of Interest

The authors declare no conflict of interest.

Keywords

conductive-AFM, ionic liquid, polymer electrolyte, silver filament

Received: May 27, 2018
Revised: July 23, 2018
Published online: August 17, 2018

[1] W. H. Meyer, *Adv. Mater.* **1998**, *10*, 439.
[2] J. Fu, D. U. Lee, F. M. Hassan, L. Yang, Z. Bai, M. G. Park, Z. Chen, *Adv. Mater.* **2015**, *27*, 5617.
[3] N. R. Hosseini, J.-S. Lee, *ACS Nano* **2015**, *9*, 419.
[4] S. Wu, T. Tsuruoka, K. Terabe, T. Hasegawa, J. P. Hill, K. Ariga, M. Aono, *Adv. Funct. Mater.* **2011**, *21*, 93.
[5] G. M. Crouch, D. Han, S. K. Fullerton-Shirey, D. B. Go, P. W. Bohn, *ACS Nano* **2017**, *11*, 4976.
[6] A. J. Hoffman, L. Alekseyev, S. S. Howard, K. J. Franz, D. Wasserman, V. A. Podolskiy, E. E. Narimanov, D. L. Sivco, C. Gmachl, *Nat. Mater.* **2007**, *6*, 946.
[7] A. Poddubny, I. Iorsh, P. Belov, Y. Kivshar, *Nat. Photonics* **2013**, *7*, 948.
[8] A. Fang, T. Koschny, C. M. Soukoulis, *Phys. Rev. B* **2009**, *79*, 245127.
[9] C.-M. Yang, H.-S. Kim, B.-K. Na, K.-S. Kum, B. W. Cho, *J. Power Sources* **2006**, *156*, 574.
[10] X. Z. Shu, Y. Liu, F. S. Palumbo, Y. Luo, G. D. Prestwich, *Biomaterials* **2004**, *25*, 1339.
[11] A. F. Visentin, S. Alimena, M. J. Panzer, *ChemElectroChem* **2014**, *1*, 718.

[12] A. F. Visentin, M. J. Panzer, *ACS Appl. Mater. Interfaces* **2012**, *4*, 2836.
[13] M. W. Schulze, L. D. McIntosh, M. A. Hillmyer, T. P. Lodge, *Nano Lett.* **2014**, *14*, 122.
[14] J. Zhang, W. Wu, T. Jiang, H. Gao, Z. Liu, J. He, B. Han, *J. Chem. Eng. Data* **2003**, *48*, 1315.
[15] N. V. Plechkova, K. R. Seddon, *Chem. Soc. Rev.* **2008**, *37*, 123.
[16] B. Rupp, M. Schmuck, A. Balducci, M. Winter, W. Kern, *Eur. Polym. J.* **2008**, *44*, 2986.
[17] W. Lu, A. G. Fadeev, B. Qi, E. Smela, B. R. Mattes, J. Ding, G. M. Spinks, J. Mazurkiewicz, D. Zhou, G. G. Wallace, D. R. MacFarlane, S. A. Forsyth, M. Forsyth, *Science* **2002**, *297*, 983.
[18] H. Yanagi, T. Ohno, *Langmuir* **1999**, *15*, 4773.
[19] G. Mao, M. L. Saboungi, D. L. Price, Y. S. Badyal, H. E. Fischer, *Eur. Lett.* **2001**, *54*, 347.
[20] S. K. Fullerton-Shirey, J. K. Maranas, *Macromolecules* **2009**, *42*, 2142.
[21] M. A. B. H. Susan, T. Kaneko, A. Noda, M. Watanabe, *J. Am. Chem. Soc.* **2005**, *127*, 4976.
[22] M. P. Scott, C. S. Brazel, M. G. Benton, J. W. Mays, J. D. Holbrey, R. D. Rogers, *Chem. Commun.* **2002**, 1370.
[23] J. Y. Song, Y. Y. Wang, C. C. Wan, *J. Power Sources* **1999**, *77*, 183.
[24] C. Tang, K. Hackenberg, Q. Fu, P. M. Ajayan, H. Ardebili, *Nano Lett.* **2012**, *12*, 1152.
[25] C. Berthier, W. Gorecki, M. Minier, M. B. Armand, J. M. Chabagno, P. Rigaud, *Solid State Ionics* **1983**, *11*, 91.
[26] S. D. Druger, M. A. Ratner, A. Nitzan, *Solid State Ionics* **1983**, *9*, 1115.
[27] T.-W. Hwang, P. W. Bohn, *ACS Nano* **2011**, *5*, 8434.
[28] T.-W. Hwang, P. W. Bohn, *ACS Nano* **2014**, *8*, 1718.
[29] C. D. Robitaille, D. Fauteux, *J. Electrochem. Soc.* **1986**, *133*, 315.
[30] Z. Gadjourova, Y. G. Andreev, D. P. Tunstall, P. G. Bruce, *Nature* **2001**, *412*, 520.
[31] G. A. Yuri, G. B. Peter, *J. Phys.: Condens. Matter* **2001**, *13*, 8245.
[32] G. S. MacGlashan, Y. G. Andreev, P. G. Bruce, *Nature* **1999**, *398*, 792.

NANO MICRO small

Supporting Information

for *Small,* DOI: 10.1002/smll.201802023

Direct-Write Formation and Dissolution of Silver Nanofilaments in Ionic Liquid-Polymer Electrolyte Composites

*Zhongmou Chao, Brian P. Radka, Ke Xu, Garrison M. Crouch, Donghoon Han, David B. Go, Paul W. Bohn, and Susan K. Fullerton-Shirey**

Supporting Information

Title: Direct-write formation and dissolution of silver nanofilaments in ionic liquid-polymer electrolyte composites

Zhongmou Chao, Brian P. Radka, Ke Xu, Garrison M. Crouch, Donghoon Han, David B. Go, Paul W. Bohn, Susan K. Fullerton-Shirey[*]

1. Sample Preparation

Poly(ethylene glycol) diacrylate (PEGDA, M_n=2,000), 1-butyl-3-methylimadazolium hexafluorophosphate ([BMIM]PF_6, ≥98.5%), 2-Hydroxy-2-methylpropiophenone(HMPP, 97%), silver hexafluorophosphate ($AgPF_6$, 99.99%) and anhydrous acetonitrile (ACN, 99.8%) were purchased form Sigma-Aldrich. All reagents were used as received without further purification. Silicon wafers (University Wafer, P/Boron, 500 ± 15 µm) were cleaned by sonication in acetone followed by a 2-Propanol rinse and N_2 blow dry. 5 nm/100 nm of Ti/Ag was deposited by electron-beam evaporation at 5 x 10^{-7} mbar base pressure (Plassys, MEB 550 S). The following steps were completed inside an argon-filled glovebox (Mbraun, MB-200B) where O_2 and H_2O < 1 ppm. $AgPF_6$, [BMIM]PF_6 (IL) and PEGDA were dissolved in ACN and combined to prepare a total of 9 samples with PEGDA/$BMIMPF_6$ compositions of 90/10, 70/30 and 50/50 wt.% at 0, 0.2 and 2 mM $AgPF_6$. In all 9 samples, the PEGDA concentration was 1 wt.% together with 0.02 wt.% of HMPP (photoinitiator). The polymer electrolytes were spin-coated on the Ag-coated silicon substrate at 4000 rpm for 30 s and annealed at 80 °C for 2 mins to drive-off ACN. Samples were photo-crosslinked with a UV lamp (UVP Compact UV Lamp, λ = 365 nm, P = 1.3 mW/cm^2 at 3 inches) at a working distance of 1.25 cm for 1 hour.

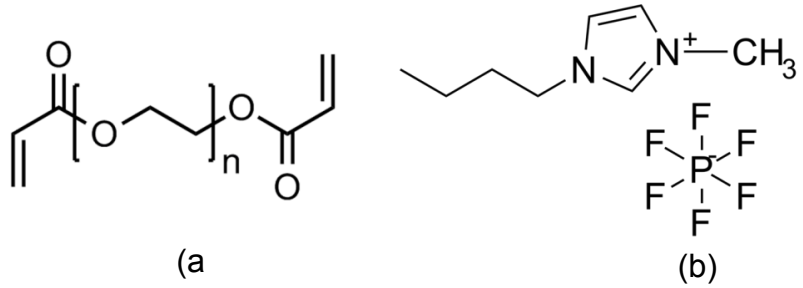

Figure S1. Chemical structures of (a) polyethylene glycol diacrylate (PEGDA) and (b) 1-butyl-3-methylimidazolium hexafluorophosphate, the ionic liquid.

2. Film Thickness Measurements

Electrolyte samples were prepared as described above, cross-sectioned by focused ion beam (FIB) milling, and then imaged by scanning electron microscopy (SEM). Cross sections of the 90/10, 70/30 and 50/50 wt.% PEGDA/IL at 0.2 mM $AgPF_6$ are shown in **Figure S2**. To protect the film during ion milling, Pt was deposited on the 90/10 sample and Pt and Pd-Au were deposited on the 70/30 and 50/50 films. The thicknesses are 41 ± 2, 44 ± 2, and 52 ± 5 nm, for 90/10, 70/30 and 50/50 PEGDA/IL with 0.2 mM $AgPF_6$, respectively. We notice fluctuations in the apparent thickness of the film with increasing IL concentration, which is likely due to the interaction between the charged IL and the ion and electron beams; thus, the silver filaments cannot be resolved using this technique.

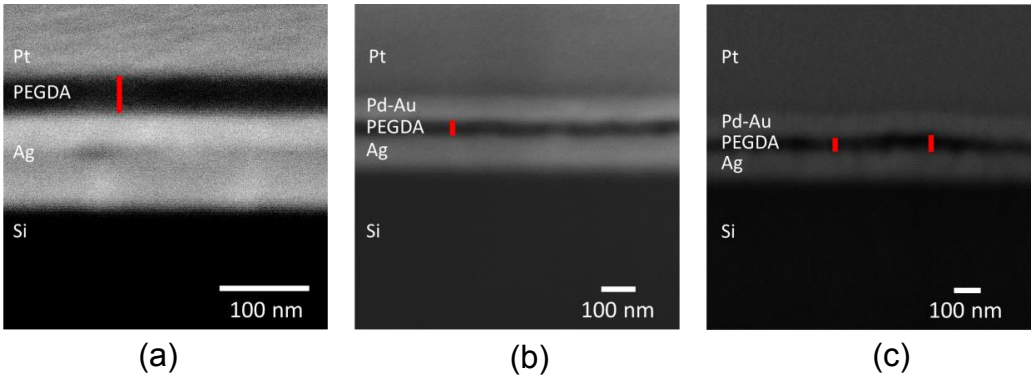

Figure S2. SEM of FIB cross-sectioned films containing 0.2 mM $AgPF_6$. (a) 90/10 (b) 70/30 and (c) 50/50 wt.% PEGDA/IL. Note the different scale bar sizes are all for 100 nm.

3. Young's Modulus Measurements

Nine samples (90/10, 70/30 and 50/50 wt.% at 0, 0.2 and 2 mM $AgPF_6$) were prepared using methods as described above. Young's modulus was measured using Bruker's PeakForce Quantitative Nanomechanical Mapping (PF-QNM) on a Bruker Dimension Icon AFM. The modulus maps are shown in **Figure S3** and the AFM probe was selected based on the working range for modulus measurement: (a,b,c) RTESPA-150 (5 - 500 MPa); (d,e,f) RTESP-300 (200 MPa- 2 GPa); (g,h,i) RTESP-525 (2 - 20 GPa). All probes were calibrated for their deflection sensitivity, spring constant, and tip radius.

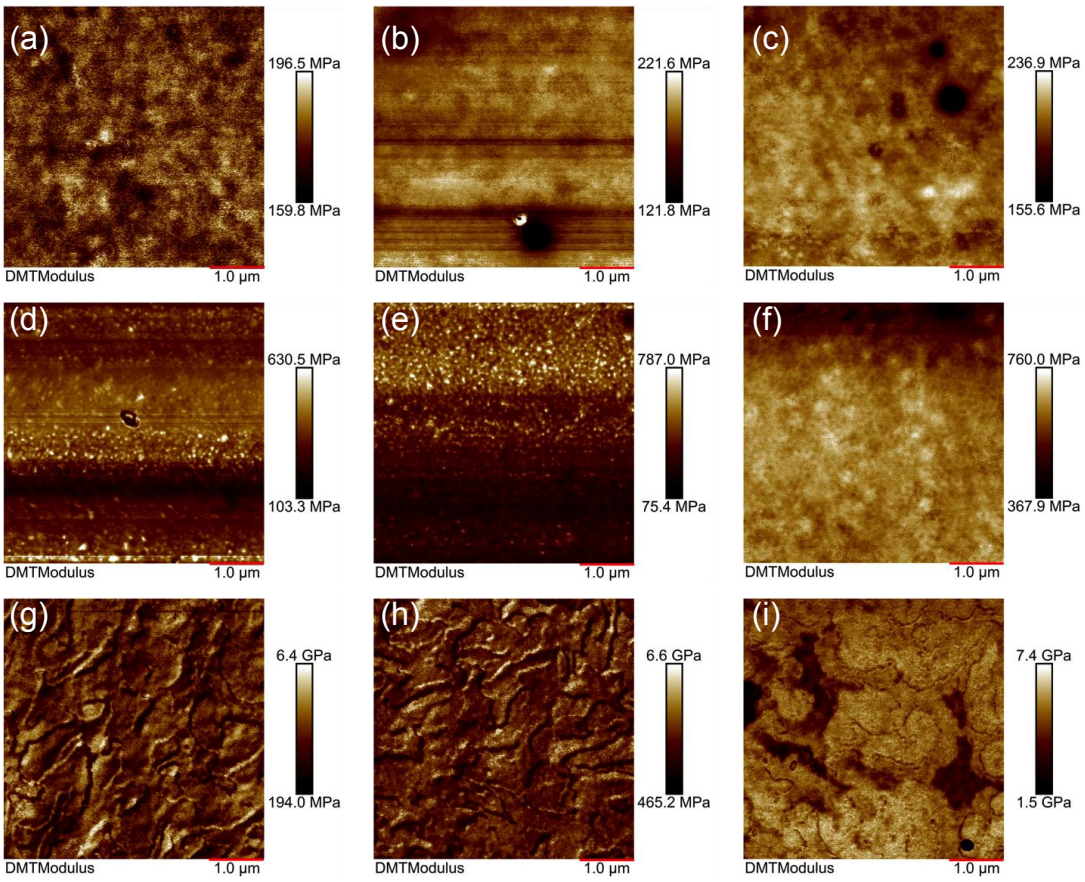

Figure S3. PF-QNM measurements of Young's modulus for PEGDA/IL (wt%) + $AgPF_6$ (mM) thin films of (a) 50/50 + 0; (b) 50/50 + 0.2; (c) 50/50 + 2; (d) 70/30 + 0; (e) 70/30 + 0.2; (f) 70/30 + 2 (g) 90/10 + 0; (h) 90/10 + 0.2; (i) 90/10 + 2. Note the different modulus range for each map.

4. Filament Formation and Dissolution – Current and Voltage Data

Conductive-AFM was used to form and dissolve silver filaments in ramp mode using the Bruker Dimension Icon AFM. Current/voltage *vs*. time data for a representative formation and dissolution event on the 90/10 wt.% PEGDA/IL + 0.2 mM $AgPF_6$ are shown in **Figure S4**. The C-AFM (probe type, SCM-PIT-V2) was operated in contact mode. Current sensitivity was set at 100 nA/V with a system compliance of approximately 600 nA. The AFM tip was

fixed at one location on the sample surface during each measurement. For the example data in **Figure S4**, the bias applied between the AFM tip and AFM stage was controlled manually. (For the formation and dissolution events reported in the paper, the AFM tip location and biasing were automated.)

The formation bias was set to 2.5 V at t = 4 s. At t = 60 s, the current starts to increase from 0 to ~ 200 nA within a short time range (i.e., seconds), indicating filament formation. A stable current was achieved at ~ 200 nA with a constant bias of 2.5 V from t = 62 s to 75 s. To dissolve the filament, the bias was set to -2.5 V at t = 75 s. The current first decreased to -500 nA and then returned to 0 nA within dozens of ms, indicating dissolution of the filament.

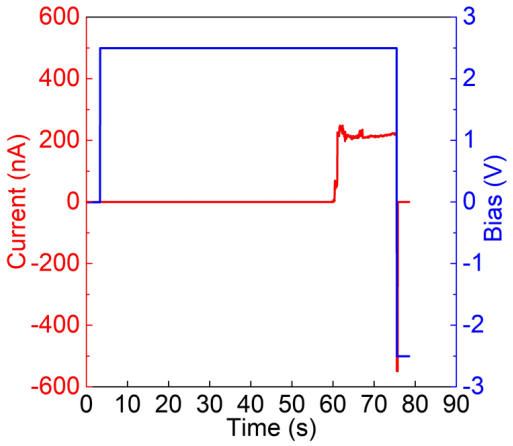

Figure S4. Current and applied bias as a function of time for a single representative formation and dissolution event. The sample is PEGDA/IL 90/10 wt.% and 0.2 mM $AgPF_6$.

5. Automated Acquisition of Filament Formation and Dissolution Data

A SCM-PIT-V2 AFM probe (Pt-Ir coating, k= 4.0 N/m) was operated in contact mode. A custom script was created to modulate the location and potential applied to the tip to: (1) move the tip from point-to-point in a raster scan pattern at a preset point spacing; (2) apply the desired voltage; (3) measure the current between the conductive AFM tip and the AFM chuck. The AFM tip was grounded, and the voltage was applied to the chuck. Electrical contact was

made between the AFM stage and the Ag layer of the substrate using copper tape (76555A711, McMaster-Carr). At each point, the chuck voltage was set to a positive formation voltage (2 V) until the current increased above a set threshold value, after which the voltage was switched to the negative dissolution voltage (-2 V) until the current (now of the opposite sign) decreased in magnitude below a set threshold.

Table S1. A summary of count percentages of Type-1 formation for different systems measured in primarily amorphous or crystalline regions.

Composition (PEGDA/IL wt.% + mM $AgPF_6$)	**Type-1 Formation (%)**	**Filaments Formed/Attempted (counts/counts)**
50/50 + 2 mM (Amorphous)	5	700/700
70/30 + 0 mM (Amorphous)	12	700/700
70/30 + 0.2 mM (Amorphous)	6	700/700
70/30 + 2 mM (Amorphous)	53	974/980
90/10 + 2 mM (Amorphous)	75	700/700
90/10 + 0 mM (Crystalline)	79	533/570
90/10 + 0.2 mM (Crystalline)	82	566/600
90/10 + 2 mM (Crystalline)	84	482/500

6. Observations of Ag Surface Overgrowth

For the 50/50/0 mM sample, a test for surface overgrowth was evaluated via performing electrodeposition experiments at 36 locations in an array covering a 6 × 6 μm region with a 1 μm pitch. A topography map was captured before and after the experiment, as shown in **Figure S5**(a) and (b). The surface topography is altered significantly after the electrodeposition measurements, indicating that electrodeposition of silver filaments changes

the surface structure of the electrolyte. No current signal was detected before the electrochemistry when applying a small bias (0.2 V) using C-AFM in contact mode, but an obvious current signal was captured after electrochemistry within the region where electrodeposition experiments were made, shown in **Figure S5**(c). From the topography and current map, we suspected surface overgrowth of the silver occurred in the 50/50/0 mM system, creating an electrically conductive deposit of silver on the electrolyte surface. Similar surface overgrowth was also observed in 50/50/0.2 mM but not in the 2 mM system. In our previous work on filament formation through a PEO-based electrolyte,[1] silver surface growth was also reported.

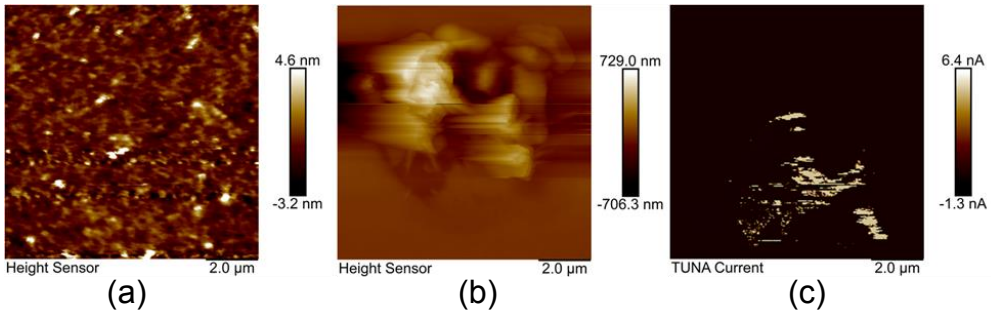

Figure S5. (a) Topography map before electrochemistry, (b) after electrochemistry, and (c) current map after electrochemistry for the 50/50/0 mM PEGDA/IL composition system.

Indirect evidence of surface overgrowth came from filament formation and dissolution events. The samples containing 50% IL showed filament formation/dissolution behavior that was noticeably different from the other samples containing less IL. As shown in **Figure S6**, the formation and dissolution time distributions for 50/50 wt.% PEGDA/IL at 0 and 0.2 mM of $AgPF_6$ overlap, meaning that additional silver salt does not affect the filament formation or dissolution kinetics in a detectable way. More noteworthy is that approximately half of the filaments did not dissolve within the time window (50 s) of the measurement. The observed silver surface overgrowth can be used to explain this abnormal results. This is because the

criteria to detect filament formation relates to detecting a change in electrical current, and if the overgrowth at one point impinges on the next point (either at the surface, or through the film thickness), the neighboring electrical measurement could be affected. Silver overgrowth could explain why nearly 50 wt.% of the locations where current was detected upon formation never registered zero current during reverse bias application, *i.e*. dissolution was not observed for nearly half the points, as shown in Figure **S6(b)**.

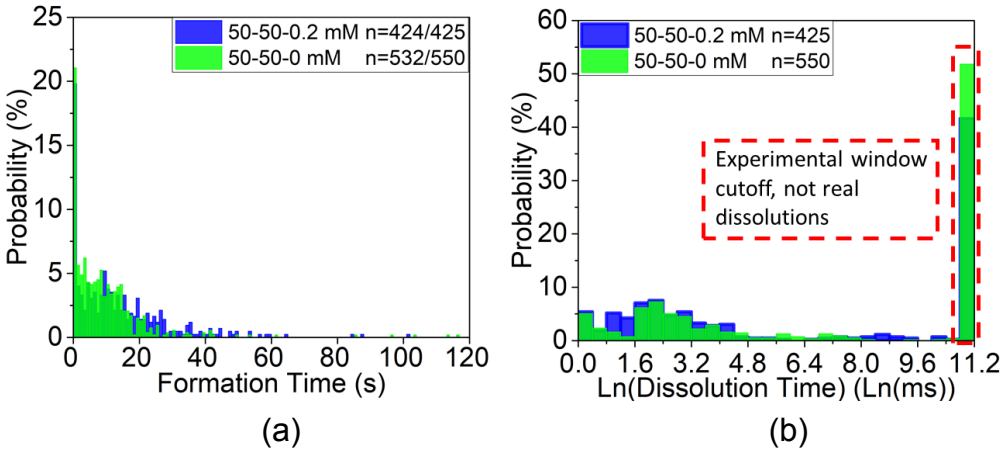

Figure S6. (a) Filament formation and (b) dissolution time distributions for the 50/50 wt.% PEGDA/IL system at 0 and 0.2 mM of $AgPF_6$. Bin width is 1 s for (a) and 0.4 Ln(ms) for (b).

Similar to the 50/50 PEGDA/IL system, signatures of silver overgrowth were also evaluated on the 70/30 sample (no $AgPF_6$). Electrodeposition was conducted at 36 locations within a 6 × 6 µm array with 1 µm pitch. A topography map was acquired both before and after the experiment as shown in **Figure S7**(a) and (b). An array of 6 × 6 protrusions is clearly distinguishable in **Figure S7**(b) and the approximate height of the protrusions is 10 nm (note that the height scale is adjusted to highlight the height of the protrusions). A line scan is also provided in **Figure S7**(c) showing the periodic protrusions. A current map was also captured before and after electrodeposition, but there were no obvious changes in the current signal.

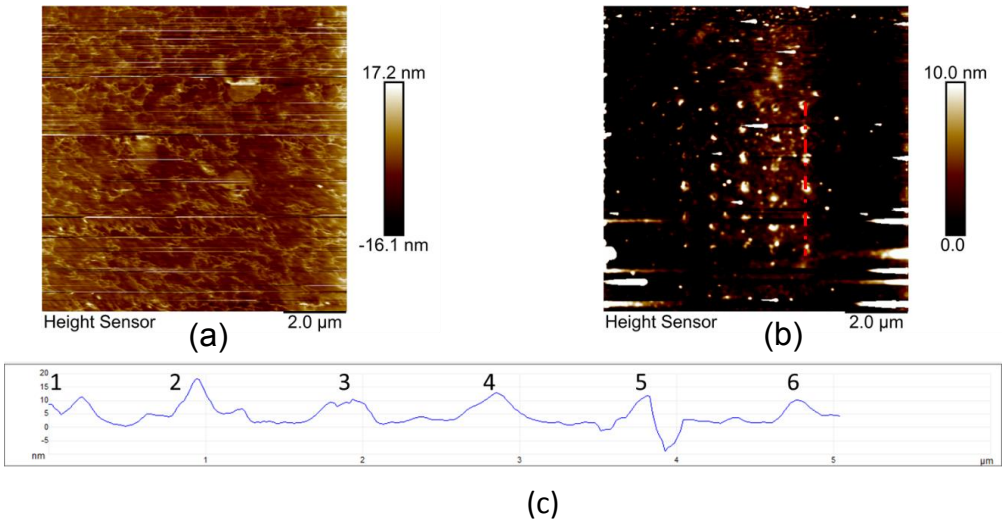

Figure S7. Topography map for the 70/30 sample (no $AgPF_6$) (a) before electrodeposition; (b) after electrodeposition; and (c) fluctuations in height along the red dashed line in (b) indicating the approximate height of 6 protrusions.

7. DSC traces of 100/0 wt.% PEGDA/IL Systems

The samples containing no IL were also measured using differential scanning calorimetry (DSC), and the traces are shown in **Figure S8**.

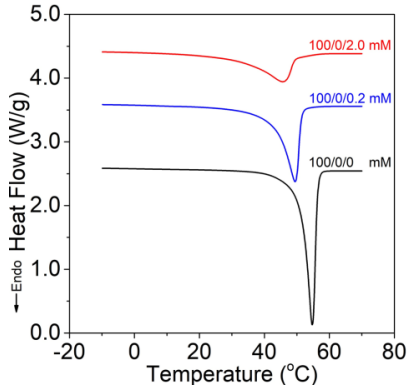

Figure S8. Heat flow (endotherm down) *vs* temperature for 100/0 wt.% PEGDA/IL at 0, 0.2, and 2 mM of $AgPF_6$ showing melting features (T_m).

8. Optical Microscopy Image of 90/10 wt.% PEGDA/IL at 2 mM $AgPF_6$

The coexistence of amorphous domains with crystalline domains is clearly visible by optical microscopy in the 90/10/2 mM sample, shown in **Figure S9**. Because it is easy to distinguish the two regions optically, electrodeposition measurements can be performed on primarily amorphous or primarily crystalline regions.

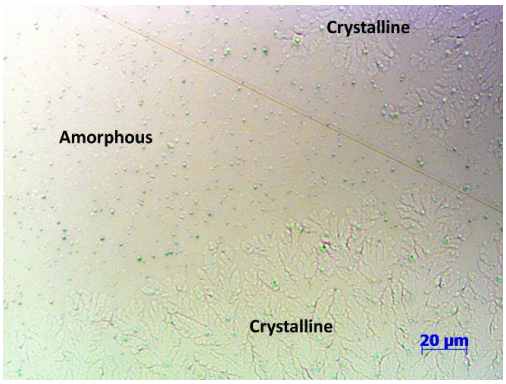

Figure S9. Optical microscopy image at 500× magnification showing crystalline features.

9. Control Experiments on 100/0 PEGDA/IL wt.% Films

Formation and dissolution measurements were also made on samples without IL, as shown in **Figure S10**(a) and (b), respectively. Formation and dissolution data for a primarily crystalline domain in the 90/10 PEGDA/IL wt.% systems are also shown in **Figures S10**(c) and (d) for comparison to the pure PEGDA system. The films without IL show longer formation and dissolution time distributions, indicating that 10 wt.% IL enhances filament formation and dissolution within primarily crystalline regions.

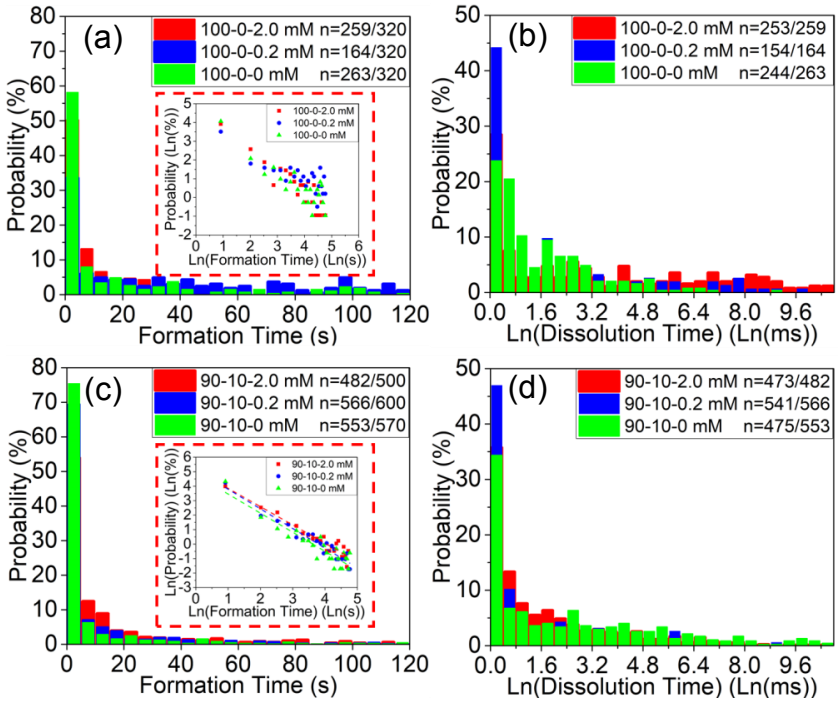

Figure S10. (a, c) Filament formation, and (b, d) dissolution time distributions for 100/0 (a, b) and 90/10 (c, d) wt.% PEGDA/IL at 0, 0.2, and 2 mM of $AgPF_6$. Bin width is 5 s for formation and 0.4 Ln(ms) for dissolution. Insets in (a) and (c) are Ln-Ln plots of formation time distributions *vs*. probability, showing a power-law dependence.

10. Melting Temperatures and Heats of Fusion

Heat of fusion for all samples are provided in **Table S2**. The corresponding data are shown in **Figures** 5(b) and **S8**.

Table S2. A summary of melting peaks and calculated heats of fusion

Composition (PEGDA/IL wt.% + mM $AgPF_6$)	**T_m Peak (°C)**	**Heat of fusion (J/g)**
100/0 + 0 mM	54.7	133.2
100/0 + 0.2 mM	49.4	111.4
100/0 + 2 mM	45.6	82.9

90/10 + 0 mM	45.6	67.2
90/10 + 0.2 mM	45.1	59.3
90/10 + 2 mM	45.0	72.0
70/30 + 0 mM	44.0	41.3
70/30 + 0.2 mM	43.8	41.3
70/30 + 2 mM	39.4	29.3
50/50 + 0 mM	25.1	6.7
50/50 + 0.2 mM	23.6	8.2
50/50 + 2.0 mM	26.0	4.6

Reference

[1] G. M. Crouch, D. Han, S. K. Fullerton-Shirey, D. B. Go, P. W. Bohn, *ACS Nano* **2017**, 11, 4976.

Appendix C

Publication #2 of 4

In this appendix the paper published in *Advanced Functional Materials* [20] and its supporting information are attached.

ADVANCED FUNCTIONAL MATERIALS
www.afm-journal.de

Silver Nanofilament Formation Dynamics in a Polymer-Ionic Liquid Thin Film by Direct Write

*Zhongmou Chao, Kutay B. Sezginel, Ke Xu, Garrison M. Crouch, Abigale E. Gray, Christopher E. Wilmer, Paul W. Bohn, David B. Go, and Susan K. Fullerton-Shirey**

Silver nanofilament formation dynamics are reported for an ionic liquid (IL)-filled solid polymer electrolyte prepared by a direct-write process using a conductive atomic force microscope (C-AFM). Filaments are electrochemically formed at hundreds of *xy* locations on a ≈40 nm thick polymer electrolyte, polyethylene glycol diacrylate (PEGDA)/[BMIM]PF_6. Although the formation time generally decreases with increasing bias from 0.7 to 3.0 V, an unexpected non-monotonic maximum is observed ≈2.0 V. At voltages approaching this region of inverted kinetics, IL electric double layers (EDLs) become detectable; thus, the increased nanofilament formation time can be attributed to electric field screening, which hinders silver electromigration and deposition. Scanning electron microscopy confirms that nanofilaments formed in this inverted region have significantly more lateral and diffuse features. Time-dependent formation currents reveal two types of nanofilament growth dynamics: abrupt, where the resistance decreases sharply over as little as a few ms, and gradual where it decreases more slowly over hundreds of ms. Whether the resistance change is abrupt or gradual depends on the extent to which the EDL screens the electric field. Tuning the formation time and growth dynamics using an IL opens the range of accessible resistance states, which is useful for neuromorphic applications.

1. Introduction

Nanoscale metal filaments are required for applications ranging from optical metamaterials[1,2] to advanced electrical probes.[3] One of the most studied applications is conductive bridge random-access memory (CBRAM), which is a type of nonvolatile resistive random-access memory (ReRAM) wherein the electrical resistance of a solid-state dielectric is set to either a high or low state.[4,5] One approach to achieve the two states is to electrochemically form and dissolve conductive metal nanofilaments through the dielectric in a metal–insulator–metal structure (MIM).[6,7] Although progress has been made in both organic and inorganic resistive memories, issues such as large device-to-device variability and poor reliability persist.[8–10] To address the challenges in polymer-based ReRAM, ionic liquids (ILs)—liquid salts that are commonly added to solid polymer electrolytes for various electrochemical applications[11–15]—are being considered. In a recent report, ILs were added to polymer-based CBRAM to reduce the formation (set) bias and increase endurance;[16] however, a detailed understanding of the role that ILs play in polymer-based resistive memory is still developing. Such understanding is important to uncover the microscopic mechanisms of conductive nanofilament formation and switching,[7] and how material structure and composition can be tailored to tune performance.

We have previously reported on the formation and dissolution of silver nanofilaments in a new type of polymer electrolyte consisting of a UV-crosslinkable polymer, polyethylene glycol diacrylate (PEGDA), and an IL, 1-butyl-3-methylimadozolium hexafluorophosphate ([BMIM]PF_6).[17] The IL enhances uniform nanofilament formation kinetics under constant applied bias and enables modulus tuning over a range of a few hundred MPa to several GPa,[11,12,17] making it more versatile than IL-free polymer electrolytes. Also, adding a sufficient amount of IL (>10 wt%) enables five times faster nanofilament formation compared to the IL-free electrolyte, but adding too much (50 wt%) slows the nanofilament kinetics by a factor of 7. These observations suggest complex dynamics, which further motivate investigation of the underlying mechanisms.

In this study, we focus on one IL concentration and study the impact of applied bias on nanofilament formation dynamics

Z. Chao, K. B. Sezginel, Dr. K. Xu, A. E. Gray, Prof. C. E. Wilmer, Prof. S. K. Fullerton-Shirey
Department of Chemical and Petroleum Engineering
University of Pittsburgh
Pittsburgh, PA 15261, USA
E-mail: fullerton@pitt.edu
Prof. C. E. Wilmer, Prof. S. K. Fullerton-Shirey
Department of Electrical and Computer Engineering
University of Pittsburgh
Pittsburgh, PA 15261, USA
G. M. Crouch, Prof. P. W. Bohn, Prof. D. B. Go
Department of Chemical and Biomolecular Engineering
University of Notre Dame
Notre Dame, IN 46556, USA
Prof. P. W. Bohn
Department of Chemistry and Biochemistry
University of Notre Dame
Notre Dame, IN 46556, USA
Prof. D. B. Go
Department of Aerospace and Mechanical Engineering
University of Notre Dame
Notre Dame, IN 46556, USA
The ORCID identification number(s) for the author(s) of this article can be found under https://doi.org/10.1002/adfm.201907950.

DOI: 10.1002/adfm.201907950

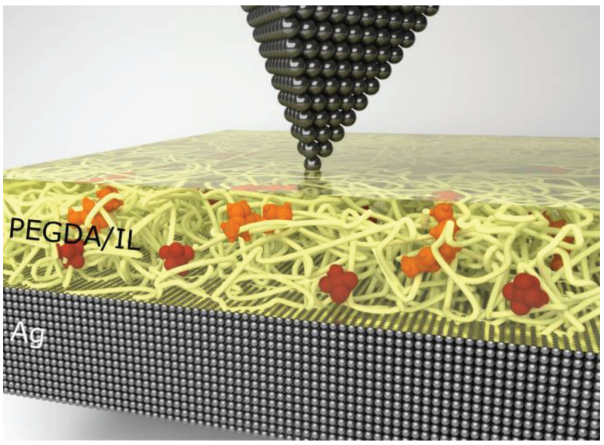

Figure 1. Schematic of the direct writing of Ag nanofilaments in a polymer electrolyte thin film on a Ag substrate. A C-AFM controls the electrochemical formation and dissolution of Ag nanofilaments through the PEGDA/IL thin film between the AFM tip and a sacrificial Ag substrate.

using conductive atomic force microscope (C-AFM) where the AFM tip serves as an inert mobile top electrode, while a sacrificial bottom electrode supplies the silver for electrodeposition (**Figure 1**). C-AFM enables the direct writing of nanofilaments by precisely defining the nucleation sites, yielding more uniform nucleation and growth.[18,19] Using an automated script, nanofilament formation events at hundreds of *xy* locations on the film are recorded as a function of applied bias. This spatially dense sampling allows us to fully capture the stochasticity of nanofilament growth and enables statistical analyses of the data, which are particularly crucial for a polymer electrolyte containing microscopic heterogeneities.

The data reveal an unexpected relationship between formation times and applied bias. Specifically, the formation times do not decrease monotonically with increasing driving force—as expected for oxide-based dielectrics[20–22]—but instead exhibit a pronounced maximum near 2.0 V. We interpret this behavior as the result of a competition between IL EDL formation and electrochemical filament growth. This competition can be used to control nanofilament morphology over multiple, well-defined resistance states—a control mechanism that should lend itself to the production and engineering of neuromorphic architectures where multiple distinguishable resistance states must be achieved to emulate the connections between neurons in an artificial neural network.[9,23]

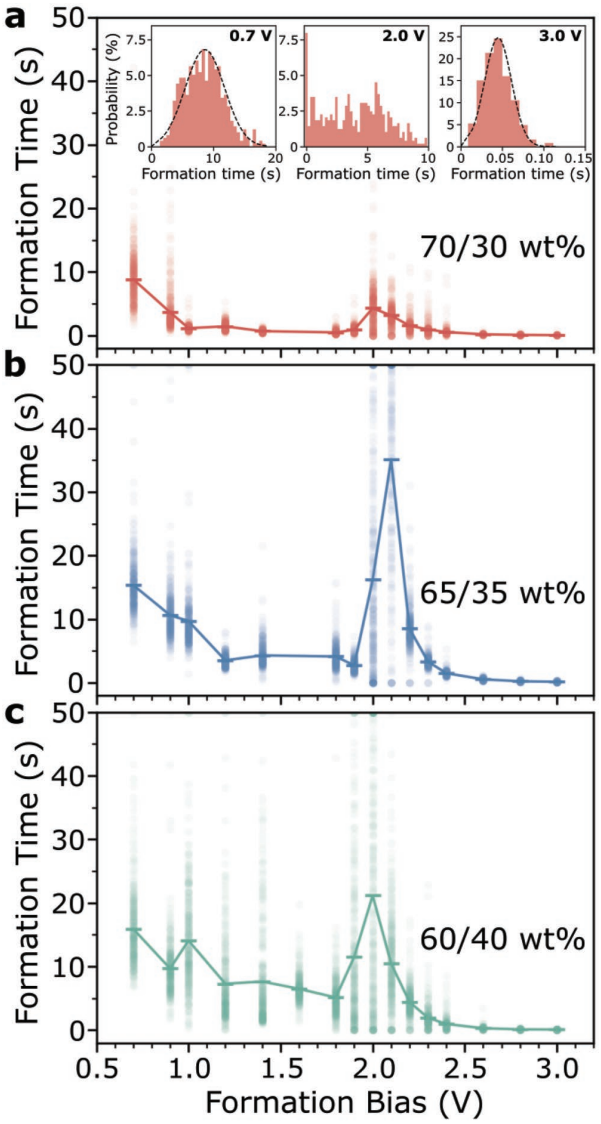

Figure 2. Nanofilament formation times as a function of applied bias for a) 70/30, b) 65/35, and c) 60/40 PEGDA/IL wt% samples. 500 formation events were collected for all samples at each bias with the exception of data at 2.1 V for 65/35%, where 339 events were collected. The average formation time at each bias is indicated by a horizontal marker and connected by the solid line. Insets in a) are the histograms of formation time distributions at 0.7, 2.0, and 3.0 V, respectively for the 70/30 PEGDA/IL wt% sample.

2. Results and Discussion

2.1. Impact of Applied Bias on Nanofilament Formation Kinetics

Formation times of all ≈500 nanofilaments formed at each bias over a range of 0.7 to 3.0 V are shown in **Figure 2** for three IL concentrations. At all IL concentrations, the formation times decrease with increasing bias over the low bias range of 0.7 to 1.8 V. Specifically, for 70/30 PEGDA/IL wt% in Figure 2a, the average formation time decreases from 8.8 s at 0.7 V to 0.5 s at 1.8 V. The trend of decreasing formation time with increasing voltage is expected and can be explained by straightforward electrochemical kinetics. That is, the driving force for both electrochemical redox reactions and silver ion migration increases with increasing formation bias. However, unexpectedly, the average formation time increases abruptly when the bias is increased to just below 2.0 V. In addition to longer formation times, a more scattered distribution of formation times is also observed. For the 30 wt% IL sample, this distribution is highlighted in the insets in Figure 2a showing formation histograms at 0.7, 2.0, and 3.0 V.

At voltages larger than 2.1 V, the formation times continue to decrease as expected, and the distribution returns to a standard Gaussian that is also observed for voltages less than 1.8 V. (For a complete set of nanofilament formation and dissolution histograms, see Figure S1, Supplemental Information, SI.) We refer to nanofilament formation kinetics near 2.0 V as "inverted" kinetics, where the average formation time first increases with increasing formation bias and then decreases again, causing unexpected non-monotonic behavior and giving rise to a peak in the average formation time versus voltage plot. Inverted formation kinetics appear for all three IL concentrations at ca. 2.0 V, with the formation time generally increasing with increasing IL concentration.

2.2. The Role of the Electrical Double Layer on Formation Kinetics

The observation that inverted kinetics at ≈2.0 V becomes more pronounced with increasing IL concentration motivates further investigation with an eye toward the possible role of the IL. One clue regarding the contribution of the IL comes from their use as high-capacitance gate dielectrics in electrolyte-gated transistors.[24,25] Here, electric double layers (EDLs) are formed by drift and diffusion of cations and anions to the surface of electrodes with opposite polarity. Specifically, when a positive bias is applied to the anode, cations drift to the cathode surface forming an EDL at the interface between the electrolyte and the cathode and induce an image charge in the electrode that is detected as a charging current. Simultaneously, an anionic EDL forms at the anode surface. In our case, we expect the cations in the IL (i.e., $[BMIM]^+$) to accumulate near the C-AFM tip (cathode) when a positive formation bias is applied. Thus, one piece of evidence for IL EDL formation would be a non-zero current at the first measurement time after a positive voltage is applied followed by a temporal decay—assuming that EDL formation is faster than nanofilament formation. Figure S2 in the Supporting Information confirms this behavior, showing the current decay over 10 ms, which is orders of magnitude faster than nanofilament formation. This behavior is identical in form to the charging current associated with EDL formation in a parallel plate capacitor.[26]

Up to half of the applied potential can drop across the EDL[27,28] (depending on the ion concentration and the geometry of the electrodes) leaving relatively little drop in the bulk of the electrolyte to drive ion migration. Thus, residual charge accumulated within any remaining EDL is likely to impact sequential nanofilament formation as the tip is moved from location to location. To address this issue, we modified the algorithm of the automation script to discharge residual EDL by grounding the tip for 100 s both before applying the formation bias at a new location, and after applying dissolution bias. The modified script was tested on the 65/35 PEGDA/IL wt% sample at 50 locations for each of six formation biases over two regions separated by >100 µm (i.e., 25 points/region) in a 4.8 × 4.8 µm array, with a pitch of 1.2 µm. Formation times with and without the tip set to ground are shown in **Figure 3**. The data clearly show that grounding the tip decreases the formation time independent of bias. Notice that this approach does not eliminate the contribution from EDL formation during the measurement, but it eliminates any residual EDL that may persist from one location to the next.

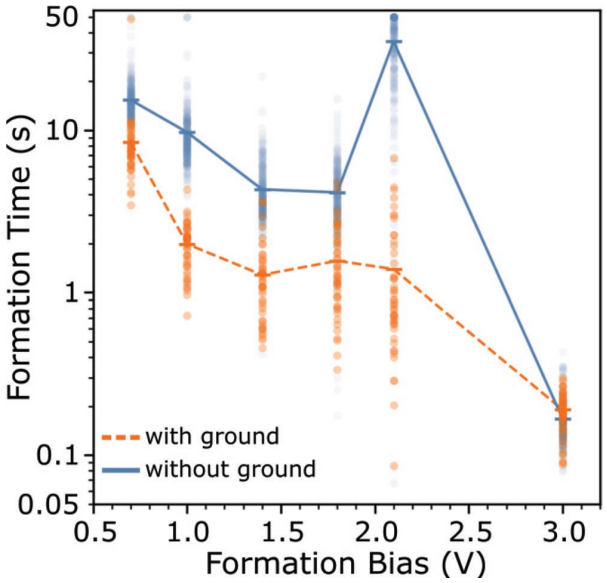

Figure 3. Filament formation times versus bias at 500 locations without grounding (blue, same data as Figure 2b) and 50 locations with grounding (orange) for 65/35 PEGDA/IL wt%; the average formation times are connected using a solid line (without ground) and dotted line (with ground).

Grounding the electrode has an especially strong impact on the formation times at voltages corresponding to the region of "inverted" formation kinetics. For example, the average formation time at 2.1 V is 20 times faster with the grounding step, whereas it is only up to 3 times faster at other biases. In contrast, at the highest applied bias of 3.0 V, filament formation is less affected by EDL formation as filaments are likely formed before the EDL screening can take effect. Therefore the grounding has relatively little effect on the formation times, as confirmed by the overlapping data at 3.0 V.

While grounding the AFM tip decreases the formation time, the distribution of times at 2.1 V remain widely scattered with a relative standard deviation of 94%, compared to ≈25% at 0.7 and 3.0 V. The results show that while discharging the previously formed EDL via grounding decreases the magnitude of the peak, it does not decrease the variability. Based on these results, we conjecture that there is an additional factor contributing to the inverted kinetics region, and we hypothesize that it is due to competition between EDL screening and silver ion electrodeposition. That is, the timescales of EDL formation and nanofilament formation are comparable at applied biases near 2.1 V, resulting in both longer nanofilament formation times and a wider distribution of formation times.

2.3. Quantifying IL EDL Formation Times as a Function of Bias

While the data in Figure 3 suggest that there may be important physics occurring at timescales shorter than those involved with nanofilament formation, it is difficult to decouple the electrical

response of EDL formation from faradic electron transfer due to electrodeposition (Ag^+ to Ag(s)) in the nanofilament growth data. Thus, we prepared control samples in which silver nanofilaments cannot form by using an Au counter electrode instead of a sacrificial Ag electrode. One control sample, consisting of 65/35 PEGDA/IL wt%, was designed to isolate the effects of IL EDL formation, and a second control sample, consisting of pure PEGDA, eliminates IL EDL formation altogether. Current-time data were collected for 50 s at three locations (separated by more than 100 µm) at biases in the range of 0.7 to 3.0 V with grounding between measurements. These data for the pure PEGDA thin film are shown in Figure S3 in the Supporting Information, and as expected, there is no detectable current above the noise threshold at any of the applied biases, because an EDL cannot form. In contrast, in **Figure 4** we observe clear current signatures of EDL formation in the 65/35 PEGDA/IL wt% sample at biases greater than 1.8 V, where three measurements are made at each voltage. Specifically, when the bias is ≥2.1 V, up to 0.1 nA of current is captured on timescales ranging from milliseconds to seconds.

Because of the low signal-to-noise ratio in these extremely low-current measurements, it is not possible to quantify a time constant for the EDL response; however, we can use these data to identify the voltage at which the EDL contribution becomes detectable. This voltage could reflect the driving force required to overcome the barrier to diffusion for the IL ions through the heavily crosslinked polymer chains. That is, while small silver cations may be able to easily traverse the crosslinked PEGDA, the much larger IL ions may only gain appreciable mobility once the voltage is sufficiently large (i.e., ≥2.0 V). In addition, the variability between the three measurements at each voltage for biases ≥2.0 V likely reflects the stochastic nature of IL EDL formation in the PEGDA/IL system. This is not surprising given the known complexity of IL EDL dynamics in parallel plate geometries.[29]

Nevertheless, the EDL formation data in Figure 4 combined with the nanofilament formation data in Figure 3 provide insight as to why EDL formation is likely to have a stronger impact on nanofilament formation kinetics in the inverted region than at lower voltages. Note that the vertical dotted lines in Figure 4 indicate ± one standard deviation from the average formation times enabling the direct comparison of nanofilament formation timescales to EDL formation. At low biases, no appreciable EDL formation occurs and, therefore, there is no competition between silver nanofilament and EDL formation. However, at a bias of 2.1 V, where the inverted region is observed in Figure 3, the nanofilament formation time is comparable to the timescale over which the EDL current becomes appreciable. This result suggests that the silver nanofilament formation is competing with EDL formation, and the screening of the field by the EDL likely gives rise to longer formation times. Because EDL formation is disruptive to nanofilament formation, this competition could also account for the larger distribution of formation times at 2.1 V. In contrast to the inverted region, at a bias of 3.0 V the nanofilaments have already formed before the EDL has a chance to respond, giving rise to fast formation times with a tight time distribution.

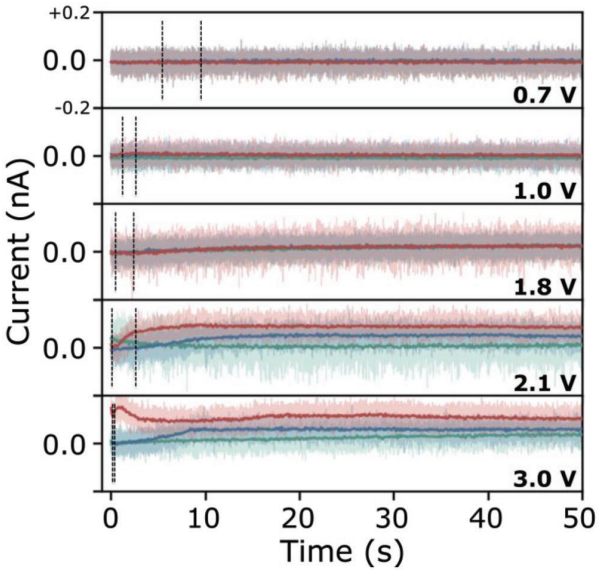

Figure 4. Time-dependent current response at various biases for the 65/35 PEGDA/IL wt% sample on Au. At each bias, measurements at three different locations are plotted in three different colors. All of the current data are included on the plot, and the average of every 10 consecutive data points is extracted and plotted as a solid line to show the trend in the current through the noise. Note that the *Y*-axis is linear. Dotted, vertical lines at each bias indicate ± one standard deviation of the average formation times from Figure 3 for the data that included grounding between measurements.

2.4. Impact of Formation Bias on Nanofilament Growth Dynamics

We have established how the nanofilament formation times at various locations and IL concentrations depend on bias, and how IL EDL formation can disrupt nanofilament formation. Here, we turn our attention to the nanofilament formation dynamics. Previous reports show how the final structure of a conductive metal nanofilament is strongly associated with its growth dynamics,[22,30,31] which are further governed by kinetic and transport properties such as the redox reaction rate and metal ion mobility in the specific dielectric system.[30] As the principal driving force for silver migration and electrodeposition in our PEGDA/IL system, the magnitude of the applied bias is expected to affect nanofilament growth dynamics, especially when a field-sensitive IL is present. Thus, we analyze the time-dependent current data and compare these results to direct imaging of the nanofilament structure as a function of bias.

Two types of time-dependent current data are detected during formation: abrupt growth and gradual growth, and both are shown schematically in **Figure 5**a. Here, we define the *nucleation time* (t_n) as the time for the current to reach a low, but detectable value of 0.5 nA, defined as the *nucleation current* (i_n). This current is ≈100 times higher than system noise, defined as i_o. The *growth time* (t_g) is defined as the time required for the current to increase from i_n to the formation threshold (4 nA at a current sensitivity of 1 nA V^{-1}). The distributions of filament

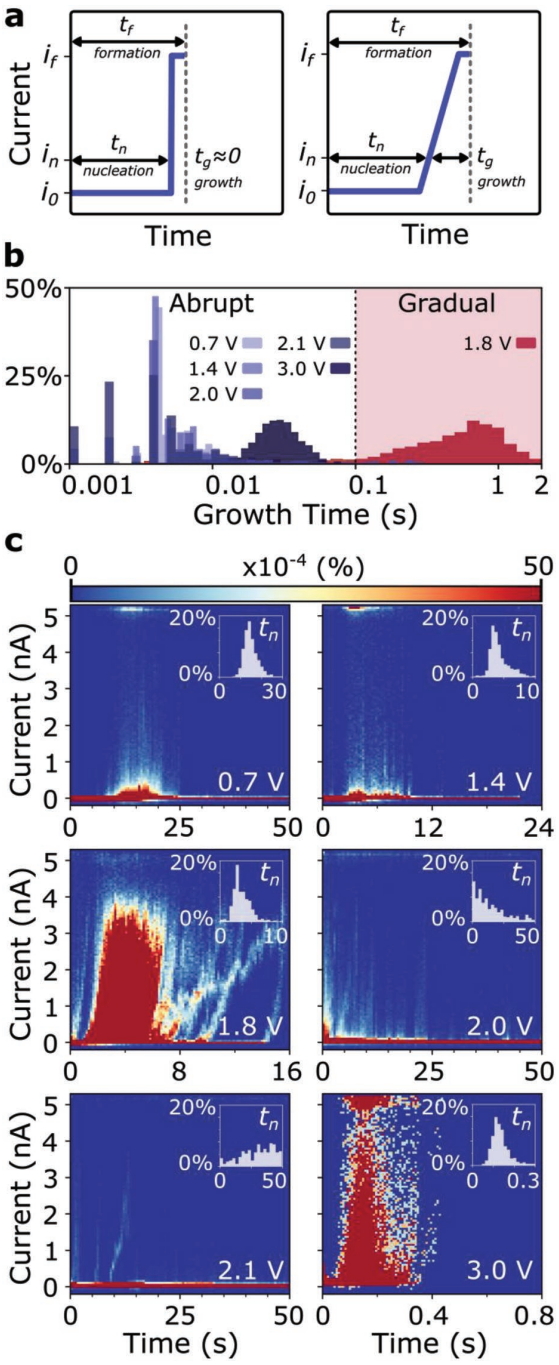

Figure 5. Time-dependent current data during nanofilament formation at various applied biases (65/35 PEGDA/IL wt%). a) Schematic of abrupt (left) versus gradual (right) growth. b) Growth time (t_g) distributions for filaments formed at different biases. c) All current versus time measurements are plotted at each bias. Note that the X-axis range is adjusted from plot-to-plot because the average formation time varies with voltage. Data density is represented by color, calculated by dividing the number of data points in each bin over the total number of data points for each bias. The scale of color bar is set from 0 to 50×10^{-4}% and each plot contains 100×100 bins (i.e., the time and current scales are equally divided into 100 parts).

growth time (t_g) at different biases are plotted in Figure 5b, where we define $t_g = 0.10$ s as the boundary that distinguishes abrupt ($t_g < 0.1$ s) versus gradual ($t_g > 0.1$ s) growth.

We extracted the t_g values in Figure 5b from the time-dependent current data leading up to nanofilament formation, which are shown in Figure 5c at six biases for the 65/35 PEGDA/IL wt% sample. Note that all current signals from hundreds of formation events at different xy locations are included in Figure 5c, where the color contours are used to represent the relative fraction of measurements with a specific current and formation time (i.e., the current data density). For nanofilaments formed at 0.7 and 1.4 V, the growth type is abrupt with an average t_g of 0.01 s; similarly abrupt transitions are observed at 3.0 V with average t_g of 0.03 s. The major difference at these voltages is the *distribution* of nucleation times (highlighted in the insets of Figure 5c): the wide t_n distributions at 0.7 and 1.4 V lead to low data density between i_n and i_f, whereas the narrower t_n distribution at 3.0 V increases the density of data as indicated by red.

In contrast, nanofilaments formed at 1.8 V show a more gradual growth (average $t_g = 0.62$ s), as shown in the t_g histogram in Figure 5b and as indicated in Figure 5c by the red data with a noticeable positive slope. When the applied bias enters the inverted region at 2.0 and 2.1 V, abrupt growth is again observed (average $t_g = 0.03$ and 0.02 s, respectively), but here it is accompanied by extremely scattered t_n. It is notable that the t_n distributions at biases outside the inverted region exhibit a normal distribution, while those in the inverted region do not.

Because the current at 1.8 V changes gradually with time after the current reaches i_n, it suggests the possibility of achieving multiple resistance states—a requirement for neuromorphic computing[9,23,32]—during a single nanofilament formation under constant formation bias. To test whether or not the PEGDA/IL system can accommodate such a requirement, we set the system compliance to 100 nA and selected eight nanofilament "programming currents" ranging from 15 to 50 nA with a step of 5 nA. The formation bias was set to 1.8 V, and after each program current was reached and maintained for 20 ms, a read bias of 0.8 V was applied for 2 s while monitoring the conductance of the nanofilament. The data are plotted in **Figure 6**. The conductance initially decreases on the timescale of ms,

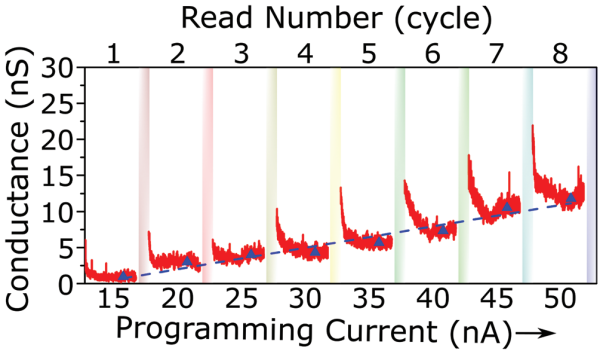

Figure 6. Conductance measured for 2 s at a 0.8 V read bias after nanofilament reached eight programming currents (15, 20, 25, 30, 35, 40, 45, and 50 nA) at 1.8 V for 20 ms (65/35 PEGDA/IL wt%). Shaded bars indicate the locations where a 1.8 V formation bias was applied.

consistent with the discharge of a portion of the EDL formed at 1.8 V, followed by a more stable current. While we cannot rule out a read disturbance at 0.8 V, the time constant for forming a nanofilament at 0.8 V is more than 50 times longer than the 2 s read time, and when the nanofilament does eventually form, the formation is abrupt and not gradual (Figure S4, Supporting Information). In addition, a linear correspondence ($R^2 = 0.95$) between nanofilament resistance states and program pulses is observed—as indicated by the dashed line in Figure 6—which is desirable for artificial neural networks.[23,32] In most cases, repeated programming pulses are used to controllably adjust resistance,[23,32] but Figure 6 strongly suggests that multiple resistance states may be achieved via the competition between the EDL formation and Ag redox reaction—thereby introducing a new mechanism to tune resistance.

The nanofilament growth dynamics captured in Figure 5 are likely to result in different nanofilament morphologies; therefore, scanning electron microscopy (SEM) was used to image the nanofilaments directly, producing both top-down and cross-section views (**Figure 7**). Four, 5 × 5 arrays of nanofilaments were created using 0.7, 1.4, 2.1, and 3.0 V nanofilament formation biases, respectively (4.8 × 4.8 µm square with a pitch of 1.2 µm). Surprisingly, the cross-sectional images in Figure 7 combined with C-AFM conductivity mapping (Figure S5, Supporting Information) show that the majority of the nanofilament structure is confined below the surface of the polymer film. The plan view image makes it clear that nanofilaments formed at 2.1 V have the largest features among all arrays, followed by 0.7 and 1.4 V, while only subtle features in the nanofilament array can be resolved at 3.0 V. The cross-section imaging shows nanofilaments formed at 0.7, 1.4, and 2.1 V all have obvious lateral buildup, especially those formed at 2.1 V. In contrast, no nanofilament structure formed at 3.0 V can be resolved through cross-section imaging.

Combining the time-dependent current data in Figure 5 with the SEM images of Figure 7 leads us to hypothesize a model of bias-dependent nanofilament growth shown schematically in **Figure 8**. At biases ≤1.4 V where abrupt nanofilament connections are made and for which nanofilaments are visible by SEM, the relatively weak vertical electric field results in more lateral build-up (i.e., thicker nanofilaments) before the final connection is made. The switching behavior shown in Figure S6 in the Supporting Information provides additional support for this interpretation in that it becomes increasingly difficult to dissolve nanofilaments with increasing switching cycles—consistent with thickening of the nanofilament during switching. While similar abrupt current transitions are also observed at 3.0 V, the vertical field is stronger, leading to faster and more directed (i.e., less lateral) growth. The hundreds of nanofilaments formed at this higher field remain switchable for at least 20 cycles (Figure S6, Supporting Information).

In the inverted region, we measure a wider distribution of nucleation times, extreme lateral growth, and both gradual and abrupt formation events consistent with a competition between redox reactions and EDL formation that weakens the vertical electric field. Clearly, 1.8 V represents the threshold at which EDL formation impacts the growth kinetics in our PEGDA/IL system—changing them from abrupt to gradual by interfering with the electric field. Here, the nanofilament morphology also changes from thin (high resistance) to thick (low resistance) over longer timescales, and this gradual and controllable

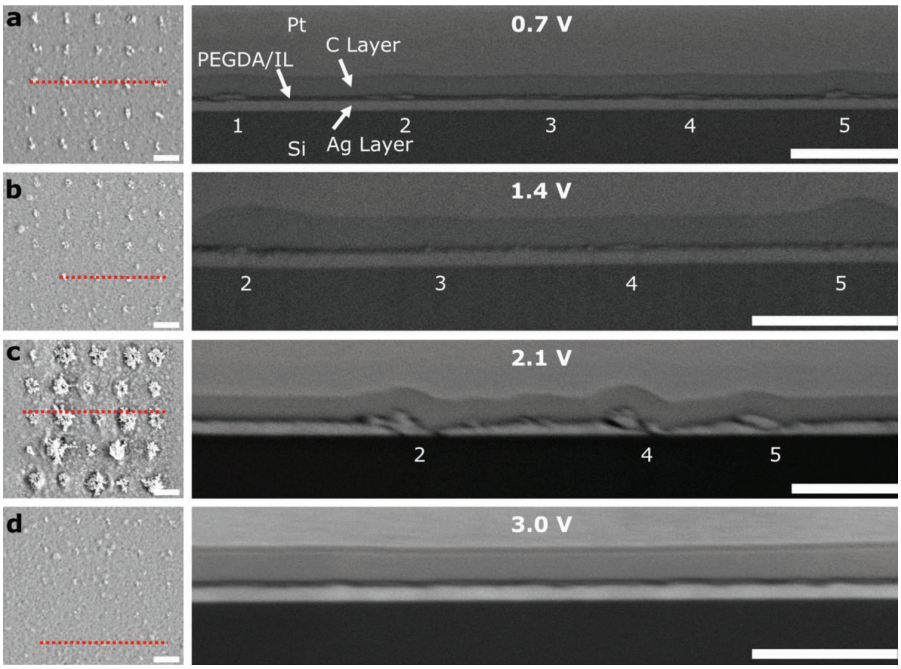

Figure 7. Plan view (left) and cross-section (right) SEM images of arrays of silver nanofilaments formed at a) 0.7, b) 1.4, c) 2.1, and d) 3.0 V. The locations of the cross-sections are indicated by red dashed line on the surface image. All scale bars are 1 µm.

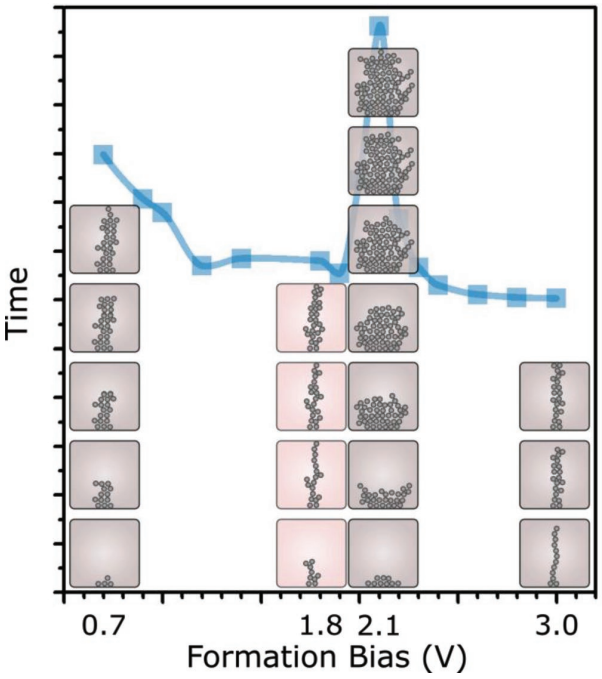

Figure 8. Schematic illustration of nanofilament formation dynamics at different applied biases. Gradual growth type (shaded red) is only observed at 1.8 V. Silver atoms are represented by grey spheres. The widths of the nanofilaments relative to the depicted atom sizes are purely for illustrative purposes and do not reflect the actual ratios.

thickening could lead to enhanced switching characteristics. In fact, of the three measured voltages, the nanofilaments formed at 1.8 V retain the best switching characteristics among those tested (Figure S6, Supporting Information). In addition, when the nanofilament does reform at 1.8 V during the switching measurements, the switching is also gradual (Figure S7, Supporting Information), another characteristic which is required for neuromorphic applications.

3. Conclusion

C-AFM-based direct-writing of nanofilaments in a PEGDA/IL electrolyte reveals an unexpected relationship between formation times and applied bias. Specifically, the nanofilament formation time does not decrease monotonically with increasing driving force, but instead exhibits a pronounced maximum near 2.0 V, described as the "inverted region". We interpret this behavior as resulting from a competition between IL EDL screening and electrochemical nanofilament growth. Time-dependent analysis of formation current over hundreds of formation events reveals two types of growth dynamics—abrupt and gradual. Gradual dynamics are observed at ≈1.8 V representing the threshold where EDL formation begins to interfere with nanofilament growth, changing it from abrupt to gradual. Here, multiple resistance states can be accessed within a single nanofilament, due to the gradual growth. The voltage-dependent dynamics are also correlated with filament structure: nanofilaments formed in the inverted region have more lateral and diffuse structures than those formed outside the voltage window. The results suggest that by tuning the competition between the IL EDL and electrochemistry, the growth dynamics and nanofilament morphology can be tuned. This control mechanism could potentially be exploited in applications such as artificial neural networks, where multiple, distinguishable resistance states are required. Further optimization of this electrolyte is expected to extend the accessible range of resistance states to smaller write/read biases, making the PEGDA/IL electrolyte a highly customizable system and potential candidate for organic electronics requiring low-power neuromorphic computing operation.

4. Experimental Section

Sample Preparation for C-AFM Measurements: PEGDA (Mn = 2000), $[BMIM]PF_6$ (≥98.5%), 2-Hydroxy-2-methylpropiophenone (HMPP, 97%), and anhydrous acetonitrile (ACN, 99.8%) were purchased from Sigma–Aldrich. All reagents were used as received without further purification. Silicon wafers (University Wafer, P/Boron, 500 ± 15 µm) were cleaned by sonication in acetone followed by a 2-Propanol rinse and N_2 blow dry. 5 nm/100 nm of Ti/Ag were deposited by electron-beam evaporation at 5×10^{-7} mbar base pressure (Plassys, MEB 550 S). The following steps were completed inside an argon-filled glovebox (Mbraun, MB-200B) where O_2 and H_2O < 1 ppm. $[BMIM]PF_6$ (IL) and PEGDA were dissolved in ACN and combined to prepare a total of three samples with PEGDA/$BMIMPF_6$ compositions of 60/40, 65/35, and 70/30 wt%. In all three samples, the PEGDA concentration was 1 wt% together with 0.02 wt% of HMPP (photoinitiator). The polymer electrolytes were spin-coated on the Ag-coated silicon substrate at 4000 rpm for 30 s and annealed at 80 °C for 2 min to drive-off ACN. Samples were photo-crosslinked with a UV lamp (UVP Compact UV Lamp, λ = 365 nm, P = 1.3 mW cm^{-2} at 3 in.) at a working distance of 0.5 in. for 1 h.

C-AFM Characterization: A Bruker Dimension Icon AFM was operated in contact mode using a C-AFM tip (SCM-PIT-V2, Pt-Ir coating, k = 4.0 N m^{-1}). A custom script was created to modulate the location and potential applied to the tip to: 1) move the tip from point-to-point in a raster scan pattern at a preset spacing; 2) apply the desired voltage; and 3) measure the current between the C-AFM tip and the chuck. The AFM tip was grounded, and the voltage was applied to the chuck. Electrical contact was made between the AFM stage and the Ag layer of the substrate using copper tape (McMaster-Carr). At each point, the chuck voltage was set to a positive formation voltage until either 1) the current increased above a set formation current threshold for two consecutive data points (2 ms) to ensure nanofilament formation while avoiding overgrowth, or 2) the maximum time window was reached, indicating no formation. In either case, the voltage was then switched to a dissolution voltage of –0.5 V until the current (now of the opposite sign) either 1) decreased in magnitude below a set threshold, or 2) reached the maximum dissolution time window meaning that the nanofilament did not dissolve. Formation and dissolution current thresholds were chosen as +4.0 and –0.5 nA, respectively, and both the maximum formation and dissolution time windows were set at 50 s. The compliance current of the instrument is ca. 5 nA at a current sensitivity of 1 nA V^{-1}, which is selected by the user.

In this work, electrolytes with IL concentrations of 30, 35, and 40 wt% were focused. This IL concentration range was chosen because they have faster formation kinetics compared to 50 wt% IL, and a more homogeneous structure (i.e., less obvious crystal features) compared to a 10 wt% IL sample.[17] The thickness of the 35 wt% IL was ≈40 nm by focused ion beam (FIB)-SEM (Figure 7), and the 30 and 40 wt% IL samples were expected to be of similar thickness as our previous report indicated no thickness variations in the range of 10 to 50 wt% IL.[17]

Silver nanofilament formation times were measured over a bias range from 0.7 to 3.0 V, with ≈100 nanofilament formation events captured at ≈5 distinct regions on each sample for a total of 500 measurements. Within each region, nanofilaments were formed and dissolved at different locations forming a square array with a pitch of 1.2 µm.

Characterization of Silver Nanofilament Structures: Arrays containing 25 nanofilaments were formed over 4.8 × 4.8 µm squares on the 65/35 PEGDA/IL wt% sample using four different biases (0.7, 1.4, 2.1, and 3.0 V). A FIB (FEI Scios DualBeam) was used to create the cross-section of PEGDA/IL film at locations that contained nanofilaments, and SEM (FEI Scios DualBeam) was used to image the cross-section.

Supporting Information

Supporting Information is available from the Wiley Online Library or from the author.

Acknowledgements

This work was supported, in part, by DARPA grant FA8650-15-C-7546. Z.C., K.X., and S.F.S. also acknowledge fellowships from PPG Industries and the University of Pittsburgh Swanson School of Engineering. G.C. was supported by a NASA Space Technology Research Fellowship (NNX16AM45H).

Conflict of Interest

The authors declare no conflict of interest.

Keywords

electric double layer, ionic liquid, neuromorphic computing, polymer electrolyte, silver nanofilament

Received: September 25, 2019
Revised: October 31, 2019
Published online:

[1] A. Fang, T. Koschny, C. M. Soukoulis, *Phys. Rev. B* **2009**, *79*, 245127.
[2] A. Poddubny, I. Iorsh, P. Belov, Y. Kivshar, *Nat. Photonics* **2013**, *7*, 948.
[3] S. S. Hong, J. J. Cha, Y. Cui, *Nano Lett.* **2011**, *11*, 231.
[4] M. Kund, G. Beitel, C. Pinnow, T. Rohr, J. Schumann, R. Symanczyk, K. Ufert, G. Muller, *IEEE InternationalElectron Devices Meeting, 2005, IEDM Technical Digest.*, IEEE, Washington DC, USA **2015**, pp. 754–757.
[5] I. Valov, R. Waser, J. R. Jameson, M. N. Kozicki, *Nanotechnology* **2011**, *22*, 254003.
[6] B. J. Choi, D. S. Jeong, S. K. Kim, C. Rohde, S. Choi, J. H. Oh, H. J. Kim, C. S. Hwang, K. Szot, R. Waser, B. Reichenberg, S. Tiedke, *J. Appl. Phys.* **2005**, *98*, 033715.
[7] R. Waser, M. Aono, *Nat. Mater.* **2007**, *6*, 833.
[8] W.-P. Lin, S.-J. Liu, T. Gong, Q. Zhao, W. Huang, *Adv. Mater.* **2014**, *26*, 570.
[9] Y. van de Burgt, A. Melianas, S. T. Keene, G. Malliaras, A. Salleo, *Nat. Electron.* **2018**, *1*, 386.
[10] H. S. Wong, S. Salahuddin, *Nat. Nanotechnol.* **2015**, *10*, 191.
[11] A. F. Visentin, S. Alimena, M. J. Panzer, *ChemElectroChem* **2014**, *1*, 718.
[12] A. F. Visentin, M. J. Panzer, *ACS Appl. Mater. Interfaces* **2012**, *4*, 2836.
[13] M. W. Schulze, L. D. McIntosh, M. A. Hillmyer, T. P. Lodge, *Nano Lett.* **2014**, *14*, 122.
[14] B. Rupp, M. Schmuck, A. Balducci, M. Winter, W. Kern, *Eur. Polym. J.* **2008**, *44*, 2986.
[15] W. Lu, A. G. Fadeev, B. Qi, E. Smela, B. R. Mattes, J. Ding, G. M. Spinks, J. Mazurkiewicz, D. Zhou, G. G. Wallace, D. R. MacFarlane, S. A. Forsyth, M. Forsyth, *Science* **2002**, *297*, 983.
[16] K. Rajan, A. Chiappone, D. Perrone, S. Bocchini, I. Roppolo, K. Bejtka, M. Castellino, C. F. Pirri, C. Ricciardi, A. Chiolerio, *RSC Adv.* **2016**, *6*, 94128.
[17] Z. Chao, B. P. Radka, K. Xu, G. M. Crouch, D. Han, D. B. Go, P. W. Bohn, S. K. Fullerton-Shirey, *Small* **2018**, *14*, 1802023.
[18] Q. Liu, S. Long, H. Lv, W. Wang, J. Niu, Z. Huo, J. Chen, M. Liu, *ACS Nano* **2010**, *4*, 6162.
[19] Y. Sun, C. Song, J. Yin, X. Chen, Q. Wan, F. Zeng, F. Pan, *ACS Appl. Mater. Interfaces* **2017**, *9*, 34064.
[20] T. Tsuruoka, K. Terabe, T. Hasegawa, M. Aono, *Nanotechnology* **2010**, *21*, 425205.
[21] T. Takuro, H. Tsuyoshi, T. Kazuya, N. Tomonobu, S. Toshitsugu, S. Hajime, K. Hisao, H. Sumio, A. Masakazu, *Jpn. J. Appl. Phys.* **2006**, *45*, L364.
[22] Y. Yang, P. Gao, S. Gaba, T. Chang, X. Pan, W. Lu, *Nat. Commun.* **2012**, *3*, 732.
[23] J. J. Yang, D. B. Strukov, D. R. Stewart, *Nat. Nanotechnol.* **2013**, *8*, 13.
[24] S. H. Kim, K. Hong, W. Xie, K. H. Lee, S. Zhang, T. P. Lodge, C. D. Frisbie, *Adv. Mater.* **2013**, *25*, 1822.
[25] W. Shi, J. Ye, Y. Zhang, R. Suzuki, M. Yoshida, J. Miyazaki, N. Inoue, Y. Saito, Y. Iwasa, *Sci. Rep.* **2015**, *5*, 12534.
[26] H.-M. Li, K. Xu, B. Bourdon, H. Lu, Y.-C. Lin, J. A. Robinson, A. C. Seabaugh, S. K. Fullerton-Shirey, *J. Phys. Chem. C* **2017**, *121*, 16996.
[27] J. A. Manzanares, S. Mafé, J. Bisquert, *Ber. Bunsen. Phys. Chem.* **1992**, *96*, 538.
[28] R. F. Hamou, P. U. Biedermann, A. Erbe, M. Rohwerder, *Electrochem. Commun.* **2010**, *12*, 1391.
[29] E. Schmidt, S. Shi, P. P. Ruden, C. D. Frisbie, *ACS Appl. Mater. Interfaces* **2016**, *8*, 14879.
[30] Y. Yang, P. Gao, L. Li, X. Pan, S. Tappertzhofen, S. Choi, R. Waser, I. Valov, W. D. Lu, *Nat. Commun.* **2014**, *5*, 4232.
[31] K. Krishnan, T. Tsuruoka, C. Mannequin, M. Aono, *Adv. Mater.* **2016**, *28*, 640.
[32] R. Islam, H. Li, P.-Y. Chen, W. Wan, H.-Y. Chen, B. Gao, H. Wu, S. Yu, K. Saraswat, H. S. Wong, *J. Phys. D: Appl. Phys.* **2019**, *52*, 113001.

ADVANCED FUNCTIONAL MATERIALS

Supporting Information

for *Adv. Funct. Mater.*, DOI: 10.1002/adfm.201907950

Silver Nanofilament Formation Dynamics in a Polymer-Ionic Liquid Thin Film by Direct Write

*Zhongmou Chao, Kutay B. Sezginel, Ke Xu, Garrison M. Crouch, Abigale E. Gray, Christopher E. Wilmer, Paul W. Bohn, David B. Go, and Susan K. Fullerton-Shirey**

Supporting Information

Silver Nanofilament Formation Dynamics in a Polymer-Ionic Liquid Thin Film by Direct-Write

*Zhongmou Chao, Kutay B. Sezginel, Ke Xu, Garrison M. Crouch, Abigale E. Gray, Christopher E. Wilmer, Paul W. Bohn, David B. Go, Susan K. Fullerton-Shirey**

1. Histograms of filament formation time

Filament formation times for the 65/35 PEGDA/IL wt% sample at different biases are binned into histograms in Figure S1. Filament formation events are measured at 500 different locations for each bias. Only 52% of filaments formed within 40 s at 0.5 V whereas 99.8% formed at 0.7 V. Thus, a formation bias of ≥ 0.7 V is required for formation to occur within a reasonable experimental time window (< 60 s). In addition, filament formation time distributions in the "inverted" region (2.0 to 2.1 V) are scattered over a broad range of time, whereas the distributions are skewed normal for most other biases. Histograms for 60/40 and 65/35 PEGDA/IL wt% samples exhibit behavior similar to the 70/30 wt% sample.

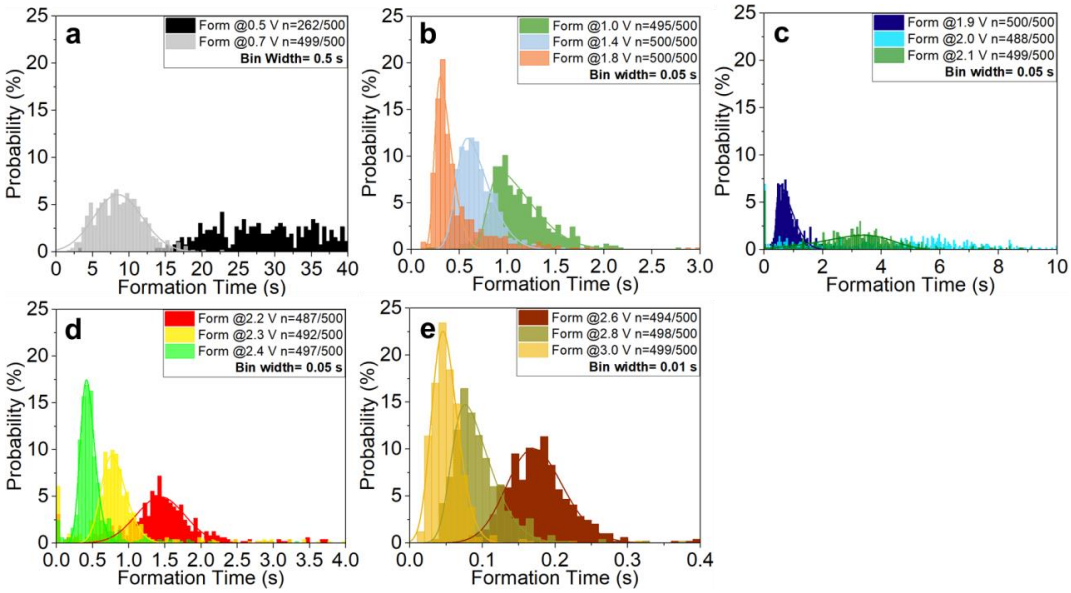

Figure S1. Filament formation time distributions at biases ranging from 0.5 to 3.0 V for the 70/30 PEGDA/IL wt% electrolyte. 500 formation measurements are conducted at distinct locations for each sample and each bias.

2. Nonzero initial current before filament formation

Figure S2 shows the current for the first 50 ms after applying a given formation bias on the 65/35 PEGDA/IL wt% sample. A positive, nonzero current quickly decays within 10 ms at potentials ≥ 1.4 V. This behavior is identical in form to the charging current associated with EDL formation in a parallel plate capacitor.[1]

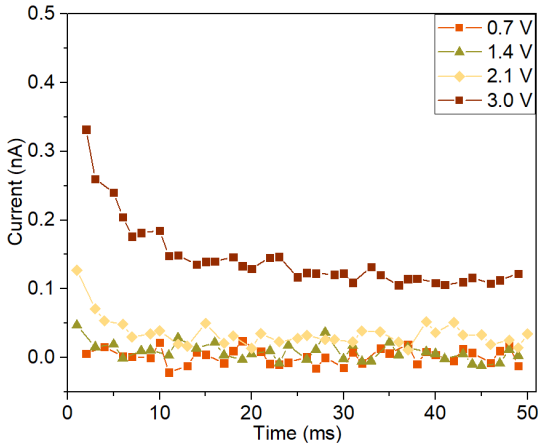

Figure S2. Example of current *versus* time for the first 50 ms after a formation bias is applied to the 65/35 PEGDA/IL wt% electrolyte.

3. Negative control on 100 wt% PEGDA sample

To eliminate IL EDL formation, a pure PEGDA sample was prepared on a gold substrate. Time-dependent current data were collected for 50 s at 0.7, 2.1 and 3.0 V. No current signal can be detected above the noise. This negative control measurement confirms that the current signal on the 65/35 PEGDA/IL wt% on gold (**Figure 4**) is due to the IL.

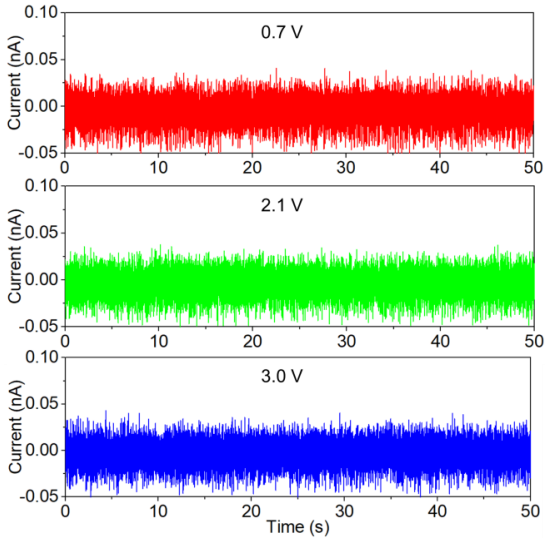

Figure S3. Current *vs.* time data after applying three biases for 50 s on the pure PEGDA sample.

4. Filament formation at 0.8 V read bias

The same sample and experimental setup in **Figure 6** were used, but instead of 2 s of read time, 0.8 V read bias was held for 100 s after filament reaching a 15 nA current compliance under 1.8 V. As shown in **Figure S4**, the time-dependent conductance suggests it takes about 100 s before filament conductance increasing abruptly to system compliance (125 nS, calculated using 100 nA system compliance current), indicating that a 0.8 V read voltage would only disturb the filament at a much longer times (50× longer than the read time in Figure 6). In addition, the abrupt growth at ~ 100 s and 0.8 V is consistent with the observed filament growth dynamics under low bias shown **Figure 5**.

The time scale of filament formation under 0.8 V in Figure S4 further suggests the 2 s read time used in Figure 6 is not likely to contribute appreciable Faradic current, and the relatively stable conductance between 1 - 100 s supports our claim that stable resistance states could be achieved over even longer times by further optimization.

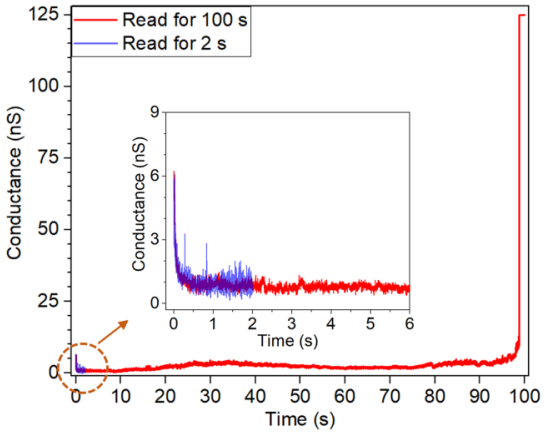

Figure S4. Time-dependent filament conductance data using a 0.8 V read bias after 15 nA program current was reached using 1.8 V write bias. Read times are kept for 100 s (red) and 2 s (blue, same data plotted in Figure 6 read 1). Data was collected at 10 nA/ V current sensitivity.

5. AFM mapping of filament array after formation

Regions containing 4 × 4 filaments formed at 2.1 V on the 65/35 PEGDA/IL wt% sample were imaged by conductive AFM (PeakForce TUNA), the imaging bias being set to +0.3 V to map the electrical conductivity. As shown in **Figure S5(a)**, the topography of the region containing filaments was significantly altered, resulting in large protrusions which agrees with SEM images in **Figure 7**. However, no current signal was detected (**Figure S5(b)**, mapping bias was set to 200 mV) indicating that the large structure is mostly confined below the polymer film, which is also confirmed by SEM cross-section imaging.

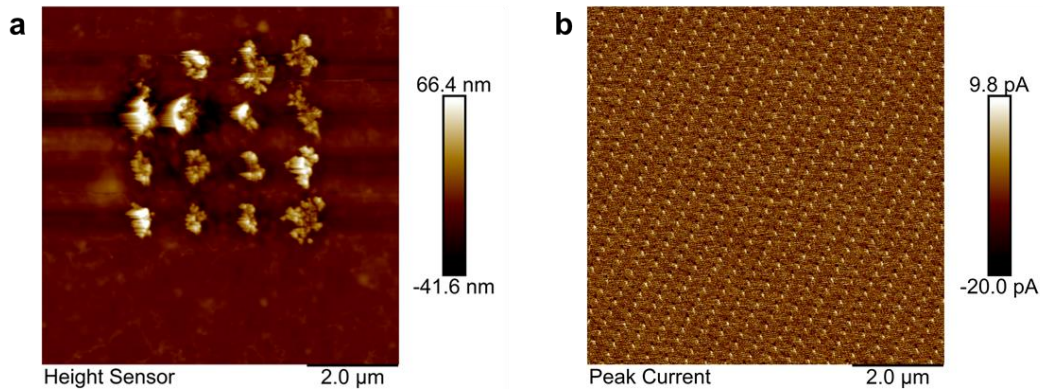

Figure S5. (a) AFM topography scan and **(b)** current mapping of the 65/35 PEGDA/IL wt% sample after filament formation in a 3.6 × 3.6 µm region (Bruker Dimension Icon, PeakForce TUNA).

6. Repeatability test on filaments formed at different formation biases

Repeated switching was tested using three different formation biases: 0.7, 1.8 and 3.0 V on 65/35 PEGDA/IL wt% sample, with the dissolution bias held constant at -0.5 V. The script was modified to test the repeated formation and dissolution at hundreds of different locations used the following protocol: 1) a positive bias was applied to form the filament; 2) -0.5 V was applied to dissolve the filament thereby completing one cycle and 3) the cycle was repeated for a user-defined number of cycles (notice that these switching measurements do not involve a "reset" where V = 0). For all three formation biases, a total of 500 filaments were tested at five regions separated by > 100 µm. Within each region, filaments were formed and dissolved for 20 cycles at 100 locations in a 12 × 12 µm array, with a pitch of 1.2 µm.

The average formation and dissolution times for all filaments at each cycle are plotted versus the number of cycles in **Figure S6**. In addition to formation and dissolution kinetics, the percentage of filaments that remain switchable after each cycle are also shown. The first reformation time (cycle = 1) is significantly shorter than the initial formation (cycle = 0) for all formation bias. This result is expected because initial formation requires the creation of a conductive pathway between the AFM tip and silver electrode, while reformation only "repairs" the portion of pathway that is broken by dissolution.

In contrast to formation, the time required to dissolve the filaments increases with the number of cycles and is especially noticeable at the 0.7 V formation bias (**Figure S6a**). When the dissolution time increases, there is a corresponding decrease in the number of switchable filaments remaining after 20 cycles. This correlation between dissolution times and switching failure is supported by the fact that almost all the failures can be attributed to dissolution not occurring within the timescale of the experiment (50 s). This is reasonable, because dissolution tends to occur at the weakest spot in filament, which will be repaired and further strengthened by repeated reformations after initial dissolution, making it harder to dissolve the filament. Even though at the 1.8 and 3.0 V formation biases almost all filaments remains switchable after 19 cycles, the dissolution time fluctuates over a larger timescale with increasing switching cycles as indicated by the larger error bars. We increased the number of cycles from 20 to 10000 (upper limit) and found the same result: the filaments formed at the lowest measured voltage (0.7 V) stop being switchable at a shorter number of cycles (averaging 36 repetitions for 100 filaments), followed by 3.0 V (averaging 93 repetitions for 100 filaments), while for the gradual type growth at 1.8 V, switching lasts for averaging 249 repetitions (from 100 filaments).

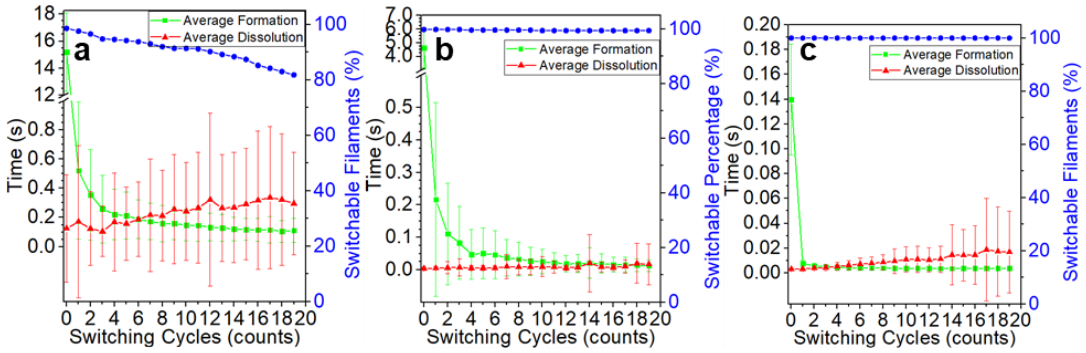

Figure S6. Average formation (green) and dissolution (red) times and percentage of switchable filaments (blue) *versus* cycle number for **(a)** 0.7 **(b)** 1.8 and **(c)** 3.0 V formation bias. Error bars represent one standard deviation from average. At each bias, filaments were formed and dissolved for 20 cycles at 100 locations in each region. Five regions were tested (separated by > 100 μm) for a total of 500 filaments.

7. Reformation current during filament repeatability test at 1.8 V

To explore the dynamics of filament re-formation at 1.8 V, filaments were formed again after dissolution at -0.5 V. Current *vs*. time data were acquired for 500 re-formation events from 500 filaments tested and are plotted in **Figure S7**. Here, the nucleation current, i_n, is 1 nA, and the nucleation time, t_n, when the current reached i_n is set to 0. Thus, we ignore nucleation and focus only on re-formation current in Figure S7. Similar to Figure 5, filaments reformed at 1.8 V also show gradual growth dynamics as indicated by the large density of data between i_n and i_f. This results suggests that like formation, switching is also gradual, which is a necessary criteria for neuromorphic computing.

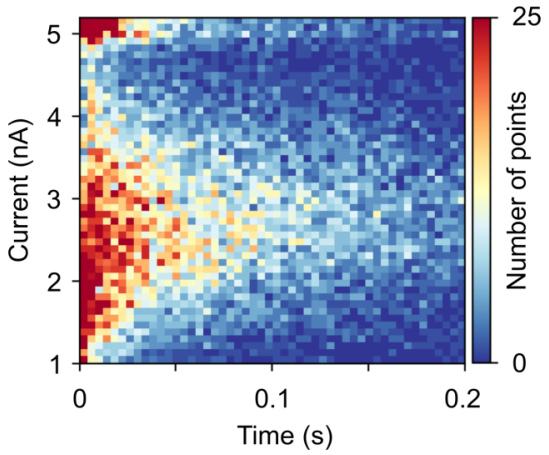

Figure S7. Time-dependent current during first filament re-formation at 1.8 V. Time = 0 represents the beginning of re-growth. Current versus time measurements for 500 filaments at five regions (separated by > 100 μm) are plotted, each filaments were formed and dissolved for 20 cycles at 100 locations in each region. Data density is represented by color, calculated by counting the number of data points in each bin. The plot contains 100 × 100 bins (scales of time and current are equally divided into 100 parts).

References

[1] Li, H.-M.; Xu, K.; Bourdon, B.; Lu, H.; Lin, Y.-C.; Robinson, J. A.; Seabaugh, A. C.; Fullerton-Shirey, S. K., *J. Phys. Chem. C* **2017,** *121* (31), 16996.

Appendix D

Publication #3 of 4

In this appendix the paper published in *Frontiers in Chemistry* [100] is attached.

frontiers in Chemistry

ORIGINAL RESEARCH
published: 10 April 2019
doi: 10.3389/fchem.2019.00216

Nanopore-Templated Silver Nanoparticle Arrays Photopolymerized in Zero-Mode Waveguides

Donghoon Han[1†], *Garrison M. Crouch*[2†], *Zhongmou Chao*[3†], *Susan K. Fullerton-Shirey*[3†], *David B. Go*[2,4†] *and Paul W. Bohn*[2,5*]

[1] Department of Chemistry, The Catholic University of Korea, Bucheon, South Korea, [2] Department of Chemical and Biomolecular Engineering, University of Notre Dame, Notre Dame, IN, United States, [3] Department of Chemical and Petroleum Engineering, University of Pittsburgh, Pittsburgh, PA, United States, [4] Department of Aerospace and Mechanical Engineering, University of Notre Dame, Notre Dame, IN, United States, [5] Department of Chemistry and Biochemistry, University of Notre Dame, Notre Dame, IN, United States

In situ fabrication of nanostructures within a solid-polymer electrolyte confined to subwavelength-diameter nanoapertures is a promising approach for producing nanomaterials for nanophotonic and chemical sensing applications. The solid-polymer electrolyte can be patterned by lithographic photopolymerization of poly(ethylene glycol) diacrylate (PEGDA)-based silver cation (Ag^+)-containing polyelectrolyte. Here, we present a new method for fabricating nanopore-templated Ag nanoparticle (AgNP) arrays by *in situ* photopolymerization using a zero-mode waveguide (ZMW) array to simultaneously template embedded AgNPs and control the spatial distribution of the optical field used for photopolymerization. The approach starts with an array of nanopores fabricated by sequential layer-by-layer deposition and focused ion beam milling. These structures have an optically transparent bottom, allowing access of the optical radiation to the attoliter-volume ZMW region to photopolymerize a PEGDA monomer solution containing AgNPs and Ag^+. The electric field intensity distribution is calculated for various ZMW optical cladding layer thicknesses using finite-element simulations, closely following the light-blocking efficiency of the optical cladding layer. The fidelity of the polyelectrolyte nanopillar pattern was optimized with respect to experimental conditions, including the presence or absence of Ag^+ and AgNPs and the concentrations of PEGDA and Ag^+. The self-templated approach for photopatterning high-resolution photolabile polyelectrolyte nanostructures directly within a ZMW array could lead to a new class of metamaterials formed by embedding metal nanoparticles within a dielectric in a well-defined spatial array.

Keywords: zero-mode waveguide, photopolymerization, solid-polymer electrolyte, recessed Ag ring electrode, nanopore array

OPEN ACCESS

Edited by:
James Rohan,
University College Cork, Ireland

Reviewed by:
Wook Ahn,
Soonchunhyang University, South Korea
Zheng Chen,
University of California, San Diego, United States

***Correspondence:**
Paul W. Bohn
pbohn@nd.edu
orcid.org/0000-0001-9052-0349

†Donghoon Han
orcid.org/0000-0003-1870-3006
Garrison M. Crouch
orcid.org/0000-0002-0056-5269
Zhongmou Chao
orcid.org/0000-0002-9882-4440
Susan K. Fullerton-Shirey
orcid.org/0000-0003-2720-0400
David B. Go
orcid.org/0000-0001-8948-1442

Specialty section:
This article was submitted to Electrochemistry, a section of the journal Frontiers in Chemistry

Received: *22 January 2019*
Accepted: *19 March 2019*
Published: *10 April 2019*

Citation:
Han D, Crouch GM, Chao Z, Fullerton-Shirey SK, Go DB and Bohn PW (2019) Nanopore-Templated Silver Nanoparticle Arrays Photopolymerized in Zero-Mode Waveguides. Front. Chem. 7:216. doi: 10.3389/fchem.2019.00216

INTRODUCTION

The increasing utilization of micro- and nanostructured devices in chemical sensing and nanophotonic applications has created a need for precise spatial, temporal, and geometric control over the formation of nanoscale systems. For example, solid-polymer electrolytes, a particularly interesting class of materials due to potential applications in batteries and actively configurable systems, have been utilized in memory devices based on resistive switching (Lin et al., 2014). Further, active control of conductive filament formation and dissolution in solid electrolytes may provide the foundation for a new class of metamaterials with reconfigurable optical properties, especially when combined with arrays of metal nanoparticles embedded in the dielectric host. Previously, we demonstrated actively reconfigurable constructs based on solid-polymer electrolyte-based nanoelectrochemical systems for the formation and dissolution of metal conductive filaments in polyethylene oxide (PEO)-based (Wu et al., 2011; Crouch et al., 2017) and poly(ethylene glycol) diacrylate (PEGDA)-based (Chao et al., 2018) electrolytes. In addition, polymer electrolytes formed by photopolymerization of polyethylene glycol (PEG)-based electrolyte have been utilized for various biomaterials and biomedical applications (Mellott et al., 2001; Burdick and Anseth, 2002; Aimetti et al., 2009; Huebsch et al., 2014; DeForest and Tirrell, 2015). Several methods have been introduced to fabricate miniaturized polymer electrolyte features, including molding (Terray et al., 2002; Fairbanks et al., 2009), printing (DeForest and Anseth, 2012), and lithography (Jang et al., 2007). Combined with patterning of polymer electrolyte composites, *in situ* polymer electrolyte photolithography can be used to determine the spatial composition pattern, e.g., molecular weight, degree of cross-linking, in a polymer electrolyte, in addition to physical shape (Bong et al., 2010; Wu et al., 2015). All of these techniques provide degrees of micro- and nanoscale control over polymer electrolyte's physical/chemical properties, and geometric resolution of micro- and nanostructures on multiple length scales.

Photopolymerization is an attractive technique as it provides unparalleled spatial and temporal control over polymer electrolyte spatial composition patterns and fabrication characteristics. Diacrylate-based polymers are particularly appealing in this context, since they exhibit exceptional transparency, color variation, robust mechanical properties, and elasticity (Mark, 2013). Acrylates can be chemically cross-linked to form polymer electrolytes for a variety of applications and are widely used in industrial chemical processes as adhesives, sealant composites, and protective coatings (Mark, 2013). In contrast to other monomers, acrylates are attractive due to their biocompatibility, semi-permeability, and chemical versatility, allowing modification with a range of mono- or multifunctional moieties (Burkoth and Anseth, 2000; Metters et al., 2000). Of specific importance to the current studies, acrylate-based polymers can controllably produce cross-linked networks *via* photopolymerization (Yu et al., 2001). To exploit these useful characteristics, polyethylene glycol (PEG)-based photo-crosslinkable polymers, based upon acrylate polymerization chemistries, have been developed (Sawhney et al., 1993; Nguyen and West, 2002).

Photoinitiated polymerization of acrylates is typically performed in the presence of a photo-initiator (PI) which generates free radicals upon exposure to UV light. Photopolymerizable acrylates are typified by poly(ethylene glycol) diacrylate (PEGDA), an ion-conducting polymer (Yang et al., 2006) frequently used in biological applications (Shu et al., 2004). It provides design flexibility, because the material can start at low-viscosity and be converted to a high-viscosity solid simply by exposing it to light. In the current work, this property could support the precise positioning of metal nanoparticles, by first placing them in a liquid-like environment, after which the metal nanoparticles are locked into place by simple UV exposure.

Placement of well-defined metallic nanostructures within a dielectric material allows the optical properties of the composite material to be tailored, potentially achieving responses not possible in a single-component material (Oldenburg et al., 1998; Prasad, 2004; Rill et al., 2008; Shukla et al., 2010a,b). This capability is most notably exploited in the rapidly advancing field of metamaterials—composite materials that exhibit unusual optical and electromagnetic properties such as a negative refractive index (Smith et al., 2004; Kuwata-Gonokami et al., 2005; Furlani and Baev, 2009b). The unique properties of metamaterials arise from the engineered electromagnetic/optical response of subwavelength structures, for example well-defined nanoporous metallic arrays, rather than the intrinsic properties of the constituent materials. These metamaterials hold promise for various applications such as far-field subwavelength imaging, nanoscale optical trapping, ultracompact waveguides, and optical power limiting (Baev et al., 2007; Furlani and Baev, 2009a). Most experimentally-realized metamaterials have been fabricated by "top-down" lithography techniques, usually either e-beam lithography (EBL) or focused-ion-beam lithography (FIBL) (Kuwata-Gonokami et al., 2005; Lee et al., 2008; Rill et al., 2008; Henzie et al., 2009). Although powerful, these serial, direct-write approaches are not amenable to large-area patterning. Another approach to metamaterials involves laser direct-writing in a polymeric structure followed by metal deposition onto the fabricated surface (Shukla et al., 2010b). Although this method is promising, full metal coverage is challenging. Thus, new fabrication methods are needed.

Here we present a new approach for the fabrication of PEGDA-based solid-polymer electrolyte nanopillars constructed from silver nanoparticles (AgNPs) templated within recessed Ag ring electrode arrays. Importantly, the Ag ring electrodes are bifunctional, serving as the optical cladding layer in zero-mode waveguides (ZMWs) during fabrication while retaining the capability to serve as working electrodes for electrochemical tuning of the array in future applications. As ZMWs, the metal layers control the spatial distribution of optical radiation used in photopolymerization and, consequently, the distribution of cross-linked PEGDA photopolymer. This approach can significantly simplify the fabrication of PEGDA solid-polymer electrolyte arrays and provide a viable route to the fabrication of three-dimensional metamaterials by photopolymerization.

Metamaterials can be realized by embedding AgNPs in a well-defined dielectric-embedded nanopore array, where the optical properties can be tuned by adjusting the number of AgNPs, the inter-pore spacing, or both. Here, we explore the controlled fabrication of ZMW nanopore-templated photopolymerization of AgNP-containing PEGDA polymeric structures. This study indicates that: (1) metal ZMW arrays may be used to template the nanopillars for the polymerization process; (2) the ZMW can be tuned to control the spatial distribution of the confined optical field and, thus, of the photopolymerization process; and (3) these properties can be realized in the presence of nanopore-embedded AgNPs and Ag^+ ions in the electrolyte.

MATERIALS AND METHODS

Chemicals

Anhydrous acetonitrile (ACN), silver nitrate ($AgNO_3$), sulfuric acid (95%), hydrogen peroxide (30%), fluorescein 5(6)-isothiocyanate (FITC), and 2-hydroxy-4′-(2-hydroxyethoxy)-2-methylpropiophenone photoinitiator (PI) were obtained from Sigma-Aldrich. Silver nanoparticles (AgNPs, 50 nm size, 5 kDa PEG capped) were purchased from nanoComposix. Poly(ethylene glycol) diacrylate (PEGDA) with number average molecular weight $M_N = 700$ was purchased from Sigma-Aldrich. Cleanroom-cleaned glass coverslips (Glass D, 75 x 25 mm, 1.0 mm thick) were obtained from Schott Nexterion. All reagents were used as received.

Fabrication of ZMW Arrays

The nanopore arrays were fabricated via a combination of standard photolithography, layer-by-layer deposition, and focused ion beam (FIB) milling. The primary processing steps are shown in **Figure 1A**. Glass slides were cleaned in piranha solution (3:1 sulfuric acid (95%):hydrogen peroxide (30%)—*Caution—Strong oxidizer, use with extreme care*), rinsed with deionized (DI) water, and dried at 120°C. A 5 nm thick Au layer was deposited by electron-beam evaporation (UNIVEX 450B, Oerlikon) after deposition of a 5 nm Ti adhesion layer. Then, a 20 nm Ag film was e-beam evaporated onto the same glass slide, after which a 150 nm thick SiN_x layer was deposited by plasma-enhanced chemical vapor deposition (PECVD 790, Plasma-Therm). Finally, an additional 50 nm thick Cr layer was deposited on the substrate. A dual-source FIB instrument (Helios Nanolab 600, FEI Corp.) was used for milling and characterization. Nanopore arrays were patterned in a 20 × 20 μm square array with a lattice spacing of 500 nm, shown in **Figures 1B,C**. FIB milling was performed at 30 kV acceleration, 0.28 nA ion aperture, and 0.1 ms dwell time to produce the recessed dual-ring electrode (RDRE) array. These FIB-milled pores exhibit a conical frustum shape with typical top diameter, d_{top}∼140–160 nm, and bottom diameter, d_{bottom}∼60–80 nm. Although milled under nominally identical conditions, small sample-to-sample variations in pore geometry were observed.

Photopolymerization of PEGDA Solution

In an argon-filled glovebox with oxygen and water concentrations controlled to <0.1 ppm, 10 and 20 mM solutions of $AgNO_3$ in anhydrous ACN were prepared. Similarly, PEGDA was dissolved in ACN to make 0.5, 1, 2, and 3 wt% PEGDA solutions, each adjusted to 1 mM of PI. To purify the AgNPs, 1,000 μL of 50 nm AgNPs was centrifuged at 10,000 rpm for 30 min (microcentrifuge RS-200, REVSCI); then the solvent was decanted, and the AgNPs were resuspended in 100 μL ACN. The AgNPs and $AgNO_3$ solution were added to the PEGDA + PI solutions in a 1:1:8 volume ratio, yielding final solutions of $AgNO_3$ in ACN with concentrations of 1 and 2 mM for PEGDA concentrations of 0.5, 1, 2, and 3 wt%, respectively. Fifty microliter of each solution was then dropcast onto the nanopore array inside the glovebox. The PEGDA-coated nanopore array was exposed to UV light (405 nm) with an intensity of 14 mW cm^{-2} for 30 min in the cleanroom. Next, the nanopore array was washed with ACN and dried in filtered air.

Fluorescence Measurements

Fluorescence measurements were performed on an Olympus IX71 wide-field epi-illumination microscope. Radiation from a 488 nm laser was passed through an excitation filter (Chroma Z488/10X), and defocused to illuminate an area *ca*. 100 × 100 μm on the Cr side of the sample to directly excite fluorescence of FITC molecules in the nanopores. The fluorescence was collected by a 100× NA 1.4 oil-immersion objective, and projected onto a 512 × 512 pixel CCD camera (Andor Technology Ltd). A dichroic mirror (Chroma Z488RDC) and emission filter (Chroma HQ525/50 m) were used to separate excitation from emission radiation.

Modeling and Calculations

Finite element simulations were performed using COMSOL Multiphysics version 5.3. The simulations were performed over a two-dimensional domain representing the geometry and dimensions of the zero-mode waveguides employed in our experiments (Han et al., 2017). We used the "Electromagnetic Waves" physics of COMSOL in a frequency domain mode to obtain the excitation field inside a ZMW. A free triangular mesh was used with "Extremely fine" resolution and refinement applied to the ZMW layer. The ZMW was represented by a single pore, consisting of an adhesion layer (Ti, $h = 5$ nm), a second adhesion layer (Au, $h = 5$ nm), an optical cladding layer (Ag, $h = 20$, 50, and 100 nm), a dielectric layer (SiN_x, $h = 150$ nm), and a top layer (Cr, $h = 50$ nm). A perfectly matched layer was incorporated in the glass substrate component to cancel any reflection artifacts from the simulation boundaries. The complex refractive indices of Ti (Werner et al., 2009), Au (Olmon et al., 2012), Ag (Werner et al., 2009), and Cr (Johnson and Christy, 1974) were taken as $n = -5.74 + i4.4$, $-1.14 + i6.1$, $-4.70 + i2.5$, and $-4.13 + i11.8$, respectively. The refractive indices of water, glass, and SiN_x were taken to be 1.33, 1.45, and 2.016, respectively. Excitation radiation at 405 nm wavelength, consistent with the UV aligner, was simulated to irradiate the bottom of the glass module, arriving perpendicular to the plane of the structure.

RESULTS AND DISCUSSION

Characterization of ZMW Devices

ZMW arrays with 500 nm inter-pore spacing were fabricated to form square arrays consisting of annular apertures of sacrificial

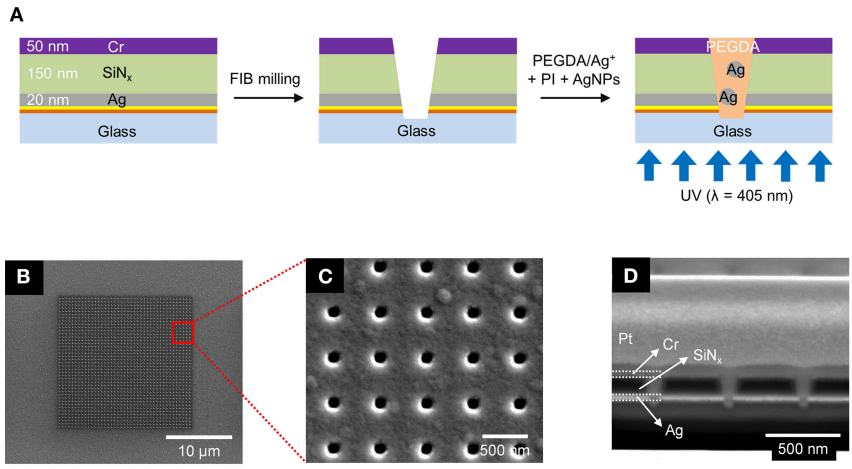

FIGURE 1 | (A) Schematics of the fabrication process for the photopolymerized ZMW array. **(B–D)** Scanning electron micrographs of a nanopore array at different magnifications and perspectives. **(B)** Top-down view of the entire 20 × 20 μm nanopore array. **(C)** Top-down view of a 5 × 5 subset of the same array. **(D)** Cross sectional SEM image of the nanopores taken at 52° tilt.

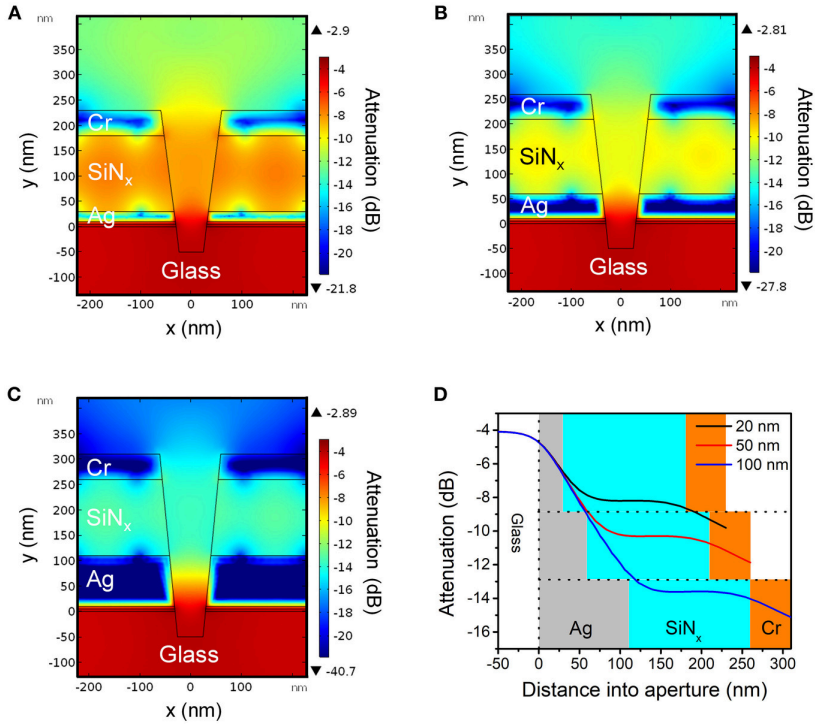

FIGURE 2 | Cross-sectional heat maps of evanescent field amplitudes in conical nanopores obtained by finite element simulations for Ag layer thicknesses of **(A)** 20 nm, **(B)** 50 nm, and **(C)** 100 nm, respectively. For all cases, bottom aperture of the nanopore structure had a diameter of d_{bottom} = 70 nm and the top aperture was determined by the ratio d_{top}/d_{bottom} = 2. **(D)** Simulated attenuation of energy density along the central axis of the ZMW for different thicknesses of Ag as indicated in the legend. Area shading corresponds to the material surrounding the opening: gray (Ag), blue (SiN_x), orange (Cr).

layer(Cr)-insulator(SiN_x)-metal layer(Ag). In these recessed Ag ring electrode nanopore stacks, the Ag layer can be electrically connected and used as an electrode for electrochemical experiments. **Figure 1A** illustrates the fabrication process using standard photolithography, layer-by-layer deposition, and FIB milling to produce nanopore recessed Ag ring electrode arrays.

This simple direct-write approach enables direct fabrication of precise nanopore structures exhibiting conical frustum shapes in contrast to the cylindrical nanopores obtained using electron beam (Dawson et al., 2012; Kleijn et al., 2012) or nanosphere lithography (Fu et al., 2018). Cylindrical pore shapes would likely result in minor alterations to the concentration parameters required for optimal pore filling due to changing in polymer wetting behavior, and the extent to which the photocrosslinking radiation can penetrate the pore. **Figures 1B,C** show SEM images of the entire array with an interpore distance 500 nm, and **Figure 1D** shows a corresponding cross-section SEM image of typical pores produced by FIB milling. The overetched region below the Ag/glass interface typically decreases with pore diameter, and well-controlled milling processes yield pores overetched by $\leq$50 nm. From bottom to top, the cross-section image in **Figure 1D** shows the bottom Ag layer (bright), silicon nitride (black), and the sacrificial Cr layer (bright). The nanopore ZMWs exhibit a conical shape with a larger aperture at the top than at the bottom electrode. The typical diameter of the top of the pore (d_{top}) is ~140–160 nm, while the bottom diameter (d_{bottom}) is ~60–80 nm.

Effect of the Thickness of Ag Layer on UV Irradiation

The spatial distribution of the optical field, both within and external to the ZMWs, is important in determining the extent of photopolymerization that will occur within the nanopores. For wavelengths above the cutoff wavelength of the nanoaperture, λ_c, where $\lambda_c \sim 1.7\ d$ and d is the pore diameter, the evanescent field decays exponentially with distance at a rate that depends on the radius and diameter (Crouch et al., 2018). In addition, the light-blocking efficiency of the Ag optical cladding layer also depends on the thickness of Ag. Experimentally, photopolymerization of PEGDA within nanopores was accomplished with collimated UV radiation from a UV aligner irradiating the bottom (Ag ring) surface of the ZMW array, as shown schematically in **Figure 1A**. To assess the effectiveness of this strategy in the ZMW nanopores studied here, finite element simulations were performed for various Ag thicknesses.

Figures 2A–C show the electric field amplitudes in a series of conical frustum pores each having different Ag layer thicknesses (20, 50, and 100 nm, respectively), but with constant ratio $d_{top}/d_{bottom} = 2$. As **Figures 2A–C** illustrate, the field decays exponentially within the nanopore, and the nanostructures provide attenuation primarily determined by the thickness of the Ag optical cladding layer, with thinner Ag thicknesses leading to less attenuation. **Figure 2D** shows the attenuation of electromagnetic energy density inside apertures with different Ag layer thicknesses, where for the 20 nm Ag thickness (black line), the smallest energy attenuation is predicted, confirming the thickness-dependent attenuation. These results indicate that thinner Ag thicknesses provide less optical field confinement and, thus, should lead to more

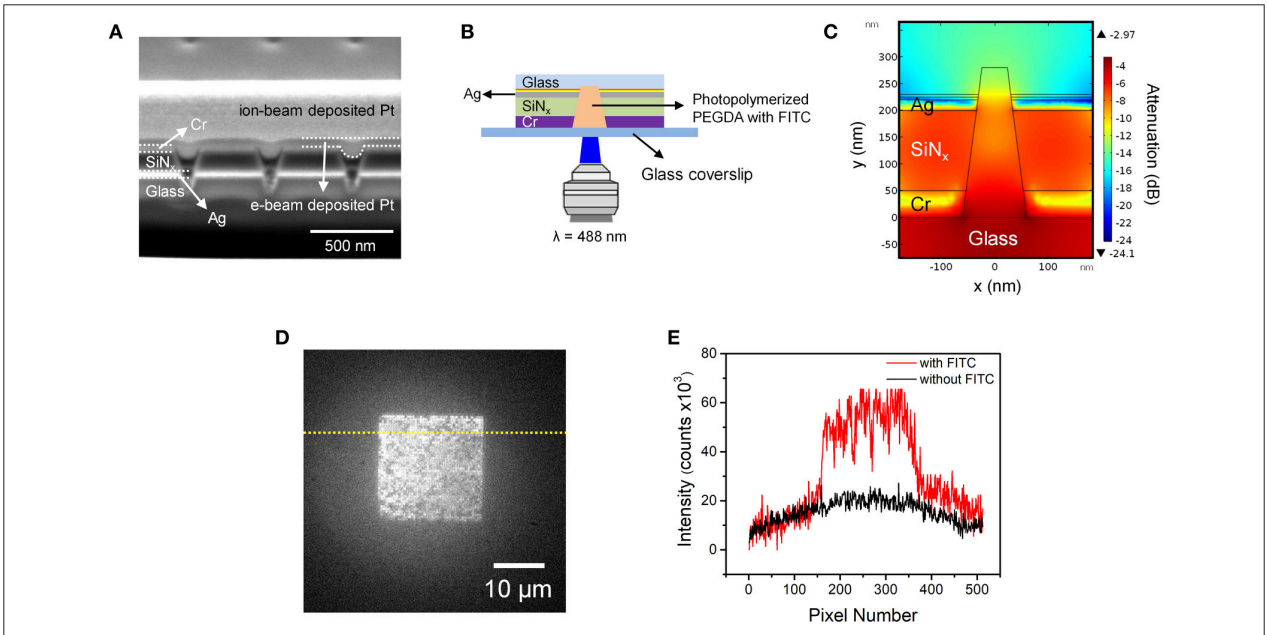

FIGURE 3 | (A) Cross-sectional SEM image of photopolymerized PEGDA-FITC in nanopores. Positions and identities of functional layers are indicated on the left, while positions of e-beam and ion-beam deposited Pt structural layers, used to obtain cross-sectional images, are indicated on the right. **(B)** Schematic diagram of the fluorescence epi-illumination geometry. In this geometry the ZMW region is distal from the illumination plane. **(C)** Cross-sectional heat map of optical field amplitude in a conical nanopore obtained from a finite element simulation. **(D)** Fluorescence micrograph of a nanopore array containing photopolymerized FITC-PEGDA in the nanopores. **(E)** Fluorescence intensity profiles obtained along the dotted lines shown in **(D)** with (red) and without (black) FITC.

spatially-extended PEGDA photopolymerization within the ZMW nanopores.

Characterization of Photopolymerized PEGDA in ZMW Devices

To further characterize the photopolymerization of PEGDA in ZMW nanopores, a fluorescent probe was added to the PEGDA monomer, and fluorescence was measured after photopolymerization. A 2.0 wt% solution of PEGDA monomer in ACN was prepared with 1 mM PI and 10 μM fluorescein isothiocyanate (FITC). The average number of fluorescent molecules occupying a single nanopore is given by $\langle n \rangle_{pore} = CVN_A$, where C is the FITC concentration, N_A is Avogadro's number, and V is the volume of the conical frustum of a single nanopore. For the 2.2 aL volume of the conical frustum nanopores used in these experiments, single molecule occupancy, $\langle n \rangle_{pore} = 1$ is expected at 0.75 μM, meaning that under the conditions of this experiment, $\langle n \rangle_{pore} \sim 13$. Before photopolymerization, the ZMW nanopores were filled with the PEDGA solution and allowed to equilibrate at room temperature for 10 min, after which the PEGDA-filled nanopore array was exposed to UV radiation from the aligner for 30 min. **Figure 3A** shows a cross-section SEM image of adjacent nanopores containing FITC.

Importantly, in this experiment the array was irradiated from the large diameter side of the conical nanopores, in the fluorescence epi-illumination geometry illustrated in **Figure 3B**. To confirm that the FITC can be effectively excited once inside the nanopore, finite element simulations were conducted for this inverted configuration. **Figure 3C** shows a cross-sectional heat map of energy intensity obtained from a simulation of a single conical nanopore, confirming its ZMW behavior. Importantly, there is little attenuation of energy intensity inside the nanopore and nearly the entire volume of the nanopore can be excited. The simulation provided confidence that fluorescent radiation can be collected from the upper (Cr) surface of the ZMW array in order to characterize the fluorescence response of the FITC within the photopolymerized PEGDA-filled nanopores.

Figure 3D shows a low magnification, wide-area fluorescence micrograph of the ZMW array. Although there is some variation in intensity among the individual nanopores, the overall image indicates significant incorporation of FITC-impregnated photopolymerized PEGDA in the individual nanopores. **Figure 3E** shows a fluorescence intensity line profile obtained along the dotted line in **Figure 3D**, both with and without FITC. This result clearly shows isolation and photoactivation of the polyelectrolyte with fluorescent probes in each pore.

Formation and Optimization of AgNPs Embedded in Polyelectrolyte Nanopore Array

Encouraged by the subwavelength control of the radial and axial field distributions provided by the ZMWs, we extended the fabrication of recessed Ag ring electrode array to include AgNPs and Ag^+ embedded in the photopolymerized PEGDA. In principle, AgNPs arrayed in the dielectric PEGDA could form the basis of a metamaterial, and the presence of Ag^+ would enable the electrochemical formation of nanofilaments connecting the AgNPs (Crouch et al., 2017; Chao et al., 2018). To understand the fabrication of nanopore-templated AgNPs embedded in PEGDA nanopillars, photopolymerization experiments were undertaken to investigate the influence of PEDGA concentration, Ag^+ concentration, and the presence or absence of AgNPs on the formation of solid-polymer electrolytes within the nanopore templates.

First, we tested the effect of PEGDA concentration in the presence of 1 mM $AgNO_3$ but without AgNPs under optimized conditions. **Figures 4A,B** show cross-sectional SEM images of a recessed Ag ring electrode array obtained after photoirradiation of 1.0 wt% and 3.0 wt% PEGDA with 1 mM $AgNO_3$, respectively. These concentrations were chosen to bracket the optimal conditions for PEGDA filling determined in initial tests, in which concentrations over 2.0 wt% PEGDA with 1 mM Ag^+ were found to yield the best filling behavior in the absence of AgNPs. Photopolymerized PEGDA was observed to fill the nanopore only to the Ag ring for the

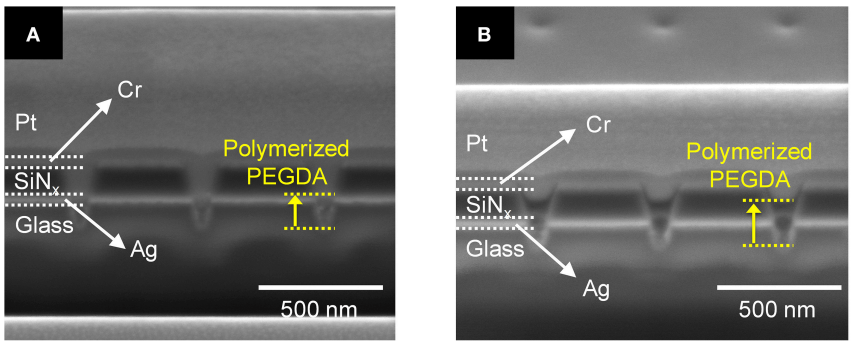

FIGURE 4 | Cross-sectional SEM images of **(A)** 1.0 wt% and **(B)** 3.0 wt% photopolymerized PEGDA with 1 mM $AgNO_3$ in a recessed Ag ring electrode array without AgNPs. The extent of the PEGDA photopolymer, after photopolymerization, is shown by the yellow dashed lines.

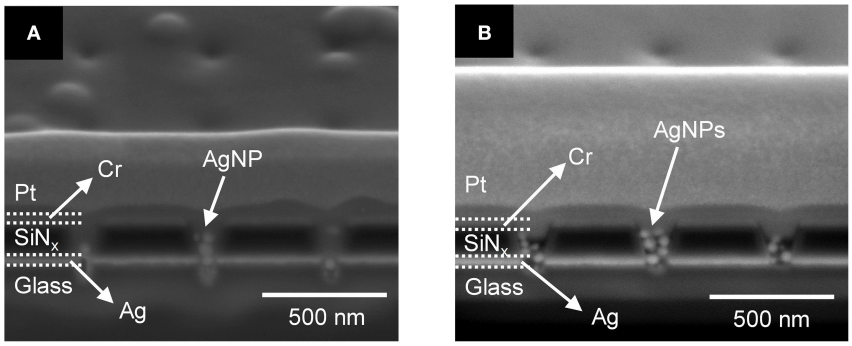

FIGURE 5 | Cross-section SEM images of 1.0 wt% photopolymerized PEGDA in a recessed Ag ring electrode array with embedded AgNPs containing **(A)** 2 mM and **(B)** 1 mM $AgNO_3$ salt.

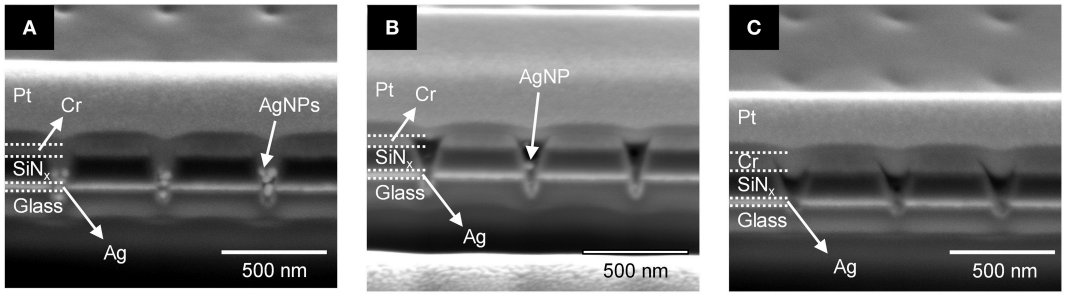

FIGURE 6 | Cross-sectional SEM images of photopolymerized polyelectrolyte in a recessed Ag ring electrode array with embedded AgNPs for different PEGDA concentrations: **(A)** 0.5 wt%, **(B)** 1.0 wt%, and **(C)** 2.0 wt%.

1.0 wt% monomer solution, but 3.0% PEGDA filled the nanopore up through the middle of the SiN_x layer, as shown in **Figure 4B**.

Silver ions in the PEGDA are required for subsequent direct-write nanofilament formation and dissolution between AgNPs (Crouch et al., 2017; Chao et al., 2018), so we also investigated how Ag^+ concentration affects the photopolymerization of PEGDA in the presence of AgNPs. **Figures 5A,B** show cross-sections of photopolymerized 1.0 wt% PEGDA with 2 mM $AgNO_3$ and 1 mM $AgNO_3$, respectively. Here, we included AgNPs in the PEGDA solution as opposed to the results in **Figure 4** with no AgNPs. At 2.0 mM, **Figure 5A**, some AgNPs can be observed in the nanopore, but there is little to no polymerized PEGDA. However, at 1 mM Ag^+ shown in **Figure 5B**, not only are individual stacked AgNPs observed, but they are in polymerized PEGDA. Surprisingly, comparison of **Figures 5A,B** shows that increasing the concentration of $AgNO_3$ inhibits polymer filling of the nanopores. Given the nanoscale dimensions of the pores, an electrostatic screening effect is plausible, however understanding the mechanism giving rise to this effect will require further detailed studies in which polymer electrolyte characteristics and nanopore surface charge are carefully controlled. Nevertheless, this serves as experimental verification that in the presence of AgNPs, Ag-containing PEGDA monomer can be UV cross-linked to form AgNPs nanopillars embedded in the polyelectrolyte inside the nanopores.

Given the above result, in which lower Ag^+ concentrations yield better fabrication of polymerized nanopillars, the photopolymerization behavior of PEGDA with AgNPs in a ZMW was also tested as a function of PEGDA concentration in the absence of Ag^+ (i.e., no $AgNO_3$). **Figure 6** shows cross-section SEM images of PEGDA photopolymerized from solutions with various concentrations of monomer in the presence of AgNPs, but without Ag^+. At the lowest concentration, 0.5 wt% PEGDA, **Figure 6A**, AgNPs fill the nanopore to the middle of the SiN_x insulator layer. Further increasing PEGDA concentration suppresses the number of AgNPs captured in the nanopore, *cf.* **Figures 6B,C**. One possible explanation is less physical crosslinking, which will decrease the likelihood of AgNP retention in the pore, although further experiments are needed to fully explore this interpretation. Interestingly, the PEGDA concentration dependence on pore filling is switched in the absence/presence of AgNPs. Higher PEGDA concentrations promote more extensive polymerization and therefore more pore filling in the absence of AgNPs, while lower PEGDA concentrations are more effective at pore filling when AgNPs are present. We tentatively

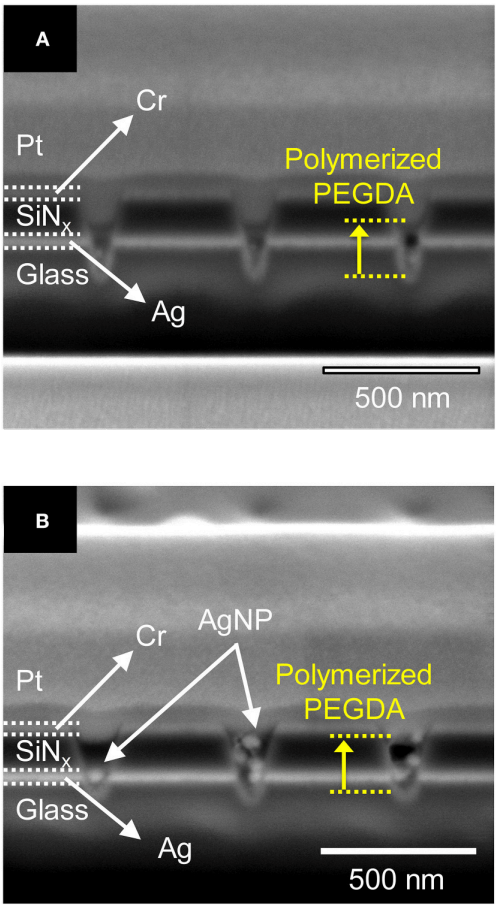

FIGURE 7 | Cross-section SEM image of 2.0 wt% photopolymerized PEGDA and 1 mM Ag^+ in a recessed Ag ring electrode array **(A)** without and **(B)** with embedded AgNPs.

assign this behavior to a volume-filling effect in the presence of AgNPs.

Based on the above parametric experiments, we asked whether it might be possible to determine a single set of conditions that would yield satisfactory PEGDA polymerization behavior both in the absence and presence of AgNPs. Thus, we experimentally tested a preparation of 2.0 wt% PEGDA monomer with 1 mM $AgNO_3$ salt in the presence and absence of AgNPs. The results shown in **Figure 7** illustrate that this formulation yields photopolymerized polyelectrolyte nanopillars inside ZMW nanopores either without, **Figure 7A**, or with, **Figure 7B**, AgNPs. The resulting structures were effectively cross-linked by UV light, thus immobilizing the polyelectrolyte in the ZMW arrays. In the presence of AgNPs, this procedure clearly yields a nanopore-templated array of AgNP-containing solid-polymer electrolyte structures that could form the basis of a reconfigurable metamaterial.

CONCLUSION

Templated pillars of AgNPs with nanometer-scale registration precision are of interest in nanophotonic and nanomanufacturing applications. Here, we describe a new fabrication strategy for producing ordered subwavelength arrays of AgNP nanopillars in PEGDA/Ag^+ polyelectrolyte, using a ZMW to control and shape the spatial distribution of the confined electromagnetic field and, therefore, the volume occupied by photopolymerized PEGDA. Both chemical and ZMW geometric effects on the fabrication process were characterized. The influence of the optical cladding layer thickness on the ZMW-directed photopolymerization predicted through finite-element simulations was found to agree with experiment. We determined that careful control of the structure was necessary and sufficient to achieve well-controlled PEGDA photopolymer volumes. In addition, we characterized the solution conditions needed to produce well-templated PEGDA either with or without AgNPs and therefore identified optimal conditions for the preparation of nanopore-templated AgNP nanopillar assemblies in PEGDA/Ag^+ polyelectrolyte. We believe that this approach employing *in situ* nanopore-templated fabrication of plasmonic and conductive nanostructures constitutes an exciting new platform for sequential formation/dissolution of nanofilaments through polyelectrolyte-confined nanopillar arrays of nanoparticles, thereby opening possible applications in actively reconfigurable metamaterials.

AUTHOR CONTRIBUTIONS

DG, SF-S, and PB designed the experiments. DH and GC performed the experiments. All authors contributed to analysis of the results, data analysis, and preparation of the final manuscript.

FUNDING

This work was supported by the Defense Advanced Research Projects Agency FA8650-15-C-7546. DH was supported by the National Research Foundation of Korea (NRF) grant funded by the Korea government (MSIT) 2018R1C1B5085888. GC was supported by NASA Space Technology Research Fellowship NNX16AM45H.

REFERENCES

Aimetti, A. A., Machen, A. J., and Anseth, K. S. (2009). Poly (ethylene glycol) hydrogels formed by thiol-ene photopolymerization for enzyme-responsive protein delivery. *Biomaterials.* 30, 6048–6054. doi: 10.1016/j.biomaterials.2009.07.043

Baev, A., Furlani, E. P., Samoc, M., and Prasad, P. N. (2007). Negative refractivity assisted optical power limiting. *J. Appl. Phys.* 102:043101. doi: 10.1063/1.2769144

Bong, K. W., Bong, K. T., Pregibon, D. C., and Doyle, P. S. (2010). Hydrodynamic focusing lithography. *Angew. Chem. Int. Ed.* 49, 87–90. doi: 10.1002/anie.200905229

Burdick, J. A., and Anseth, K. S. (2002). Photoencapsulation of osteoblasts in injectable RGD-modified PEG hydrogels for bone tissue engineering. *Biomaterials.* 23, 4315–4323. doi: 10.1016/S0142-9612(02)00176-X

Burkoth, A. K., and Anseth, K. S. (2000). A review of photocrosslinked polyanhydrides:: *in situ* forming degradable networks. *Biomaterials.* 21, 2395–2404. doi: 10.1016/S0142-9612(00)00107-1

Chao, Z., Radka, B. P., Xu, K., Crouch, G. M., Han, D., Go, D. B., et al. (2018). Direct-write formation and dissolution of silver nanofilaments in ionic liquid-polymer electrolyte composites. *Small.* 14:1802023. doi: 10.1002/smll.201802023

Crouch, G. M., Han, D., and Bohn, P. W. (2018). Zero-mode waveguide nanophotonic structures for single molecule characterization. *J. Phys. D.* 51:193001. doi: 10.1088/1361-6463/aab8be

Crouch, G. M., Han, D., Fullerton-Shirey, S. K., Go, D. B., and Bohn, P. W. (2017). Addressable direct-write nanoscale filament formation and dissolution by nanoparticle-mediated bipolar electrochemistry. *ACS Nano.* 11, 4976–4984. doi: 10.1021/acsnano.7b01657

Dawson, K., Wahl, A., Murphy, R., and O'Riordan, A. (2012). Electroanalysis at single gold nanowire electrodes. *J. Phys. Chem. C* 116, 14665–14673. doi: 10.1021/jp302967p

DeForest, C. A., and Anseth, K. S. (2012). Photoreversible patterning of biomolecules within click-based hydrogels. *Angew. Chem. Int. Ed.* 51, 1816–1819. doi: 10.1002/anie.201106463

DeForest, C. A., and Tirrell, D. A. (2015). A photoreversible protein-patterning approach for guiding stem cell fate in three-dimensional gels. *Nat. Mater.* 14:523. doi: 10.1038/nmat4219

Fairbanks, B. D., Schwartz, M. P., Halevi, A. E., Nuttelman, C. R., Bowman, C. N., and Anseth, K. S. (2009). A versatile synthetic extracellular matrix mimic via thiol-norbornene photopolymerization. *Adv. Mater.* 21, 5005–5010. doi: 10.1002/adma.200901808

Fu, K., Han, D., Kwon, S. R., and Bohn, P. W. (2018). Asymmetric nafion-coated nanopore electrode arrays as redox-cycling-based electrochemical diodes. *ACS Nano* 12, 9177–9185. doi: 10.1021/acsnano.8b03751

Furlani, E. P., and Baev, A. (2009a). Free-space excitation of resonant cavities formed from cloaking metamaterial. *J. Mod. Opt.* 56, 523–529. doi: 10.1080/09500340802582706

Furlani, E. P., and Baev, A. (2009b). Optical nanotrapping using cloaking metamaterial. *Phys. Rev. E* 79:026607. doi: 10.1103/PhysRevE.79.026607

Han, D., Crouch, G. M., Fu, K., Zaino, L. P. III., and Bohn, P. W. (2017). Single-molecule spectroelectrochemical cross-correlation during redox cycling in recessed dual ring electrode zero-mode waveguides. *Chem. Sci.* 8, 5345–5355. doi: 10.1039/C7SC02250F

Henzie, J., Lee, J., Lee, M. H., Hasan, W., and Odom, T. W. (2009). Nanofabrication of plasmonic structures. *Annu. Rev. Phys. Chem.* 60, 147–165. doi: 10.1146/annurev.physchem.040808.090352

Huebsch, N., Kearney, C. J., Zhao, X., Kim, J., Cezar, C. A., Suo, Z., et al. (2014). Ultrasound-triggered disruption and self-healing of reversibly cross-linked hydrogels for drug delivery and enhanced chemotherapy. *Proc. Natl. Acad. Sci. U.S.A.* 111, 9762–9767. doi: 10.1073/pnas.1405469111

Jang, J. H., Dendukuri, D., Hatton, T. A., Thomas, E. L., and Doyle, P. S. (2007). A route to three-dimensional structures in a microfluidic device: stop-flow interference lithography. *Angew. Chem. Int. Ed.* 46, 9027–9031. doi: 10.1002/anie.200703525

Johnson, P., and Christy, R. (1974). Optical constants of transition metals: Ti, V, Cr, Mn, Fe, Co, Ni, and Pd. *Phys. Rev. B* 9:5056. doi: 10.1103/PhysRevB.9.5056

Kleijn, S. E., Yanson, A. I., and Koper, M. T. (2012). Electrochemical characterization of nano-sized gold electrodes fabricated by nano-lithography. *J. Electroanal. Chem.* 666, 19–24. doi: 10.1016/j.jelechem.2011.11.022

Kuwata-Gonokami, M., Saito, N., Ino, Y., Kauranen, M., Jefimovs, K., Vallius, T., et al. (2005). Giant optical activity in quasi-two-dimensional planar nanostructures. *Phys. Rev. Lett.* 95:227401. doi: 10.1103/PhysRevLett.95.227401

Lee, K.-S., Kim, R. H., Yang, D.-Y., and Park, S. H. (2008). Advances in 3D nano/microfabrication using two-photon initiated polymerization. *Prog. Polym. Sci.* 33, 631–681. doi: 10.1016/j.progpolymsci.2008.01.001

Lin, W. P., Liu, S. J., Gong, T., Zhao, Q., and Huang, W. (2014). Polymer-based resistive memory materials and devices. *Adv. Mater.* 26, 570–606. doi: 10.1002/adma.201302637

Mark, H. F. (2013). *Encyclopedia of Polymer Science and Technology, Concise*. New York, NY: John Wiley and Sons.

Mellott, M. B., Searcy, K., and Pishko, M. V. (2001). Release of protein from highly cross-linked hydrogels of poly (ethylene glycol) diacrylate fabricated by UV polymerization. *Biomaterials* 22, 929–941. doi: 10.1016/S0142-9612(00)00258-1

Metters, A. T., Bowman, C. N., and Anseth, K. S. (2000). A statistical kinetic model for the bulk degradation of PLA-b-PEG-b-PLA hydrogel networks. *J. Phys. Chem. B* 104, 7043–7049. doi: 10.1021/jp000523t

Nguyen, K. T., and West, J. L. (2002). Photopolymerizable hydrogels for tissue engineering applications. *Biomaterials.* 23, 4307–4314. doi: 10.1016/S0142-9612(02)00175-8

Oldenburg, S., Averitt, R., Westcott, S., and Halas, N. (1998). Nanoengineering of optical resonances. *Chem. Phys. Lett.* 288, 243–247. doi: 10.1016/S0009-2614(98)00277-2

Olmon, R. L., Slovick, B., Johnson, T. W., Shelton, D., Oh, S.-H., Boreman, G. D., et al. (2012). Optical dielectric function of gold. *Phys. Rev. B* 86:235147. doi: 10.1103/PhysRevB.86.235147

Prasad, P. N. (2004). *Nanophotonics.* New York, NY: John Wiley and Sons. doi: 10.1002/0471670251

Rill, M. S., Plet, C., Thiel, M., Staude, I., Von Freymann, G., Linden, S., et al. (2008). Photonic metamaterials by direct laser writing and silver chemical vapour deposition. *Nat. Mater.* 7:543. doi: 10.1038/nmat2197

Sawhney, A. S., Pathak, C. P., and Hubbell, J. A. (1993). Bioerodible hydrogels based on photopolymerized poly (ethylene glycol)-co-poly (alpha.-hydroxy acid) diacrylate macromers. *Macromolecules.* 26, 581–587. doi: 10.1021/ma00056a005

Shu, X. Z., Liu, Y., Palumbo, F. S., Luo, Y., and Prestwich, G. D. (2004). *In situ* crosslinkable hyaluronan hydrogels for tissue engineering. *Biomaterials.* 25, 1339–1348. doi: 10.1016/j.biomaterials.2003.08.014

Shukla, S., Baev, A., Jee, H., Hu, R., Burzynski, R., Yoon, Y.-K., et al. (2010a). Large-area, near-infrared (IR) photonic crystals with colloidal gold nanoparticles embedding. *ACS Appl. Mater. Interfaces.* 2, 1242–1246. doi: 10.1021/am100109f

Shukla, S., Kumar, R., Baev, A., Gomes, A., and Prasad, P. (2010b). Control of spontaneous emission of CdSe nanorods in a multirefringent triangular lattice photonic crystal. *J. Phys. Chem. Lett.* 1, 1437–1441. doi: 10.1021/jz100134y

Smith, D. R., Pendry, J. B., and Wiltshire, M. C. (2004). Metamaterials and negative refractive index. *Science.* 305, 788–792. doi: 10.1126/science.1096796

Terray, A., Oakey, J., and Marr, D. W. (2002). Fabrication of linear colloidal structures for microfluidic applications. *Appl. Phys. Lett.* 81, 1555–1557. doi: 10.1063/1.1503176

Werner, W. S., Glantschnig, K., and Ambrosch-Draxl, C. (2009). Optical constants and inelastic electron-scattering data for 17 elemental metals. *J. Phys. Chem. Ref. Data.* 38, 1013–1092. doi: 10.1063/1.3243762

Wu, C. Y., Owsley, K., and Di Carlo, D. (2015). Rapid software-based design and optical transient liquid molding of microparticles. *Adv. Mater.* 27, 7970–7978. doi: 10.1002/adma.201503308

Wu, S., Tsuruoka, T., Terabe, K., Hasegawa, T., Hill, J. P., Ariga, K., et al. (2011). A polymer-electrolyte-based atomic switch. *Adv. Funct. Mater.* 21, 93–99. doi: 10.1002/adfm.201001520

Yang, C.-M., Kim, H.-S., Na, B.-K., Kum, K.-S., and Cho, B. W. (2006). Gel-type polymer electrolytes with different types of ceramic fillers and lithium salts for lithium-ion polymer batteries. *J. Power Sources* 156, 574–580. doi: 10.1016/j.jpowsour.2005.06.018

Yu, Q., Nauman, S., Santerre, J., and Zhu, S. (2001). Photopolymerization behavior of di (meth) acrylate oligomers. *J. Mater. Sci.* 36, 3599–3605. doi: 10.1023/A:1017980523677

Conflict of Interest Statement: The authors declare that the research was conducted in the absence of any commercial or financial relationships that could be construed as a potential conflict of interest.

Appendix E

Publication #4 of 4

In this appendix the paper published in *ACS Applied Materials & Interfaces* [101] and its supporting information are attached.

ACS APPLIED MATERIALS & INTERFACES

Research Article

Cite This: ACS Appl. Mater. Interfaces 2019, 11, 35879−35887

www.acsami.org

Electric Double-Layer Gating of Two-Dimensional Field-Effect Transistors Using a Single-Ion Conductor

Ke Xu,*[,†,∥] Jierui Liang,[†,∥] Aaron Woeppel,[†] M. Eli Bostian,[†] Hangjun Ding,[†,‡] Zhongmou Chao,[†] James R. McKone,[†] Eric J. Beckman,[†,‡] and Susan K. Fullerton-Shirey*[,†,§]

[†]Department of Chemical and Petroleum Engineering, [‡]Mascaro Center for Sustainable Innovation, and [§]Department of Electrical and Computer Engineering, University of Pittsburgh, Pittsburgh, Pennsylvania 15260, United States

Supporting Information

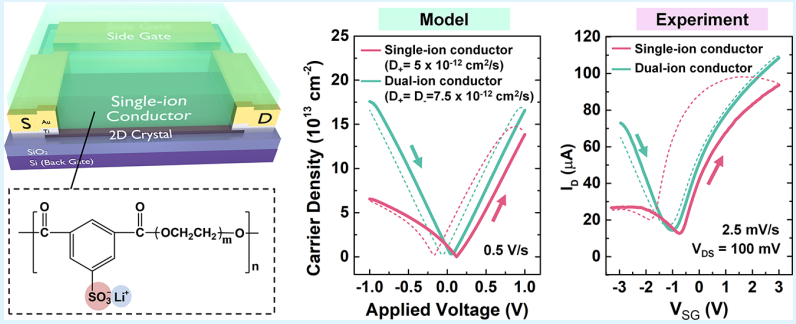

ABSTRACT: Electric double-layer (EDL) gating using a custom-synthesized polyester single-ion conductor (PE400-Li) is demonstrated on two-dimensional (2D) crystals for the first time. The electronic properties of graphene and $MoTe_2$ field-effect transistors (FETs) gated with the single-ion conductor are directly compared to a poly(ethylene oxide) dual-ion conductor (PEO:$CsClO_4$). The anions in the single-ion conductor are covalently bound to the backbone of the polymer, leaving only the cations free to form an EDL at the negative electrode and a corresponding cationic depletion layer at the positive electrode. Because the cations are mobile in both the single- and dual-ion conductors, a similar enhancement of the n-branch is observed in both graphene and $MoTe_2$. Specifically, the single-ion conductor decreases the subthreshold swing in the n-branch of the bare $MoTe_2$ FET from 5000 to 250 mV/dec and increases the current density and on/off ratio by two orders of magnitude. However, the single-ion conductor suppressed the p-branch in both the graphene and the $MoTe_2$ FETs, and finite element modeling of ion transport shows that this result is unique to single-ion conductor gating in combination with an asymmetric gate/channel geometry. Both the experiments and modeling suggest that single-ion conductor-gated FETs can achieve sheet densities up to 10^{14} cm^{-2}, which corresponds to a charge density that would theoretically be sufficient to induce several percent strain in monolayer 2D crystals and potentially induce a semiconductor-to-metal phase transition in $MoTe_2$.

KEYWORDS: *electric double layer, ion gating, two-dimensional, single-ion conductor, field-effect transistor, EDLT, iontronics*

INTRODUCTION

Similar to conventional semiconductor materials such as silicon,[1,2] the electrical and optical properties of two-dimensional (2D) crystals can be strongly influenced by strain. For example, strain can transform 2D semiconductors from indirect to direct band gap materials with enhanced radiative efficiencies[3] or tune the emission wavelength of the 2D crystals.[4,5] In addition, monolayer 2D transition-metal dichalcogenides (TMDs) such as Mo- and W-dichalcogenide van der Waals crystals are predicted to undergo a complete phase change from the semiconducting 2H phase to the metallic 1T′ under strain.[6,7] Experimentally, phase transitions in $MoTe_2$ have been demonstrated by inducing local strain using an atomic force microscope (AFM) tip[8] and more recently, by inducing global strain via an electric field applied to a ferroelectric substrate in contact with $MoTe_2$.[9] Dynamically tuning the band gap in 2D crystals is not only fundamentally interesting but could be useful for applications such as low-voltage transistors[10−12] and flexible electronics.[13,14] For these applications, it would be desirable to create a gate dielectric that can be deposited at low temperatures, achieve large gate capacitance (e.g., 1−4 $\mu F/cm^2$),[15,16] and induce strain locally via field effect.

To address this need, we propose a new concept: a single-ion conductor electric double-layer transistor (EDLT) based on 2D crystals. Our approach is unique compared with EDL gating with dual-ion conductors (i.e., those with mobile cations and anions), which are commonly used for electronic and

Received: July 1, 2019
Accepted: September 5, 2019
Published: September 5, 2019

DOI: 10.1021/acsami.9b11526
ACS Appl. Mater. Interfaces 2019, 11, 35879−35887

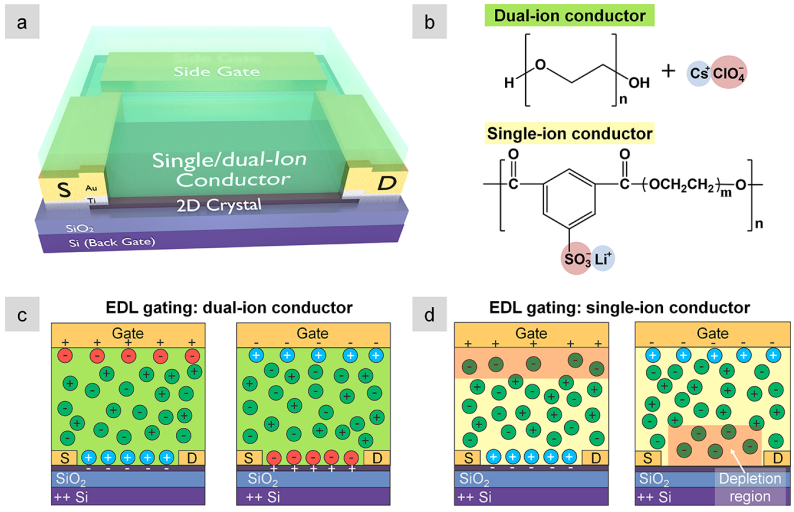

Figure 1. (a) Schematic of a 2D crystal FET (either graphene or $MoTe_2$) that can be operated by using a back gate or a single/dual-ion conductor using a metal side gate. (b) Chemical structures of the dual- and single-ion conductors: PEO:$CsClO_4$ (top row) and the ionically functionalized polyester (PE400-Li) (bottom row), respectively. Anions are shaded in red and cations are shaded in blue. Schematics of the (c) dual-ion conducting and (d) single-ion conducting FETs under two polarities. In the single-ion case, only cations are mobile while the anions are bound to the polymer backbone and therefore fixed. This immobility leads to cationic depletion regions (shaded in pink) at either the gate/single-ion conductor ($V_G > 0$) or single-ion conductor/semiconductor interface ($V_G < 0$), depending on the polarity of the applied field.

optoelectronic device studies.[17−21] Moreover, a wide variety of EDLTs have been demonstrated on 2D crystals.[15,16,22−25] Dual-ion conductors can induce charge densities on the order of ~10^{14} cm^{-2} for electrons and holes.[26,27] This corresponds to a capacitance density up to 10 $\mu F/cm^2$ and a large electric field strength of ~V/nm at the interface, allowing access to regimes of transport in semiconductors that cannot be achieved with conventional gate dielectrics.[25,28,29] In contrast to a dual-ion conductor, the anions of a single-ion conductor, or ionomer, are covalently bound to the backbone of the polymer, leaving only the cations free to move in response to an applied field. When polarized, an EDL consisting of densely packed cations is created at the negative electrode, but there is no corresponding anionic EDL at the positive electrode. In response to this imbalance, one side of the single-ion conductor (near the negative electrode) undergoes longitudinal expansion. The mechanism to induce strain using single-ion conductors has been well investigated for ionic polymer metal composites (IPMCs), which are useful for biomimetic actuators and artificial muscles.[30] In electronics, single-ion conductors have been used previously to gate organic transistors[31−33] where the motivation for immobilizing one ion over the other was to avoid electrochemical reactions within the organic channel. To our knowledge, there has been no report directly comparing single- and dual-ion conductors with similar chemistries in the same 2D crystal FETs or distinguishing the electrostatic gating effects between cationic EDLs and cationic depletion layers on 2D crystals.

We present the first demonstration of a single-ion conductor multilayer 2D crystal EDLT and lay the groundwork for demonstrating flexible 2D FETs with new functionalities induced by an EDL via strain. Experimentally, we used an ionically functionalized polyester (created via the condensation of poly(ethylene glycol) oligomers with dimethyl 5-sulfoisophthalate salt[34]) to electrostatically gate both graphene and $MoTe_2$ FETs. Compared with back gating through SiO_2, transfer characteristics using a side gate to control the location of the ions within both the single- and dual-ion conductors reveal a comparable enhancement of the n-branch current (e.g., 20-fold improvement of subthreshold swing and two orders of magnitude increase in on/off for $MoTe_2$ FETs). The dual-ion conductor gating results agree well with previous reports.[16,25,26,35] However, unlike the dual-ion conductor, the single-ion conductor quenches the p-branch in graphene and $MoTe_2$ FETs, which has not been reported before. Finite element modeling of ion transport in response to an applied field shows that the p-branch quenching is unique to single-ion conductor gating via the formation of a cationic depletion region (as opposed to an anionic EDL) in combination with an asymmetric gate/channel geometry. Both the experiments and modeling suggest that single-ion conductor-gated FETs can achieve sheet densities up to 10^{14} cm^{-2}, which could possibly induce sufficient strain to access the strain-induced electronic and optoelectronic properties described above.[36,37]

RESULTS AND DISCUSSION

The EDL-gated multilayer 2D crystal FETs use a side-gate geometry, as shown in Figure 1a. Graphene and $MoTe_2$ were mechanically exfoliated onto a p-doped Si substrate with 90 nm SiO_2 (used as a back gate). The source/drain and gate contacts (Ti/Au) were patterned by electron beam lithography (EBL) with the side gate located 10 μm away from the channel. The solid-state single-ion conductor is poly(ethylene glycol benzene-1,3-dicarboxylate-5-sulfoisophthalate lithium), abbreviated as PE400-Li, and the solid-state dual-ion conductor is poly(ethylene oxide), abbreviated as (PEO):$CsClO_4$. The chemical structures of the dual- and single-ion conductors are similar and shown in Figure 1b. The PE400-Li is a polyester with each repeat unit consisting of the ionic group, namely, dicarboxylic 5-sulfoisophthalate, and a spacer of poly(ethylene glycol) 400, which provides the same repeat unit as PEO.[34] Unlike PEO:$CsClO_4$ where the anion, ClO_4^-, is free to respond to the applied field, the negatively charged functional group (SO_3^-) in PE400-Li is covalently bound to

DOI: 10.1021/acsami.9b11526
ACS Appl. Mater. Interfaces 2019, 11, 35879−35887

the polymer backbone, while the cation Li^+ is free to move under an applied field. The ether oxygen to cation molar ratios are 76:1 for the dual-ion conductors and 9:1 for the single-ion conductors. Differential scanning calorimetry (DSC) shows that the single-ion conductor has a markedly higher glass transition temperature (T_g = 14.5 °C) than the PEO:$CsClO_4$ electrolyte (T_g = −31.5 °C) (Figure S1, Supporting Information), which is consistent with the single-ion conductor having a larger salt concentration.[38] This difference in T_g suggests that the single-ion conductor will have lower ionic conductivity than the dual-ion conductor.

When no voltage is applied, cations and anions are homogeneously distributed throughout the electrolyte for both the single- or dual-ion conductors. The steady-state locations of cations and anions under $V_G > 0$ and $V_G < 0$ are illustrated in Figure 1c,d for the dual-ion conductor and single-ion conductor, respectively. When a positive gate bias is applied to a dual-ion conductor (Figure 1c, left), cations (Cs^+) are driven to the channel where they induce image charges (in this case, image charges are electrons) forming a cationic EDL at the channel/electrolyte interface. An analogous anionic EDL will form as anions (ClO_4^-) accumulating at the electrolyte/gate interface. When the polarity of the applied bias is reversed, an anionic EDL forms at the channel and a cationic EDL forms at the gate (Figure 1c, right).

For a single-ion conductor, shown in Figure 1d, a positive gate bias does not result in an anionic EDL at the gate/electrolyte interface; instead, there exists a cationic depletion layer (Figure 1d, left). When the polarity is reversed, the cation depletion layer forms at the channel/electrolyte interface (Figure 1d, right). Crucially, the negative charge stored by anions in the cationic depletion layer equals the positive charge in the cationic EDL, while the volumetric charge density of anions in the depletion layer is fixed and smaller than the volumetric charge density of the closely packed cations in the EDL. Thus, the depletion layer requires larger thickness (or volume when considered in 3D) than the EDL to store the same amount of charge. The presence of such a thick depletion layer also suggests that the device geometry will affect the interface capacitance of devices gated by the single-ion conductor because the depletion layer thicknesses will depend on the areas of both channel and gate. In contrast, the EDL thickness is always the distance between the ion and channel surface (i.e., <1 nm) and is independent of the channel size. Nonetheless, a depletion layer, albeit significantly thicker than the EDL, will still serve as a capacitor just with a smaller capacitance density than the EDL.[31]

To understand how the ion and voltage distributions differ under an applied voltage in a single-ion conductor compared to a dual-ion conductor and how their distributions will change with respect to the device geometry, we modeled ion transport using finite element analysis via COMSOL Multiphysics. A modified Nernst−Planck−Poisson system of equations[39,40] was solved for both single-ion and dual-ion conductors in two parallel plate capacitor geometries: one with electrodes of equivalent sized and another where one electrode is 10 times larger than the other (i.e., modeling the FET scenario where the channel is smaller than the gate). Figure 2 shows the resulting steady-state voltage distributions for applied voltages of equal and opposite polarities; the voltage is applied to the right electrode with the left electrode grounded. We first consider the scenarios where the electrodes have equivalent size (Figure 2a,b). In the case of a dual-ion conductor, anions and cations accumulate adjacent to their respective electrodes, producing EDLs of equal charge and thickness. The result is a symmetric voltage profile across the thickness of the capacitor where half of the applied voltage drops on each EDL regardless of the voltage polarity (Figure 2a), and the voltage drop through the bulk of the electrolyte is nearly zero.

In the case of the single-ion conductor, the majority of the voltage always drops across the depletion layer, regardless of polarity. The voltage drop is approximately 3 times larger across the depletion layer than the EDL, and the depletion layer is also approximately 3 times thicker than the EDL (Figure 2b). This result is sensible when considering conservation of charge across the parallel plate capacitor. Charge (Q) is expressed as $Q = V_{int}C_{int} = V_{int}\varepsilon_0\varepsilon_r\frac{A}{d}$, where V_{int} is the voltage across the interface, C_{int} is the interface capacitance, A is the area of channel, and d is the thickness of the interface capacitive layer (i.e., thickness of EDL or the depletion layers). Thus, the thicker depletion layer has lower interface capacitance and therefore requires a larger voltage drop to balance the charge.

For the scenario of equal sized electrodes discussed above, the voltage distribution across the single-ion conductor differs from the dual-ion conductor because the depletion region in a single-ion conductor requires the majority of the voltage drop. However, when the electrodes are unequal in length, similar to what would exist between the channel and the gate in a side-gated EDLT geometry, the voltage profiles between the single- and dual-ion conductors are remarkably similar because the geometry induces the majority of the voltage drop. Specifically, the length of the left (grounded) electrode decreased to one-tenth of the right electrode, and for the dual-ion conductor, 90% of the voltage drop across the EDL occurs adjacent to the shorter electrode, regardless of the voltage polarity (Figure 2c). The asymmetric voltage drop again results from charge conservation: the shorter electrode requires a larger voltage drop to compensate for its smaller capacitance.

In the case of the single-ion conductor (Figure 2d), the majority of voltage drop is also adjacent to the shorter electrode for the reason mentioned above, but the details of the ion and voltage distributions are more complicated. For $V > 0$ applied to the longer electrode, ∼85% of the voltage drop is distributed across the ∼0.5 nm-thick cationic EDL at the shorter electrode. When the polarity is reversed to $V < 0$, almost all of the applied voltage (97%) falls within the ∼1.5 nm-thick depletion layer near the shorter electrode (Figure 2d). This result is significantly different from Figure 2b where the electrode sizes are equal. To understand this difference, we focus on the voltage distributions near the grounded electrode only because the shorter grounded electrode is similar to the channel in the transfer measurements where $V_S = 0$ V and $V_{DS} \ll V_{GS}$ (see parts 2 and 6 in the Supporting Information). Focusing on the inset of Figure 2d, the depletion layer is ∼3 times thicker than the EDL even though the voltage drop is only 14% larger. This occurs because the grounded electrode is 10 times smaller and requires the majority of the potential drop regardless of the polarity of V. Even though the depletion layer thickness is 3 times larger, it is not possible for this layer to have 3 times larger potential drop than the EDL at the same electrode, and therefore, the charge at the grounded electrode will be lower for $V < 0$ compared to $V > 0$. This result suggests that the single-ion conductor in a side-gated EDLT geometry will exhibit weaker p-type doping compared to n-type doping.

DOI: 10.1021/acsami.9b11526
ACS Appl. Mater. Interfaces 2019, 11, 35879−35887

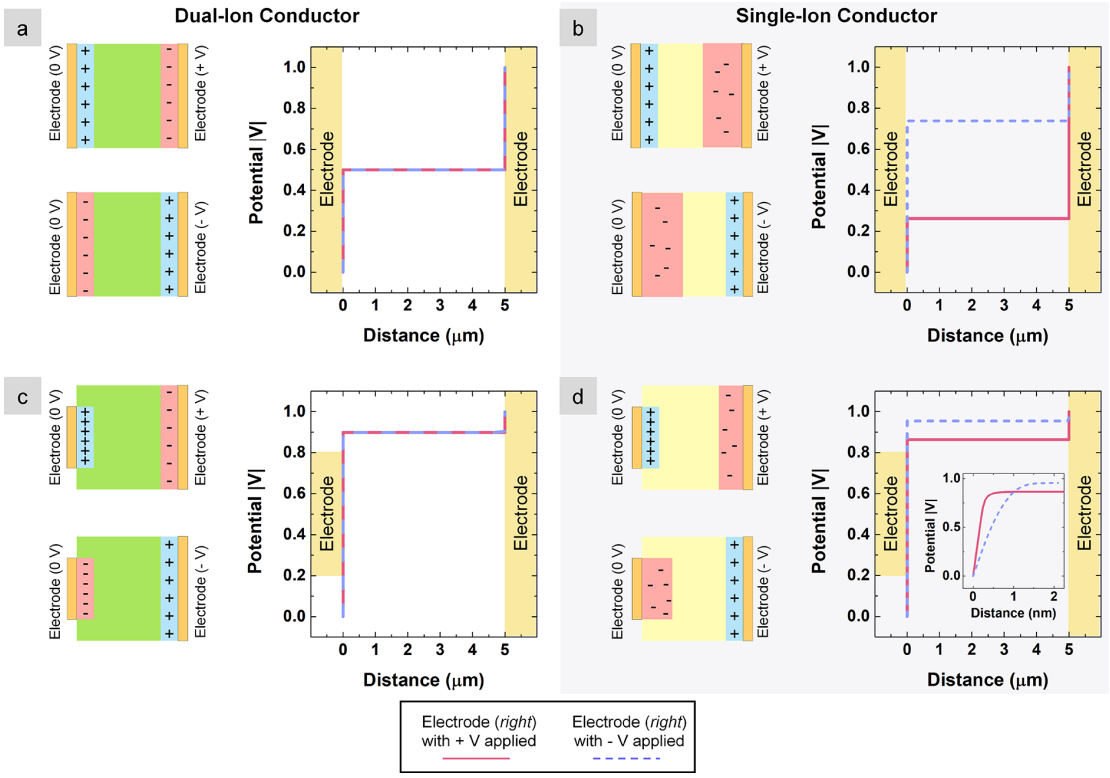

Figure 2. Steady-state voltage distributions from COMSOL Multiphysics and the corresponding device schematics showing ion positions for both (a, c) dual-ion and (b, d) single-ion conductors in two parallel plate capacitor geometries: electrodes of equal size (upper row) and electrodes of unequal size where the right electrode is 10 times larger than left (bottom row). Note that the schematics are not drawn to scale. Either ±1 V is applied on the right-side electrode. Cation and anion layers are highlighted in blue and red, respectively. The anion EDL (dual-ion) or cationic depletion layer (single-ion) thickness differences are illustrated qualitatively. Specifically, for the dual-ion conductor, the anionic EDL layer thickness is similar to the cationic EDL layer thickness; while for the single-ion conductor, the cationic depletion layer thickness is larger and influenced by the electrode size. The steady-state potential distributions under positive and negative voltages are highlighted in the red solid and dashed blue lines, respectively.

To test these predictions experimentally, we chose graphene as the first 2D material for two reasons. First, because it is a semi-metal, graphene is highly conductive and ambipolar with an intrinsic charge neutrality point at zero gate voltage, making it ideal for sensing both p- and n-type changes in conductivity. Second, EDL gating of graphene FETs using a dual-ion conductor has been widely demonstrated,[26,35] making it straightforward to benchmark against previously published results.

Graphene FETs with side gate geometry were fabricated by EBL as depicted above in Figure 1a. After device fabrication and before the single-ion conductor deposition, the channel surface was cleaned using an AFM in contact mode to remove e-beam resist residue.[41] Preparing a residue-free surface is essential to achieve the maximum gating effect because the EDL forms within a few nanometers of the surface, similar to the typical thickness of the EBL residue.[41] Figure 3a shows the AFM images of a graphene device after AFM cleaning. The root mean square roughness (R_q) of the channel surface was reduced from ∼1.30 nm before cleaning to ∼0.37 nm after cleaning, which is close to the reported value for freshly exfoliated graphene on SiO_2 (∼0.32 nm).[42] Note that all R_q are reported for a 400 × 400 nm area. The line scan indicates a flake thickness of 1.5 nm, corresponding to ∼5 layers of graphene.

The transfer characteristics of the graphene FETs (without electrolyte) were first measured with a back gate (Figure 3b, blue line), and the devices show a Dirac point around V_{BG} = 0 V, suggesting that there is negligible intrinsic doping in the exfoliated flakes. Under V_{DS} = 100 mV, the transfer curve exhibits highly symmetric n- and p-branches with a current maxima of ∼100 μA (25.4 μA/μm) at $|V_{BG}|$ = 30 V. The output characteristics of the bare graphene FET (Figure 3c, blue lines) also indicate that I_D is a linear function of V_{DS}, suggesting good ohmic contact at the source/drain terminals. These results on the bare graphene FETs are in good agreement with prior reports.[35,43,44]

After deposition of the single-ion conductor, the transfer and output measurements were repeated with EDL gating using the side gate 10 μm away from the channel. A sweep rate of 2.5 mV/s was used, which is 2000 times slower than that of the bare FET to allow sufficient time for the ions to respond to the field. This relatively slow sweep rate is consistent with the high T_g of the single-ion conductor that reflects slow ion mobility. Compared to the bare FET, the maximum I_D increased in the n-branch (V_{SG} > 0 V) by 50% to ∼152 μA at V_{SG} = 3 V. The increased current is expected for the EDL gating because of the large interfacial capacitance (1−4 μF/cm^2) induced by EDLs.[15,16] However, unlike conventional EDL gating with dual-ion conductors where the current is enhanced in both the

DOI: 10.1021/acsami.9b11526
ACS Appl. Mater. Interfaces 2019, 11, 35879−35887

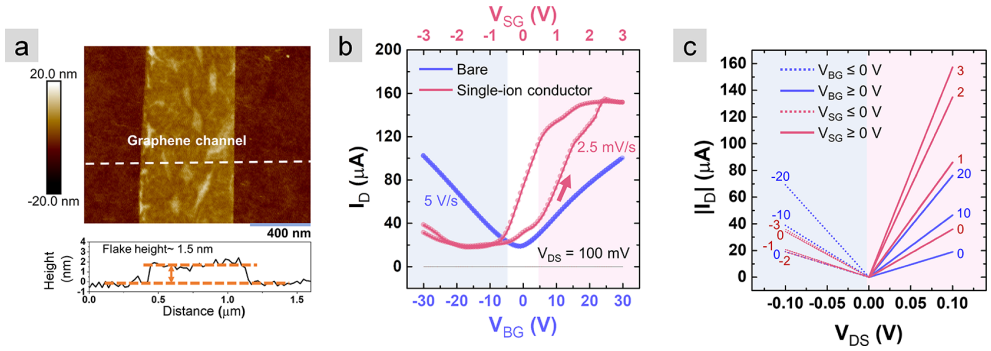

Figure 3. (a) AFM topography scan of a bare graphene FET channel (before electrolyte deposition). The location of the line scan is indicated by the white dashed line. (b) Transfer characteristics of the graphene FET: the blue data corresponds to the back-gated measurement of a bare FET while the red corresponds to a side-gated measurement on the same FET with the single-ion conductor. (c) Output characteristics of the back-gated (blue) and side-grated (red) graphene FETs.

n- and p-branches of an ambipolar FET, the single-ion conductor-gated FET shows a suppressed p-branch (V_{SG} < 0 V). The maximum I_D for the p-branch decreased by 65% to ~35 μA at V_{SG} = −3 V. This observation agrees well with the predictions from Figure 2d. The channel current, $I_D = \mu\varepsilon_0\varepsilon_r\frac{A}{d}(V_{int} - V_T)\frac{W}{L}V_{DS}$, where V_{int} is the interface voltage, d is the interface capacitive layer thickness, and $A/W/L$ is the area/width/length of the channel. When V_G is negative (corresponding to the p-branch), the depletion layer thickness next to the channel is expected to be much larger than the EDL thickness next to the channel when V_G is positive (corresponding to the n-branch). However, we learned from Figure 2d that the voltage drop across the depletion layer at the short electrode (i.e., channel) is only slightly larger than that across the EDL; thus, the channel current should be lower in the p-branch than in the n-branch.

Output characteristics as a function of side gate voltages are shown in Figure 3c (red lines). Compared with the back-gated data, the maximum I_D under positive (negative) side gate voltages are higher (lower), which is congruent with the transfer characteristics. Note that the results shown in Figure 3c are double sweeps, including the single-ion conductor-gated results, and the overlap of the forward and reverse sweeps indicates that the single-ion conductor gating is stable at each measured gate voltage, as long as adequate time is provided for the ions to respond to the field.

Thus far, the electrical characteristics of the single-ion conductor-gated FETs qualitatively agree with our predictions; however, it is essential to benchmark the single-ion conductor gating performance against a commonly used dual-ion conductor. To do this, we removed the single-ion conductor by solvent washing (dimethylformamide, DMF) and AFM cleaning. After the two-step cleaning process, the root mean square roughness (R_q) of the graphene channel is close to the value of freshly exfoliated flakes (Supporting Information, Figure S8).[42] Then, we redeposited a dual-ion polymer electrolyte, PEO:$CsClO_4$, on the same device and repeated the transfer measurements. Figure 4 shows the transfer curves for two such FETs (device 1 and 2) with (1) Si/SiO_2 back gate (no electrolyte), (2) EDL side gate using the single-ion conductor, and (3) EDL side gate using the dual-ion polymer electrolyte, PEO:$CsClO_4$. The solid lines correspond to the forward sweeps, and the dashed lines correspond to the reverse sweeps. For the transfer curves obtained using PEO:$CsClO_4$

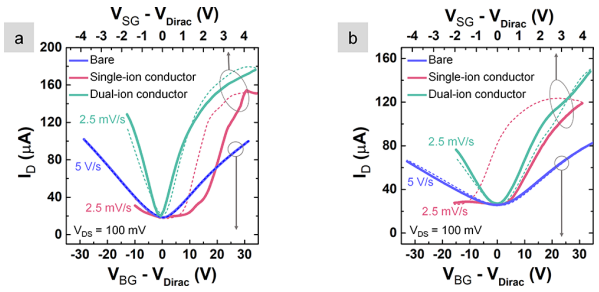

Figure 4. (a, b) Transfer characteristics of two graphene FETs. Back-gated bare devices (blue), side-gated with single-ion conductor (red), and side-gated with dual-ion conductor (green). Solid and dotted lines indicate scans from negative to positive gate voltages and from positive to negative gate voltages, respectively. Note that the gate voltages were normalized with respected to V_{Dirac} to facilitate comparison between n- and p-branches currents using different gating methods. The original data are provided in Supporting Information, Part 3.

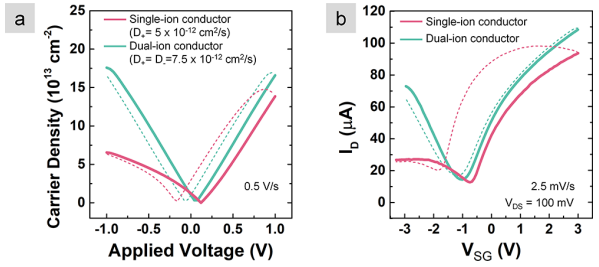

Figure 5. (a) COMSOL simulations of corresponding charge carrier densities within the grounded electrode in a parallel-plate capacitor geometry with the single-ion conductor (red) and the dual-ion conductor (green). (b) Transfer characteristics of both ion conductors on one graphene FET (device 3): the single-ion conductor is red and the dual-ion conductor (PEO:$CsClO_4$) is green. In both (a) and (b), the voltage is swept from negative to positive (solid lines) and then reversed (dotted lines).

(green), both the n- and p-branches are clearly observable and show increased current compared to the bare, back-gated devices. Overall, for the n-branch, EDL gating with either dual- or single-ion conductor shows enhanced on current (~80 and 60% for dual- and single-ion conductors, respectively) over back gating through SiO_2. This improvement is attributed to

DOI: 10.1021/acsami.9b11526
ACS Appl. Mater. Interfaces 2019, 11, 35879−35887

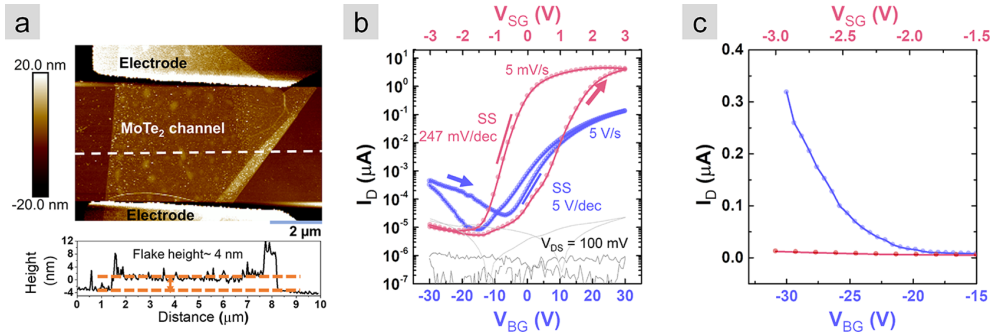

Figure 6. (a) AFM topography scan of a bare $MoTe_2$ FET channel (before electrolyte deposition). The location of the line scan is indicated by the white dash line. (b) Transfer characteristics of the $MoTe_2$ FET in log scale with back-gated transfer measurements from V_{BG} = −30 to 30 V on the bare FET in blue and side-gated transfer of the same FET from V_{SG} = −3 to 3 V with single-ion conductor in red. (c) Zoomed transfer curves on a linear *y* axis over a negative range of V_{BG} to highlight the suppressed p-branch when using the single-ion conductor.

the larger EDL capacitance and agrees with previous reports.[15,16] For the p-branch, the enhancement of on current is again observed for the dual-ion conductor but is suppressed for the single-ion conductor. Note also that the Dirac point location in the transfer measurements shifts to negative V_{SG} after the deposition of the single-ion conductor and does not return to zero after removing the electrolyte with solvent and AFM cleaning (Supporting Information, Figure S5). However, this shift is commonly observed in EDL gating of graphene FETs using dual-ion conductors[23,35] and reflects that the electrolyte induces doping of the graphene channel even in the absence of a gate voltage. The original data and discussion of the differences between devices are provided in Supporting Information, Part 3.

The successful ambipolar modulation of the channel current using a dual-ion conductor indicates that the single-ion conductor did not change the graphene channel in a way that would prevent hole conduction. This further supports the understanding that suppressed p-branch current in the single-ion conductor is caused by the cation depletion layer having weaker gate modulation compared to the EDL. This effect can be captured by modeling the dynamic response of single- and dual-ion conductors in response to a voltage sweep. A time-dependent Nernst−Plank−Poisson equation was used with a geometry identical to Figure 2c,d. The voltage is applied to the right electrode, and the ion distribution near the left (grounded) electrode is monitored. The ion mobility of the single-ion conductor is lower than that of the dual-ion conductor (as mentioned above and in Figure S1), and we therefore set the diffusion coefficient of the dual-ion conductor to be 1.5 times larger than that of the single-ion conductor.

Figure 5a shows the predicted carrier density in response to a voltage sweep in the range of ±1 V. For the dual-ion conductor, anions and cations accumulate at the electrodes identically, resulting in a symmetric carrier density with respect to the applied voltage polarity. In contrast, for the single-ion conductor, the carrier density at the grounded electrode is lower under a negative voltage corresponding to the cation depletion region, compared to positive voltage corresponding to a cationic EDL. These results agree with the smaller capacitance at the depletion layer, as discussed above regarding Figure 2.

If we consider only EDL gating of the single- and dual-ion conductors (i.e., $V_G > 0$), the maximum predicted carrier densities are similar (15×10^{13} cm^{-2} and 17×10^{13} cm^{-2} for single and dual-ion conductors, respectively). The similarity is also reflected in the steady-state modeling results in Figure 2c,d where the voltage dropped across the grounded electrode is similar for single-ion (0.85 V) and dual-ion conductors (0.89 V). The EDL thicknesses are also similar (~0.5 nm), and therefore, the charge densities are expected to be similar.

To compare directly between modeling and experiments, Figure 5b shows the transfer curves measured experimentally on a third device (device 3) using both single- and dual-ion conductors (see also Figure S5, Supporting Information). The experimental results of all three devices shown in Figures 4 and 5 exhibit similar trend and match closely with simulations.

The similar n-type doping performance between the single- and dual-ion conductors is encouraging because it suggests the possibility of using the single-ion conductor to induce high charge density similar to dual-ion conductors, which is up to 10^{14} cm^{-2} as measured experimentally[25,26] and also predicted in simulations in Figure 5a. Note that a higher applied voltage is required experimentally to achieve the same carrier density as the simulation because of the geometry differences and imperfect ion packing. In addition, we measured the EDL capacitance induced by the single-ion conductor by a series of V_{SG} transfer measurements under various V_{BG} (Figure S6, Supporting Information). The EDL capacitance of the single-ion conductor (1.66 $\mu F/cm^2$) is very similar with the reported value of dual-ion conductors (1−4 $\mu F/cm^2$),[15,26,45] which also implies the possibility of achieving similar n-type gating. The ability to pack ion densely is critical for creating electrostatic imbalance in the single-ion conductor, which can lead to mechanical bending of the electrolyte if it is placed on a semirigid support (i.e., a suspended 2D flake).

Lastly, to make sure that the gating performance of the single-ion conductor is not unique to graphene and can also be observed in 2D crystals, $MoTe_2$ FETs were fabricated with the same device geometry as the graphene FETs. We choose $MoTe_2$ because one potential use for single-ion conductor gating is to explore the strain-induced semiconductor-to-metal transition for which $MoTe_2$ is predicted to have one of the smallest strain requirements (i.e., <3%).[6] Moreover, the transition has been experimentally demonstrated in $MoTe_2$.[8,9] The AFM scans of one $MoTe_2$ FET are shown in Figure 6a, and the line scan shows the channel thickness to be 4 nm (~6 $MoTe_2$ layers). The majority of the flake is in uniform thickness, and therefore, we expect minimal impact from thickness variations on the electrical properties.[46] Back-

DOI: 10.1021/acsami.9b11526
ACS Appl. Mater. Interfaces 2019, 11, 35879−35887

gated transfer characteristics were measured on bare devices, as indicated by the blue transfer curve in Figure 6b. The bare $MoTe_2$ FET is ambipolar with a minimum current of $\sim 10^{-5}$ μA at V_{BG} of ~ -15 V. The on/off ratio of the n-branch from $-5 < V_{BG} < 30$ V is $<10^4$, and the p-branch from $-30 < V_{BG} < -17$ V is <100.

Using the single-ion conductor, the maximum current through $MoTe_2$ at V_{SG} = 3 V is ~32 times larger compared to the maximum current of the bare FET at V_{BG} = 30 V (Figure 6b). Output characteristics also show effective gate control of the channel current using the single-ion conductor (Figure S9). The on/off ratio of the n-branch increases from 10^4 for the bare FET to $\sim 10^6$ with the single-ion conductor. Also, the subthreshold swing (SS) of the n-branch decreases with the single-ion conductor (from 5000 mV/dec by back-gating the bare device to 247 mV/dec). The strong current modulation and the enhanced on/off ratio further confirm the strong EDL modulation by the single-ion conductor. Similar to the graphene FETs, the I_D of the p-branch remains suppressed, in this case, at the off level of 10^{-5} μA. The suppressed p-branch is highlighted in a linear plot in Figure 6c.

CONCLUSIONS

EDL gating using a custom-synthesized single-ion conductor is demonstrated for the first time on both graphene and $MoTe_2$ FETs. Transfer characteristics for all the FETs show an enhanced n-branch using the single-ion conductor and a suppressed p-branch compared with back-gated measurements of bare FETs. Finite element modeling of ion transport in response to an applied field shown that the p-branch suppression results from the combination of using a single-ion conductor and an asymmetric gate/channel geometry. In addition, the two ion conductors compared on the same FETs both show similar performance in the n-branch (i.e., on/off ratio and maximum ion current), suggesting that the single-ion conductor can achieve cationic ion densities similar to the well-studied dual-ion conductor (i.e., up to 10^{14} cm^{-2}). This achievable carrier density is also predicted by modeling and would be theoretically sufficient to induce several percent strain in a 2D crystal. This is the first demonstration of a single-ion conductor-gated multilayer 2D crystal FET, and the results lay the groundwork for inducing strain in 2D materials locally via field effect and for demonstrating the 2H to 1T′ phase transition. These features are potentially useful for creating an electronic switch with a low turn-on voltage and steep subthreshold swing and for 2D flexible electronics with functionality controlled by strain.

EXPERIMENTAL SECTION

Device Fabrication and Electrical Characterization. Freshly cleaved few-layer graphene and $MoTe_2$ flakes (1.5 nm−5 nm-thick) were mechanically exfoliated from their bulk sources (2D semiconductors) to p-doped silicon substrate with 90 nm SiO_2 (Graphene Supermarket, resistivity of 0.001−0.005 ohm·cm). The flake topography and thickness were measured by AFM (Bruker Dimension Icon, ScanAsyst mode). Source/drain electrodes and side gates were patterned by EBL (Raith e-LINE). Also, Ti (3 nm)/Au (120 nm) metals were deposited by e-beam evaporation (Plassys MEB550S electron beam evaporator) at a base pressure of $<10^{-6}$ Torr. After liftoff, FETs were transferred to a cryogenic vacuum probe station (Lakeshore, CRX-VF) for vacuum annealing (400 K, 4 h at a pressure of 2×10^{-6} Torr) and initial electrical measurements. After annealing, FETs were transferred from the probe station to an Ar-filled glovebox using an Ar-filled load lock without exposure to ambient air for electrolyte deposition, before transferring back to the probe station for electrical measurements. The electrical measurements were conducted using a Keysight B1500A semiconductor parameter analyzer at a constant temperature of 300 K.

Single-Ion Conductor Synthesis. The polyester single-ion conductor was synthesized by a two-step melt condensation between poly(ethylene glycol) (PEG) 400 (M_w = 400 g mol^{-1}) and dimethyl 5-sulfoisophthalate sodium salt.[34] The resulting polyester Na was then sealed in semipermeable dialysis membranes and exposed to an excess of LiCl (0.5 M) in deionized water to exchange Na^+ for Li^+.[34] The final product, polyester Li (PE400-Li), was dissolved in dimethylformamide (DMF) inside an Ar-filled glovebox to obtain a 3 wt % solution. The solution was drop-cast on graphene and $MoTe_2$ FETs (8 μL on the 1 cm^2 chip), and the DMF was removed by evaporating naturally in the glovebox overnight. The FETs coated with the single-ion conductor were transferred back to the probe station using the load lock for subsequent measurements.

Dual-Ion Conductor. The dual-ion conducting polymer electrolyte (PEO:$CsClO_4$) was prepared similarly to previously published work.[15] PEO (Polymer Standards Service, M_w = 94600 g mol^{-1}) and $CsClO_4$ (Sigma-Aldrich, 99.9%) were dissolved in anhydrous acetonitrile (Sigma-Aldrich) to make a 1 wt % solution with an ether oxygen to Cs molar ratio of 76:1. Twenty-five microliters of the solution was drop-cast onto the 1 cm^2 sample of graphene FETs in the glovebox, dried at room temperature until the majority of the solvent evaporated, and then annealed at 80 °C for 3 min.

Modeling. The time-dependent, modified Nernst−Planck−Poisson relationship was used in COMSOL Multiphysics to predict ion accumulation in response to voltage. Ion migration was modeled using a modified version of the Nernst−Plank equation: $\frac{dc}{dt} = \nabla(D_{\pm}\nabla c_{\pm} + \frac{D_{\pm}F}{RT} z_{\pm} c_{\pm} \nabla V + \gamma$, where c is the ion concentration, D is the ion diffusion coefficient, F is faraday's constant, RT is the thermal energy, γ is the steric repulsion term, and V is the electrolyte potential. The potential is coupled to Poisson's equation $\nabla^2(-\varepsilon V) = F\sum_{i=1}^{2}(z_i c_i)$, where ε is the permittivity of the electrolyte ($\sim 10\ \varepsilon_0$)[36] and z is the ion charge number (+1 for cations, −1 for anions). A stern layer, defined by $\nabla^2(-\varepsilon V) = 0$, was used directly adjacent to the electrode and SiO_2 boundaries and set to equal 2 Å. The bulk concentration of ions corresponds to an ether oxygen to lithium ratio of 20:1, and the density of the polymer is assumed to be 1 g/cm^3.

For all four geometries, a 50 μm-long by 5 μm-thick electrolyte was used; electrodes were modeled as boundary conditions with the appropriate potentials. In the models involving geometries of equal-sized electrodes, the electrode surfaces constituted the entire 50 μm boundary. A zero charge boundary condition (defined as $n \cdot D = 0$, where n is the surface normal vector and $D = -\varepsilon \nabla V$ was used for the nonelectrode boundaries). The mesh size near the electrode interfaces was decreased until the EDL concentrations remained within 1% of its previous value.

In the models involving unequal electrodes, boundary conditions for nonelectrode boundaries were defined to mimic SiO_2 by using a modification of the previous boundary condition: $n \cdot D = -\frac{\varepsilon_{SiO2}\phi}{t}$, where ε_{SiO2} is the permittivity of SiO_2, ϕ is the local electrolyte potential at the interface, and t is the oxide thickness (90 nm). This modification allowed for a nonzero electric flux through the nonelectrode boundaries (i.e., 90 nm oxide) and therefore allowed ions to accumulate near the oxide surface. To determine the carrier density in ions/cm^2 through the electrolyte, the volumetric charge density was integrated using trapezoid approximation along a cutline taken across the electrolyte perpendicular to the center of the grounded electrode beginning at the electrode surface and terminating at the center of the electrolyte.

DSC Measurements. The DSC samples were prepared inside the Ar-filled glovebox. PE400-Li (8.7 mg) and PEO:$CsClO_4$ (7.1 mg) were hermetically sealed in aluminum DSC pans. Measurements were made on TA 250 calibrated with an indium standard. To measure T_g (glass transition temperature) and T_m (melting temperature), samples were heated to 100 °C to erase the thermal history, cooled to −70 °C at 3 °C min^{-1}, and heated to 100 °C at 5 °C min^{-1}.

DOI: 10.1021/acsami.9b11526
ACS Appl. Mater. Interfaces 2019, 11, 35879−35887

■ ASSOCIATED CONTENT

Supporting Information

The Supporting Information is available free of charge on the ACS Publications website at DOI: 10.1021/acsami.9b11526.

DSC measurements; 2D potential profiles from COMSOL modeling; transfer measurements on device 3; estimation of EDL capacitance in the single-ion conductor-gated FET; impact of device geometry on charge density from COMSOL simulations; effective gate size; and output characteristics of single-ion conductor-gated $MoTe_2$ FETs (PDF)

■ AUTHOR INFORMATION

Corresponding Authors

*E-mail: ke.xu@pitt.edu (K.X.).
*E-mail: fullerton@pitt.edu (S.F.-S.).

ORCID

Ke Xu: 0000-0003-2692-1935
Jierui Liang: 0000-0003-1207-8959
Zhongmou Chao: 0000-0002-9882-4440
James R. McKone: 0000-0001-6445-7884
Susan K. Fullerton-Shirey: 0000-0003-2720-0400

Author Contributions

‖K.X. and J.L. contributed equally to this work. The manuscript was written through contributions of all authors. All authors have given approval to the final version of the manuscript.

Notes

The authors declare no competing financial interest.

■ ACKNOWLEDGMENTS

This work was supported by NSF-DMR-EPM grant no. 1607935. J.R.M. acknowledges support from the University of Pittsburgh, Swanson School of Engineering.

■ REFERENCES

(1) Thompson, S. E.; Armstrong, M.; Auth, C.; Alavi, M.; Buehler, M.; Chau, R.; Cea, S.; Ghani, T.; Glass, G.; Hoffman, T.; et al. A 90-Nm Logic Technology Featuring Strained-Silicon. *IEEE Trans. Electron Devices* **2004**, *51*, 1790−1797.

(2) Jacobsen, R. S.; Andersen, K. N.; Borel, P. I.; Fage-Pedersen, J.; Frandsen, L. H.; Hansen, O.; Kristensen, M.; Lavrinenko, A. V.; Moulin, G.; Ou, H.; et al. Strained Silicon as a New Electro-Optic Material. *Nature* **2006**, *441*, 199−202.

(3) Desai, S. B.; Seol, G.; Kang, J. S.; Fang, H.; Battaglia, C.; Kapadia, R.; Ager, J. W.; Guo, J.; Javey, A. Strain-Induced Indirect to Direct Bandgap Transition in Multilayer WSe2. *Nano Lett.* **2014**, *14*, 4592−4597.

(4) Roldán, R.; Castellanos-Gomez, A.; Cappelluti, E.; Guinea, F. Strain Engineering in Semiconducting Two-Dimensional Crystals. *J. Phys. Condens. Matter* **2015**, *27*, 313201.

(5) Amorim, B.; Cortijo, A.; de Juan, F.; Grushin, A. G.; Guinea, F.; Gutiérrez-Rubio, A.; Ochoa, H.; Parente, V.; Roldán, R.; San-Jose, P.; et al. Novel Effects of Strains in Graphene and Other Two Dimensional Materials. *Phys. Rep.* **2016**, *617*, 1−54.

(6) Duerloo, K.-A. N.; Li, Y.; Reed, E. J. Structural Phase Transitions in Two-Dimensional Mo- and W-Dichalcogenide Monolayers. *Nat. Commun.* **2014**, *5*, 4214.

(7) Sharma, M.; Kumar, A.; Ahluwalia, P. K.; Pandey, R. Strain and Electric Field Induced Electronic Properties of Two-Dimensional Hybrid Bilayers of Transition-Metal Dichalcogenides. *J. Appl. Phys.* **2014**, *116*, No. 063711.

(8) Song, S.; Keum, D. H.; Cho, S.; Perello, D.; Kim, Y.; Lee, Y. H. Room Temperature Semiconductor−Metal Transition of $MoTe_2$ Thin Films Engineered by Strain. *Nano Lett.* **2015**, *16*, 188−193.

(9) Hou, W.; Azizimanesh, A.; Sewaket, A.; Peña, T.; Watson, C.; Liu, M.; Askari, H.; Wu, S. M. Strain-Based Room-Temperature Non-Volatile $MoTe_2$ Ferroelectric Phase Change Transistor. *Nat. Nanotechnol.* **2019**, *14*, 668.

(10) Shukla, N.; Thathachary, A. V.; Agrawal, A.; Paik, H.; Aziz, A.; Schlom, D. G.; Gupta, S. K.; Engel-Herbert, R.; Datta, S. A Steep-Slope Transistor Based on Abrupt Electronic Phase Transition. *Nat. Commun.* **2015**, *6*, 7812.

(11) Seabaugh, A.; Fathipour, S.; Li, W.; Lu, H.; Park, J. H.; Kummel, A. C.; Jena, D.; Fullerton-Shirey, S. K.; Fay, P. Steep Subthreshold Swing Tunnel FETs: GaN/InN/GaN and Transition Metal Dichalcogenide Channels. In *2015 IEEE International Electron Devices Meeting (IEDM)*; IEEE: 2015, 35−36. DOI: 10.1109/IEDM.2015.7409835.

(12) Lu, H.; Seabaugh, A. Tunnel Field-Effect Transistors: State-of-the-Art. *IEEE J. Electron Devices Soc.* **2014**, *2*, 44−49.

(13) Akinwande, D.; Petrone, N.; Hone, J. Two-Dimensional Flexible Nanoelectronics. *Nat. Commun.* **2014**, *5*, 5678.

(14) Kim, S. J.; Choi, K.; Lee, B.; Kim, Y.; Hong, B. H. Materials for Flexible, Stretchable Electronics: Graphene and 2D Materials. *Annu. Rev. Mater. Res.* **2015**, *45*, 63−84.

(15) Xu, H.; Fathipour, S.; Kinder, E. W.; Seabaugh, A. C.; Fullerton-Shirey, S. K. Reconfigurable Ion Gating of 2H-$MoTe_2$ Field-Effect Transistors Using Poly(Ethylene Oxide)-$CsClO_4$ Solid Polymer Electrolyte. *ACS Nano* **2015**, *9*, 4900−4910.

(16) Xu, K.; Islam, M. M.; Guzman, D. M.; Seabaugh, A.; Strachan, A.; Fullerton-Shirey, S. K. Pulse Dynamics of Electric Double Layer Formation on All-Solid-State Graphene Field-Effect Transistors. *ACS Appl. Mater. Interfaces* **2018**, *10*, 43166.

(17) Kim, J.; Na, J.; Joo, M.-K.; Suh, D. Low-Voltage-Operated Highly Sensitive Graphene Hall Elements by Ionic Gating. *ACS Appl. Mater. Interfaces* **2019**, *11*, 4226−4232.

(18) Zhao, W.; Bi, S.; Balke, N.; Rack, P. D.; Ward, T. Z.; Kalinin, S. V.; Dai, S.; Feng, G. Understanding Electric Double-Layer Gating Based on Ionic Liquids: From Nanoscale to Macroscale. *ACS Appl. Mater. Interfaces* **2018**, *10*, 43211−43218.

(19) Jiang, J.; Hu, W.; Xie, D.; Yang, J.; He, J.; Gao, Y.; Wan, Q. 2D Electric-Double-Layer Phototransistor for Photoelectronic and Spatiotemporal Hybrid Neuromorphic Integration. *Nanoscale* **2019**, *11*, 1360−1369.

(20) Paletti, P.; Yue, R.; Hinkle, C.; Fullerton-Shirey, S. K.; Seabaugh, A. Two-Dimensional Electric-Double-Layer Esaki diode. *npj 2D Mater. Appl.* **2019**, *3*, 19.

(21) Ren, X.; Wang, Y.; Xie, Z.; Xue, F.; Leighton, C.; Frisbie, C. D. Gate-Tuned Insulator-Metal Transition in Electrolyte-Gated Transistors Based on Tellurene. *Nano Lett.* **2019**, 4738.

(22) Fathipour, S.; Pandey, P.; Fullerton-Shirey, S.; Seabaugh, A. Electric-Double-Layer Doping of WSe_2 field-effect Transistors Using Polyethylene-Oxide Cesium Perchlorate. *J. Appl. Phys.* **2016**, *120*, 234902.

(23) Kinder, E. W.; Fuller, A.; Lin, Y.-C.; Robinson, J. A.; Fullerton-Shirey, S. K. Increasing the Room-Temperature Electric Double Layer Retention Time in Two-Dimensional Crystal FETs. *ACS Appl. Mater. Interfaces* **2017**, *9*, 25006−25013.

(24) Xu, K.; Lu, H.; Kinder, E. W.; Seabaugh, A.; Fullerton-Shirey, S. K. Monolayer Solid-State Electrolyte for Electric Double Layer Gating of Graphene Field-Effect Transistors. *ACS Nano* **2017**, *11*, 5453−5464.

(25) Bisri, S. Z.; Shimizu, S.; Nakano, M.; Iwasa, Y. Endeavor of Iontronics: From Fundamentals to Applications of Ion-Controlled Electronics. *Adv. Mater.* **2017**, *29*, 1607054.

(26) Efetov, D. K.; Kim, P. Controlling Electron-Phonon Interactions in Graphene at Ultrahigh Carrier Densities. *Phys. Rev. Lett.* **2010**, *105*, 256805.

(27) Yuan, H.; Shimotani, H.; Tsukazaki, A.; Ohtomo, A.; Kawasaki, M.; Iwasa, Y. High-Density Carrier Accumulation in ZnO Field-Effect

Transistors Gated by Electric Double Layers of Ionic Liquids. *Adv. Funct. Mater.* **2009**, *19*, 1046−1053.
(28) Ueno, K.; Shimotani, H.; Yuan, H.; Ye, J.; Kawasaki, M.; Iwasa, Y. Field-Induced Superconductivity in Electric Double Layer Transistors. *J. Phys. Soc. Jpn.* **2014**, *83*, No. 032001.
(29) Du, H.; Lin, X.; Xu, Z.; Chu, D. Electric Double-Layer Transistors: A Review of Recent Progress. *J. Mater. Sci.* **2015**, *50*, 5641−5673.
(30) Vargantwar, P. H.; Roskov, K. E.; Ghosh, T. K.; Spontak, R. J. Enhanced Biomimetic Performance of Ionic Polymer-Metal Composite Actuators Prepared with Nanostructured Block Ionomers. *Macromol. Rapid Commun.* **2012**, *33*, 61−68.
(31) Choi, J.-H.; Xie, W.; Gu, Y.; Frisbie, C. D.; Lodge, T. P. Single Ion Conducting, Polymerized Ionic Liquid Triblock Copolymer Films: High Capacitance Electrolyte Gates for N-Type Transistors. *ACS Appl. Mater. Interfaces* **2015**, *7*, 7294−7302.
(32) Herlogsson, L.; Crispin, X.; Tierney, S.; Berggren, M. Polyelectrolyte-Gated Organic Complementary Circuits Operating at Low Power and Voltage. *Adv. Mater.* **2011**, *23*, 4684−4689.
(33) Malti, A.; Gabrielsson, E. O.; Berggren, M.; Crispin, X. Ultra-Low Voltage Air-Stable Polyelectrolyte Gated n-Type Organic Thin Film Transistors. *Appl. Phys. Lett.* **2011**, *99*, 063305.
(34) Dou, S.; Zhang, S.; Klein, R. J.; Runt, J.; Colby, R. H. Synthesis and Characterization of Poly(Ethylene Glycol)-Based Single-Ion Conductors. *Chem. Mater.* **2006**, *18*, 4288−4295.
(35) Li, H.-M.; Xu, K.; Bourdon, B.; Lu, H.; Lin, Y.-C.; Robinson, J. A.; Seabaugh, A. C.; Fullerton-Shirey, S. K. Electric Double Layer Dynamics in Poly(Ethylene Oxide) $LiClO_4$ on Graphene Transistors. *J. Phys. Chem. C* **2017**, *121*, 16996−17004.
(36) Lee, A. A.; Colby, R. H.; Kornyshev, A. A. Electroactuation with Single Charge Carrier Ionomers: The Roles of Electrostatic Pressure and Steric Strain. *Soft Matter* **2013**, *9*, 3767.
(37) Lee, A. A.; Colby, R. H.; Kornyshev, A. A. Statics and Dynamics of Electroactuation with Single-Charge-Carrier Ionomers. *J. Phys. Condens. Matter* **2013**, *25*, No. 082203.
(38) Fullerton-Shirey, S. K.; Maranas, J. K. Effect of $LiClO_4$ on the Structure and Mobility of PEO-Based Solid Polymer Electrolytes. *Macromolecules* **2009**, *42*, 2142−2156.
(39) Kilic, M. S.; Bazant, M. Z.; Ajdari, A. Steric Effects in the Dynamics of Electrolytes at Large Applied Voltages. II. Modified Poisson-Nernst-Planck Equations. *Phys. Rev. E* **2007**, DOI: 10.1103/PhysRevE.75.021503.
(40) Wang, H.; Pilon, L. Accurate Simulations of Electric Double Layer Capacitance of Ultramicroelectrodes. *J. Phys. Chem. C* **2011**, *115*, 16711.
(41) Liang, J.; Xu, K.; Toncini, B.; Bersch, B.; Jariwala, B.; Lin, Y.-C.; Robinson, J.; Fullerton-Shirey, S. K. Impact of Post-Lithography Polymer Residue on the Electrical Characteristics of MoS_2 and WSe_2 Field Effect Transistors. *Adv. Mater. Interfaces* **2019**, *6*, 1801321.
(42) Geringer, V.; Liebmann, M.; Echtermeyer, T.; Runte, S.; Schmidt, M.; Rückamp, R.; Lemme, M. C.; Morgenstern, M. Intrinsic and Extrinsic Corrugation of Monolayer Graphene Deposited on SiO_2. *Phys. Rev. Lett.* **2009**, *102*, 076102.
(43) Schwierz, F. Graphene Transistors. *Nat. Nanotechnol.* **2010**, *5*, 487−496.
(44) Craciun, M. F.; Russo, S.; Yamamoto, M.; Tarucha, S. Tuneable Electronic Properties in Graphene. *Nano Today* **2011**, *6*, 42−60.
(45) Lin, Y.-C.; Jariwala, B.; Bersch, B. M.; Xu, K.; Nie, Y.; Wang, B.; Eichfeld, S. M.; Zhang, X.; Choudhury, T. H.; Pan, Y.; et al. Realizing Large-Scale, Electronic-Grade Two-Dimensional Semiconductors. *ACS Nano* **2018**, *12*, 965−975.
(46) Lavini, F.; Calò, A.; Gao, Y.; Albisetti, E.; Li, T.-D.; Cao, T.; Li, G.; Cao, L.; Aruta, C.; Riedo, E. Friction and Work Function Oscillatory Behavior for an Even and Odd Number of Layers in Polycrystalline MoS_2. *Nanoscale* **2018**, *10*, 8304−8312.

DOI: 10.1021/acsami.9b11526
ACS Appl. Mater. Interfaces 2019, 11, 35879−35887

Supporting Information

Electric double layer gating of two-dimensional field-effect transistors using a single-ion conductor

Ke Xu,[1,‡,] Jierui Liang,[1,‡] Aaron Woeppel,[1] M. Eli Bostian,[1] Hangjun Ding,[1,2] Zhongmou Chao,[1] James R. McKone,[1] Eric J. Beckman,[1,2] and Susan Fullerton-Shirey [1,3,]**

[1]Department of Chemical and Petroleum Engineering, University of Pittsburgh, Pittsburgh, PA, USA

[2] The Mascaro Center for Sustainable Innovation, University of Pittsburgh, Pittsburgh, Pennsylvania 15260, United States

[3] Department of Electrical and Computer Engineering, University of Pittsburgh, Pittsburgh, Pennsylvania 15260, United States

* Author to whom correspondence should be addressed. Electronic mail: **fullerton@pitt.edu; ke.xu@pitt.edu**

‡ K.Xu and J. Liang contributed equally to this work.

Part 1. DSC of single-ion conductor

DSC samples were prepared inside the Ar-filled glovebox. 8.7 mg of single-ion conductor (PE400-Li) and 7.1 mg PEO:$CsClO_4$ were hermetically sealed in an aluminum DSC pan. Measurements were made on a TA 250 calibrated with an indium standard. To measure the glass transition temperature (T_g) and the melting temperature (T_m), samples were heated to 100 °C to erase thermal history, cooled to -70 °C at 3 °C min^{-1} and heated to 100 °C at 5 °C min^{-1}. As shown in **Figure S1 (a)**, the glass transition temperature of single-ion conductor is identified at 14.5 °C, while only a very subtle melting feature is found at around 75 °C (see the inset in **(a)**). In contrast, the dual-ion conductor, PEO:$CsClO_4$ (ether oxygen to Cs molar ratio = 76:1), has a T_g of -31.5 °C with a distinct melting peak (T_m) at 63.6 °C shown in **(b)**. Although the single-ion conductor is almost completely amorphous, the higher T_g indicates slower segmental polymer mobility and therefore lower ion mobility. This result is consistent with the larger hysteresis in the transfer measurements observed for the single-ion conductor compared to the dual (Figures 4 and 5(a)).

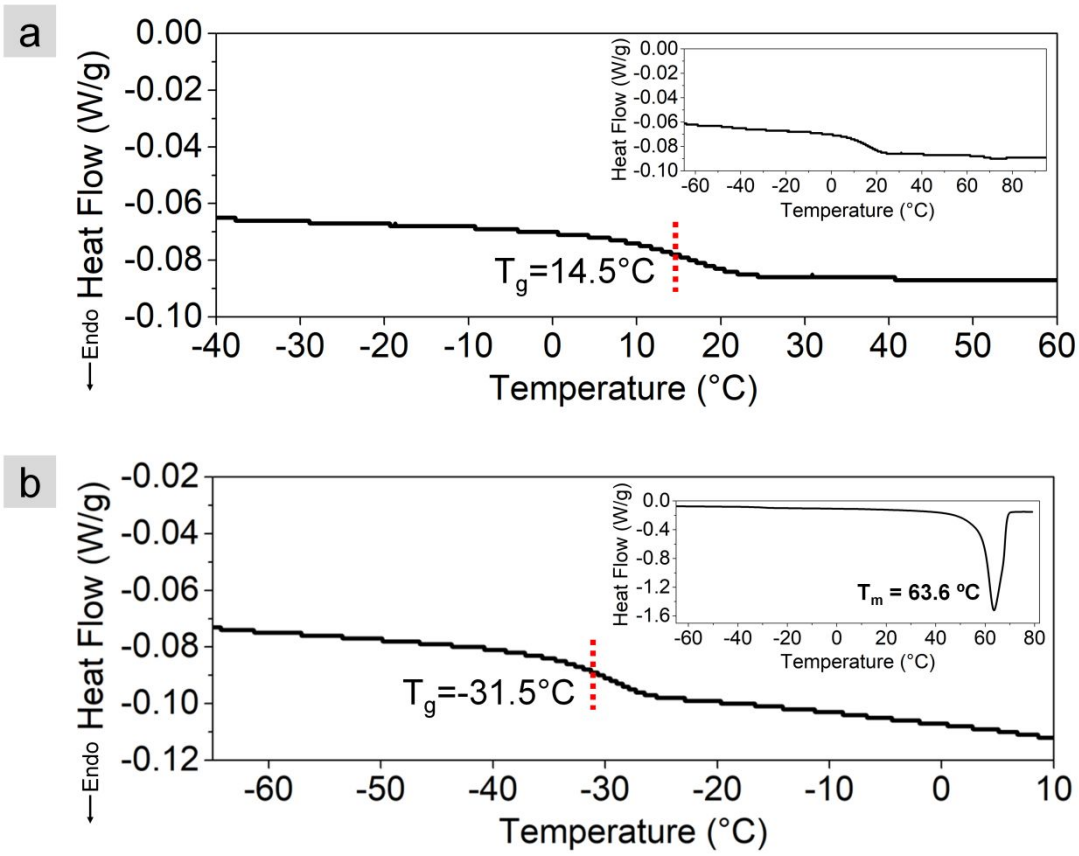

Figure S1. Heat flow versus temperature for **(a)** single-ion conductor and **(b)** dual-ion conductor (PEO:$CsClO_4$, ether oxygen to Cs equals 76:1) showing glass transition (T_g) and melting (T_m) temperatures (inset plots) during the second heating.

Part 2. Two-Dimensional Potential Profiles

One-dimensional, steady-state, voltage profiles are shown in the manuscript (Figure 2) for both the dual- and single-ion conductors at a voltage of ±1 V. Ion drift was modeled using a modified Nernst-Planck-Poisson relationship including a Stern layer set to a thickness equivalent to one ionic radius (2 Å), where the charge density, through which Poisson's equation couples ion concentration and potential, equals zero (i.e., $\nabla \cdot (-\varepsilon_r \varepsilon_0 \nabla V) = 0$).[1,2] The diffusion coefficients of the cations and anions in the dual ion conductor and the cation in the single-ion conductor were set to ~10^{-12} cm^2/s. The anions were held stationary by decreasing the diffusion coefficient to ~10^{-30} cm^2/s; this value was sufficiently low that the location of the anions remained constant on the time scale of study (1 - 10^3 s).

Figures S2 – S4 show potential profiles at time = 0 and at steady-state, and include the corresponding two-dimensional potential profile plots for all geometries considered in Figure 2 of the manuscript. These plots assume that for each geometry the electrodes and electrolytes are uniform in the out-of-plane direction. Note that the electrolyte in Figures S2 – S4 has been rotated horizontally from Figure 2 such that the grounded

electrode is now located at the bottom. At steady state, the two-dimensional surfaces were plotted on a log scale to emphasize the potential adjacent to grounded electrodes where the EDL or depletion layers exist.

2.1 Equal sized Electrode Geometry

Panels on the left column of **Figure S2** (**(a)**, **(c)** and **(e)**) consider the case of a dual-ion conductor with electrodes of equal area. For clarity, only a two-dimensional cross-section of a three-dimensional electrode/electrolyte system with uniform out of plane depth is shown. For simplicity, cations and anions were modeled with the same effective radius, and diffusion coefficient. Voltages were applied to the top boundary and the bottom boundary was grounded. **Figure S2 (c)** shows the potential profile before ions respond to the electric field (i.e., t = 0). Before ions can move, the potential decays linearly across the electrolyte (**Figure S2 (a)**, blue dash) producing parallel vertical field lines (**Figure S2 (c)**). This result is expected for a parallel plate capacitor with an insulating dielectric. At time > 0, the ions migrate in response to the field and accumulate adjacent to electrodes to form two electric double layers (EDLs) at the two electrode surfaces. This results in half of the potential dropped at each electrode producing an axis of symmetry parallel to

both electrodes as shown in **Figure S2 (a)** (red line). The potential drop through the bulk of the electrolyte is nearly zero because the ions in the EDLs screen the field.

The right panels of **Figure S2 (b), (d)** and **(f)** consider the single-ion conductor. Like the dual-ion conductor, a linear potential profile is observed immediately after the electric field is applied (**Figure S2 (b)**, blue dash, and **(d)**). However, as steady state is achieved, cations accumulate and form an EDL adjacent to the lower potential electrode (bottom electrode), while depleting near the opposite electrode (top electrode). The difference in the thickness of accumulation and depletion regions eliminates the axis of symmetry seen in the dual ion conductor case, and the resulting asymmetric profile distributions are shown in **Figure S2 (b)** (red line) and **(f)**.

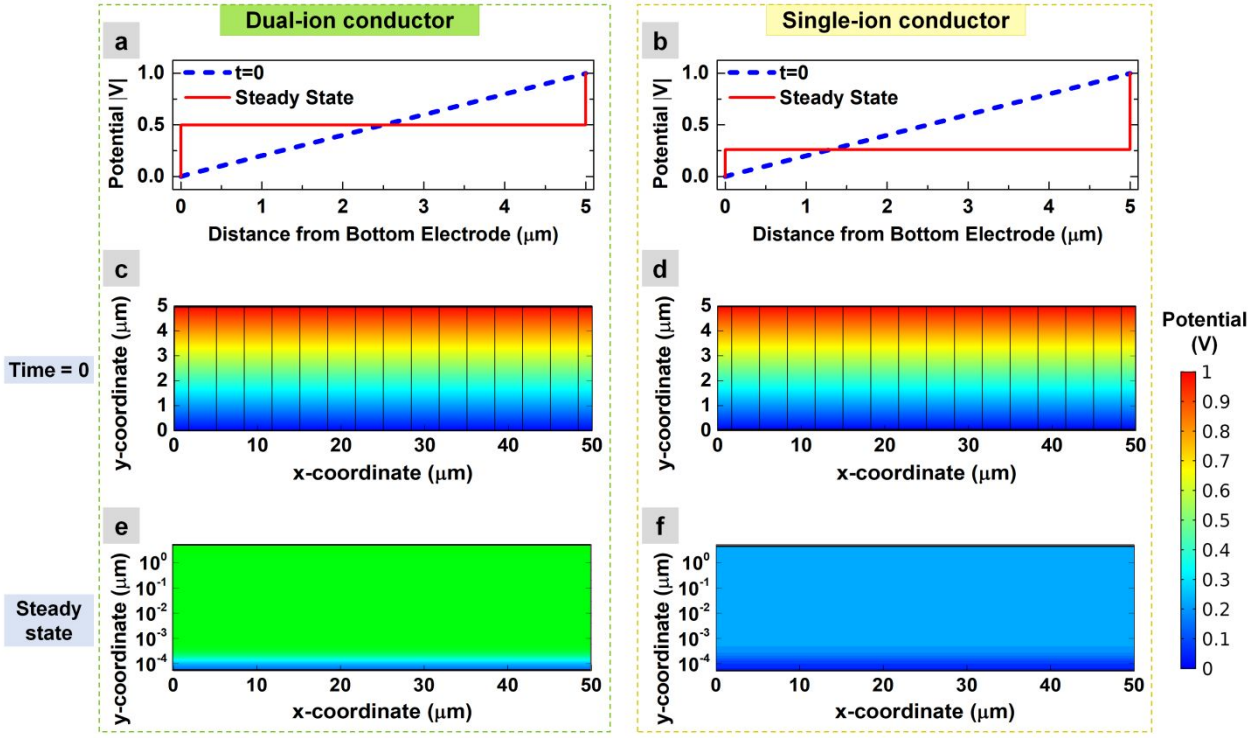

Figure S2. COMSOL modeling of a parallel-plate capacitor with electrodes of equal area. Left column is the dual-ion conductor while the right is the single-ion conductor. Top row: 1D potential profiles of **(a)** dual-ion and **(b)** single-ion conductor at time = 0 (blue dash) when the voltage is applied and at steady state (red line). The potential profiles are obtained at the vertical cutline in the middle (x coordinate = 25 μm) in potential surface maps. Middle row: potential surface maps at time = 0 for the **(c)** dual-ion and **(d)** single-ion conductors with electric field lines included. Bottom row: potential surface maps at steady state for the **(e)** dual-ion and **(f)** single-ion conductors plotted in log scale to emphasize the potential drop adjacent to the grounded electrode due to the EDL.

2.2 Unequal Sized Electrode Geometry

Figures S3 and **S4** show the two-dimensional profile plots resulting from capacitors where the grounded electrode is one tenth the area of its non-grounded counterpart under

positive and negative bias, respectively. This geometry was used to more closely model the geometry of our devices where the channel size is smaller than gate size (see additional discussion in **Part 6** below). Like the previous geometry, with equal sized electrodes, only a two-dimensional cross section of a 3D electrode/electrolyte system with constant out of plane depth is considered. Voltages were again applied to the top boundary while the bottom boundary was grounded. The remaining non-electrode boundaries were defined to mimic a dielectric (e.g., SiO_2). Additional discussions are in the experimental details in the manuscript. The same magnitude of bias (±1 V) was used as the previous geometry containing equally sized electrodes.

For dual-ion conductor, at time = 0, the potential surface above the grounded electrode (analogous to a channel) is similar to that of the previous geometry (equal sized electrodes), where field lines are vertical and parallel (**Figure S3 (c)**). At time > 0 ions start to move and accumulate near their respective electrodes. Once they reach steady state, a potential distribution shown in **Figure S3 (e)** is produced. The steady state surface shows that the electrode area dictates the EDL area, even with the SiO_2 boundary. While the potential is uniform across the bulk, this geometry results in a greater potential drop

near the smaller electrode. This is the result of the grounded electrode having a smaller length (and, by extension, area), and a lower total capacitance, than its non-grounded counterpart, as discussed in the manuscript. The surface map also suggests that ions accumulate uniformly at each point along the length of the grounded electrode (i.e., ion distribution is identical at the center or edge of the grounded electrode).

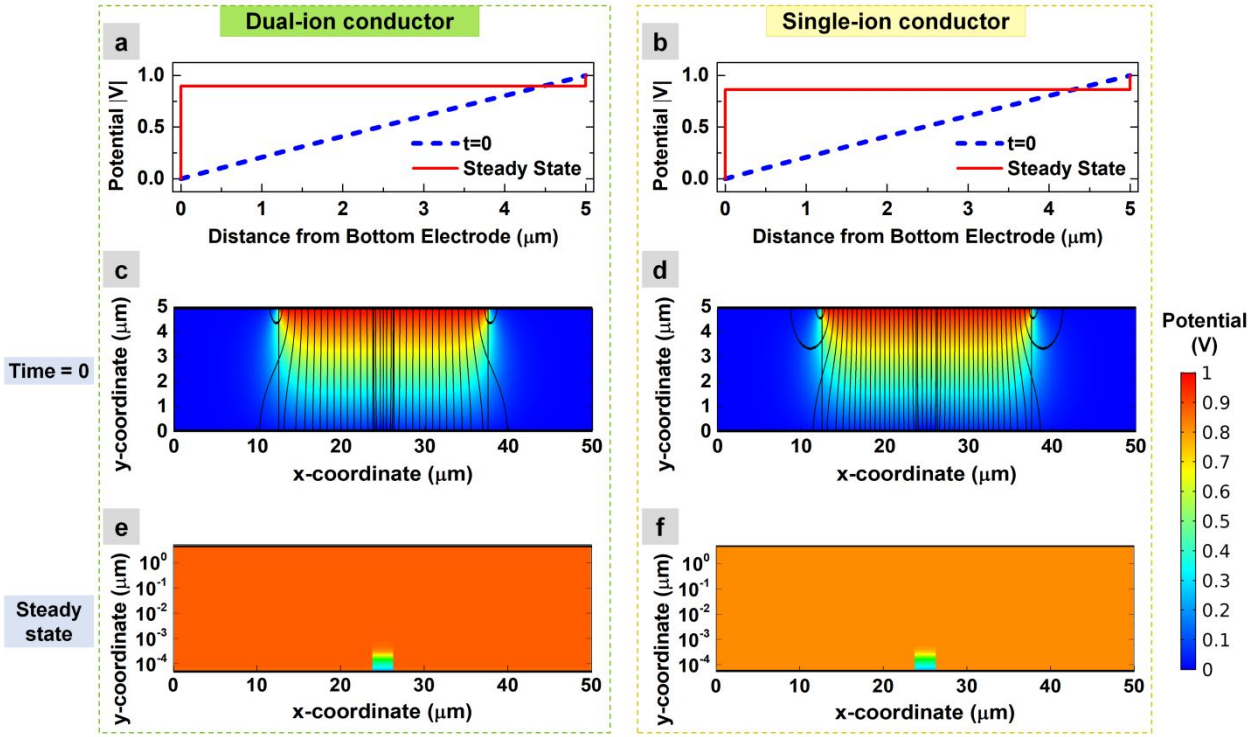

Figure S3. COMSOL modeling of a parallel-plate capacitor with electrodes of unequal areas: the bottom electrode (grounded, 2.5 μm) is one tenth the size of the top electrode (25 μm) where the positive voltage (+1 V) is applied. Left column is the dual-ion conductor

while the right is the single-ion conductor. Top row: 1D potential profiles of **(a)** dual-ion and **(b)** single-ion conductor at time = 0 (blue dash) when the voltage is applied and at steady state (red line). The vertical cutline to obtain the profile is in the middle (x coordinate = 25 μm) in potential surface maps. Middle row: potential surface maps at time = 0 for the **(c)** dual-ion and **(d)** single-ion conductors with electric field lines included. Bottom row: potential surface maps at steady state for the **(e)** dual-ion and **(f)** single-ion conductors plotted in log scale to emphasize the potential drop adjacent to the grounded electrode due to the EDL.

The second column of **Figure S3** shows how the single-ion conductor response in the unequal sized electrodes geometry under same positive bias. The positive bias causes cations to accumulate near the small grounded electrode and deplete near the large ungrounded electrode. The length of the EDL or depletion region always equals to the length of the electrode. Unlike in the previous geometry with equal sized electrodes where the depletion length is always the same as the EDL length, now the depletion length is 10

times the EDL length, reflecting the 10 times difference in electrode length. Since the depletion length is now much larger than that of the EDL, it no longer needs to be significantly thicker than the EDL to conserve charge; instead it will have a thickness comparable to that of the EDL. This results in a surface similar to the dual-ion conductor.

Figure S4 shows the two electrolytes in the same geometry as **Figure S3,** but the polarity is reversed (a bias of -1 V is applied). **Figures S4 (a)** (red line) and **(c)** shows that, for the dual-ion conductor, the unequal electrode length again produce unequal potential drops adjacent to each electrode; however, the fraction of potential to drop near the grounded electrode does not depend on the polarity. This is because the ions modeled in the dual-ion conductor have opposite charge but have identical effective radius and diffusion coefficient; this allows anions and cations to produce equal magnitude EDL. However, the potential distribution for the single-ion conductor does depend on polarity. At time > 0, the depletion region is now adjacent to the small electrode. Its thickness is comparable to its counterpart in the previous geometry (equal sized electrodes), but since it is near a small electrode, the required potential drop is much larger (**Figure S4 (a)** and **(b)**, red line) and therefore constitutes essentially all of the applied potential.

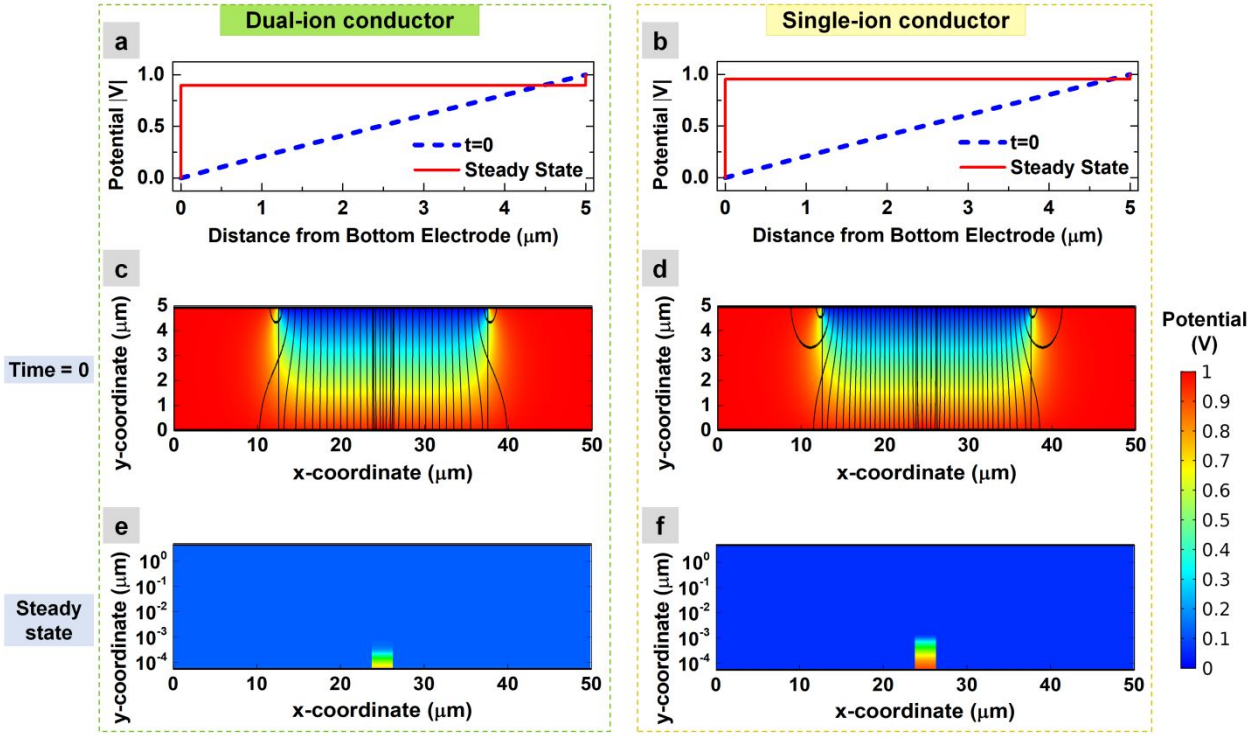

Figure S4. COMSOL modeling of a parallel-plate capacitor with electrodes of unequal areas: the bottom electrode (grounded, 2.5 μm) is one tenth the size of the top electrode (25 μm) where the positive voltage (+1 V) is applied. Left column is the dual-ion conductor while the right is the single-ion conductor. Top row: 1D potential profiles of **(a)** dual-ion and **(b)** single-ion conductor at time = 0 (blue dash) when the voltage is applied and at steady state (red line). The vertical cutline to obtain the profile is in the middle (x coordinate = 25 μm) in potential surface maps. Middle row: potential surface maps at time = 0 for the **(c)** dual-ion and **(d)** single-ion conductors with electric field lines included.

Bottom row: potential surface maps at steady state for the **(e)** dual-ion and **(f)** single-ion conductors plotted in log scale to emphasize the potential drop adjacent to the grounded electrode due to the EDL.

Part 3. Transfer measurements

3 different graphene FETs were fabricated and measured. The results of Devices 1 and 2 are shown in Figure 4 of the manuscript, and the ionic gating results of Device 3 is shown in Figure 5. As mentioned in the manuscript, the Dirac point location in transfer measurements shifts to negative V_{SG} after the deposition of the single-ion conductor, and does not return to zero after removing the electrolyte with solvent and AFM cleaning. This shift is not observable in Figure 4 because the transfer curves are plotted with respect to V_G-V_{Dirac} to better compare the *n*- and *p*-branch current using different gating methods. In **Figure S5** below the complete measurement results of all 3 device are summarized and the shift is clearly observable. However, this shift is commonly observed in EDL gating of graphene FETs using dual-ion conductors,[3,4] and reflects that the electrolyte induces doping of the graphene channel even in the absence of a gate voltage.

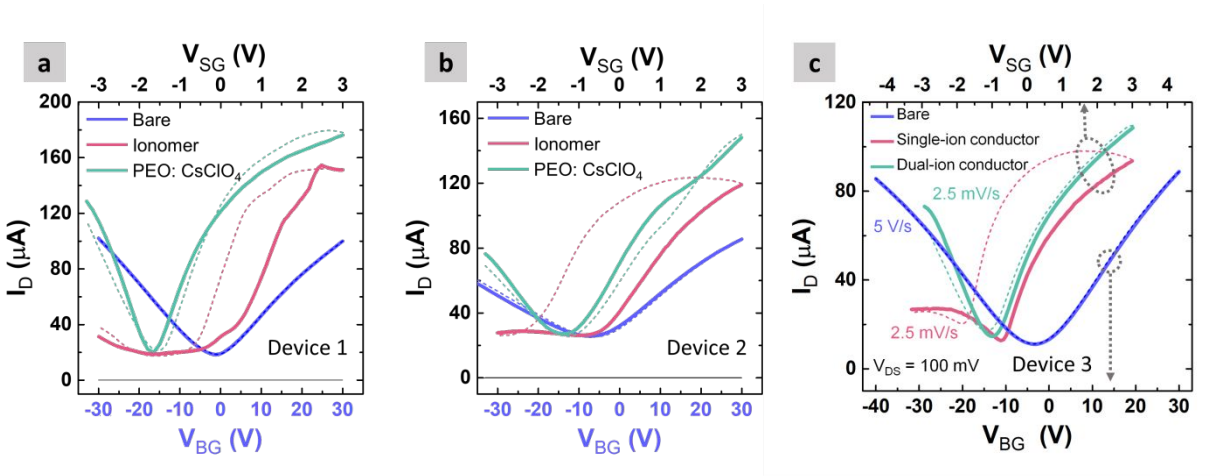

Figure S5. Transfer characteristics of all three graphene FETs (Device 1/2/3 corresponds to Figure S5a/b/c) with the comparison between back gating on the bare FET (no ion conductors, blue curves), EDL gating using the single-ion (red curves) and dual-ion conductors (green curves). The solid lines indicate that the transfer scans are from negative to positive gate voltages, while the dotted line are from the reverse scanning direction.

The differences in p-branch current and hysteresis between the three devices are likely due to the difference in intrinsic doping level of the flake, which can be understood by considering the transfer characteristics of bare FET without electrolyte. As shown in Figure S5, the as-fabricated Devices 1 and 3 have Dirac points located close to zero

(V_{Dirac} = -0.5 V and -2.75 V), while Device 2 is more n-type doped (V_{Dirac} = -7.5 V). Additionally, for both Devices 1 and 3, their n- and p-branch currents are similar as-fabricated, while Device 2 has a p-branch current about 60% of the n-branch current (compared after subtracting the minimal conducting current at Dirac point). These intrinsic difference could possibly explain the differences in the transfer characteristics when the single-ion conductor gating is used. For example, for Devices 1 and 3, the p-branches are both about 12% of the n-branch; while in Device 2, there is no observable p-branch within the measurement window, presumably because it is more strongly n-doped. In addition, from the modeling results in Figure 5(a) we know for single-ion conductor gating, the hysteresis is larger in the n-branch than the p-branch. In Device 2, more of the n-branch is captured and therefore more hysteresis is expected compared to Devices 1 and 3.

Part 4. Estimation of EDL capacitance in the single-ion conductor device

The EDL capacitance induced by the single-ion conductor is estimated by a DC measurement. A series of V_{SG} transfer measurements under various V_{BG} are plotted in **Figure S6 (a)**. V_{BG} was held at one value while sweeping V_{SG} with V_{DS} fixed at 0.05 V. The location of the Dirac point in the side gate transfer scans is a function of V_{BG}. Specifically, the Dirac point shifts towards positive V_{SG} values as the V_{BG} becomes more negative. The extent of the shift along the V_{SG} axis is almost linearly proportional to the applied V_{BG}, as shown in **Figure S6 (b)**. The blue squares are experimental data and the solid lines represent a linear fit. The slope of the solid line (*i.e.*, $\Delta V_{BG}/\Delta V_{SG}$) is 43.33. For the double-gated device with a thin channel and thick back gate oxide, this ratio can be used to calculate the capacitance of the electric double layer (C_{EDL}) as $C_{EDL}/C_{OX} = -\Delta V_{BG}/\Delta V_{SG}$.[5,6] Using $\varepsilon_{OX} = 3.9$ and $t_{OX} = 90$ nm, C_{OX} is 0.0383 μF/cm^2, and the calculated C_{EDL} is ~1.66 μF/cm^2, which is similar as the C_{EDL} measured on dual-ion conductors.[7] Nearly equivalent capacitances between the single- and dual-ion conductors implies the possibility of achieving similar gating capability and carrier densities, which is in

agreement with the experimental findings and simulation results presented in the manuscript.

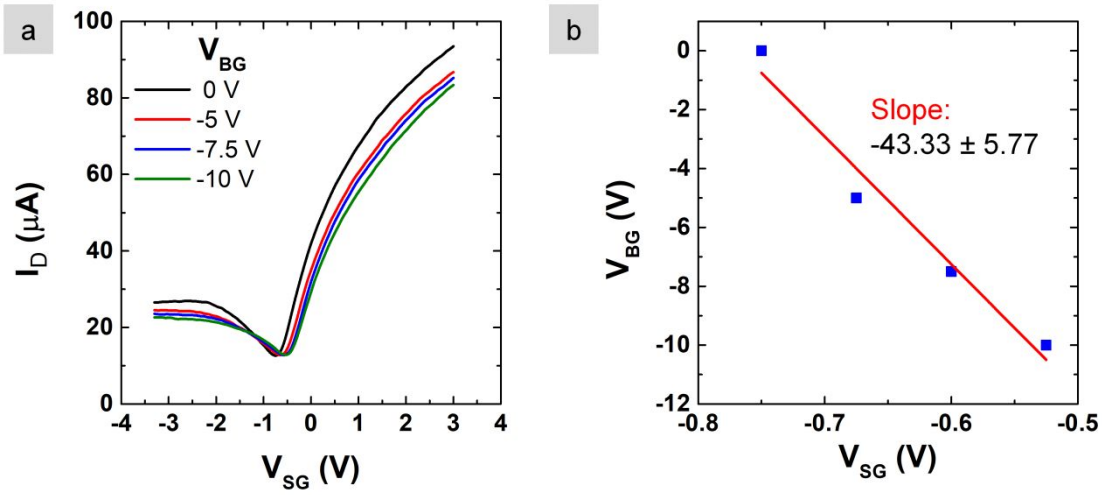

Figure S6. (a) Transfer characteristics of a graphene FET gated by the single-ion conductor (through a side gate, V_{SG}) while under a series of constant back gate voltages (V_{BG} = 0, -5, -7.5, -10 V). **(b)** Dirac point (blue dot) in the side gate transfer curves (V_{SG}) as a function of V_{BG}.

Part 5. Impact of device geometry on charge density

Figure 4 in the manuscript presented how the single ion conductor produces different magnitudes of carrier density under positive and negative voltage. This unequal charge density is directly related to device geometry. To elaborate on this, the transient carrier densities for both conductors are shown in **Figure S7** to highlight the dependence of carrier densities on geometry. We modeled 3 geometries including: **(a)** the grounded electrode (2.5 μm) is 10 times smaller than ungrounded electrode (25 μm); **(b)** both electrodes are long (50 μm in length); and **(c)** both electrodes are equally small (2.5 μm).

The modeling shows that a dual-ion conductor will always produce EDLs with equal carrier density under both positive and negative applied voltage, regardless of whether electrode sizes is equal. Meanwhile, a single-ion conductor will only produce symmetric carrier densities (either constituting an EDL or depletion region) if the electrodes are equally sized.

In addition, the magnitude of charge density depends on the ratio between the area of the two electrodes. Using the unequally sized electrodes (**Figure S7 (a)**) resulted in a greater carrier density per area adjacent to the grounded electrode than using equally sized electrodes (**Figures S7 (b) and (c)**). This is because the large electrode will have a higher capacitance requiring less voltage drop to sustain the same charge. Since the depletion region near the larger electrode requires less voltage drop, EDLs near the smaller (grounded) electrode can produce larger voltage drops resulting in greater carrier density. The voltage sweeps shown in **Figure S7 (a)** show such an increase in carrier density (compared with **S7 (b)** or **(c)**). The only exception is when a depletion region forms near the grounded electrode. When the two electrodes have equal area, the depletion

region already requires a large voltage drop (0.75 out of 1 V). When the depletion region is adjacent to a small grounded electrode, it requires an even larger voltage drop constituting nearly the entirety of the applied voltage (0.95 out of 1 V). Because of the large voltage drop required to create a depletion region near a small electrode, the single-ion conductor does not produce a significantly higher carrier density under negative bias after implementing the new geometry.

To ensure the increase in sheet density was the result of unequal electrode length and not simply changing the area of the electrode of interest, both electrodes were decreased to the smaller size (2.5 μm), and results are shown in **Figure S7 (c).** Zero charge boundary conditions were once again employed to maximize similarity between this geometry and the original equally sized electrode geometry. This geometry resulted in carrier densities **(Figure S7 (c))** of similar magnitude to the geometry in **Figure S7 (b)** where the two electrodes are both 50 μm long.

Interestingly, we also noticed that reducing the ungrounded electrode (right side) size also reduced the achievable carrier density for both the single- and dual-ion conductors. This could suggest that – as a general rule – it is desirable to design the gate electrode larger than channel size for EDL gating to achieve a higher carrier density in the channel.

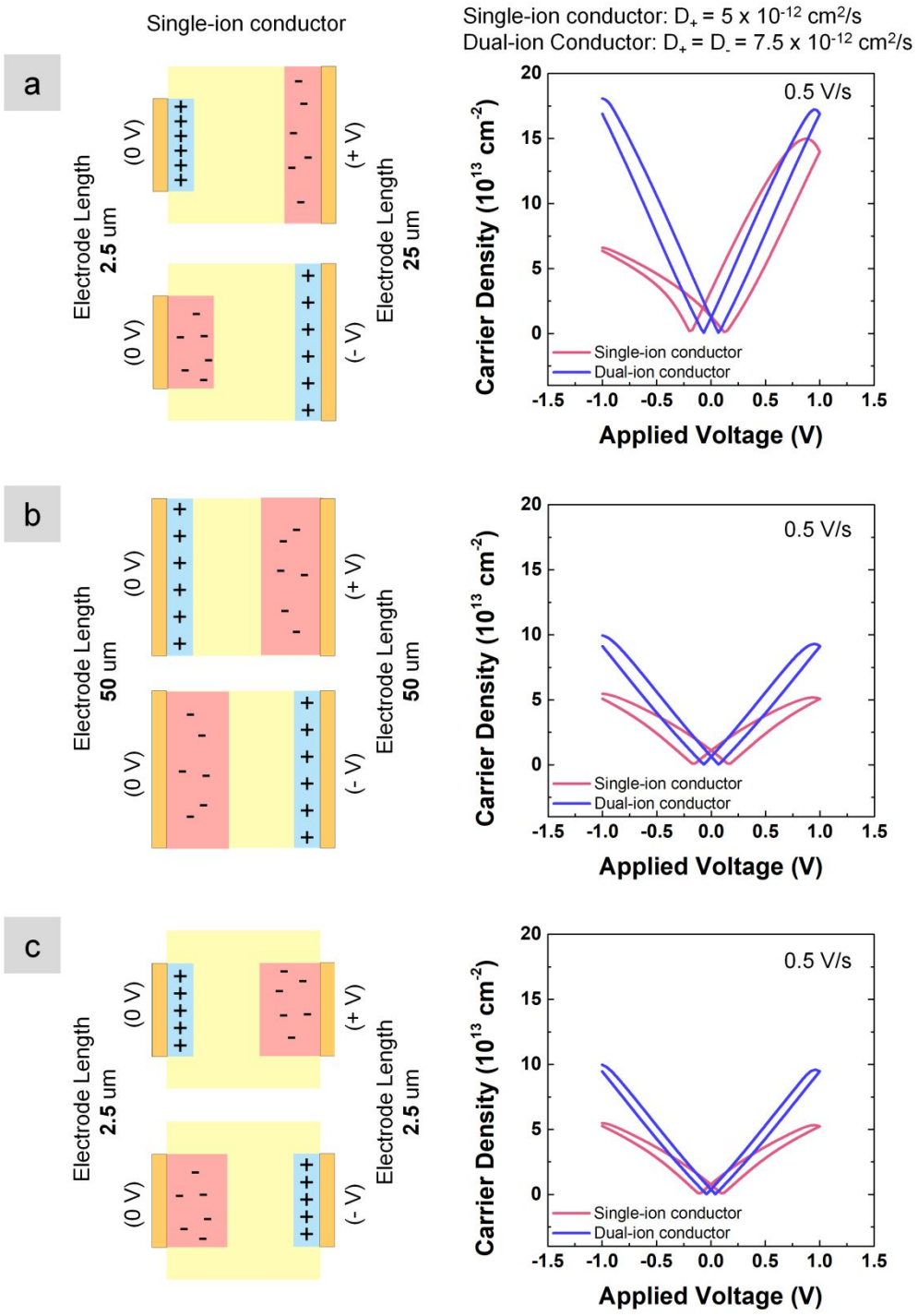

Figure S7. (Left column) Schematics of a single-ion conductor with charge accumulations under the applied voltages, and (right column) the corresponding accumulated charge

carrier densities for the single-ion (red) and dual-ion conductors (blue) during sweeping the applied voltages. The dependence of charge density on the ratio of electrode size is illustrated in 3 geometries during 1D modeling: **(a)** electrode size (right, 25 μm in length) = 10x electrode (left, grounded, 2.5 μm); **(b)** equally sized electrodes (50 μm in length); and **(c)** equally sized small electrodes (2.5 μm in length).

Part 6. Effective gate size during EDL-gated transfer measurements

Experimentally, the graphene and $MoTe_2$ FETs are fabricated based on exfoliated flakes. The length and the width of the channels vary slightly from device to device depending on the size of the flakes. For each device, the side gate is 10 μm away from the channel, and the length of the side gate (i.e., the length of the edge that is closest to the channel) is the same as the channel length. However, during EDL-gated transfer measurements (using either single or dual-ion conductor) the *effective* gate size is larger than channel size. This is because under a gate voltage, the EDL forms across not only the edge of side gate that is closest to the channel, but also the entire gate metal area

that is in contact with electrolyte. For example, under a positive gate voltage (V_{GS} > 0 V), anions migrate towards the gate metal. Under steady state condition, if we consider the entire geometry as a Metal-Insulator-Metal (MIM) capacitor, the total gate metal surface area is essentially one side of a large capacitor plate. Similarly, a cationic EDL forms across, and induces electrons in, all of the channel, the source metal, and the drain metal area. However, because a small but non-zero V_{DS} is applied (i.e., V_{GS} >> V_{DS} > 0 V), electrons flow from source through channel to drain. The transport of electrons between source and drain is limited by the transport through the channel, making the channel area the *effective area* of the other side of the capacitor plate. The same conclusion that the effective gate size is larger than channel size can also be identified by comparing the experimental results with modeling. As shown in **Figure S7 (b)** and **(c),** modeling suggests that if the effective gate and channel area are the same, then 1) the transfer measurement should be symmetric for both the single- and dual-ion conductors, and 2) the gating capability (e.g., maximum achievable charge density) of single-ion conductor is 50% of the dual-ion conductor. However, experimentally we observe a suppressed *p*-branch for all the measured devices on both graphene and $MoTe_2$, and we see a similar gating

capability between single-ion conductor and dual-ion conductor for the *n*-branch. This result closely matches the modeling results in **Figure S7 (a),** where the electrode on which the voltage is being applied (*i.e.* the gate) is 10 times larger than the other electrode that is grounded (*i.e*. the channel).

Part 7. AFM topology scan after single-ion conductor removal

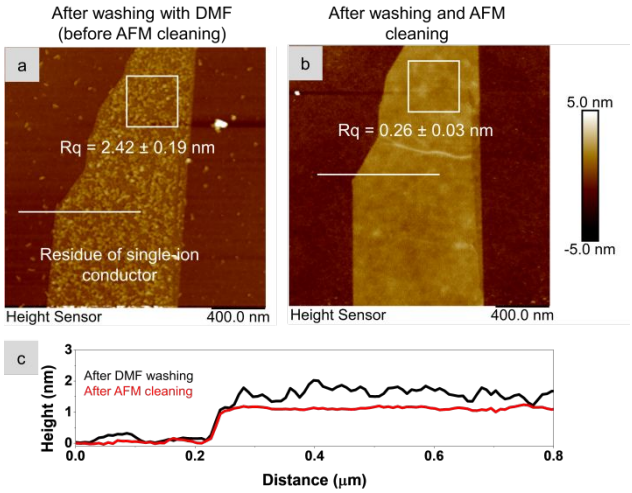

Figure S8. AFM topology scan of one graphene FET channel (a) after washing the single-ion conductor with Dimethylformamide (DMF) but before AFM cleaning, and (b) after AFM cleaning. The averaged roughness (Rq) values are reported where the error represents one standard deviation from the mean. Rq was calculated based on 6 different locations,

with one of the locations indicated by the 400 × 400 nm white box. (c) Line scans of flake height before (black) and after AFM cleaning (red line). The positions of line scans are indicated by white lines on AFM images.

Part 8. Output characteristics of single-ion conductor gated $MoTe_2$ FET

The output characteristics of a single-ion conductor gated $MoTe_2$ FET under four different gate voltages is shown in **Figure S9 (a)** and zoomed-in for the small current region in **(b).** I_D increases as the gate voltage increases from 0 to 3 V, indicating the effective gate control of channel current using the single-ion conductor. No saturation is observed up to V_D = 1 V.

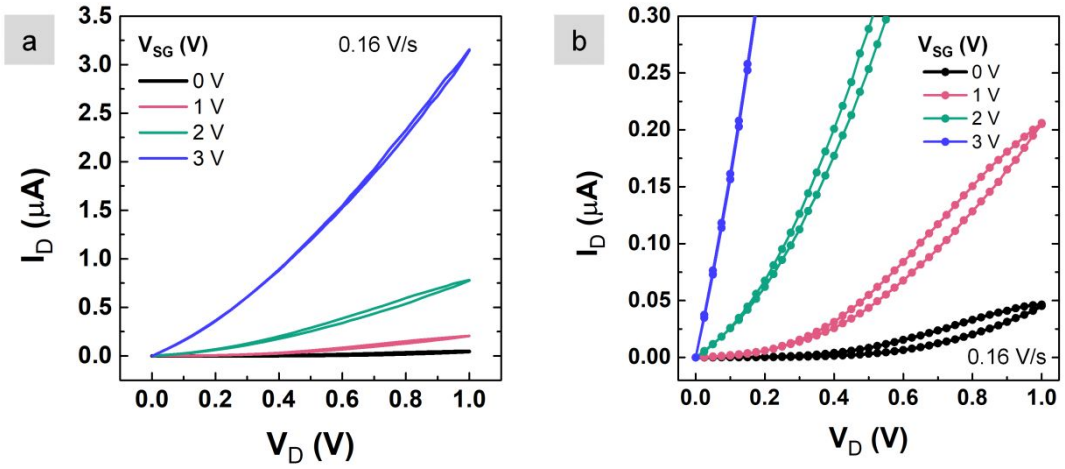

Figure S9. (a) Output characteristics of a single-ion conductor gated $MoTe_2$ FET under four different gate voltages (0 – 3 V). **(b)** The zoomed-in plot at small I_D region on the same output characteristics.

References

(1) Kilic, M. S.; Bazant, M. Z.; Ajdari, A. Steric Effects in the Dynamics of Electrolytes at Large Applied Voltages. II. Modified Poisson-Nernst-Planck Equations. *Phys. Rev. E - Stat. Nonlinear, Soft Matter Phys.* **2007**.

(2) Wang, H.; Pilon, L. Accurate Simulations of Electric Double Layer Capacitance of Ultramicroelectrodes. *J. Phys. Chem. C* **2011**.

(3) Kinder, E. W.; Fuller, A.; Lin, Y. C.; Robinson, J. A.; Fullerton-Shirey, S. K. Increasing the Room-Temperature Electric Double Layer Retention Time in Two-Dimensional Crystal FETs. *ACS Appl. Mater. Interfaces* **2017**, *9*, 25006–25013.

(4) Li, H. M.; Xu, K.; Bourdon, B.; Lu, H.; Lin, Y. C.; Robinson, J. A.; Seabaugh, A. C.; Fullerton-Shirey, S. K. Electric Double Layer Dynamics in Poly(Ethylene Oxide) LiClO4 on Graphene Transistors. *J. Phys. Chem. C* **2017**, *121*, 16996–17004.

(5) Ernst, T.; Cristoloveanu, S.; Ghibaudo, G.; Ouisse, T.; Horiguchi, S.; Ono, Y.; Takahashi, Y.; Murase, K. Ultimately Thin Double-Gate SOI MOSFETs. *IEEE Trans. Electron Devices* **2003**, *50*, 830–838.

(6) Ortiz-Conde, A.; García-Sánchez, F. J.; Muci, J.; Malobabic, S.; Liou, J. J. A Review of Core Compact Models for Undoped Double-Gate SOI MOSFETs. *IEEE Transactions on Electron Devices*, 2007, *54*, 131–140.

(7) Xu, K.; Islam, M. M.; Guzman, D. M.; Seaubaugh, A.; Strachan, A.; Fullerton-Shirey, S. K. Pulse Dynamics of Electric Double Layer Formation on All-Solid-State Graphene Field-Effect Transistors. *ACS Appl. Mater. Interfaces* **2018**,

acsami.8b13649.

Bibliography

[1] Karthik Krishnan, Tohru Tsuruoka, Cedric Mannequin, and Masakazu Aono. Mechanism for conducting filament growth in self-assembled polymer thin films for redox-based atomic switches. *Advanced Materials*, 28(4):640–648, 2016.

[2] Daniele Ielmini. Resistive switching memories based on metal oxides: mechanisms, reliability and scaling. *Semiconductor Science and Technology*, 31(6):063002, 2016.

[3] Sen Liu, Nianduan Lu, Xiaolong Zhao, Hui Xu, Writam Banerjee, Hangbing Lv, Shibing Long, Qingjiang Li, Qi Liu, and Ming Liu. Eliminating negative-set behavior by suppressing nanofilament overgrowth in cation-based memory. *Advanced Materials*, 28(48):10623–10629, 2016.

[4] Rainer Waser, Regina Dittmann, Georgi Staikov, and Kristof Szot. Redox-based resistive switching memories–nanoionic mechanisms, prospects, and challenges. *Advanced materials*, 21(25-26):2632–2663, 2009.

[5] Ilia Valov, Rainer Waser, John R Jameson, and Michael N Kozicki. Electrochemical metallization memories—fundamentals, applications, prospects. *Nanotechnology*, 22(25):254003, 2011.

[6] Yangyin Chen. Reram: History, status, and future. *IEEE Transactions on Electron Devices*, 67(4):1420–1433, 2020.

[7] Hiroyuki Akinaga and Hisashi Shima. Resistive random access memory (reram) based on metal oxides. *Proceedings of the IEEE*, 98(12):2237–2251, 2010.

[8] Adnan Mehonic, Manveer S Munde, Wing H Ng, Mark Buckwell, Luca Montesi, MALAJ Bosman, AL Shluger, and AJ Kenyon. Intrinsic resistance switching in amorphous silicon oxide for high performance siox reram devices. *Microelectronic Engineering*, 178:98–103, 2017.

[9] Sparsh Mittal, Jeffrey S Vetter, and Dong Li. A survey of architectural approaches for managing embedded dram and non-volatile on-chip caches. *IEEE Transactions on Parallel and Distributed Systems*, 26(6):1524–1537, 2014.

[10] Yexin Deng, Peng Huang, Bing Chen, Xiaolin Yang, Bin Gao, Juncheng Wang, Lang Zeng, Gang Du, Jinfeng Kang, and Xiaoyan Liu. Rram crossbar array with cell selection device: A device and circuit interaction study. *IEEE transactions on Electron Devices*, 60(2):719–726, 2012.

[11] Lixue Xia, Peng Gu, Boxun Li, Tianqi Tang, Xiling Yin, Wenqin Huangfu, Shimeng Yu, Yu Cao, Yu Wang, and Huazhong Yang. Technological exploration of rram crossbar array for matrix-vector multiplication. *Journal of Computer Science and Technology*, 31(1):3–19, 2016.

[12] K Tsunoda, Kentaro Kinoshita, H Noshiro, Y Yamazaki, T Iizuka, Y Ito, A Takahashi, A Okano, Y Sato, T Fukano, et al. Low power and high speed switching of ti-doped nio reram under the unipolar voltage source of less than 3 v. In *2007 IEEE International Electron Devices Meeting*, pages 767–770. IEEE, 2007.

[13] MJ Kim, IG Baek, YH Ha, Seung Jae Baik, JH Kim, DJ Seong, SJ Kim, YH Kwon, CR Lim, HK Park, et al. Low power operating bipolar tmo reram for sub 10 nm era. In *2010 International Electron Devices Meeting*, pages 19–3. IEEE, 2010.

[14] H-S Philip Wong and Sayeef Salahuddin. Memory leads the way to better computing. *Nature nanotechnology*, 10(3):191, 2015.

[15] Yang Zhang, Ziqing Duan, Rui Li, Chieh-Jen Ku, Pavel I Reyes, Almamun Ashrafi, Jian Zhong, and Yicheng Lu. Vertically integrated zno-based 1d1r structure for resistive switching. *Journal of Physics D: Applied Physics*, 46(14):145101, 2013.

[16] BJ Choi, Doo Seok Jeong, SK Kim, C Rohde, S Choi, JH Oh, HJ Kim, CS Hwang, K Szot, R Waser, et al. Resistive switching mechanism of tio 2 thin films grown by atomic-layer deposition. *Journal of applied physics*, 98(3):033715, 2005.

[17] Rainer Waser and Masakazu Aono. Nanoionics-based resistive switching memories. In *Nanoscience And Technology: A Collection of Reviews from Nature Journals*, pages 158–165. World Scientific, 2010.

[18] Michael Kund, Gerhard Beitel, C-U Pinnow, Thomas Rohr, Jorg Schumann, Ralf Symanczyk, K Ufert, and Gerhard Muller. Conductive bridging ram (cbram): An emerging non-volatile memory technology scalable to sub 20nm. In *IEEE InternationalElectron Devices Meeting, 2005. IEDM Technical Digest.*, pages 754–757. IEEE, 2005.

[19] Garrison M Crouch, Donghoon Han, Susan K Fullerton-Shirey, David B Go, and Paul W Bohn. Addressable direct-write nanoscale filament formation and dissolution by nanoparticle-mediated bipolar electrochemistry. *Acs Nano*, 11(5):4976–4984, 2017.

[20] Zhongmou Chao, Kutay B Sezginel, Ke Xu, Garrison M Crouch, Abigale E Gray, Christopher E Wilmer, Paul W Bohn, David B Go, and Susan K Fullerton-Shirey. Silver nanofilament formation dynamics in a polymer-ionic liquid thin film by direct write. *Advanced Functional Materials*, 30(6):1907950, 2020.

[21] Elia Ambrosi, Alessandro Bricalli, Mario Laudato, and Daniele Ielmini. Impact of oxide and electrode materials on the switching characteristics of oxide reram devices. *Faraday discussions*, 213:87–98, 2019.

[22] Huaqiang Wu, Xinyi Li, Feiyang Huang, An Chen, Zhiping Yu, and He Qian. Stable self-compliance resistive switching in aloδ/ta2o5- x/taoy triple layer devices. *Nanotechnology*, 26(3):035203, 2014.

[23] Alexander Poddubny, Ivan Iorsh, Pavel Belov, and Yuri Kivshar. Hyperbolic metamaterials. *Nature photonics*, 7(12):948, 2013.

[24] Anthony J Hoffman, Leonid Alekseyev, Scott S Howard, Kale J Franz, Dan Wasserman, Viktor A Podolskiy, Evgenii E Narimanov, Deborah L Sivco, and Claire Gmachl. Negative refraction in semiconductor metamaterials. *Nature materials*, 6(12):946–950, 2007.

[25] Anan Fang, Thomas Koschny, and Costas M Soukoulis. Optical anisotropic metamaterials: Negative refraction and focusing. *Physical Review B*, 79(24):245127, 2009.

[26] Yoeri van de Burgt, Ewout Lubberman, Elliot J Fuller, Scott T Keene, Grégorio C Faria, Sapan Agarwal, Matthew J Marinella, A Alec Talin, and Alberto Salleo. A non-volatile organic electrochemical device as a low-voltage artificial synapse for neuromorphic computing. *Nature materials*, 16(4):414–418, 2017.

[27] Kwabena Boahen. A neuromorph's prospectus. *Computing in Science & Engineering*, 19(2):14–28, 2017.

[28] Yoeri Van De Burgt, Armantas Melianas, Scott Tom Keene, George Malliaras, and Alberto Salleo. Organic electronics for neuromorphic computing. *Nature Electronics*, 1(7):386–397, 2018.

[29] J Joshua Yang, Dmitri B Strukov, and Duncan R Stewart. Memristive devices for computing. *Nature nanotechnology*, 8(1):13, 2013.

[30] Zhongrui Wang, Saumil Joshi, Sergey E Savel'ev, Hao Jiang, Rivu Midya, Peng Lin, Miao Hu, Ning Ge, John Paul Strachan, Zhiyong Li, et al. Memristors with diffusive dynamics as synaptic emulators for neuromorphic computing. *Nature materials*, 16(1):101–108, 2017.

[31] Zhongrui Wang, Saumil Joshi, Sergey Savel'ev, Wenhao Song, Rivu Midya, Yunning Li, Mingyi Rao, Peng Yan, Shiva Asapu, Ye Zhuo, et al. Fully memristive neural networks for pattern classification with unsupervised learning. *Nature Electronics*, 1(2):137–145, 2018.

[32] Wen-Peng Lin, Shu-Juan Liu, Tao Gong, Qiang Zhao, and Wei Huang. Polymer-based resistive memory materials and devices. *Advanced materials*, 26(4):570–606, 2014.

[33] Shosuke Fujii, Jean Anne C Incorvia, Fang Yuan, Shengjun Qin, Fei Hui, Yuanyuan Shi, Yang Chai, Mario Lanza, and H-S Philip Wong. Scaling the cbram switching layer diameter to 30 nm improves cycling endurance. *IEEE Electron Device Letters*, 39(1):23–26, 2017.

[34] Nagarajan Raghavan. Performance and reliability trade-offs for high-κ rram. *Microelectronics Reliability*, 54(9-10):2253–2257, 2014.

[35] Qi Liu, Shibing Long, Hangbing Lv, Wei Wang, Jiebin Niu, Zongliang Huo, Junning Chen, and Ming Liu. Controllable growth of nanoscale conductive filaments in solid-electrolyte-based reram by using a metal nanocrystal covered bottom electrode. *ACS nano*, 4(10):6162–6168, 2010.

[36] Yiming Sun, Cheng Song, Jun Yin, Xianzhe Chen, Qin Wan, Fei Zeng, and Feng Pan. Guiding the growth of a conductive filament by nanoindentation to improve resistive switching. *ACS applied materials & interfaces*, 9(39):34064–34070, 2017.

[37] Akihito Sawa. Resistive switching in transition metal oxides. *Materials today*, 11(6):28–36, 2008.

[38] A Manuel Stephan. Review on gel polymer electrolytes for lithium batteries. *European polymer journal*, 42(1):21–42, 2006.

[39] Qingzhou Wan, Mohammad T Sharbati, John R Erickson, Yanhao Du, and Feng Xiong. Emerging artificial synaptic devices for neuromorphic computing. *Advanced Materials Technologies*, 4(4):1900037, 2019.

[40] Raisul Islam, Haitong Li, Pai-Yu Chen, Weier Wan, Hong-Yu Chen, Bin Gao, Huaqiang Wu, Shimeng Yu, Krishna Saraswat, and HS Philip Wong. Device and materials requirements for neuromorphic computing. *Journal of Physics D: Applied Physics*, 52(11):113001, 2019.

[41] Stefano Ambrogio, Pritish Narayanan, Hsinyu Tsai, Robert M Shelby, Irem Boybat, Carmelo di Nolfo, Severin Sidler, Massimo Giordano, Martina Bodini, Nathan CP Farinha, et al. Equivalent-accuracy accelerated neural-network training using analogue memory. *Nature*, 558(7708):60–67, 2018.

[42] XiaoLiang Hong, Desmond JiaJun Loy, Putu Andhita Dananjaya, Funan Tan, Chee-Mang Ng, and WenSiang Lew. Oxide-based rram materials for neuromorphic computing. *Journal of materials science*, 53(12):8720–8746, 2018.

[43] Pai-Yu Chen, Xiaochen Peng, and Shimeng Yu. Neurosim+: An integrated device-to-algorithm framework for benchmarking synaptic devices and array architectures. In *2017 IEEE International Electron Devices Meeting (IEDM)*, pages 6–1. IEEE, 2017.

[44] Chun-Mo Yang, Hyung-Sun Kim, Byung-Ki Na, Kyong-Soo Kum, and Byung Won Cho. Gel-type polymer electrolytes with different types of ceramic fillers and lithium salts for lithium-ion polymer batteries. *Journal of power sources*, 156(2):574–580, 2006.

[45] MS Cho, B Shin, SD Choi, Y Lee, and KG Song. Gel polymer electrolyte nanocomposites pegda with mg–al layered double hydroxides. *Electrochimica acta*, 50(2-3):331–334, 2004.

[46] Xiao Zheng Shu, Yanchun Liu, Fabio S Palumbo, Yi Luo, and Glenn D Prestwich. In situ crosslinkable hyaluronan hydrogels for tissue engineering. *Biomaterials*, 25(7-8):1339–1348, 2004.

[47] Adam F Visentin, Stephanie Alimena, and Matthew J Panzer. Influence of ionic liquid selection on the properties of poly (ethylene glycol) diacrylate-supported ionogels as solid electrolytes. *ChemElectroChem*, 1(4):718–721, 2014.

[48] Adam F Visentin and Matthew J Panzer. Poly (ethylene glycol) diacrylate-supported ionogels with consistent capacitive behavior and tunable elastic response. *ACS applied materials & interfaces*, 4(6):2836–2839, 2012.

[49] Morgan W Schulze, Lucas D McIntosh, Marc A Hillmyer, and Timothy P Lodge. High-modulus, high-conductivity nanostructured polymer electrolyte membranes via polymerization-induced phase separation. *Nano letters*, 14(1):122–126, 2014.

[50] Barbara Rupp, Martin Schmuck, Andrea Balducci, Martin Winter, and Wolfgang Kern. Polymer electrolyte for lithium batteries based on photochemically crosslinked poly (ethylene oxide) and ionic liquid. *European polymer journal*, 44(9):2986–2990, 2008.

[51] Wen Lu, Andrei G Fadeev, Baohua Qi, Elisabeth Smela, Benjamin R Mattes, Jie Ding, Geoffrey M Spinks, Jakub Mazurkiewicz, Dezhi Zhou, Gordon G Wallace, et al. Use of ionic liquids for π-conjugated polymer electrochemical devices. *Science*, 297(5583):983–987, 2002.

[52] Krishna Rajan, Annalisa Chiappone, Denis Perrone, Sergio Bocchini, Ignazio Roppolo, Katarzyna Bejtka, Micaela Castellino, Candido Fabrizio Pirri, Carlo Ricciardi, and Alessandro Chiolerio. Ionic liquid-enhanced soft resistive switching devices. *RSC advances*, 6(96):94128–94138, 2016.

[53] Jianmin Zhang, Weize Wu, Tao Jiang, Haixiang Gao, Zhimin Liu, Jun He, and Buxing Han. Conductivities and viscosities of the ionic liquid [bmim][pf6]+ water+ ethanol and [bmim][pf6]+ water+ acetone ternary mixtures. *Journal of Chemical & Engineering Data*, 48(5):1315–1317, 2003.

[54] Natalia V Plechkova and Kenneth R Seddon. Applications of ionic liquids in the chemical industry. *Chemical Society Reviews*, 37(1):123–150, 2008.

[55] Zhongmou Chao, Brian P Radka, Ke Xu, Garrison M Crouch, Donghoon Han, David B Go, Paul W Bohn, and Susan K Fullerton-Shirey. Direct-write formation and dissolution of silver nanofilaments in ionic liquid-polymer electrolyte composites. *Small*, 14(39):1802023, 2018.

[56] T Tsuruoka, K Terabe, T Hasegawa, and M Aono. Forming and switching mechanisms of a cation-migration-based oxide resistive memory. *Nanotechnology*, 21(42):425205, 2010.

[57] Takuro Tamura, Tsuyoshi Hasegawa, Kazuya Terabe, Tomonobu Nakayama, Toshitsugu Sakamoto, Hajime Sunamura, Hisao Kawaura, Sumio Hosaka, and Masakazu Aono. Switching property of atomic switch controlled by solid electrochemical reaction. *Japanese journal of applied physics*, 45(4L):L364, 2006.

[58] Yuchao Yang, Peng Gao, Siddharth Gaba, Ting Chang, Xiaoqing Pan, and Wei Lu. Observation of conducting filament growth in nanoscale resistive memories. *Nature communications*, 3(1):1–8, 2012.

[59] Ugo Russo, Daniele Ielmini, Carlo Cagli, and Andrea L Lacaita. Self-accelerated thermal dissolution model for reset programming in unipolar resistive-switching memory (rram) devices. *IEEE Transactions on Electron Devices*, 56(2):193–200, 2009.

[60] G Mao, M-L Saboungi, David L Price, YS Badyal, and HE Fischer. Lithium environment in peo-liclo4 polymer electrolyte. *EPL (Europhysics Letters)*, 54(3):347, 2001.

[61] Susan K Fullerton-Shirey and Janna K Maranas. Effect of liclo4 on the structure and mobility of peo-based solid polymer electrolytes. *Macromolecules*, 42(6):2142–2156, 2009.

[62] Md Abu Bin Hasan Susan, Taketo Kaneko, Akihiro Noda, and Masayoshi Watanabe. Ion gels prepared by in situ radical polymerization of vinyl monomers in an ionic liquid and their characterization as polymer electrolytes. *Journal of the American Chemical Society*, 127(13):4976–4983, 2005.

[63] Mark P Scott, Christopher S Brazel, Michael G Benton, Jimmy W Mays, John D Holbrey, and Robin D Rogers. Application of ionic liquids as plasticizers for poly (methyl methacrylate). *Chemical communications*, (13):1370–1371, 2002.

[64] JY Song, YY Wang, and C Cv Wan. Review of gel-type polymer electrolytes for lithium-ion batteries. *Journal of power sources*, 77(2):183–197, 1999.

[65] Changyu Tang, Ken Hackenberg, Qiang Fu, Pulickel M Ajayan, and Haleh Ardebili. High ion conducting polymer nanocomposite electrolytes using hybrid nanofillers. *Nano letters*, 12(3):1152–1156, 2012.

[66] C Berthier, W Gorecki, M Minier, MB Armand, JM Chabagno, and Ph Rigaud. Microscopic investigation of ionic conductivity in alkali metal salts-poly (ethylene oxide) adducts. *Solid State Ionics*, 11(1):91–95, 1983.

[67] Stephen D Druger, Mark A Ratner, and A Nitzan. Polymeric solid electrolytes: Dynamic bond percolation and free volume models for diffusion. *Solid State Ionics*, 9:1115–1120, 1983.

[68] Tai-Wei Hwang and Paul W Bohn. Robust au–ag–au bimetallic atom-scale junctions fabricated by self-limited ag electrodeposition at au nanogaps. *ACS nano*, 5(10):8434–8441, 2011.

[69] Tai-Wei Hwang and Paul W Bohn. Potential-dependent restructuring and chemical noise at au–ag–au atomic scale junctions. *ACS nano*, 8(2):1718–1727, 2014.

[70] CD Robitaille and D Fauteux. Phase diagrams and conductivity characterization of some peo-lix electrolytes. *Journal of The Electrochemical Society*, 133(2):315–325, 1986.

[71] Zlatka Gadjourova, Yuri G Andreev, David P Tunstall, and Peter G Bruce. Ionic conductivity in crystalline polymer electrolytes. *Nature*, 412(6846):520–523, 2001.

[72] Yuri G Andreev and Peter G Bruce. Using crystallography to understand polymer electrolytes. *Journal of Physics: Condensed Matter*, 13(36):8245, 2001.

[73] Graham S MacGlashan, Yuri G Andreev, and Peter G Bruce. Structure of the polymer electrolyte poly (ethylene oxide) 6: Liasf 6. *Nature*, 398(6730):792–794, 1999.

[74] Se Hyun Kim, Kihyon Hong, Keun Hyung Lee, and C Daniel Frisbie. Performance and stability of aerosol-jet-printed electrolyte-gated transistors based on poly (3-hexylthiophene). *ACS applied materials & interfaces*, 5(14):6580–6585, 2013.

[75] Wu Shi, Jianting Ye, Yijin Zhang, Ryuji Suzuki, Masaro Yoshida, Jun Miyazaki, Naoko Inoue, Yu Saito, and Yoshihiro Iwasa. Superconductivity series in transition metal dichalcogenides by ionic gating. *Scientific reports*, 5:12534, 2015.

[76] Hua-Min Li, Ke Xu, Buchanan Bourdon, Hao Lu, Yu-Chuan Lin, Joshua A Robinson, Alan C Seabaugh, and Susan K Fullerton-Shirey. Electric double layer dynamics in poly (ethylene oxide) liclo4 on graphene transistors. *The Journal of Physical Chemistry C*, 121(31):16996–17004, 2017.

[77] JA Manzanares, S Mafé, and J Bisquert. Electric double layer at the membrane/solution interface: distribution of electric potential and estimation of the charge

stored. *Berichte der Bunsengesellschaft für physikalische Chemie*, 96(4):538–544, 1992.

[78] RF Hamou, Paul Ulrich Biedermann, Andreas Erbe, and Michael Rohwerder. Numerical analysis of debye screening effect in electrode surface potential mapping by scanning electrochemical potential microscopy. *Electrochemistry communications*, 12(10):1391–1394, 2010.

[79] Elliot Schmidt, Sha Shi, P Paul Ruden, and C Daniel Frisbie. Characterization of the electric double layer formation dynamics of a metal/ionic liquid/metal structure. *ACS applied materials & interfaces*, 8(23):14879–14884, 2016.

[80] Yuchao Yang, Peng Gao, Linze Li, Xiaoqing Pan, Stefan Tappertzhofen, ShinHyun Choi, Rainer Waser, Ilia Valov, and Wei D Lu. Electrochemical dynamics of nanoscale metallic inclusions in dielectrics. *Nature communications*, 5(1):1–9, 2014.

[81] Filipp Akopyan, Jun Sawada, Andrew Cassidy, Rodrigo Alvarez-Icaza, John Arthur, Paul Merolla, Nabil Imam, Yutaka Nakamura, Pallab Datta, Gi-Joon Nam, et al. Truenorth: Design and tool flow of a 65 mw 1 million neuron programmable neurosynaptic chip. *IEEE transactions on computer-aided design of integrated circuits and systems*, 34(10):1537–1557, 2015.

[82] Elliot J Fuller, Scott T Keene, Armantas Melianas, Zhongrui Wang, Sapan Agarwal, Yiyang Li, Yaakov Tuchman, Conrad D James, Matthew J Marinella, J Joshua Yang, et al. Parallel programming of an ionic floating-gate memory array for scalable neuromorphic computing. *Science*, 364(6440):570–574, 2019.

[83] Eveline RW van Doremaele, Paschalis Gkoupidenis, and Yoeri van de Burgt. Towards organic neuromorphic devices for adaptive sensing and novel computing paradigms in bioelectronics. *Journal of Materials Chemistry C*, 7(41):12754–12760, 2019.

[84] Paschalis Gkoupidenis, Dimitrios A Koutsouras, and George G Malliaras. Neuromorphic device architectures with global connectivity through electrolyte gating. *Nature communications*, 8(1):1–8, 2017.

[85] Dimitrios A Koutsouras, Themis Prodromakis, George G Malliaras, Paul WM Blom, and Paschalis Gkoupidenis. Functional connectivity of organic neuromorphic devices by global voltage oscillations. *Advanced Intelligent Systems*, 1(1):1900013, 2019.

[86] Robert A Erb. Wettability of gold. *The Journal of Physical Chemistry*, 72(7):2412–2417, 1968.

[87] Maged A Osman and Beat A Keller. Wettability of native silver surfaces. *Applied surface science*, 99(3):261–263, 1996.

[88] Le Zhong, Liudi Jiang, Ruomeng Huang, and CH De Groot. Nonpolar resistive switching in cu/sic/au non-volatile resistive memory devices. *Applied Physics Letters*, 104(9):093507, 2014.

[89] Chao Chen, Shuang Gao, Guangsheng Tang, Cheng Song, Fei Zeng, and Feng Pan. Cu-embedded aln-based nonpolar nonvolatile resistive switching memory. *IEEE electron device letters*, 33(12):1711–1713, 2012.

[90] Yiyang Li, Elliot J Fuller, Shiva Asapu, Sapan Agarwal, Tomochika Kurita, J Joshua Yang, and A Alec Talin. Low-voltage, cmos-free synaptic memory based on li x tio2 redox transistors. *ACS applied materials & interfaces*, 11(42):38982–38992, 2019.

[91] John S Wilkes. A short history of ionic liquids—from molten salts to neoteric solvents. *Green Chemistry*, 4(2):73–80, 2002.

[92] Jerry L Atwood. Multidentate macromolecular complex salt clathrates, January 29 1985. US Patent 4,496,744.

[93] A Guerfi, M Dontigny, P Charest, M Petitclerc, M Lagacé, A Vijh, and K Zaghib. Improved electrolytes for li-ion batteries: Mixtures of ionic liquid and organic electrolyte with enhanced safety and electrochemical performance. *Journal of Power Sources*, 195(3):845–852, 2010.

[94] Irene Osada, Henrik de Vries, Bruno Scrosati, and Stefano Passerini. Ionic-liquid-based polymer electrolytes for battery applications. *Angewandte Chemie International Edition*, 55(2):500–513, 2016.

[95] A Harada, H Yamaoka, S Tojo, K Watanabe, A Sakaguchi, Kentaro Kinoshita, S Kishida, Y Fukaya, K Matsumoto, R Hagiwara, et al. Improved performance of a conducting-bridge random access memory using ionic liquids. *Journal of Materials Chemistry C*, 4(30):7215–7222, 2016.

[96] Xin Kang, Jiajun Guo, Yingjie Gao, Shuxia Ren, Wei Chen, and Xu Zhao. Nio-based resistive memory devices with highly improved uniformity boosted by ionic liquid pre-treatment. *Applied Surface Science*, 480:57–62, 2019.

[97] Hee-Jin Rhoo, Hee-Tak Kim, Jung-Ki Park, and Taek-Sung Hwang. Ionic conduction in plasticized pvcpmma blend polymer electrolytes. *Electrochimica acta*, 42(10):1571–1579, 1997.

[98] Wan-Jin Lee, Hong-Ryun Jung, Moo Sung Lee, Jong-Ho Kim, and Kap Seung Yang. Preparation and ionic conductivity of sulfonated-sebs/sio2/plasticizer composite polymer electrolyte for polymer battery. *Solid State Ionics*, 164(1-2):65–72, 2003.

[99] Mo Chen, Robert Pendrill, Goran Widmalm, John W Brady, and Jakob Wohlert. Molecular dynamics simulations of the ionic liquid 1-n-butyl-3-methylimidazolium chloride and its binary mixtures with ethanol. *Journal of chemical theory and computation*, 10(10):4465–4479, 2014.

[100] Donghoon Han, Garrison M Crouch, Zhongmou Chao, Susan K Fullerton-Shirey, David B Go, and Paul W Bohn. Nanopore-templated silver nanoparticle arrays photopolymerized in zero-mode waveguides. *Frontiers in chemistry*, 7:216, 2019.

[101] Ke Xu, Jierui Liang, Aaron Woeppel, M Eli Bostian, Hangjun Ding, Zhongmou Chao, James R McKone, Eric J Beckman, and Susan K Fullerton-Shirey. Electric double-layer gating of two-dimensional field-effect transistors using a single-ion conductor. *ACS applied materials & interfaces*, 11(39):35879–35887, 2019.